MINIATURE MEMS-BASED ADAPTIVE ANTENNAS ON FLEXIBLE SUBSTRATES

by

Gordon Michael Coutts

A thesis
presented to the University of Waterloo
in fulfillment of the
thesis requirement for the degree of
Doctor of Philosophy
in
Electrical and Computer Engineering

Waterloo, Ontario, Canada, 2007

AUTHOR'S DECLARATION

I hereby declare that I am the sole author of this thesis. This is a true copy of the thesis, including any required final revisions, as accepted by my examiners.

I understand that my thesis may be made electronically available to the public.

ABSTRACT

Current trends in technology are moving to increased use of wireless communication with rapidly increasing data transmission rates and higher frequencies. Miniaturization is essential to allow electronics of increasing complexity to fit into smaller devices. Adaptive technologies allow a single system to operate across multiple wireless protocols, adjusting to changing conditions to minimize interference and enhance performance. Flexibility is essential as the use of wireless technology increases and spreads to new industries.

The objective of this research is twofold: to develop novel reconfigurable electromagnetic structures and a novel process to fabricate microelectromechanical systems (MEMS) devices on flexible substrates. The novel electromagnetic structures are passive frequency-switchable parasitic antennas, conformal MEMS-tunable frequency selective surfaces (FSS) and MEMS-tunable electromagnetic bandgap (EBG) structures. Fabricating the reconfigurable conformal FSS and EBG structures requires the development of a new fabrication process to produce MEMS devices monolithically integrated onto a flexible substrate.

Novel frequency-switchable parasitic antenna arrays are developed, fabricated and measured. The structure radiates efficiently when placed over metal and absorbing material, improving the range of conventional RFID systems, as well as minimizing blind spots to provide continuous coverage in a hemisphere. A novel analysis method is developed to characterize frequency-switchable parasitic patch arrays. The purpose of the analysis is to provide an approximation of the input impedance and variation of the radiation pattern with frequency. The analysis combines models based on electromagnetic theory and circuit theory to provide a fast and yet reasonable approximation of the parasitic array characteristics. The analysis also provides a good deal of physical insight into the operation of multi-mode parasitic patch arrays. The end result is an initial array design which provides a good starting point for full EM simulation and optimization. The new analysis method is validated alongside measured and simulated results, with good correlation for both impedance characteristics and far-field radiation patterns.

A MEMS-based switched parasitic antenna array is designed, fabricated and measured with good correlation between simulated and measured results. The structure is a direct-coupled parasitic patch array which is capable of frequency steering and has additional MEMS-enabled beam-steering capabilities at each frequency.

An EBG-based multi-mode radiating structure design is presented, which is capable of frequency-switchable beam steering. The antenna area is significantly reduced compared to the parasitic patch array structure, but at a considerable cost in terms of gain and efficiency.

A novel MEMS process is developed to fabricate large numbers of high-performance MEMS devices monolithically integrated onto a rigid-flex organic substrate using low-temperature processes. The rigid-flex substrate is all dielectric, which is amenable to low-loss electromagnetic structures. The substrate provides mechanical support to the MEMS devices while maintaining overall flexibility. The adaptation of each fabrication process step to handle flexible substrates is analyzed and documented in detail.

The newly-developed MEMS process is used to fabricate a MEMS reconfigurable frequency-selective surface. A practical bias network is incorporated into the structure design to ensure that all devices are actuated simultaneously. FSS structures operating in the Ku and Ka bands are fabricated and tested, with good correlation between simulated and measured results for individual devices as well as the entire FSS structures. The newly-developed MEMS process is also used to fabricate a MEMS reconfigurable electromagnetic bandgap structure. An EBG structure operating in the Ka band is fabricated and tested to verify the validity of the proposed concept.

ACKNOWLEDGEMENTS

These past few years at Waterloo have been an interesting and rewarding experience. I would like to thank my advisers Professor Raafat Mansour and Professor Sujeet Chaudhuri for their constant support, encouragement and advice. I would also like to thank Bill Jolley and Roger Grant for their help and support in using the RF lab and clean room facility. Thank you to my colleagues at the Centre for Integrated RF Engineering for the training and advice in the art and science of MEMS fabrication processes. Thank you to Professor Safavi-Naeini for the enlightening discussions about antenna theory. Thank you to my Parents for raising me in the loving, nurturing environment, surrounded by books, which led to an insatiable thirst for knowledge.

Finally, I dedicate this thesis to my brilliant loving wife Pauline and my wonderful son Joshua. Thank you for all of your love and support.

TO PAULINE AND JOSHUA

TABLE OF CONTENTS

LIST OF FIGURES

LIST OF TABLES

CHAPTER 1

INTRODUCTION

1.1 MOTIVATION

Current trends in technology are moving to increased use of wireless communication with rapidly increasing data transmission rates and higher frequencies. Miniaturization is essential to allow electronics of increasing complexity to fit into smaller devices. Adaptive technologies allow a single system to operate across multiple wireless protocols, adjusting to changing conditions to minimize interference and enhance performance. Flexibility is essential as the use of wireless technology increases and spreads to new industries.

1.1.1 RADIO FREQUENCY IDENTIFICATION

A significant emerging wireless industry is global logistics, which is moving towards the ubiquitous deployment of radio frequency identification (RFID) for asset tracking and monitoring. Passive RFID tags derive their power from the incident RF signal and modulate

the backscatter, which is decoded by a reader. Typical long-range passive RFID tags use folded dipole antennas, and have a maximum read range on the order of 3 meters [1].

There is a growing necessity to monitor container shipments due to increasing global trade and security issues. There is a need for greater range at ports, on ships, and to read information from containers on passing trains and trucks. Conventional passive RFID systems are unsuitable for such applications since dipole antennas cannot radiate efficiently when attached to a metal container, in addition to their limited range and large blind spots.

To overcome these limitations, microstrip patch antennas are the obvious choice of radiating structure as they are low-profile and radiate efficiently in the presence of metal. Individual antennas, however, radiate broadside. This prevents the reader from accessing the RFID tag unless it is directly facing the patch antenna. Previously, researchers have used coupled parasitic patch antennas to enhance the impedance bandwidth of microstrip antennas [2]-[4]. It was noted that the radiation pattern changed with frequency across the bandwidth of the parasitic patch arrays [2]. For most applications, it is desirable to minimize radiation pattern variation across the band. For the proposed application, however, it is desirable to maximize the changes in radiation pattern with varying frequency.

Conventional steerable antennas require active devices (switches, varactors, phase shifters) which need a power supply. For a passive frequency-steerable antenna array, no active devices are required to steer the beam. The array is designed with multiple resonant modes, such that the radiation pattern changes with frequency. The direction of communication can therefore be changed by simply changing the RFID reader frequency. The switching speed is virtually instantaneous, limited only by the inductance and capacitance of the antenna structure. The larger aperture offered by an array, combined with the ability to direct more of the radiated signal in a given direction, will significantly increase the read range compared to that of a conventional RFID system. Additional advantages of the parasitic patch array arise in the unique ability to pinpoint the location and orientation of RFID tags with multiple readers, since the direction of communication changes with frequency. Another system consideration is the anticollision performance, in which the RFID reader must handle

communication with multiple tags in its read range that respond simultaneously to interrogation. At each frequency, the angular direction of tag communication is limited for the proposed array, enhancing the anticollision performance since fewer tags will communicate with the reader at any given time.

1.1.2 Frequency Selective Surfaces for Satellite Applications

Currently, many direct broadcast satellites operate in the Ku band, and next generation systems such as Spaceway operate in the Ka band to offer broadband services [5], [6]. Broadband applications include high-speed data, audio and video streaming, and internet access [5]. Communications satellites are extremely costly to design, manufacture and launch. Flexibility is essential for future broadcast satellites, namely the ability to modify the services provided to customers and the ability to move capacity from one coverage area to another where it may be better used [7]. Satellites in geostationary orbit use large reflector antennas with multiple feeds to generate spot beams that target specific geographic regions and allow frequency-reuse [8]. Next generation satellites have on-board switching and support for Internet Protocol (IP) to allow for some adaptation to changing conditions [5]-[8]. The ability to add reconfigurability to the satellite antennas would enhance the ability of the satellite to move capacity to where it is needed, further mitigating investment risk.

A candidate technology for reconfigurable satellite antennas are frequency selective surfaces (FSS), which act as 2-dimensional filters to propagating electromagnetic waves. Fixed-frequency conformal frequency-selective surfaces on Kapton [9] film have flown on deep-space missions such as Voyager and Cassini [10]. On these spacecraft, the conformal FSS formed part of the main reflector antenna, and was mounted on a hyperboloidal secondary reflector. By selectively reflecting or transmitting signals at different frequencies, a single reflector antenna could be used for multiple bands, with feeds located on either side of the FSS.

Additional military applications of frequency-selective surfaces are conformal radomes [10]. A FSS-based radome shields antenna arrays that have large out-of band radar cross-sections [10], [12]. The FSS is transparent across the limited bandwidth over which the

antennas operate. For wideband and multiple band antennas, a tunable radome will provide out-of-band shielding while allowing transmission at multiple frequencies.

MEMS-Tunable FSS structures have been fabricated on rigid substrates [11], but a conformal structure on a flexible substrate is required to mount the FSS on the curved surfaces of a reflector antenna. We propose a MEMS-tunable conformal FSS monolithically integrated onto a novel bulk micromachined rigid-flex Kapton substrate. This structure provides additional reconfigurability for multi-band reflector antennas, which would be useful in the aforementioned satellite applications. Operation in the Ku and Ka bands enable compatibility with current and next generation satellite systems.

Tunable frequency selective surfaces have been fabricated using varactor diodes [13], pin diodes [14] and ferrite substrates [15]. PIN diodes and tunable ferrite substrates require a substantial amount of biasing current. Discrete devices such as varactor diodes and PIN diodes requiring hybrid integration are not amenable to periodic structures having a large number of devices operating at the Ka band. To fabricate the proposed FSS structures in a cost-effective way, MEMS is the enabling technology. Large numbers of high-performance devices are monolithically integrated onto a rigid-flex organic substrate using low-temperature processes. Researchers have fabricated MEMS on rigid-flex substrates that used islands of silicon to mechanically support the devices [16], [17]. The proposed rigid-flex substrate is all dielectric, which is amenable to low-loss electromagnetic structures. Monolithic integration of MEMS devices will result in structures capable of high-frequency operation in the Ka band and beyond. Large numbers of electrostatically actuated MEMS devices may be actuated simultaneously with almost no sustained biasing current.

1.1.3 ELECTROMAGNETIC BANDGAP STRUCTURES

Electromagnetic Bandgap (EBG) structures are periodic arrays of electrically small unit cells that suppress surface currents over a limited bandwidth [18]. This approximates a zero tangential magnetic field causing the structure to behave as a magnetic conductor [18]. Using conventional technology, a monopole or dipole antenna in close proximity to a ground plane will not radiate since the reflected radiated field from an electrical conductor is out of phase

with the incident signal, canceling the radiated energy. For the band over which an EBG structure behaves as a magnetic conductor, the incident and reflected fields are in-phase, resulting in constructive interference that permits low-profile printed monopole and dipole antennas to radiate [18]. The EBG structure thus offers additional degrees of freedom to the designer for the purpose of developing reconfigurable antennas. The addition of tunable elements to an EBG structure will further enhance reconfigurability.

Varactor-tuned planar EBG reflectors capable of two-dimensional beam steering have recently been reported [19]. Lumped-element EBG structures fabricated in [19] and [20], however, show a significant amount of loss. Other researchers have endeavored to maximize the EBG losses to produce low-profile tunable absorbers [21]-[23].

As for the case of tunable frequency-selective surfaces, MEMS is an enabling technology for tunable EBG structures designed to operate in the Ka band and beyond since the performance of semiconductor devices degrades significantly at millimeter wave frequencies. Large numbers of MEMS devices may be monolithically integrated to produce a cost-effective reconfigurable EBG structure. With current technology, a MEMS-based EBG structure on a flexible substrate may function as a conformal tunable absorber. A tunable EBG structure integrated with antennas would increase the ability of a communication system to adapt to changing conditions. A conformal MEMS-tunable reflector would significantly enhance reconfigurability of antennas used in satellite applications. Further advances in materials technology would be required to mitigate losses before such applications would become practical. Although the concept of a reconfigurable electromagnetic bandgap structure is currently visionary, demonstrating the capabilities of fabricated hardware as a proof of concept will be vital for developing future applications [24].

1.2 RESEARCH OBJECTIVES

The objective of this research is twofold: to develop novel reconfigurable electromagnetic structures and a novel process to fabricate MEMS devices on flexible substrates. The novel

electromagnetic structures are passive frequency-switchable parasitic antennas, conformal MEMS-tunable frequency selective surfaces and MEMS-tunable electromagnetic bandgap structures. Fabricating the conformal FSS and EBG structures requires the development of a new MEMS process to produce devices monolithically integrated onto a flexible substrate.

i. **Design and fabrication of frequency-switchable antennas:** Frequency-switchable parasitic patch arrays are to be developed for RFID applications. The arrays will radiate efficiently when placed over metal and absorbing material, improving the range of conventional RFID systems, as well as minimizing blind spots to provide continuous coverage in a hemisphere. Switchable versions of the arrays are to be realized using hybrid assembly of MEMS switches. Performance enhancement using electromagnetic bandgap structures will be investigated.

ii. **Develop an analysis method for frequency-switchable parasitic patch arrays:** The purpose of the analysis is to provide an approximation of the input impedance and variation of the radiation pattern with frequency. The analysis allows the designer to avoid a time-consuming trial-and-error process by combining models based on electromagnetic theory and circuit theory to provide a reasonable approximation of the parasitic array characteristics. The analysis also provides a good deal of physical insight into the operation of multi-mode parasitic patch arrays. The end result is an initial array design which provides a good starting point for full EM simulation and optimization.

iii. **Develop a fabrication process for MEMS on flexible substrates:** Large numbers of high-performance MEMS devices are to be monolithically integrated onto a rigid-flex organic substrate using low-temperature processes. The rigid-flex substrate is all dielectric, which is amenable to low-loss electromagnetic structures. The substrate provides mechanical support to the MEMS devices while maintaining overall flexibility. The new fabrication process is to be developed in the Center for Integrated RF Engineering (CIRFE) clean room at the University of Waterloo.

iv. **Design and fabrication of MEMS reconfigurable frequency selective surfaces and electromagnetic bandgap structures:** The newly-developed MEMS process will be used to fabricate a MEMS reconfigurable frequency-selective surface. A practical bias network must be incorporated into the structure design to ensure that all devices are actuated simultaneously. Hardware designed to operate in the Ku and Ka bands will be fabricated and tested. The newly-developed MEMS process will also be used to fabricate a MEMS reconfigurable electromagnetic bandgap structure. Hardware designed to operate in the Ka band will be fabricated and tested. Reconfigurable antennas fabricated over this tunable EBG structure will be investigated.

1.3 STRUCTURE OF THE THESIS

Chapter 2 provides an overview of the theory surrounding the principal topics covered in this thesis, as well as a survey of relevant literature. The topics include RFID, MEMS fabrication processes on flexible substrates, reconfigurable frequency selective surfaces and reconfigurable EBG structures. Chapter 3 develops a frequency switchable parasitic antenna array for passive RFID applications. A novel analysis method is developed to reduce the time required to design the new antenna arrays. The analysis method is validated against measured data as well as results simulated using commercially available electromagnetic simulation software. The parasitic antenna structure functionality is further enhanced using MEMS switches, as well as EBG structures. Chapter 4 documents the development of a novel process to fabricate MEMS devices on an all-dielectric rigid-flex substrate. The documentation includes the modification of each fabrication process step required to handle the flexible materials. Moreover, information on material compatibility and a detailed justification of the choice of specific materials and processes provides a starting point for future research. Chapter 5 develops a reconfigurable MEMS-based frequency selective surface using the process developed in Chapter 4, as well as a MEMS-based reconfigurable EBG structure. A detailed description of the relevant design parameters and sensitivity analyses are provided, along with a discussion of measurement considerations for both

structures. Hardware was fabricated and tested, and results are presented alongside theoretical predictions. An experimental investigation of antenna performance over the reconfigurable EBG structure is carried out. Chapter 6 summarizes the significant contributions of this thesis research and proposes future areas of work.

CHAPTER 2

BACKGROUND INFORMATION

2.1 INTRODUCTION

This chapter provides a brief introduction to the theory surrounding the principal topics covered in this thesis, as well as a survey of relevant literature. This information is intended to provide context for the research projects that have been carried out by documenting the current state of the art.

Section 2.2 provides an introduction to the topic of radiofrequency identification, providing background for the RFID antennas developed in Chapter 3. Section 2.3 is a survey of the published MEMS fabrication processes on flexible substrates, which is relevant to the process development documented in Chapter 4. Section 2.4 documents the reconfigurable frequency-selective surfaces that have been reported in the literature, providing a background for the MEMS reconfigurable FSS covered in Chapter 5. Finally, Section 2.5 provides a brief

introduction to the extensive topic of electromagnetic bandgap structures, followed by a survey of reconfigurable structures that have been published. The EBG topics provide background information relevant to the EBG antenna documented in Chapter 3, as well as the MEMS reconfigurable EBG structure of Chapter 5.

2.2 RADIOFREQUENCY IDENTIFICATION (RFID)

Radiofrequency Identification (RFID) systems enable remote wireless access to data stored in the memory of a transponder, which is referred to as an RFID tag [25]. RFID systems, which have been around for decades, were originally used as aircraft identification transponders during the Second World War. The RFID tag consists of an antenna, a data storage device, and a transceiver. An RFID reader, which sends and receives RF signals, sends an interrogation command to the tag, which responds by transmitting the requested information back to the reader. Depending on the system requirements, data may be written to the tags, or they may be read-only.

Active RFID tags require a power source to operate all or part of the tag circuitry. Passive tags have no built-in power source. The passive tags must therefore obtain all power from the incident RF interrogation signal to run the on-board circuitry, which typically modulates and reflects part of the signal back to the reader.

The method of communicating between the reader and tags depends on the frequency of operation. Lower frequency tags use magnetic induction to couple energy from tag to reader. In this case, the range is limited to a few centimeters since the field intensity varies as $1/r^3$ for magnetic induction. Applications include access control cards, inventory control, animal identification and smart cards [25]. The 'low frequency' passive tags, which communicate via magnetic induction, operate from 100-500kHz. The 'intermediate frequency' passive tags also operate using magnetic induction at frequencies from 10-15MHz.

High frequency tags operate at 433MHz, 850-950MHz, and at microwave frequencies in the range of 2.4-5.8GHz. Passive high-frequency tags have much longer ranges than their low frequency counterparts since they communicate using far-field propagating waves which

vary as $1/r^2$. Passive tag ranges may be over 10 meters and even farther for active tags which have built-in power supplies. High-frequency tags have the advantage of a longer range and faster data transfer rate, but they are more expensive than low-frequency tags and require line-of-sight communication [25]. Applications of high-frequency RFID systems include railroad car monitoring, road-toll collection and inventory control.

2.3 MEMS ON FLEXIBLE SUBSTRATES

MEMS devices are essentially integrated circuits with moving parts. Conventional integrated circuit techniques fabricate devices one layer at a time in additive or subtractive steps using photolithographic techniques. In order to produce a freely moving mechanical structure, a temporary supporting layer is used during fabrication as shown in Figure 2.1a. This layer is commonly referred to as a sacrificial layer since it is removed as the final step of a MEMS fabrication process as shown in Figure 2.1b.

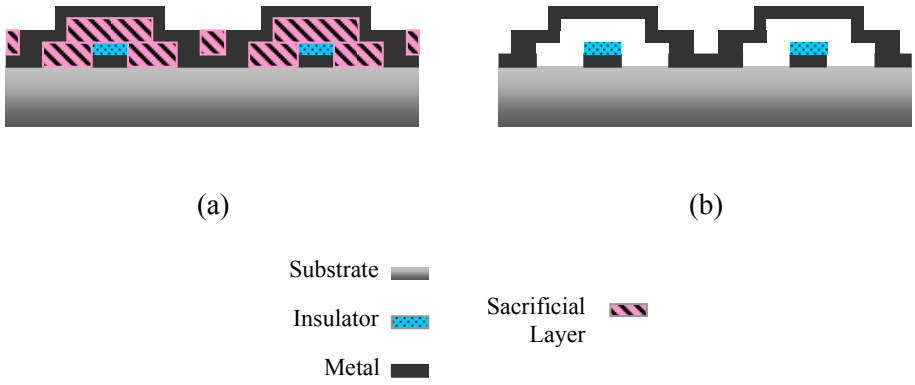

Figure 2.1: Typical MEMS device (a) Fabricated using sacrificial layer as a temporary support and (b) after releasing the device.

Radiofrequency MEMS devices may be passive or active. Passive RF MEMS devices are often used as sensors, where the RF properties of the device are dependent on some external condition such as pressure or temperature. Active RF MEMS devices are commonly used as

switches or variable capacitors. Depending on the choice of materials and device geometry, an applied force using thermal expansion, electrostatic or magnetostatic forces will change the geometry which correspondingly modifies the RF properties of the MEMS structure. A typical RF MEMS cantilever structure, which is shown in Figure 2.1b, is a popular choice of design since it may be actuated by electrostatic force, which results in a fast response time and no sustained current after switching. The MEMS device is actuated by applying a voltage between the cantilever and a pull-down electrode under the cantilever. The resultant electrostatic force pulls the cantilever down, and the insulating layer prevents a short circuit between the cantilever and electrode. The change in air gap with applied voltage results in a change in capacitance, which may be used for tuning or switching depending on the design parameters.

Conventional MEMS fabrication processes are designed to produce devices on rigid substrates such as silicon, glass and alumina. Fabricating MEMS devices on flexible substrates presents a significant challenge since the substrate must remain flat during processing, and the presence of organic materials limits the process temperature range. Several creative approaches to fabricating MEMS devices on flexible substrates have been reported in the literature, which are surveyed in this section. Section 2.3.1 documents several published processes in which the MEMS devices are mechanically supported by a rigid islands of silicon. Section 2.3.2 surveys the published MEMS processes for flexible substrates that are temporarily bonded to a rigid carrier for mechanical support.

2.3.1 MEMS DEVICES SUPPORTED BY RIGID SILICON ISLANDS

Figure 2.2 shows a published process used to produce a MEMS conformal array of pressure sensors on a flexible substrate [16]. MEMS devices are situated on the top side of the silicon wafer. Silicon nitride is used as a mask on the back side of the wafer, and completely covers the top of the wafer. The overall wafer thickness is reduced by wet etching using KOH (potassium hydroxide) or TMAH (tetra methyl ammonium hydroxide). The final thickness of the silicon is less than 100μm, so that the area between the silicon islands, when etched using reactive ion etching (RIE), will result in side walls that are almost vertical.

Following the back-side etch, aluminum is evaporated onto the top side of the wafer and patterned. The aluminum acts as an etch stop when the silicon islands are formed. The aluminum will bend as part of the flexible material between the silicon islands.

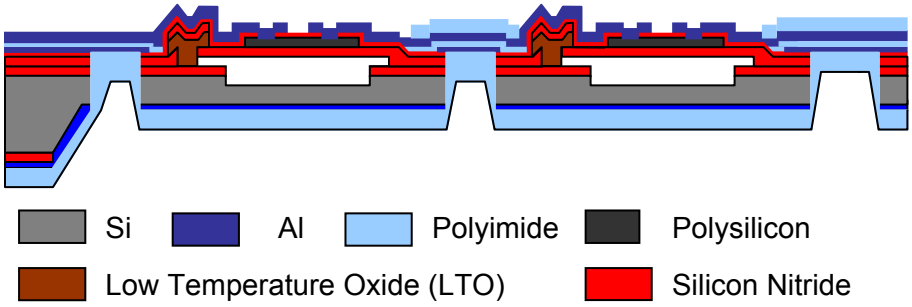

Figure 2.2: Conformal MEMS Sensor Array [16]

A 3-4µm polyimide layer is spin-coated, cured and patterned to cover the aluminum etch stop areas. The contacts used to connect the MEMS devices are exposed by etching the silicon nitride protective layer. A second layer of aluminum, used for the interconnections, is deposited and patterned. A second layer of polyimide is spin-coated, cured and patterned to cover the flexible network of interconnections.

Aluminum is deposited and patterned to form a mask on the back side of the wafer. SF_6 based RIE etching removes the silicon and silicon nitride between the islands. The silicon nitride must be removed as it is brittle and will crack when the substrate bends.

The final 10µm layer of polyimide is spin-coated and cured on the back side of the wafer to completely encapsulate the silicon islands. According to [16], the peel-off force of the polyimide from silicon is 0.23g/mm which is weak. Fully encapsulating the islands greatly increases the maximum tensile force to 3.57kg/mm.

The thickness of the silicon islands is less than 100µm, and allows for minimum island dimensions of 100µm x 100µm, and a minimum spacing between islands of 50µm [16]. It should be noted that the wafers are very fragile, and the individual array of devices must be

kept sufficiently small so that it will survive the fabrication process. The array of devices in [16] is 1cm by 3cm. The silicon islands are 450μm by 550μm and 75μm thick.

Figure 2.3 illustrates the effect of using different etching techniques on the geometry of the silicon islands, as shown in [16]. Figure 2.3a shows a cross-section of the silicon islands formed using HNA, an aggressive wet etching technique using a mixture of Hydrofluoric acid, Nitric Acid and Acetic Acid. The HNA etch is isotropic, resulting in the island tapering to a very thin edge that is extremely fragile. Figure 2.3b shows a more robust geometry formed by anisotropic wet etching (TMAH or KOH). Figure 2.3c uses a combination of anisotropic wet etching and RIE to yield a geometry that ensures a minimum thickness at the edges of the islands. The geometry of Figure 2.3c is the most robust of the three examples in Figure 2.3.

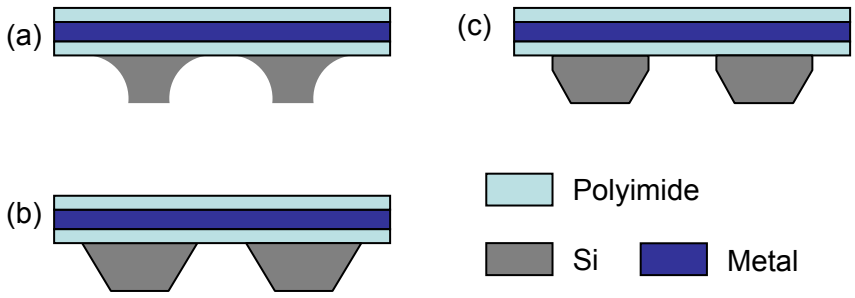

Figure 2.3: Comparison of different etch methods to produce silicon islands [16].

The process outlined in [26] and in Figure 2.4 produces an array of solid silicon probes with interconnects that are integrated onto a flexible substrate. The starting material is a double-oxide Si Wafer. Metal wires (Cr and Ni) are patterned over the oxide before spin-coating and curing polyimide to produce the flexible substrate. The silicon wafer is etched to form the probes using a combination of isotropic dry etching using XeF_2 and anisotropic Deep Reactive Ion Etching (DRIE). The final step is to coat the devices with spin on polyimide for insulation and to prevent the probes from detaching from the substrate.

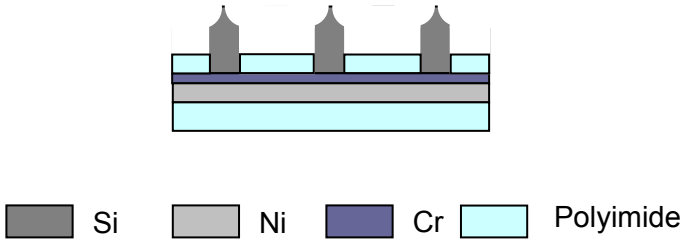

Figure 2.4: Silicon Probe Array [26]

The technique outlined in [17] uses boron doped silicon as the flexible substrate, and no polyimide. The heavily doped silicon is inherently flexible, and also acts as an etch stop for KOH wet etching [17]. Figure 2.5 shows the device, which has thick regions of undoped silicon as rigid islands, connected together with the flexible doped silicon.

The first step in the process is to define the islands with a deep boron diffusion. The flexible interconnect region is defined by a shallow boron diffusion. Defining the geometry using diffusion regions leads to rounded structures, which are more robust as they do not contain sharp corners that crack easily [17].

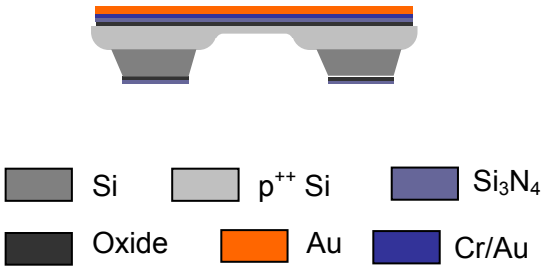

Figure 2.5: Flexible circuit process using boron diffusion [17]

A plating base of evaporated Cr, followed by Gold, is deposited on the top side of the wafer. The next step is to electroplate the gold conductor layer over the plating base. A

protective layer of nickel is then electroplated over the top side of the wafer since it is impervious to KOH wet etching.

The nickel protects the top of the wafer, and the silicon nitride protects the silicon islands. The boron diffusion acts as an etch stop, defining the final thickness of the flexible substrate. After completing the KOH etch step, the nickel and plating base are removed, leaving the interconnected silicon islands.

2.3.2 Flexible Substrates Temporarily Supported During MEMS Fabrication

Figure 2.6 shows a device fabricated using the procedure outlined in [27] and [28], where a silicon wafer is used to temporarily support the structure during fabrication. Silicon nitride is first deposited onto the Si wafer. The flexible substrate is built up by repeatedly spin-coating and curing layers of polyimide onto the wafer, until reaching the desired thickness. A layer of silicon nitride over the polyimide acts as both a passivation layer and an adhesion layer for the MEMS devices. After depositing the silicon nitride, the MEMS device is fabricated on the supported flexible substrate, shown in Figure 2.6. Upon completing the MEMS device fabrication, the final step is to release the flexible substrate from the silicon wafer.

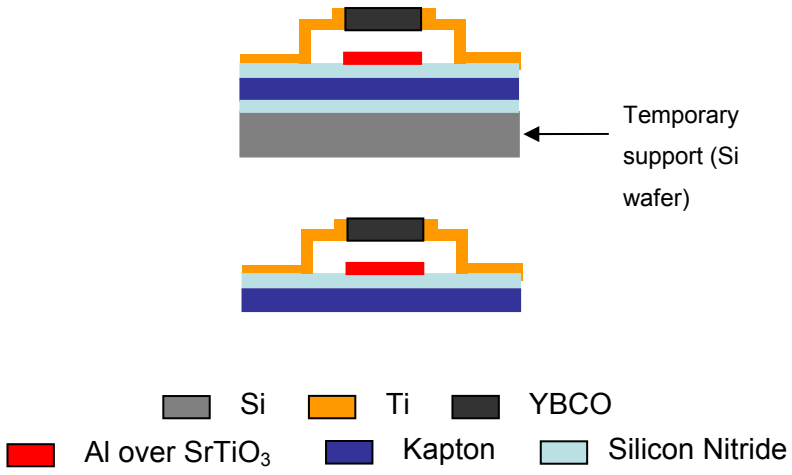

Figure 2.6: MEMS on Flexible Substrates Created on a Temporary Rigid Wafer Support [27], [28]

The process outlined in [29] uses micromachining techniques to produce conductive bumps that connect to MEMS integrated circuits in a hybrid assembly process (see Figure 2.7). Kapton film is the flexible substrate used for this process. PDMS (polydimethylsiloxane) temporarily attaches the Kapton to a silicon wafer to maintain flatness during the fabrication process. The flexible substrate can be easily peeled off after fabrication [29].

Gold is first deposited and patterned on the Kapton (with a Cr adhesion layer) to form the wires and bond pads. A laser then cuts out part of the Kapton film, and a thermoplastic conductive polymer is patterned using a lift-off technique with thick photoresist. The final step is to peel the Kapton film from the PDMS layer.

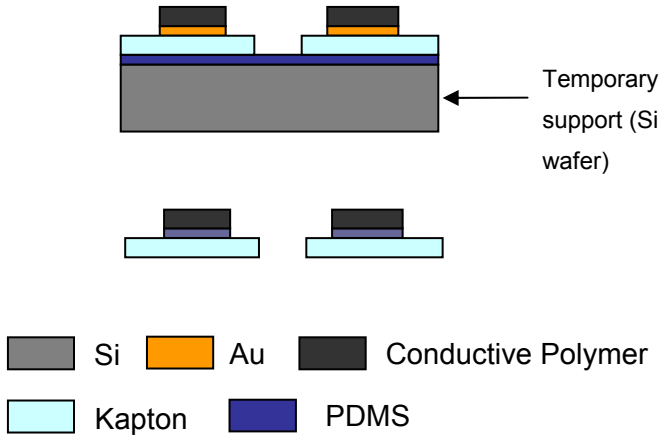

Figure 2.7: Process Flow for Flexible Circuit [29]

Recently, researchers have fabricated MEMS phase shifters on liquid crystal polymer (LCP) substrates [30], [31]. They address the flexibility issue by either temporarily bonding the material to a smooth rigid carrier using adhesives or by permanently attaching the LCP to a support using a thermal bonder. The unprocessed substrate, having 5-10 micron surface

roughness, is not sufficiently smooth for MEMS device fabrication. Two planarization methods were used to mitigate roughness issues: spin-coating and curing polyimide over the rough LCP surface [30], as well as mechanical polishing using an alumina slurry [30], [31]. As shown in Figure 2.8, electrostatically actuated MEMS cantilevers were fabricated using gold for the metal structure, and PECVD silicon nitride as a pull-down electrode insulator [30], [31]. Photoresist was used as a sacrificial layer, which was wet released in the final process steps, before drying the devices using a supercritical dryer.

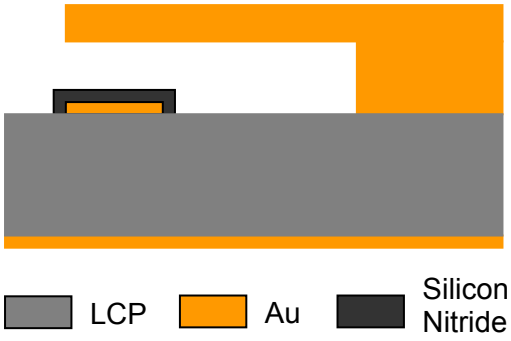

Figure 2.8: MEMS devices fabricated on LCP substrates [30], [31]

In [32], MEMS tactile sensor devices were fabricated on LCP substrates. RIE Oxygen plasma was used to etch bulk substrate material at a rate of 0.22-0.27μm/min. The researchers either directly laminated the LCP material to a rigid carrier or used photoresist as an adhesive. The MEMS sensors were fabricated on LCP with a NiCr strain gauge overlapping thick and thin substrate regions to form the transducer as shown in Figure 2.9. The first step is to pattern the strain gauge, followed by etching the back side of the LCP substrate using an Al etch mask and RIE oxygen plasma. The final steps are to pattern the gold traces and form a polyimide bump on the top.

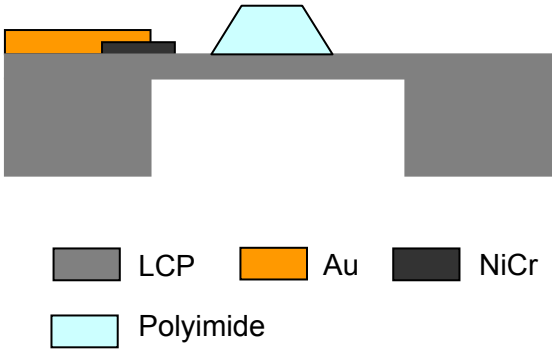

Figure 2.9: MEMS tactile sensor devices on LCP substrate [32]

In [33]-[34], a novel MEMS process fabricates inverted MEMS devices on a silicon wafer, which are then transferred to a flexible FR-4 substrate. Before fabricating devices, a silicon nitride layer is first deposited on the Si wafer. The next step is to fabricate the MEMS devices, which are cantilever structures that use silicon nitride as the pull-down electrode insulator and silicon dioxide as a sacrificial layer. After fabricating the inverted MEMS devices, the silicon wafer is flipped over and attached to the FR-4 substrate with an epoxy-based film using a wafer bonder. The final stage of the process is to eliminate the silicon wafer to leave the correctly oriented MEMS devices on the new substrate. Most of the Si wafer is removed by grinding, and the last 100 microns are KOH etched. The newly exposed silicon nitride layer, which protected the MEMS devices from KOH, is removed using RIE. The final process step is to release the MEMS devices using HF.

2.4 RECONFIGURABLE FREQUENCY SELECTIVE SURFACES

Two-dimensional periodic structures have the ability to filter propagating electromagnetic waves of certain frequencies. A periodic array of conducting patch or aperture elements may be used as a frequency-selective surface [10]. Arrays of patch elements, as shown in Figure 2.10a, reflect high frequency signals and transmit low frequencies, thus acting like a low-pass filter [10]. From a wave propagation point of view, when the patch is sufficiently large compared to the signal wavelength, the signal is scattered. Arrays of aperture elements, as

shown in Figure 2.10b, have a high-pass response that reflects low-frequency signals and transmits high-frequencies [10]. This is similar in principle to waveguides in which signals at frequencies below cutoff do not propagate.

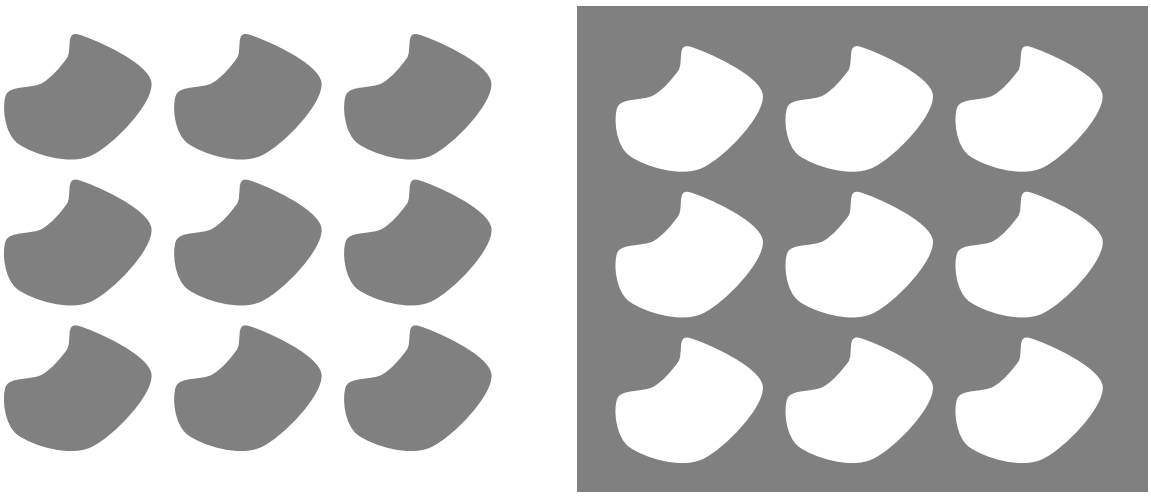

(a) (b)

Figure 2.10: Frequency selective surfaces (dark areas are conducting) consisting of (a) patch elements and (b) aperture elements

As will be shown in this survey, periodic arrangements of resonant structures may exhibit bandpass and bandstop responses. The elements and structure may be designed with symmetry for a similar response to signals of all polarizations, or designs may be intended to respond only to a specific polarization. For example, arrays of dipole elements have a stop band for a one linear polarization direction, and crossed-dipole elements respond to multiple polarizations.

This section surveys several different approaches which have been used to fabricate reconfigurable frequency-selective surfaces. The electromagnetic characteristics may be dynamically changed by using a ferrite substrate in an applied DC magnetic field or introducing a liquid dielectric behind the FSS as shown in Section 2.4.1. PIN diode and varactor diode tuning has been reported in several publications covered in Section 2.4.2. Published MEMS-tunable FSS structures are discussed in Section 2.4.3.

2.4.1 FSS TUNING BY CHANGING SUBSTRATE PROPERTIES OR GEOMETRY

In [35], a convoluted slot FSS with a bandpass response was fabricated with a hollow substrate that could be filled with liquid paraffin having relative dielectric constant 2.2. The FSS, which is shown in Figure 2.11, initially had 2.8dB insertion loss, and experienced a -3GHz frequency shift from 17GHz when liquid was added.

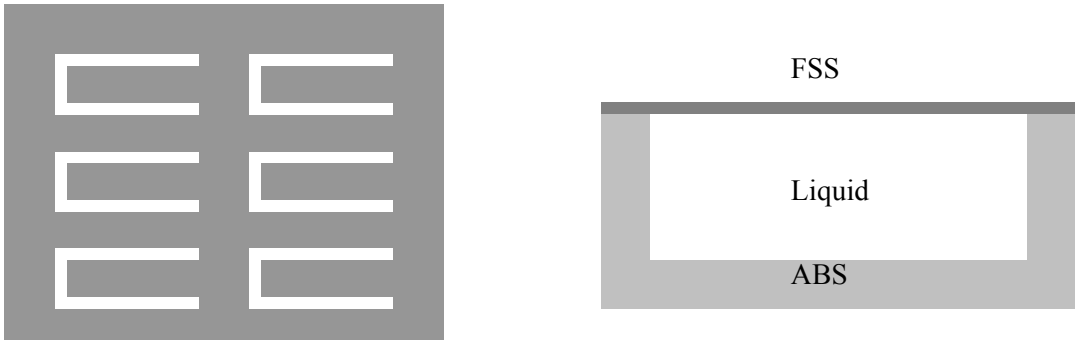

Figure 2.11: Tunable FSS from [35]. (a) Top view showing 6.5mm wide unit cells with 0.3mm wide slots (b) cross-sectional view showing 2mm thick liquid-filled cavity behind the FSS

Lockyer *et al* [36] used two closely spaced dipole FSS arrays to form a 2-layer structure. Tuning the stopband response was accomplished by laterally shifting the two structures relative to each other. The resonant frequency was shifted from 29GHz down to 14GHz with stopband rejection greater than 30dB. In [37], Lockyer *et al* accomplished similar tuning from 36GHz to 20GHz for a bandpass FSS.

In [15], a different approach to tuning involved fabricating a square loop FSS on a ferrite substrate. Two square loop unit cells were fabricated and measured in a waveguide test set achieving a bandstop response tunable from 8.7GHz to 14GHz. Switching performance at 8.7GHz showed 5dB on-state transmission loss and 30dB off-state isolation.

In [38], Edenhofer *et al* fabricated a FSS which was loaded with ferrite material and placed in a DC magnetic field where 0-1A current provided FSS tuning from 9.4GHz to 10.7GHz. The measurements were carried out using waveguides.

2.4.2 RECONFIGURABLE FSS USING DIODES

In addition to the ferrite FSS, Edenhofer *et al* fabricated a reconfigurable dipole grid FSS which used a more conventional tuning method [38]. Varactors were used to achieve a 7% frequency shift at 9.9GHz for capacitive loading variation between 25fF and 75fF. Bias lines with 10kΩ resistance connected the varactors.

In [39], varactor diodes are used to tune two loop resonators in a waveguide FSS setup between 1.6GHz and 2.6GHz. The bandstop response had 25-30dB rejection.

In [13] and [40], researchers fabricated bandstop FSS structures with perpendicular meandered dipole elements designed to operate in the 2.5GHz band and C-band respectively. A grid which provided bias to the devices was loaded with series-connected 390kΩ resistors to prevent unwanted resonances. The resistors, however, degraded transmission loss at frequencies below the stop band. The far-field C-band rejection, measured by placing the structure between horn antennas, was in the range of 8-12dB, likely degraded due to the varactor diode series resistance [40].

Chang *et al* [14] fabricated a switchable FSS comprised of broken square loop resonators with PIN diode switches that are forward biased to complete the loops. With the diodes on (forward bias), a waveguide test setup showed a 20dB bandstop transmission loss centered at 12.6GHz. Reverse biasing the diodes shifted the resonance to 36GHz, leaving the FSS in a transparent state with 0.5dB transmission loss at 12.6GHz.

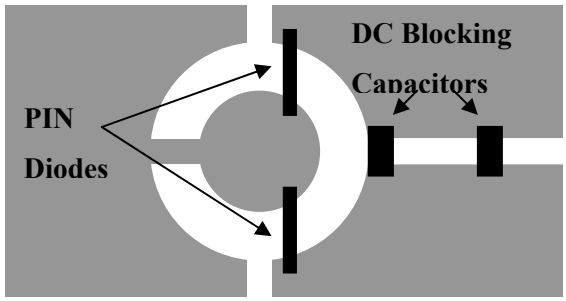

Figure 2.12: Switched bandpass FSS unit cell (dimensions 22.86mm x 10.13mm) from [41]

In [41], PIN diodes were used to control a switched bandpass FSS. A single fabricated unit cell, as shown in Figure 2.12, was measured in a waveguide test setup. The FSS was transparent when the diodes were reverse biased, with 1dB-5dB transmission loss between 9.5GHz and 12.5GHz. With 50mA forward bias current, the structure became reflective, with 20dB-30dB isolation over the 9.5-12.5GHz band.

2.4.3 RECONFIGURABLE MEMS-BASED FSS

A tunable FSS using magnetic MEMS devices has been fabricated in [42]-[44]. The FSS is an array of MEMS dipoles which were fabricated using plated CoNi magnetic material. As shown in Figure 2.13, the dipole is connected on one end to a polysilicon torsion beam. In an applied magnetic field, the dipole tilts away from the substrate, held at one end by the torsion beam. By varying the current through a coil surrounding the FSS, tilt angles from 0º to 71º were obtained. At the zero-tilt resonant frequency of 85GHz, the bandstop transmission loss was -18dB. The bandstop resonant frequency could be tuned +2GHz with a 30 degree deflection.

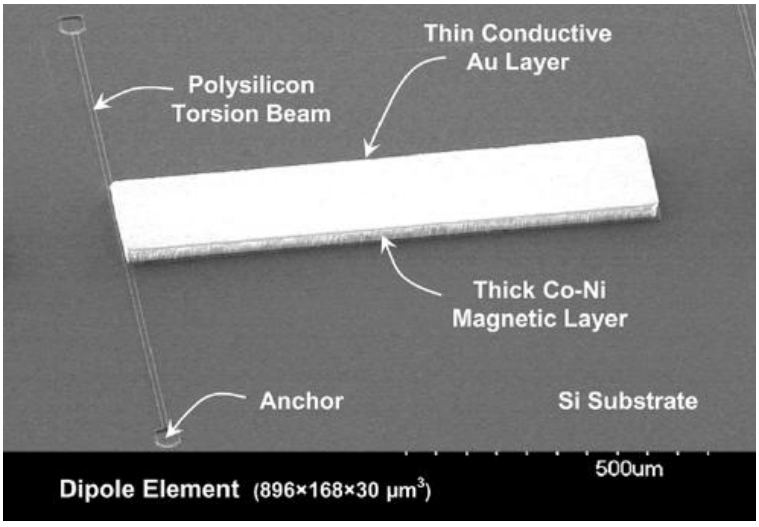

Figure 2.13: Magnetic MEMS-Tunable FSS structure from [44].

In [11], MEMS-tunable FSS structures have been fabricated on rigid substrates. The FSS is a 4-legged loaded element, as shown in Figure 2.14, which has a bandpass response. MEMS bridges keep the center elements connected together and isolated from the conducting plane. Electrostatically actuated MEMS switches load the centre of the structure to render the FSS electrically opaque at the upstate passband frequencies. The structure has a 30.2GHz up-state resonant frequency with 2.0dB transmission loss and 3.2GHz 3dB bandwidth. At a pull-down voltage of 17V, the transmission response drops to -27.5dB at 30.2GHz.

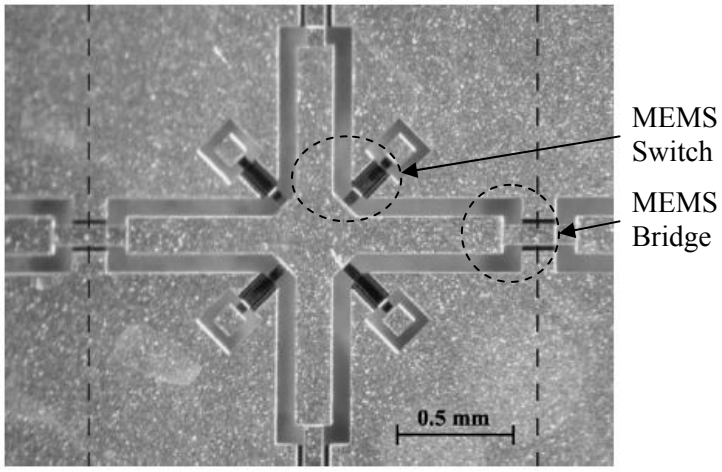

Figure 2.14: MEMS-Tunable FSS structure from [11]

2.5 RECONFIGURABLE ELECTROMAGNETIC BANDGAP STRUCTURES

This section covers the topic of reconfigurable EBG structures. Section 2.5.1 provides a brief overview of EBG theory. Section 2.5.2 and 2.5.3 survey reconfigurable EBG structures that have been reported in the literature. Section 2.5.2 documents the published 1-Dimensional reconfigurable EBG structures which operate based on the principle of periodically loaded transmission lines. Section 2.5.3 surveys 2-Dimensional reconfigurable EBG structures which have many potential applications in the field of antennas and electromagnetics.

2.5.1 EBG THEORY

Electromagnetic Bandgap (EBG) structures are periodic arrays of electrically small unit cells that suppress surface currents over a limited bandwidth [18]. EBG performance is often described from a physical perspective relating to the band theory of solids in which there exist allowed energy bands and forbidden gaps [45]. The physical model, which analyses electromagnetic waves propagating through a periodic structure (crystalline lattice) of charged atomic nuclei [45], may be scaled to analyze macroscopic structures. EBG theory may also be described using well-known principles governing the electrical performance of periodic structures in microwave engineering [46]. Mathematically, both methods are similar since the underlying principle is the same, namely wave propagation through a periodic structure. The microwave model, which we will examine in more detail, analyzes electromagnetic energy propagating along a transmission line periodically loaded with lumped-element reactive components [46]. Both models accurately predict signal propagation at certain frequencies, and strong attenuation at bandgap frequencies. The models of [45] and [46] simplify the analysis to a 1-dimensional case which may be expanded to 2 and 3 dimensions.

Following the microwave analysis of [46], we begin with a transmission line periodically loaded with lumped components of normalized susceptance $j\overline{B}$ spaced apart at a distance d. It is assumed that the periodic structure is formed by cascading an infinite number of identical loaded transmission line segments as shown in Figure 2.15a, which are equivalent to the transmission line segments of Figure 2.15b that have a complex propagation constant γ given by

$$\gamma = \alpha + j\beta . \tag{2.1}$$

The value α is the attenuation constant and β is the propagation (phase) constant. The characteristics of the frequency-dependent propagation constant γ are analyzed to determine propagating and evanescent (bandgap) frequencies.

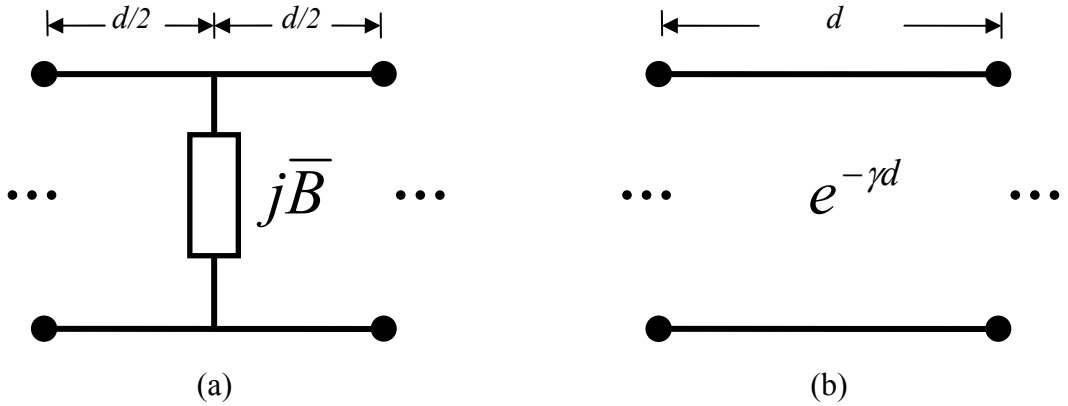

Figure 2.15: Infinite periodic structure model from [46] (a) Lumped-element loaded cascaded transmission line segment (b) Equivalent transmission line segment with complex propagation constant

The overall ABCD matrix for the short d/2 transmission line sections and lumped susceptance of Figure 2.15a are first derived, and equated to the equivalent transmission line expression of Figure 2.15b. Solving the eigenvalue equation yields the following expression for the complex propagation constant of the periodic structure [46]:

$$\cosh(\gamma d) = \cos(\theta) - \frac{\overline{B}}{2}\sin(\theta), \tag{2.2}$$

where the value θ is the phase shift along the transmission line segments of Figure 2.15. From this expression, it can be seen that for values

$$\left|\cos(\theta) - \frac{\overline{B}}{2}\sin(\theta)\right| < 1, \quad \gamma = j\beta, \ \alpha = 0, \tag{2.3}$$

the propagation constant is purely imaginary, which represents a propagating mode for frequencies and susceptance values that meet this criteria. For values

$$\cos(\theta) - \frac{\overline{B}}{2}\sin(\theta) > 1, \quad \gamma = \alpha, \ \ \beta = 0, \tag{2.4}$$

and

$$\cos(\theta) - \frac{\overline{B}}{2}\sin(\theta) < -1, \quad \gamma = \alpha + j\frac{\pi}{d}, \tag{2.5}$$

the propagation constant has a significant real component and frequency-independent imaginary value consistent with an evanescent wave. The frequencies which meet the criteria of Equations (2.4) and (2.5) form the bandgaps, where the signal experiences significant attenuation.

2.5.2 One-Dimensional Reconfigurable EBG Structures

Several reconfigurable EBG structures have been reported in the literature based on the 1-dimensional periodically loaded transmission line structure. MEMS-switchable periodic ground-plane defects are proposed in [47] which varies the propagation constant of microstrip feed lines to array antennas. Hard-wired prototypes demonstrated array beam steering by changing the feed line electrical length and therefore adjusting the signal phase at each antenna. In this case, the periodic structures were operating away from the bandgap frequencies.

Bandstop filters have been designed with periodically spaced patterns in coplanar waveguide ground planes that exhibit bandgap phenomena [48]-[50]. Additional transmission line loading with MEMS switches added tunability to the EBG-based filters. Hardware was

fabricated in [50] which exhibited bandstop response tuning from 17.3GHz – 19GHz with 1.3dB to 2.4dB lower passband insertion loss, and higher loss values above the stopband.

In [51], dipoles were periodically spaced under a microstrip transmission line, perpendicular to the direction of propagation, to create a bandstop filter. Part of the dipole conductor was replaced by high resistivity silicon. Tuning was accomplished by shining light on the structure, thus utilizing the photoconductive properties of silicon. The lower stopband edge could be decreased by approximately 20%.

In [52] and [53], a coplanar waveguide transmission line is periodically loaded with varactor diodes which permit cutoff frequency tunability. In [52], a 35% tuning range was reported in the 0.6-0.8GHz range, and in [53], a 3.5% tuning range is achieved around 9 GHz with maximum 4.75dB insertion loss.

2.5.3 TWO-DIMENSIONAL RECONFIGURABLE EBG STRUCTURES

Two-dimensional planar EBG structures have been reported extensively in the literature. The two-dimensional structures follow the same principal as the one-dimensional periodic structures described above. The 2-dimensional EBG structure consists of a repeating pattern of alternating electrical properties, such as conducting and insulating regions. Over certain bandwidths, surface waves will not propagate, thus approximating a zero tangential magnetic field causing the structure to behave as a magnetic conductor [18]. The basic EBG structures of [18], which are based on a 2-dimensional periodic array of patches over a grounded dielectric substrate, are illustrated in Figure 2.16. The resonant frequency may be reduced by designing a structure with two layers of overlapping patches [18].

Using conventional technology, a monopole or dipole antenna in close proximity to a ground plane will not radiate since the reflected radiated field from an electrical conductor is out of phase with the incident signal, canceling the radiated energy. For the band over which an EBG structure behaves as a magnetic conductor, the incident and reflected fields are in-phase, resulting in constructive interference that permits low-profile printed monopole and dipole antennas to radiate [18].

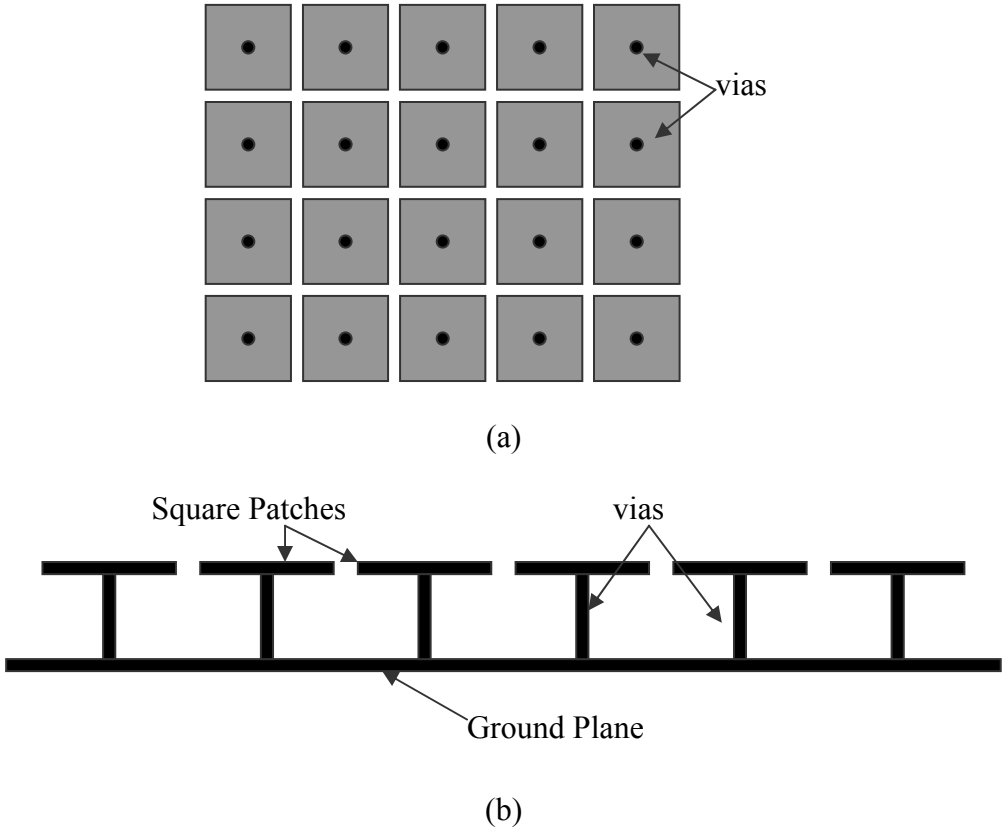

Figure 2.16: EBG structure reflector from [18] (a) Overhead view (b) Cross-sectional view

Varactor-tuned planar EBG reflectors capable of two-dimensional beam steering have recently been reported [19]. The EBG was fabricated on a 1.6mm thick RT/Duroid 5880 substrate, similar in geometry to the structure in Figure 2.16, with 9.2mm square patches separated by 0.4mm gaps. As shown in Figure 2.17, varactor diodes add capacitance between grounded square patches on the EBG surface, and alternating patches that are biased. Changing the varactor diode capacitance, which may vary between 0.2-0.8pF for the selected devices, adjusts the resonant frequency of the structure from 3.5-4.5GHz. At 4.5GHz, the reflection magnitude value is within the -3dB to -4dB range. For higher values of capacitance, however, the reflection magnitude decreases, attaining a value of -30dB at 3.5GHz. At 4.5GHz, where the structure had minimal loss, the varactor diodes were biased to

produce a capacitance distribution across the structure thus enabling reflective beam steering of up to 40 degrees, with 65% reflection efficiency.

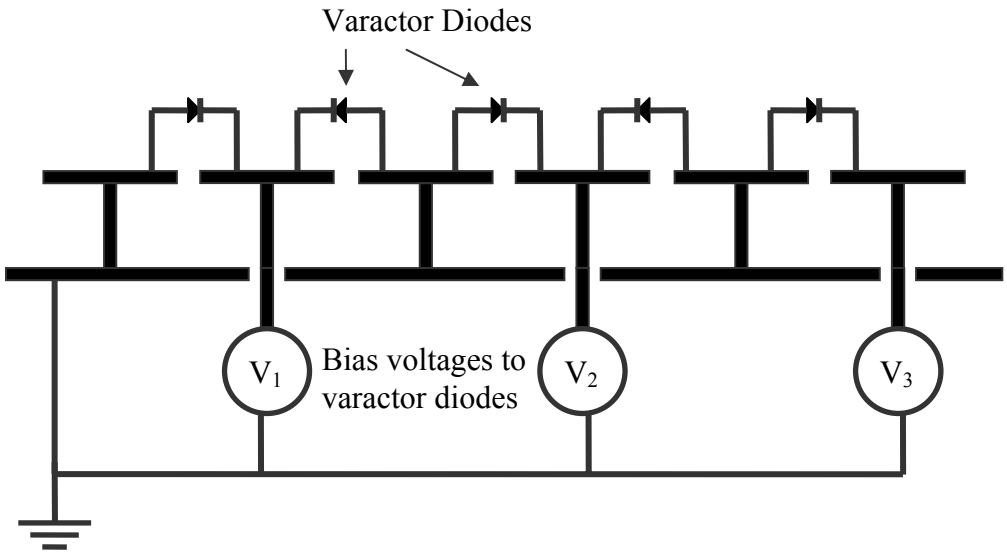

Figure 2.17: Varactor-tuned planar EBG reflector [19]

A varactor-tuned EBG structure was fabricated in [20], which has a different biasing scheme as shown in Figure 2.18. For this example, the substrate is 1.6mm thick FR-4, with 24.5mm grounded square patches separated by 3mm gaps. A DC isolated grid pattern between the grounded patches, having a 1mm conductor width, provides bias to the varactors. The EBG resonant frequency could be tuned from approximately 2.04GHz to 2.27GHz with reflection magnitude values that vary from -7dB to -16dB.

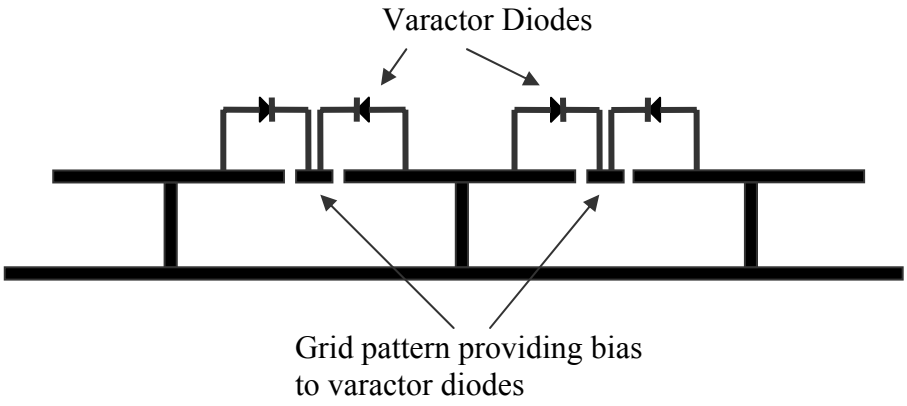

Figure 2.18: Varactor-tuned planar EBG reflector [20]

In [54], a tunable EBG was proposed having two layers separated by a thin dielectric. As shown in Figure 2.19, concentric conducting rings on the top layer partially overlap square patches on the bottom layer. Each conducting ring has 4 gaps which can either be left open, or shorted to complete the loop. The resonant frequency can be switched in discreet steps by setting the switches to select different loop combinations. Hardwired prototypes were fabricated for four states, which varied in frequency over more than a 3:1 bandwidth.

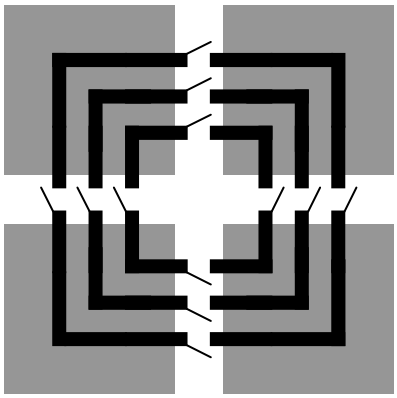

Figure 2.19: Switched tunable EBG structure proposed in [54]

In [55]-[57], tunable EBG structures have been simulated for dual-band operation. Optimization routines were developed in [56]. [57] provides simulated results of a planar

open-sleeve dipole antenna over a tunable EBG structure consisting of square patches connected by lumped capacitors. The antenna was positioned 5mm above the EBG structure. The maximum simulated gain was in the broadside direction, with values of 6.27dBi at 1.4GHz and 7.73dBi at 2.0 GHz.

In [58] and [59], the sidewalls of 30-40GHz waveguides were replaced by EBG structures as shown in Figure 2.20. For the bandwidth over which the EBG structure functions as an artificial magnetic conductor, surface currents are suppressed, permitting a nonzero tangential electric field at the sidewall. Additionally, fields are configured such that the tangential magnetic field is zero at the sidewall. The longitudinal magnetic field component therefore drops to zero. The overall result is configuration of uniform electric and magnetic fields across both transverse directions, and the propagation of a TEM wave along the waveguide. In [59], tunability is added by monolithically integrating InP triple quantum barrier varactors into the EBG structure. This enables the waveguide to operate as a reconfigurable phase shifter. Measured results indicate 320 degrees phase shift at 38GHz, with an average of 6dB insertion loss, with a maximum 10dB loss due to the varactor diode resistance. It is speculated that GaAs Schottky diodes would reduce the loss to 2dB.

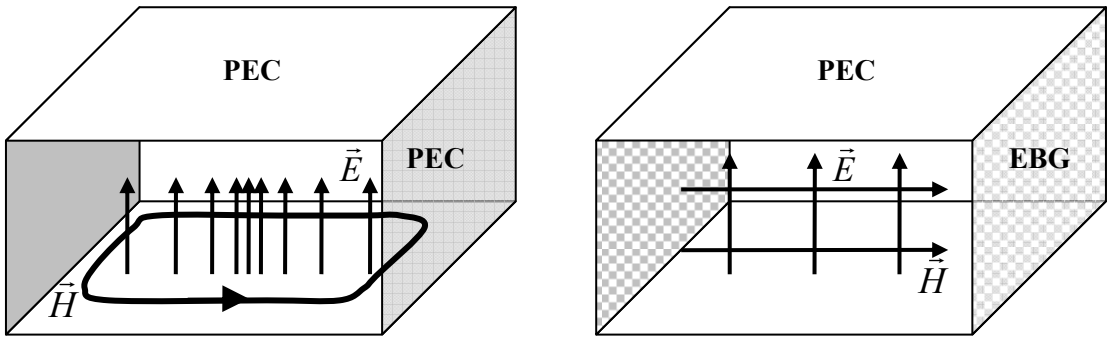

Figure 2.20: (a) Field configuration for propagating TE_{10} mode in a rectangular waveguide (b) TEM wave propagating in a waveguide with EBG sidewalls.

In [60], researchers propose a MEMS-based tunable millimeter-wave EBG structure operating in the 70-95GHz range. The structure is based on rows of overlapping patches separated by a silicon dioxide dielectric layer. A fixed-frequency prototype was fabricated, as shown in Figure 2.21, with an 80GHz resonant frequency and -5dB reflection amplitude. Measurements were taken with the structure placed over the end of a WR-10 waveguide.

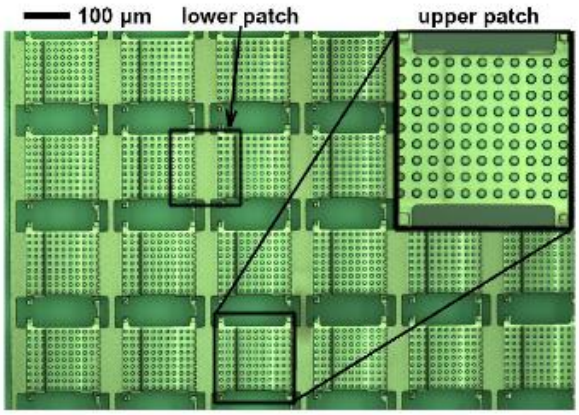

Figure 2.21: Fixed-frequency prototype of MEMS-based millimeter wave EBG structure from [60].

Other researchers have endeavored to maximize the EBG losses to produce low-profile tunable absorbers as shown in the simulated results of [21], [22]. The EBG structures are high-resistivity uniplanar grid patterns where tuning is accomplished by changing capacitive loading between elements [22]. It was found in [21] that maximum absorption occurs for a 40s/m conductivity at approximately 4GHz, where the optimized absorption value was measured as a -35dB reflection magnitude.

In [23], researchers placed a resistive sheet of indium tin oxide (ITO) 3.3mm over a varactor-loaded EBG structure as shown in Figure 2.22. The structure consists of 15.33mm square patches over a 1.6mm FR-4 substrate. Varactors are tuned from 20pF to 2pF to vary the frequency from 1.6GHz to 2.7GHz. Theoretical predictions indicate absorption in the range of 16-21dB.

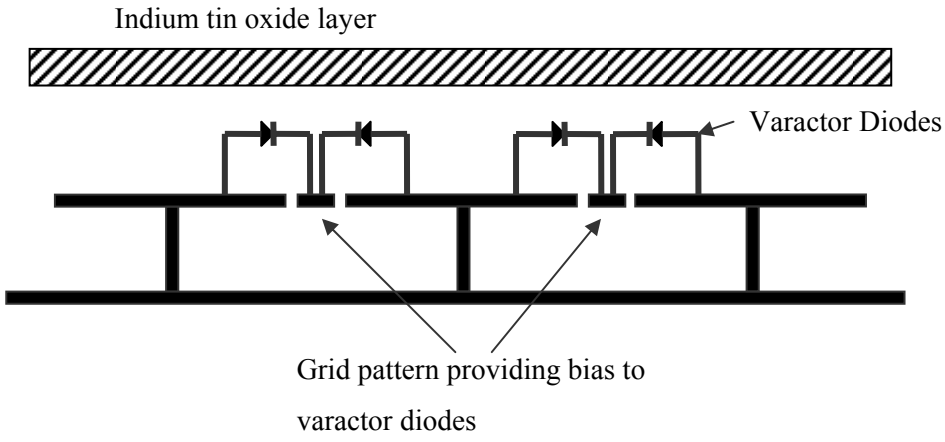

Figure 2.22: Tunable EBG absorber from [23].

2.5.4 SUMMARY

This chapter provided a background overview of the topics relevant to research projects pursued for this thesis, as well as a survey of relevant literature. First, the topic of radiofrequency identification was introduced with an emphasis on passive systems. The antennas developed in Chapter 3 are designed to improve the range of passive RFID systems which is severely constrained since the tags, which have no power supply, modulate backscattered signals back to the reader.

It was apparent from the survey of published MEMS fabrication processes on flexible substrates that applications of the current state of the art are limited. Several researchers have fabricated small MEMS devices on flexible dielectric substrates that are temporarily supported during fabrication before a final release step. Large MEMS devices on flexible materials, however, require mechanical support to prevent distortion when bending the substrate. Rigid-flex substrates with thick silicon islands provide sufficient mechanical support, but are not amenable to producing low-loss electromagnetic structures which is the focus of this thesis. Consequently, there is a need for a rigid-flex MEMS process with an all-dielectric substrate, which is developed in Chapter 4.

Several innovative frequency-selective surfaces have been reported in the literature, including MEMS-tunable devices on rigid substrates. For satellite applications, however, there is a need for flexible structures which may conform to the curved surfaces of reflector antennas. Additionally, radome applications would greatly benefit from a conformal tunable frequency-selective surface.

Finally, the topic of reconfigurable electromagnetic bandgap structures was surveyed. The current state of the art shows potential EBG applications as reconfigurable reflectors, phase shifters and tunable absorbers. Researchers have developed varactor tuned structures and fixed MEMS prototypes on rigid substrates. New research in MEMS-tunable EBG structures on flexible substrates will advance the state of the art. Military applications will benefit from conformal tunable absorbers as well as reconfigurable reflectors on non-planar surfaces.

CHAPTER 3

RECONFIGURABLE ANTENNAS

3.1 INTRODUCTION

Multi-mode parasitic patch antenna arrays are proposed for completely passive Radiofrequency Identification (RFID) tags capable of changing the direction of communication based on signal frequency. Passive RFID tags derive their power from the incident RF signal and modulate the backscatter, which is decoded by a reader. Although the range of this system is very limited, the RFID reader power and antenna gain cannot increase due to regulatory limits. We must therefore increase the gain of the RFID tag antenna to improve passive RFID system range. Although high-gain patterns offer increased range, they are inherently narrow, limiting the directions of communication as shown in Figure 3.1. To overcome this limitation, we propose a multi-mode parasitic patch array that has divergent high-gain radiation patterns at different frequencies.

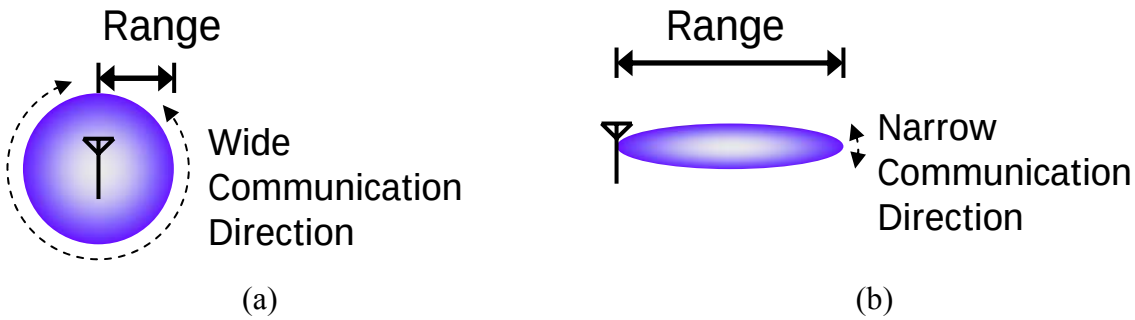

Figure 3.1: (a) Low-gain radiation pattern having wide communication direction but limited range (b) High-gain radiation pattern having increased range, but narrow direction of communication.

Figure 3.2 illustrates the multi-mode RFID tag performance alongside a conventional tag which uses a dipole antenna. The blue (dark) region of Figure 3.2a shows the limited range of a dipole RFID tag for a conventional system operating in a single band. The coloured (darkened) regions of Figure 3.2b show the extended range of three orthogonal high-gain radiation patterns at three resonant frequencies f1, f2 and f3.

Previously, researchers have used coupled parasitic patch antennas to enhance the impedance bandwidth of microstrip antennas [61]-[63]. It was noted that the radiation pattern changed with frequency across the bandwidth of the parasitic patch arrays [61]. For most applications, it is desirable to minimize radiation pattern variation across the band. For our application, however, we endeavour to maximize the changes in radiation pattern with varying frequency.

The layout of the proposed multi-mode parasitic array is shown in Figure 3.3. A single RF port connects to the centre patch, and no active devices are required to steer the beam. The array is designed with multiple resonant modes such that the radiation pattern changes with frequency. The direction of communication can therefore be switched by simply changing

the RFID reader frequency. The switching speed is virtually instantaneous, limited only by the inductance and capacitance of the antenna structure. The larger aperture offered by an array, combined with the ability to direct more of the radiated signal in a given direction, will significantly increase the read range compared to that of a conventional RFID system.

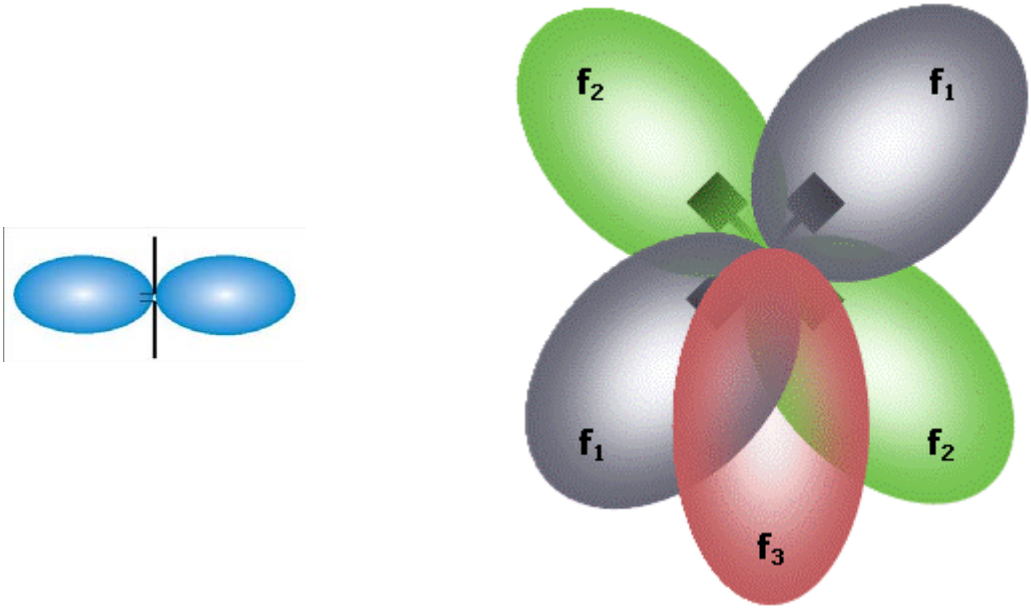

(a) (b)

Figure 3.2: (a) Radiation patterns of a conventional RFID tag having a low-gain antenna (b) Frequency switchable multi-mode RFID tag with high-gain radiation patterns

This chapter documents the theory, design and analysis of multi-mode parasitic patch arrays with divergent radiation patterns. Section 3.2 provides a detailed overview of the patch array structure and theory of operation. Section 3.3 expands on this theory to analyze the parasitic array performance in the context of a passive RFID system.

Frequency-switchable parasitic patch array hardware has been designed and fabricated. Section 3.4 provides detailed measurement results that are compared with simulated and calculated results. The design of multi-mode parasitic patch array structures is time-consuming when using electromagnetic simulators to model the entire structure. In the absence of simple models, many time-consuming iterations are required to complete a

design. We propose a novel analysis technique that combines existing well-established models based on both electromagnetic and circuit theory. Section 3.5 documents the analysis, which provides a good deal of physical insight into the operation of multi-mode parasitic patch arrays. The end result is an initial array design which provides a good starting point for full EM simulation and optimization.

Section 3.6 documents additional hardware that was designed and fabricated to augment the capabilities of the multi-mode parasitic patch arrays by adding RADANT MEMS switches [64]. The MEMS-based arrays have additional beam-steering capabilities at each frequency. Section 3.7 summarizes initial results using electromagnetic bandgap (EBG) structures to reduce the size and enhance performance of frequency switchable arrays.

3.2 STRUCTURE AND THEORY

The structure is a 5-element direct coupled parasitic patch antenna array on a 20mil Teflon substrate. Each antenna element is a 16.5mm square patch antenna that has a 5.8GHz resonant frequency when isolated. This structure may be scaled to operate at different frequencies and have different substrate characteristics.

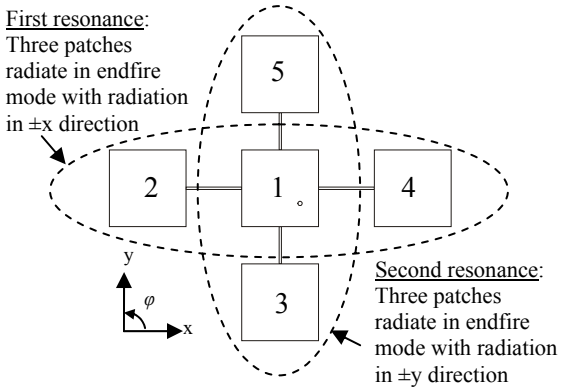

Figure 3.3. Switchable Parasitic Antenna Structure.

As shown in Figure 3.3, the centre patch antenna is connected to a coaxial feed. The feed point is located 4mm in the x-direction and 5mm in the y-direction from the lower right corner as shown in Figure 3.3. The feed location is chosen to excite the desired modes as the frequency changes.

Four parasitic elements surround the centre antenna, as shown in Figure 3.3. The two parasitic elements situated along the x-direction are connected to the centre patch by coupling lines that are 12mm long and 0.5mm wide. These three x-oriented patches act as coupled resonators, providing the lowest frequency resonance (5.65GHz as shown in Figure 3.4). The two parasitic elements situated along the y-direction are connected to the centre patch by coupling lines that are 8mm long and 0.5mm wide. The three y-oriented patches resonate at the next highest frequency (5.81GHz as shown in Figure 3.4). The 8mm and 12mm dimensions are chosen to isolate the resonant structures from an electromagnetic point of view. In addition to the two endfire modes, broadside resonant modes are excited with a wide 10dB bandwidth from 6.12GHz to 6.26GHz, as shown in Figure 3.4, corresponding to a 2.3% bandwidth.

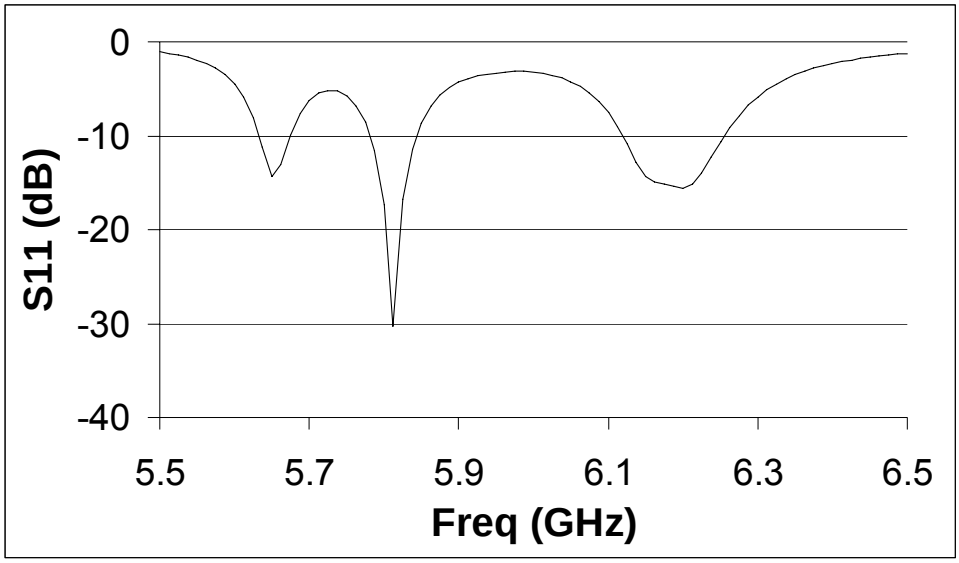

Figure 3.4: RFID Antenna Simulated S11 (Structure shown in Figure 3.3)

The radiation characteristics of the two lowest frequency modes are endfire patterns since the parasitic patch antennas exhibit odd-mode coupling to the centre patch. The resultant patch current distribution leads to equivalent magnetic line sources, at the parasitic antennas, that are out of phase with main patch as shown in Figure 3.5. Consequently, the far-field radiation adds constructively towards the ±x and ±y directions for the first two resonant modes.

Figure 3.5: Equivalent magnetic line sources showing odd-mode coupling between centre and parasitic patch antennas.

In addition to the two endfire resonances, a broadside resonant mode is excited at higher frequencies, in which the parasitic patch coupling to the centre patch is even mode. In this case, the equivalent magnetic line sources at the centre and parasitic antennas are in phase as shown in Figure 3.6. Consequently, the far-field radiation adds constructively towards the +z direction

Figure 3.6: Equivalent magnetic line sources showing even-mode coupling between centre and parasitic patch antennas.

For the lowest frequency (5.65GHz) resonance, the majority of the radiation pattern is oriented in the positive and negative x directions as shown in Figure 3.7. The x-directed patches are radiating, and couple to the centre patch in the odd mode as shown in Figure 3.7b-c. The simulated directivity is 8.3dBi, with a gain of 7.6dBi, corresponding to a radiation efficiency of 85.9%. This gain value corresponds to a 5.4dB increase in sensitivity compared to a dipole antenna.

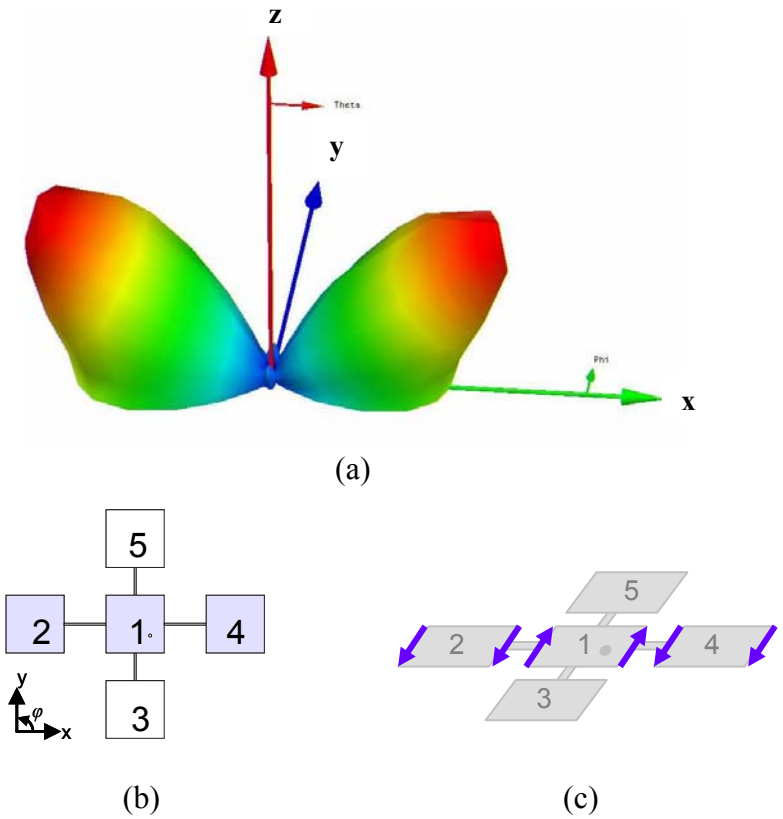

Figure 3.7. (a) Simulated radiation pattern of first resonance at 5.65 GHz (b) x-directed patches contributing to the far-field radiation (c) Equivalent magnetic line sources showing odd-mode coupling between x-directed patches.

By changing frequency to the second (5.81GHz) resonance, the pattern steers 90 degrees such that the endfire pattern is oriented in the positive and negative y directions, as can be seen in Figure 3.8. The y-directed patches are radiating, and couple to the centre patch in the odd mode as shown in Figure 3.8b-c. The simulated directivity is 8.1dBi, with a 7.5dBi gain, corresponding to a radiation efficiency of 85.7%. This gain value corresponds to a 5.3dB increase in sensitivity compared to a dipole antenna.

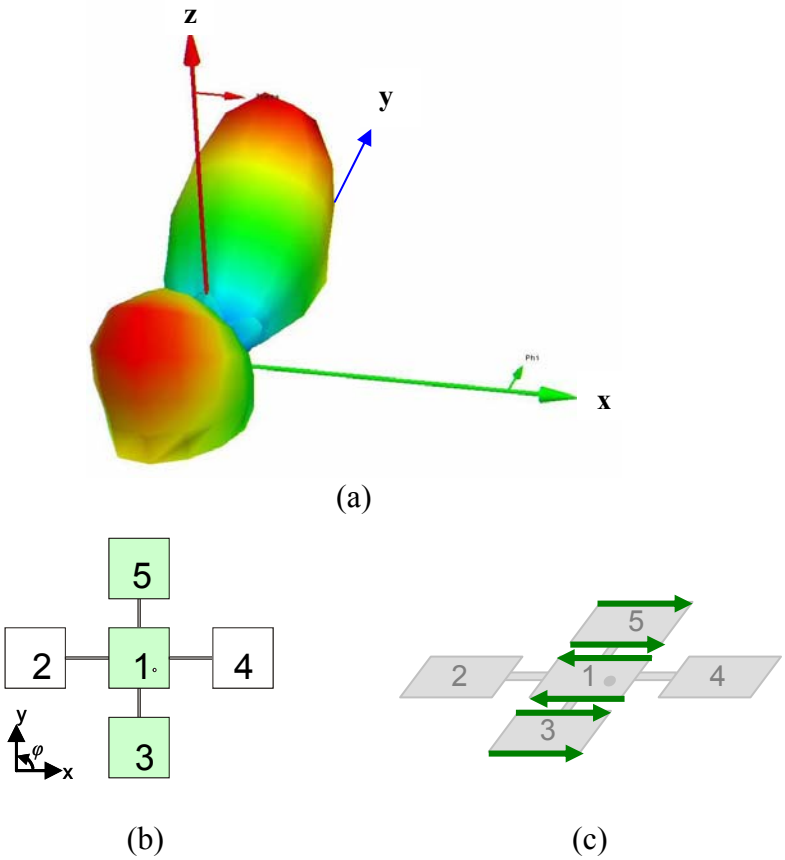

Figure 3.8. (a) Simulated radiation pattern of second resonance at 5.81 GHz (b) y-directed patches contributing to the far-field radiation (c) Equivalent magnetic line sources showing odd-mode coupling between y-directed patches.

For the broadside mode, all patches are radiating, and couple to the centre patch in the even mode as shown in Figure 3.8b-c. The simulated directivity at 6.2GHz is 12.0dBi, with a gain of 11.5dBi corresponding to a radiation efficiency of 88.1%. This gain value corresponds to a 9.3dB increase in sensitivity compared to a dipole antenna.

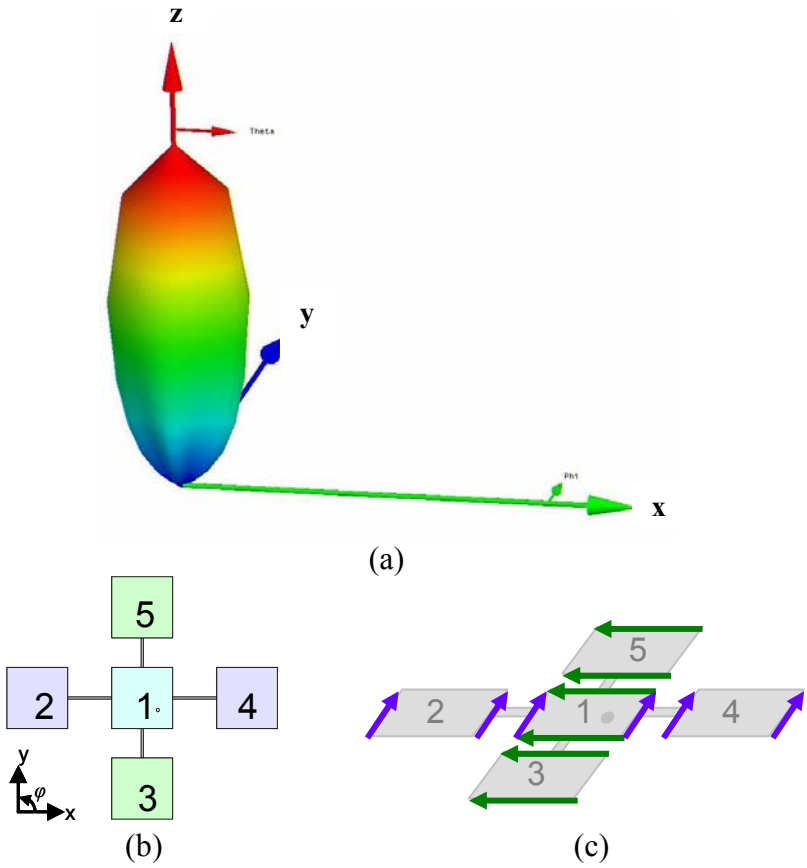

Figure 3.9. (a) Simulated radiation pattern of third resonance at 6.2 GHz (b) All patches contributing to the far-field radiation (c) Equivalent magnetic line sources showing even-mode coupling between x and y directed patches.

3.3 ARRAY PERFORMANCE IN RFID SYSTEMS

This section outlines the system performance of RFID tags using the new multi-mode parasitic patch arrays compared to conventional RFID tags using dipole antennas. The figures of merit to be evaluated are blind spots in the antenna patterns as well as operation in close proximity to conducting materials. The section will finish with some comments on impedance matching to RFID chips.

3.3.1 BLIND SPOTS

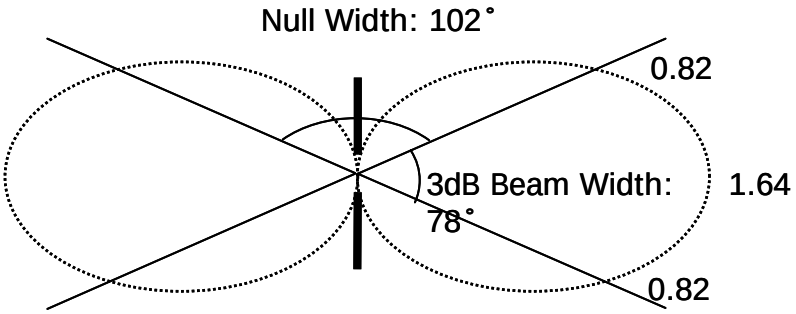

Figure 3.10: Dipole antenna pattern cross-section showing the 78 degree 3dB beam width and 102 degree blind spot.

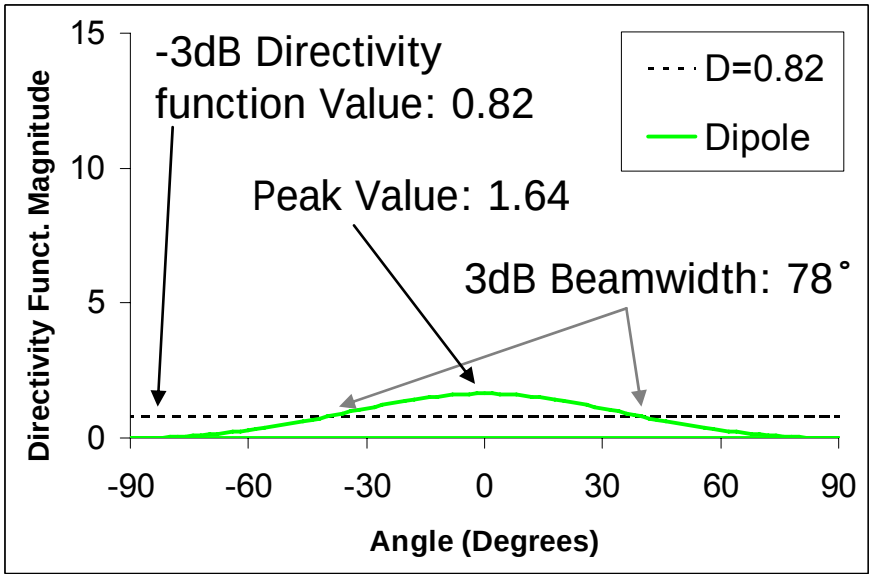

Figure 3.11: Rectangular plot of dipole antenna directivity function showing the 78 degree beam width.

As shown in Figure 3.10, a dipole antenna has a 3dB beam width of 78 degrees, and an associated null (blind spot) width of 102 degrees. Since the RFID tag is placed in close proximity to shielding in practical settings, we only consider half of the dipole pattern from -90˚ to +90˚ as shown in Figure 3.11. The peak directivity function value is 1.64, and the 3dB

beam comprises directivity function values greater than 0.82 or half the maximum value as shown in Figure 3.11. This 0.82 directivity function value serves as a point of reference for comparison between conventional and multi-mode patch antenna RFID systems. When analyzing the directivity function patterns of the multi-mode arrays, blind spots will also be defined as regions in which the value drops below 0.82.

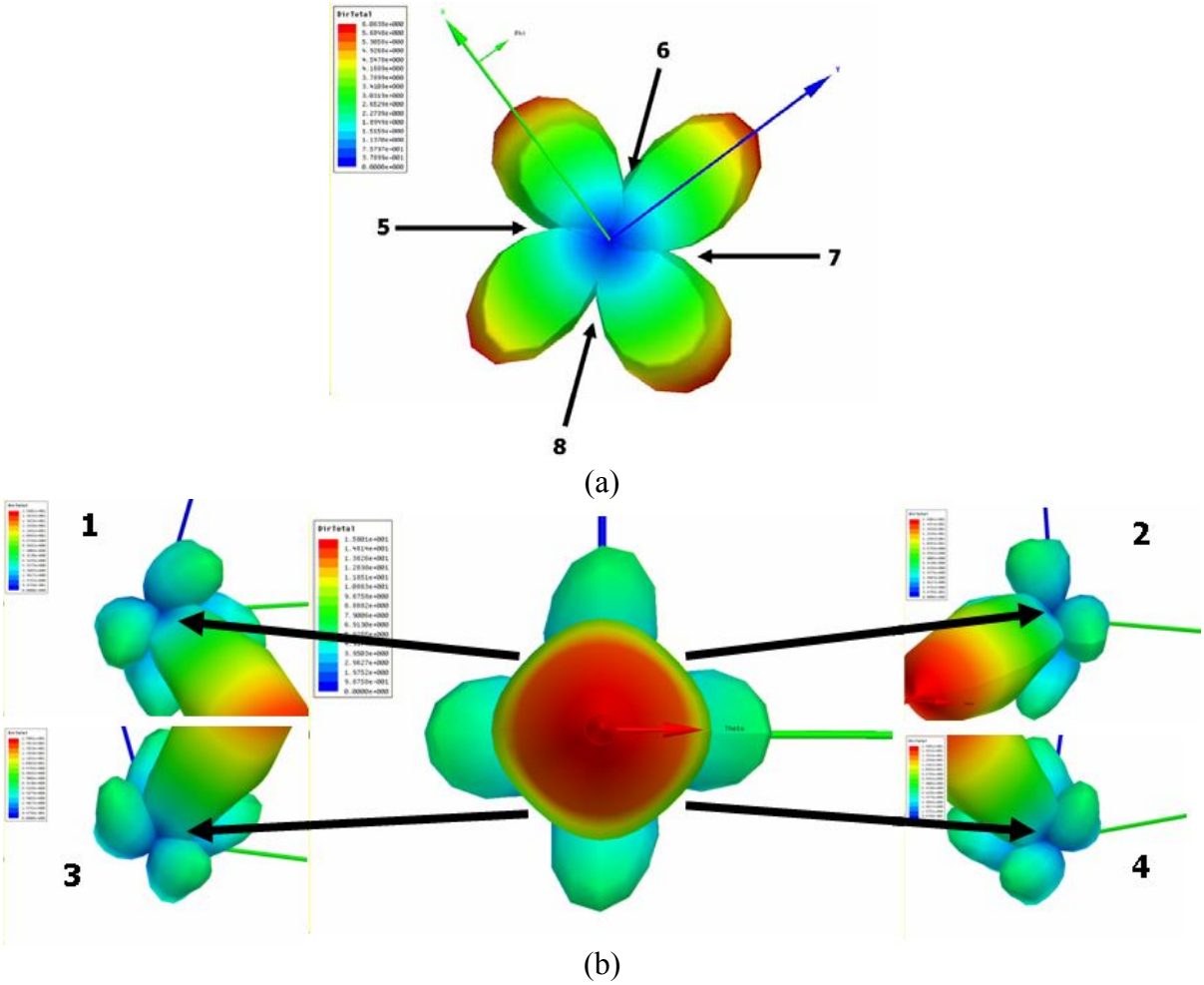

Figure 3.12: Overlapping radiation patterns for f1, f2 and f3 of the multi-mode parasitic array (a) View from overhead (+z) (b) View from below (-z)

To analyze the parasitic patch array, the directivity patterns at each resonant frequency are superimposed on the same axes as shown in Figure 3.12. The patterns have some overlap, which indicates that continuous coverage in the hemisphere is possible. Figure 3.12 shows that there are 8 principal minima in the overlapping radiation patterns of the three resonant frequencies. Upon further

analysis, the minimum directivity function value in the entire hemisphere for the overlapping patterns is 1.35 at point 3 as shown in Figure 3.12b. Since this is well above the 3dB dipole value of 0.82, the simulated results show continuous coverage with no blind spots. It is important to note, however, that the above results assume an infinite ground plane.

For an array having a finite ground plane, there is a drop in radiated power towards the ground plane, where θ=90 degrees, as shown in Figure 3.13. For θ=80 degrees, the worst-case directivity function value drops to 0.85. The array is therefore limited in communication direction to inclinations greater than 10 degrees above the ground plane.

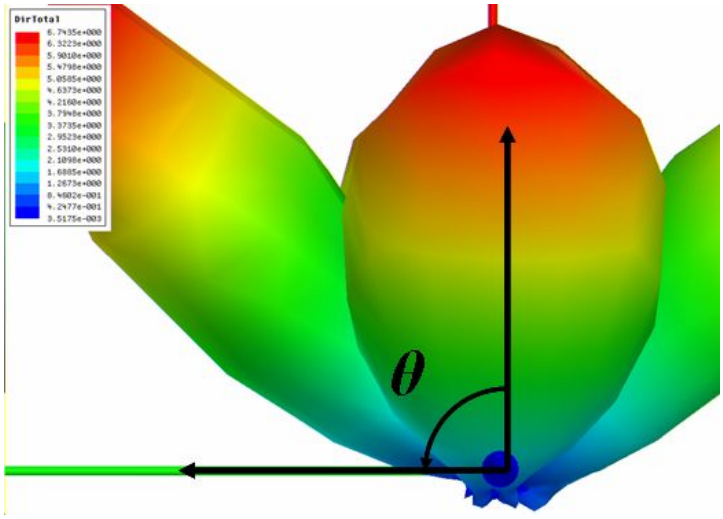

Figure 3.13: Overlapping radiation patterns for multi-mode parasitic patch array with finite ground plane.

3.3.2 Operation in Close Proximity to Conductive Materials

This section provides a comparison of conventional dipole and multi-mode parasitic patch array operation in a practical setting where the RFID tag is mounted on different materials and in different orientations.

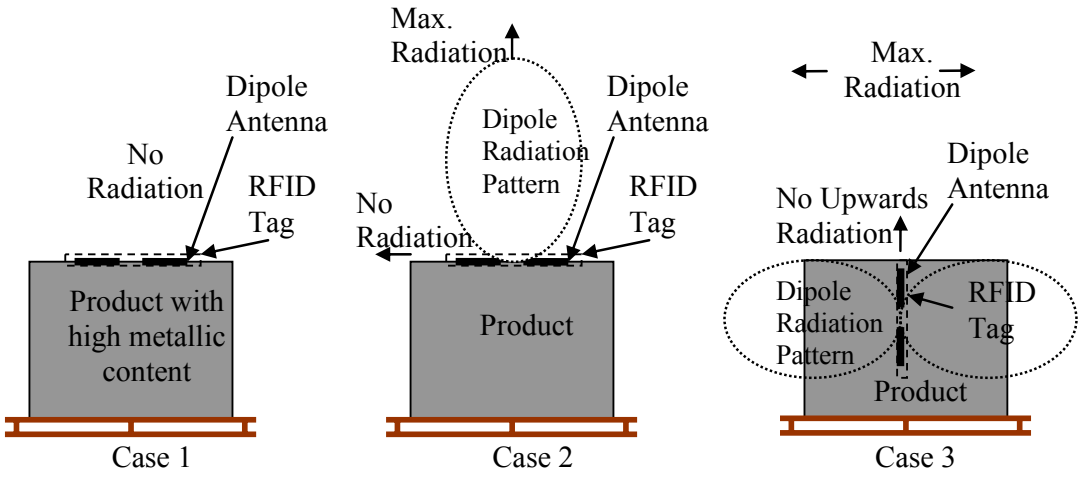

Figure 3.14: Radiation characteristics of RFID tag with dipole antenna. Case 1: Antenna mounted on product with high metallic content. Case 2: Antenna mounted horizontally. Case 3: Antenna mounted vertically.

Figure 3.14 shows three cases where RFID tags having dipole antennas are mounted on a product. The first case shows that a tag mounted on a product with high metallic content will not radiate due to the proximity of metal to a dipole antenna. For the other cases in which the antenna radiates, it is assumed that the product shields the RF signal. For this reason, only radiation away from the product is considered. For Case 2 of Figure 3.14, the dipole is mounted horizontally, leaving large blind spots that prevent communication in one horizontal direction. For Case 3 of Figure 3.14, the dipole is mounted vertically, leaving large blind spots that prevent communication in the vertical direction.

Significant performance improvements are obtained by using RFID tags having multi-mode parasitic patch arrays as shown in Figure 3.15. For the first case of a product with high metallic content, radiation is not adversely affected due to the presence of a ground plane under microstrip antennas. In fact, the performance may be improved since a metal product will effectively increase the ground plane dimensions. As discussed in Section 3.3.1, a larger ground plane may reduce the parasitic array blind spot for small inclinations above a finite ground plane. For the other two cases of Figure 3.15, both horizontally and vertically mounted parasitic patch arrays show significantly reduced blind spots in comparison to a

dipole antenna. The hemispherical coverage is almost complete, except for the blind spot at inclinations of less than 10 degrees above the ground plane as demonstrated in Section 3.3.1.

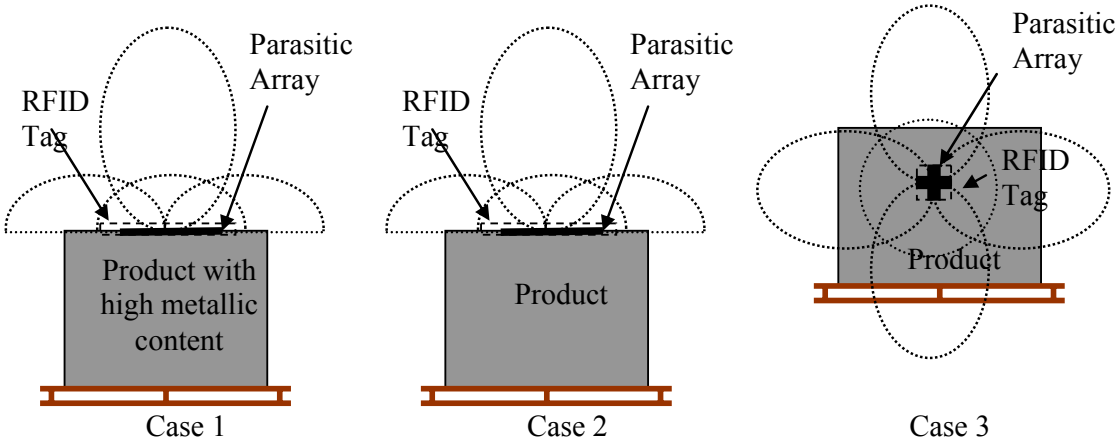

Figure 3.15: Radiation characteristics of RFID tag with multi-mode patch antenna. Case 1: Antenna mounted on product with high metallic content. Case 2: Antenna mounted horizontally. Case 3: Antenna mounted vertically.

3.3.3 Impedance Match to RFID Chips

As shown in Figure 3.3, the centre patch antenna of the multi-mode array connects to a coaxial feed. The modes discussed above have been simultaneously matched to a 50-ohm port, as seen in the S11 plot of Figure 3.4, by optimizing the coaxial feed location. It is also important to consider impedance matching of the antenna array to an RFID chip. Due to the rectifier circuit, the RFID chip typically has a high input resistance in the order of hundreds of ohms in parallel with a large capacitance in the order of 1pF [65], [66]. The impedance could be matched using a transformer such as that proposed by Bahl [67] to convert the complex impedance to a real value, and selecting an appropriate feed point on the centre patch of the array.

3.4 FABRICATED RFID TAG HARDWARE

Two versions of the RFID tag were fabricated on a 3.25" by 3.5" Teflon substrate. The first, shown in Figure 3.16, has the same antenna structure as previously described. Since it is designed to be a practical RFID tag, the feed point and RFID transceiver are situated on the antenna side, permitting the tag to be mounted flat on a metal container. The second version of the tag has a coaxial feed from the back side of the antenna, to facilitate return loss and radiation pattern measurements.

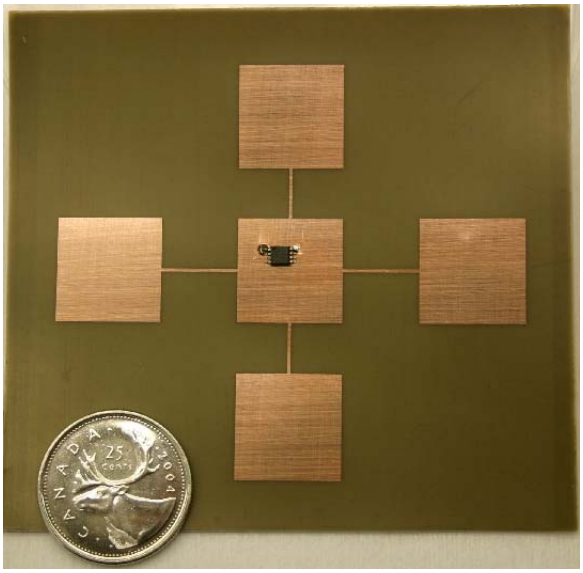

Figure 3.16. Fabricated RFID Tag.

Figure 3.17 shows a comparison of simulated S_{11} magnitude for the RFID tag antenna with the antenna side feed versus the back side feed. The resonant frequencies do not change when the feed is changed from back side to front side.

3.4.1 MEASUREMENTS OF RFID TAG WITH ANTENNA-SIDE FEED

As a proof of concept, a Philips SL3S1001FTT RFID chip in a TSSOP8 package [68] is mounted on the top side of the array. One side of the RFID chip antenna port connects directly to the antenna array, and the other side connects to the ground plane by way of a via,

as can be seen in Figure 3.16. Although the transceiver is designed to operate at the 900MHz and 2.4-2.5GHz RFID bands, it will rectify an incoming RF signal at the antenna array frequencies. We measured changes in the DC voltage across the RF terminals of the Philips chip while changing the tag orientation with respect to a CW transmitter. Although the voltage values are low since we are well outside the specified frequency range of the chip, the experiment provides a qualitative indication of how the actual hardware behaves as an RFID tag with changing frequency and orientation.

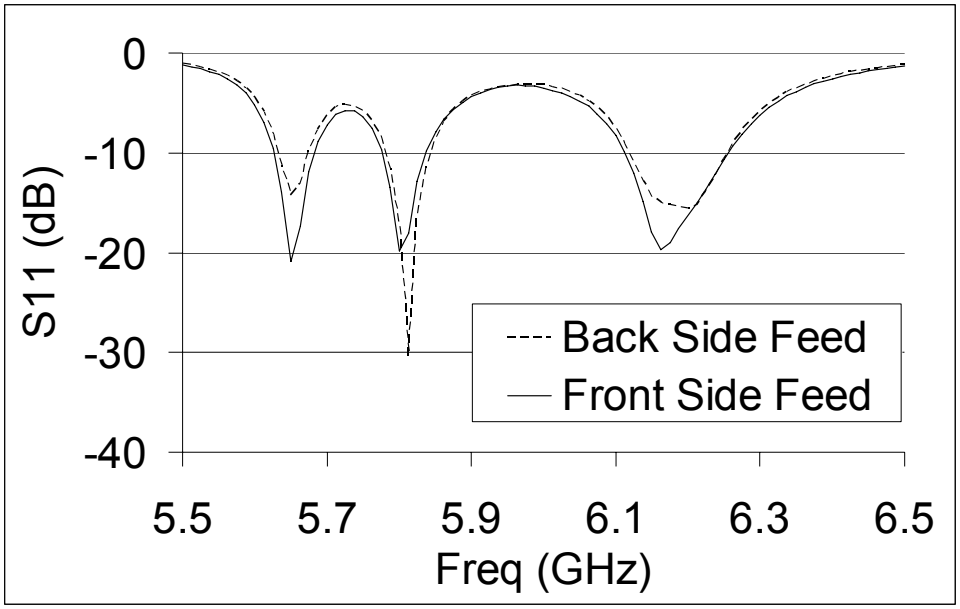

Figure 3.17. Comparison of simulated S_{11} magnitude for the antenna feed located on the back side versus the antenna feed on the front side.

The angles are measured relative to the broadside orientation, which is set to 0 degrees. The first measurement was taken at the lowest resonant frequency (5.77GHz). As expected from observing the simulated antenna pattern of Figure 3.7, the maximum voltage values of 1.1mV and 1.5mV occur, respectively, at -45 degrees and +45 degrees offset from broadside when the array is rotated around the y-axis.

The next set of measurements was taken at the second resonant frequency of 5.97GHz. As expected, the maximum voltage values of 2.3mV and 2.5mV occur, respectively, at -45 degrees and +45 degrees offset from broadside when the array is rotated around the x-axis.

The third set of measurements was taken at the broadside resonant frequency of 6.37GHz. As expected, the maximum voltage value of 15.7mV occurs in the broadside direction at 0 degrees.

3.4.2 MEASUREMENTS OF RFID TAG WITH BACK-SIDE FEED

Figure 3.18 shows a comparison of simulated and measured S_{11} Magnitude of the second fabricated version of the RFID tag having a back-side coaxial feed. The measured shape of the curve and relative positions of the resonant frequencies correspond well between the simulated and measured results.

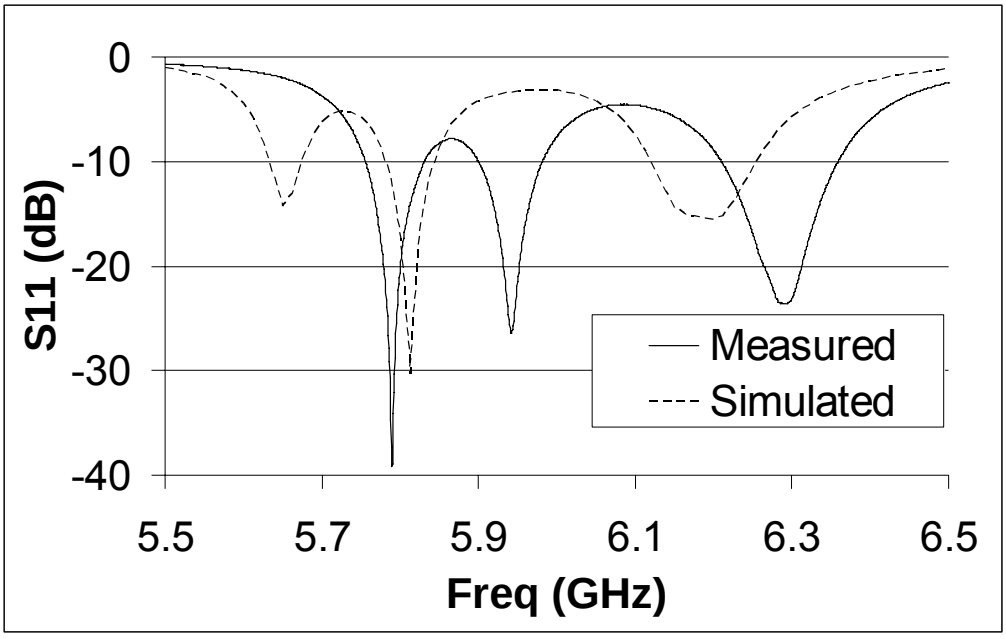

Figure 3.18. Comparison of Simulated and Measured S11 Magnitude.

The measured resonant frequencies are slightly higher than the simulated values (1.4% - 2.4% difference as shown in Table 3.1). This was a result of over etching in the fabrication process which reduced the patch antenna size thus increasing the resonant frequency.

Table 3.1: Comparison of Simulated and Measured Resonant Frequencies of the Back Side Coaxial-Fed RFID Tag

	Sim. (GHz)	Meas. (GHz)	% Difference
$\mathbf{f_1}$	5.65	5.79	2.4%
$\mathbf{f_2}$	5.81	5.94	2.2%
$\mathbf{f_3}$	6.20	6.29	1.4%

Figure 3.19 and Figure 3.20 show a comparison of simulated and measured far-field radiation patterns at the three resonant frequencies listed in Table 3.1. All of the far-field plots are in the form of the directivity function. The centre of the plot at 0 degrees corresponds to the broadside direction. For the measurements of Figure 3.19, the widest dimension is horizontal, and the axis of rotation is *y*. There is good correlation between simulated and measured radiation patterns. The beam steering with frequency can be clearly seen as the frequency transitions from 5.79GHz to 6.29GHz. The second resonant frequency of 5.94GHz is isolated in this configuration.

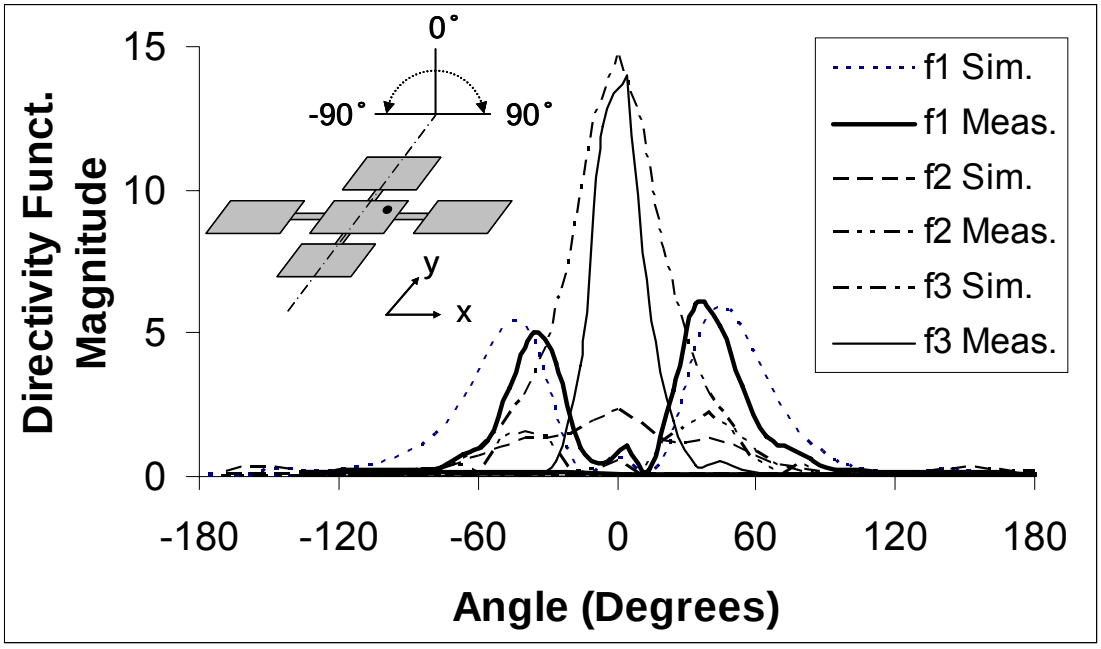

Figure 3.19. Comparison of the simulated and measured far-field radiation patterns, rotating the array around the *y*-axis, with the broadside direction at 0 Degrees. f1=5.79GHz, f2=5.94GHz, and f3=6.29GHz.

For the measurements of Figure 3.20, the array is rotated 90 degrees such that the longest dimension is vertical, and the axis of rotation is *x*. There is good correlation between simulated and measured radiation patterns. The beam steering occurs as the frequency transitions from 5.94GHz to 6.29GHz. The first resonant frequency of 5.79GHz is isolated in this configuration. Figure 3.19 and Figure 3.20 verify the passive frequency-controlled beam steering capability of the proposed RFID tag.

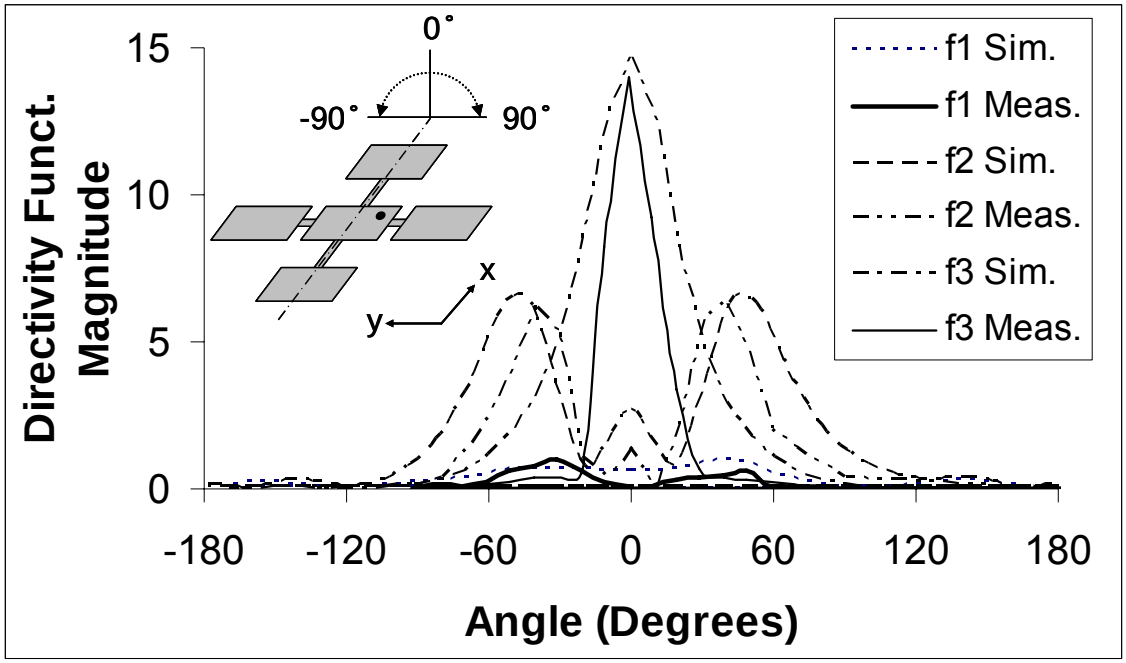

Figure 3.20. Comparison of the simulated and measured far-field radiation patterns, rotating the array around the *x*-axis, with the broadside direction at 0 Degrees. f1=5.79GHz, f2=5.94GHz, and f3=6.29GHz.

3.5 ANALYSIS AND DESIGN

For the purpose of designing the parasitic arrays, we propose a novel analysis technique that combines well-established models. The purpose of the analysis is to provide an approximation of the input impedance and variation of the radiation pattern with frequency. The analysis allows the designer to avoid the time-consuming trial-and-error process by combining models based on electromagnetic theory and circuit theory to provide a reasonable approximation of the parasitic array characteristics.

We begin by using a modified version of the coupling matrix model [69]-[70], combined with the patch antenna cavity model of [71]-[72]. As described in [72], the resonant characteristics of a single patch antenna may be modeled as shown in Figure 3.21. For the purpose of our simplified model, patches are assumed to be square with the feed along the diagonal as shown in Figure 3.21. It was found that the higher order modes could be neglected, and L_M was set to zero. The resistor R (shown in Figure 3.21) represents the

radiated power, dielectric loss and finite conductivity, and is assumed constant at frequencies close to resonance. We obtain the RLC values using an electromagnetic simulator such as HFSS.

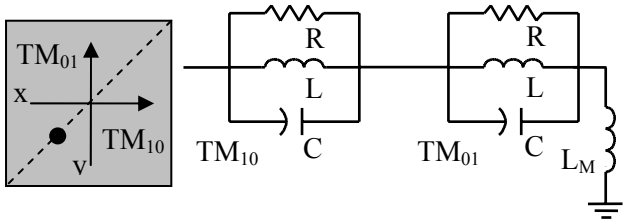

Figure 3.21. Equivalent circuit model of the centre patch antenna [72]

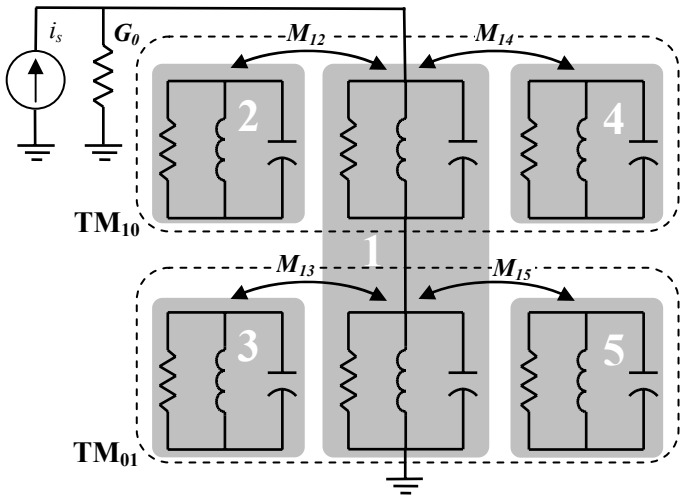

Figure 3.22. Equivalent circuit of the multi-mode parasitic patch array.

The next step is to combine the coupling matrix model, which is traditionally used for filter analysis [69]-[70], with the patch antenna model as shown in Figure 3.22. Each resonant mode of a patch antenna is represented by an RLC circuit. The patches are numbered as shown in the physical layout of Figure 3.3.

As a first-order approximation, it is assumed that there is no coupling between non-adjacent patch antennas and only a single mode is excited in the parasitic patches. Following the analysis of [70], the coupled resonator circuits may be modeled by a normalized admittance matrix given by

$$\overline{\mathbf{Y}} = \frac{1}{\omega_0 C \cdot FBW}\mathbf{Y} \quad . \tag{3.1}$$

For the purpose of this analysis, the fractional bandwidth term *FBW*, typically used for filter design, has little meaning. We therefore set *FBW* to 1 since it cancels out at the end of the analysis. The normalized *n* x *n* admittance matrix, where *n* is the number of coupled resonators associated with a centre patch mode, is given by

$$\overline{\mathbf{Y}} = \frac{1}{q}\mathbf{I} + p\mathbf{I} - j\overline{\mathbf{M}} \, . \tag{3.2}$$

The matrix $\mathbf{I}$ is the identity matrix and *q* is the normalized unloaded resonator quality factor given by

$$q = \frac{R}{\omega_0 L} \cdot FBW \, . \tag{3.3}$$

The value *p* is the normalized frequency variable given by

$$p = \frac{j}{FBW}\left(\frac{f}{f_0} - \frac{f_0}{f}\right), \tag{3.4}$$

and $\overline{\mathbf{M}}$ is the normalized coupling matrix, which is given by

$$\overline{\mathbf{M}} = \begin{pmatrix} m_{11} & m_{12} & \cdots & m_{1n} \\ m_{21} & m_{22} & & m_{2n} \\ \vdots & & \ddots & \vdots \\ m_{n1} & m_{n2} & \cdots & m_{nn} \end{pmatrix} . \tag{3.5}$$

Following the analysis outlined in [70], the diagonal elements of the coupling matrix are zero for synchronously tuned resonators. The non-diagonal terms are the normalized coupling coefficients between the patches.

Coupling coefficients between two patches may be calculated from the electric (even-mode) and magnetic (odd-mode) coupling frequencies. An effective way to determine the frequencies of electric and magnetic coupling is to simulate a patch antenna in HFSS with half of the coupling structure terminated, respectively, in an electric or magnetic wall as shown in Figure 3.23.

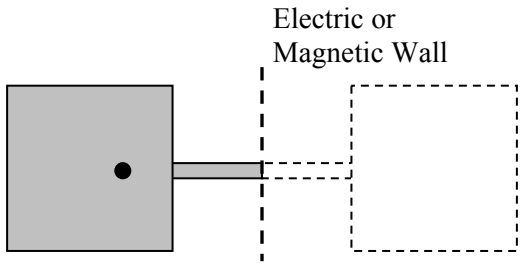

Figure 3.23. Equivalent coupled patch antenna model for electric and magnetic wall analysis.

By simulating the electric and magnetic coupling frequencies, while varying the coupling line length, we may generate a set of design curves for any type of patch antenna. The coupling coefficient *k* may be calculated from [70]

$$k = \frac{f_e^2 - f_m^2}{f_e^2 + f_m^2}, \tag{3.6}$$

where f_e is the electric coupling frequency determined using the electric wall simulation. The value f_m is the magnetic coupling frequency determined using the magnetic wall simulation. The normalized elements for the coupling matrix of (3.5) are given by [70]

$$m_{ij} = \frac{k_{i,j}}{FBW}.$$

(3.7)

Figure 3.24 shows a plot of varying electric and magnetic coupling frequencies, as well as coupling coefficients, for different coupling trace lengths. The patch antennas are 16.5mm square on a 20mil Teflon substrate, and the coupling traces are 0.5mm wide.

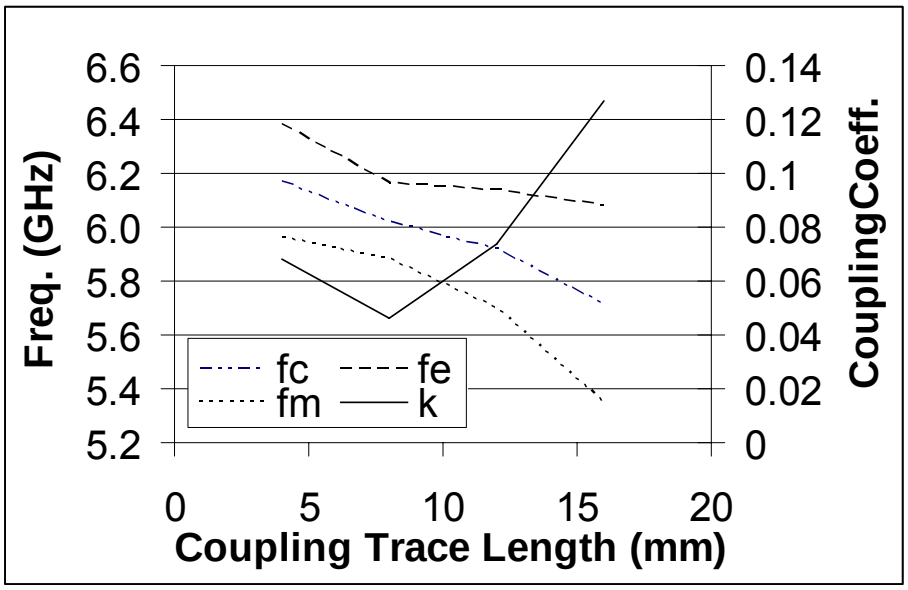

Figure 3.24. Variation in coupling coefficient k (right y-axis scale), and fc,fe, fm (left y-axis scale) with coupling trace length.

It is important to note that the centre frequency of the coupled resonators, as shown in Figure 3.24, changes with trace length due to loading caused by the transmission line effects of the coupling trace. The calculated centre frequency, for a given trace length, replaces the frequency f_0 in (3.4). The overall admittance matrix of the coupled patch array combines the admittance matrices for each centre patch mode as

$$\overline{\mathbf{Y}} = \left(\left[\overline{\mathbf{Y}}_{10} \right]^{-1} + \left[\overline{\mathbf{Y}}_{01} \right]^{-1} \right)^{-1}.$$

(3.8)

Following the analysis of [70], we add the reciprocal of the normalized external quality factor, given by

$$\frac{1}{q_e} = \frac{\omega_0 L G_0}{FBW},$$

(3.9)

to the matrix element $\overline{\mathbf{Y}}_{1,1}$ to account for the loading effects of the source impedance. The S_{11} is calculated as

$$S_{11} = \left[1 - \frac{2}{q_e} \cdot \left[\overline{\mathbf{Y}}^{-1} \right]_{1,1} \right].$$

(3.10)

Figure 3.25 shows a comparison of HFSS simulated, calculated and measured S_{11} for the 5-element array of Section 3.4.2, which has 16.5mm square patch antennas on a 20 mil Teflon substrate. As can be seen in Figure 3.25, the calculated S_{11} correlates well with HFSS simulations. The calculated 5.64 GHz TM_{10} and 5.76GHz TM_{01} endfire resonant frequencies are, respectively, 0.3% and 0.6% below the values predicted by HFSS. The broadside resonance correlates well, with the calculated 6.16GHz main resonant frequency 0.8% lower than the HFSS simulated value. The measured resonant frequencies are 1.4%-2.4% higher than simulated values.

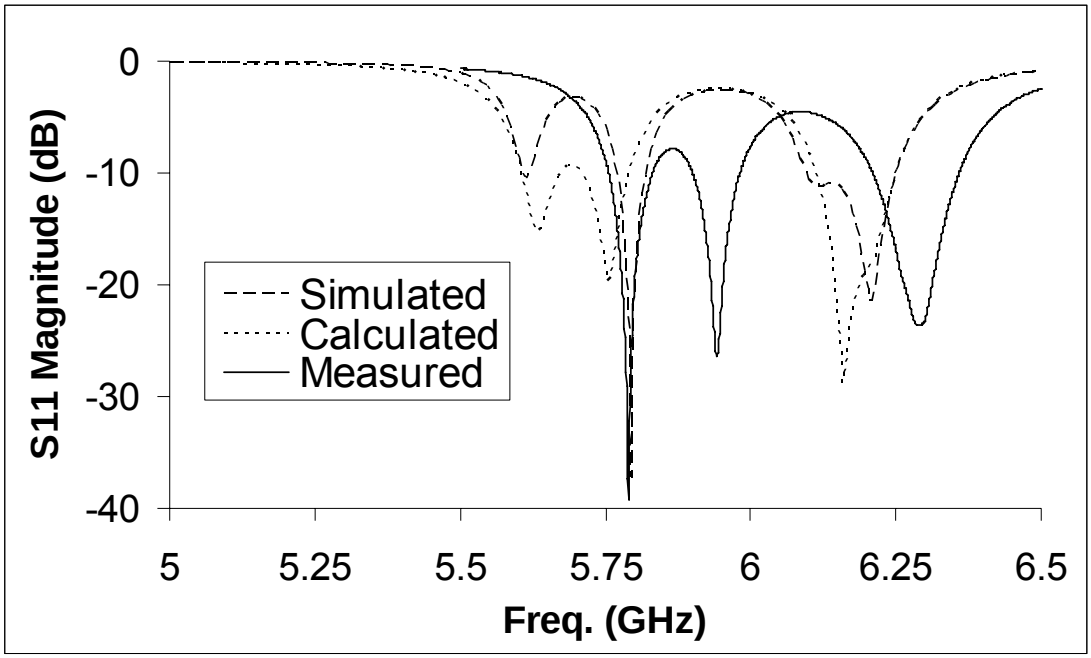

Figure 3.25: Comparison of calculated, HFSS simulated, and measured S_{11} of the array in Section 3.4.2

The next step in the analysis is to calculate the radiation pattern, starting with the standard patch model as described in [73]. The two radiating slots of each patch antenna mode are modeled by two magnetic line sources with magnitude and phase directly proportional to the current input to the patch antenna [73]. The radiation from the individual patch antennas is combined, using an array factor, to model the overall far-field pattern of the array.

The current on the centre patch, which is used as the reference, is set to unity. The current on each parasitic patch arises due to the mutual coupling as discussed above. The relative parasitic patch current is therefore calculated from the admittance matrices for the centre patch $TM_{m,n}$ mode, as

$$I_{rel,i} = \frac{\left[\overline{\mathbf{Y}}_{m,n}\right]_{i,1}}{\left[\overline{\mathbf{Y}}_{m,n}\right]_{1,1}}. \tag{3.11}$$

A separate array of magnetic line sources models each resonant mode. The equivalent antenna array for each centre patch mode, and parasitic patches, is shown in Figure 3.26.

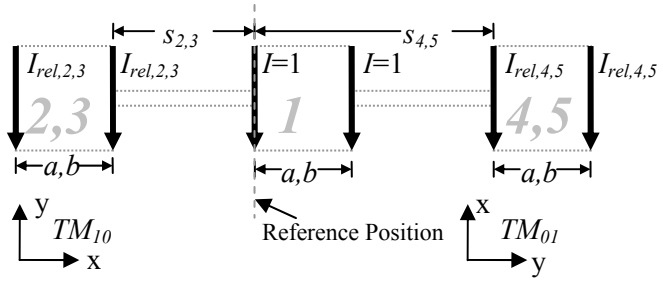

Figure 3.26. Equivalent array of magnetic line sources used to model the radiation of the centre patch TM_{10} mode and x-directed parasitic antennas (nos. 2 and 4), and TM_{01} mode and y-directed parasitic antennas (nos. 3 and 5).

The TM_{10} array factor for the equivalent model of Figure 3.26 is given by

$$AF_{10} = 1 + e^{jk_0 a} + \sum_i \left(\left| I_{rel,i} \right| \left(e^{jk_0 s_i + j\angle I_{rel,i}} + e^{jk_0 (s_i + a) + j\angle I_{rel,i}} \right) \right), \tag{3.12}$$

where the index i represents each parasitic antenna. The value s_i is the physical spacing between the reference position and the nearest parasitic edge, as shown in Figure 3.26. The value k_0 is the free-space propagation constant. The value a is the patch antenna dimension in the x-direction.

The TM_{01} array factor for the equivalent model of Figure 3.26 is given by

$$AF_{01} = 1 + e^{jk_0 b} + \sum_i \left(\left| I_{rel,i} \right| \left(e^{jk_0 s_i + j\angle I_{rel,i}} + e^{jk_0 (s_i + b) + j\angle I_{rel,i}} \right) \right), \tag{3.13}$$

where the value b is the patch antenna dimension in the y-direction.

Note that the array factors of (3.12) and (3.13) assume the equivalent magnetic line sources for each half-wave patch antenna are in-phase, which is valid for the TM10 and TM01 modes. It may be necessary to add a phase shift of π radians for higher order modes where

the two radiating slot magnetic currents, representing a single patch antenna, are out of phase.

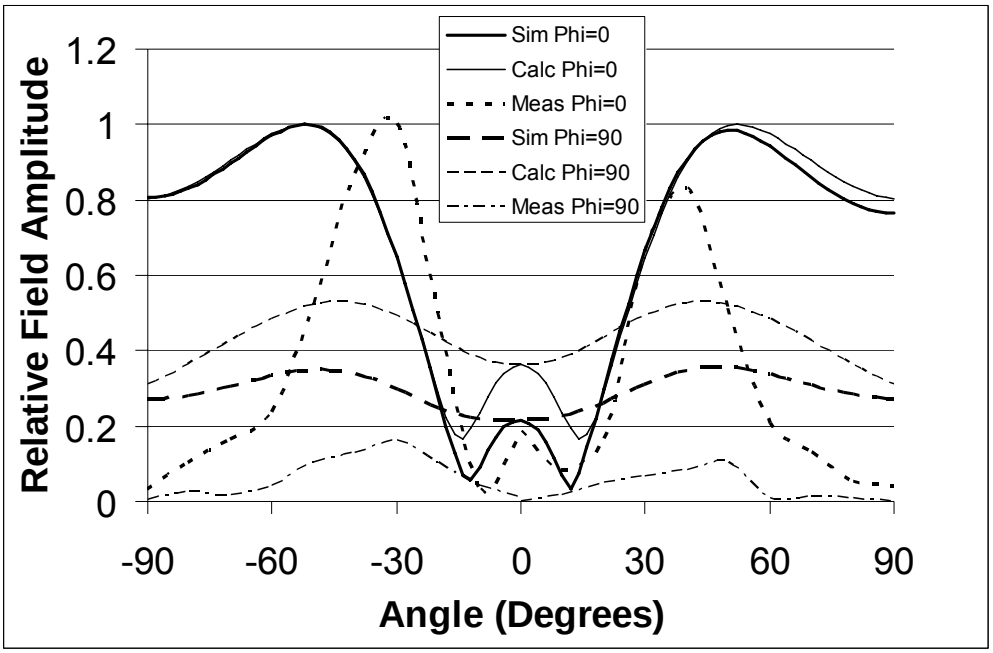

Figure 3.27. Comparison of HFSS simulated, calculated and measured far-field radiation pattern at the first resonant frequency corresponding to the TM_{10} endfire mode of the array in Section 3.4.2.

After determining the array factor, the radiation pattern is easily calculated using the patch antenna analysis of [73]. The far-field amplitude is calculated by summing the total contributions from all radiating modes.

Figure 3.27, Figure 3.28 and Figure 3.29 show a comparison of calculated, HFSS simulated, and measured far-field radiation patterns simulated for the antenna array from Section 3.4.2. The broadside direction is 0 degrees, and the ground plane is assumed to be infinite for the simulated and calculated results.

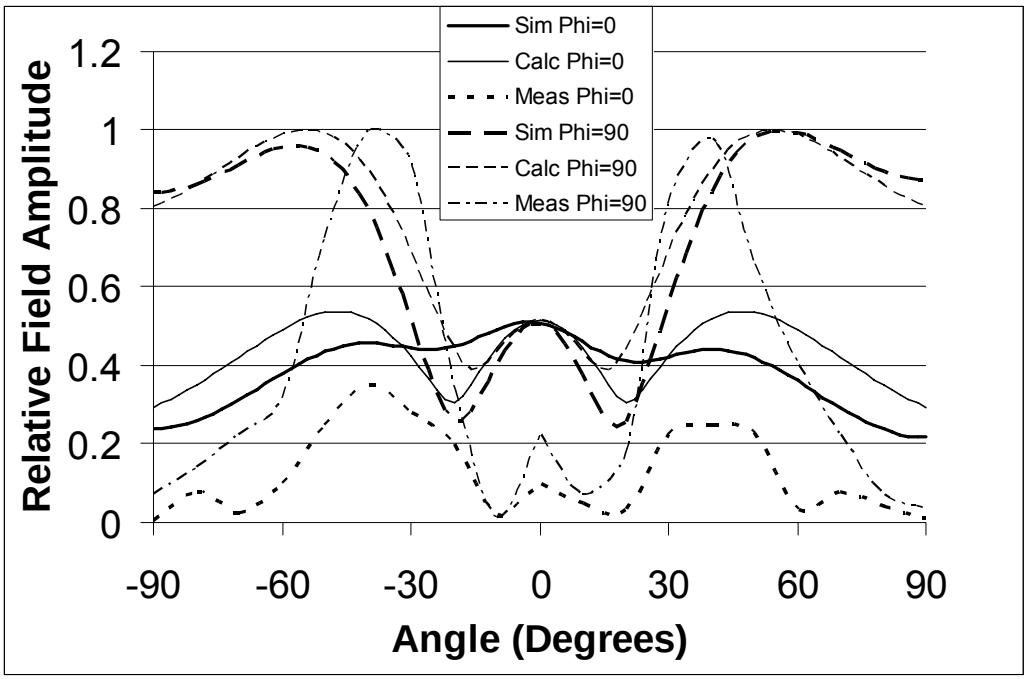

Figure 3.28. Comparison of HFSS simulated, calculated and measured far-field radiation pattern at the second resonant frequency corresponding to the TM_{01} endfire mode of the array in Section 3.4.2.

Figure 3.27 shows the antenna operating at the first resonant frequency (5.64GHz in this example), corresponding to the TM_{10} endfire mode. Note that when Phi=0, the axis of rotation is the y-axis and when Phi=90, the axis of rotation is the x-axis as shown in Figure 3.3. Figure 3.28 shows the antenna operating at the second resonant frequency (5.76GHz in this example), corresponding to the TM_{01} endfire mode with the pattern steered by 90 degrees. Figure 3.29 shows the antenna operating at the middle of the broadside resonance (6.18GHz in this example). The far-field radiation plots show that the calculated radiation response correlates well with simulated and measured values. Although some differences in the measured far-field pattern arise due to the finite ground plane of the fabricated array, the proposed analysis method correctly predicts the frequency-dependent beam steering of the multi-mode parasitic patch array.

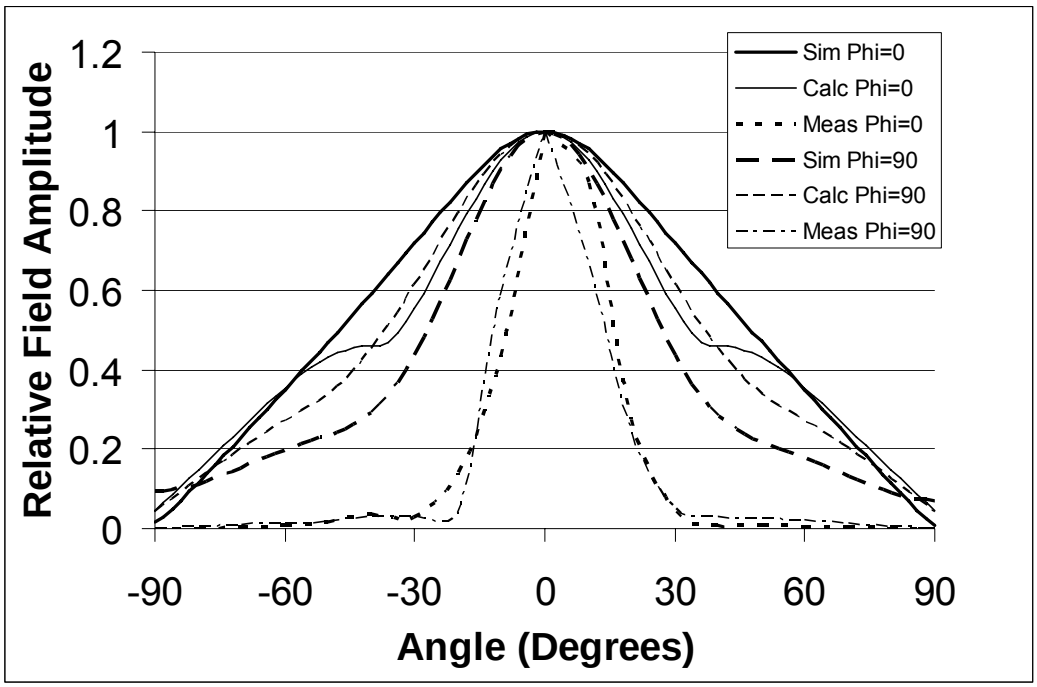

Figure 3.29. Comparison of HFSS simulated, calculated and measured far-field radiation pattern at the third resonant frequency corresponding to the broadside mode of the array in Section 3.4.2.

It is important to note that the beam steering occurs at discrete intervals, and that the radiation patterns of Figure 3.27-Figure 3.29 change very little across the 10dB bandwidth of each resonant mode. The scan sensitivity of the array therefore remains fixed at 0°/MHz within each band. The antenna scans by 90 degrees in the Phi direction when the frequency switches between each endfire resonance. When transitioning from either endfire resonance to the high frequency broadside mode, the main lobe scans by approximately 40° as shown in the measured response of Figure 3.27-Figure 3.29. The measured 10dB bandwidths of each measured resonance, shown in Figure 3.25, are 75MHz, 81MHz and 148MHz in order of ascending frequency. Since the radiation patterns are stable in each operating band, the patch arrays are amenable to frequency-hopping systems. According to the FCC Section 15 regulations, at least 75 hopping frequencies must be used in a frequency-hopping spread-spectrum (FHSS) system for the 5.8GHz band, with a maximum 1MHz channel bandwidth.

Appropriate system design would ensure that a compliant FHSS signal is transmitted through radiating modes of the patch array.

To further validate the proposed analysis method, we designed multi-mode patch arrays in the 800-960HMz and 2-3GHz bands. First, a large array with five 10.6cm square patch antennas on a 130 mil Teflon substrate was designed with endfire resonant frequencies calculated to be 828 MHz and 864 MHz. The broadside resonance occurred at 958 MHz. The second array with five 38mm square patch antennas on a 50mil Teflon substrate had endfire resonances calculated to be 2.40GHz and 2.51GHz, with a broadside resonance at 2.82 GHz. The calculated resonant frequencies for both arrays were all within 1% of values predicted using HFSS to simulate the entire structure.

3.6 FABRICATED MEMS-SWITCHED ANTENNA HARDWARE

The second application for which hardware has been fabricated and tested is a MEMS-based actively switched version of the parasitic patch array. Figure 3.30 shows the 3-element fabricated antenna array. The central patch is coaxially fed along the diagonal, and one parasitic element couples to each degenerate mode. The 3-element array offers similar beam steering characteristics to the 5-element arrays hitherto discussed, with reduced gain as expected with fewer radiating structures.

The three patches are 16.5mm square, connected by coupling lines that are 8mm long by 0.5mm wide. RADANT MEMS SPST switches [64] are positioned adjacent to the coupling lines as can be seen in Figure 3.30. Wire bonds connect the MEMS devices between the coupling line and a short-circuited 0.5mm wide transmission line. Electrically, the shorted line is equivalent to a 4mm open-circuited transmission line stub used to load the coupling line thus reducing the endfire resonant frequency. The stub was extended by a quarter wavelength at the patch resonant frequency and short-circuited to provide the required DC ground to the MEMS device. A 0.25mm wide trace, isolated from the RF circuit, provides the MEMS switching voltage to the device.

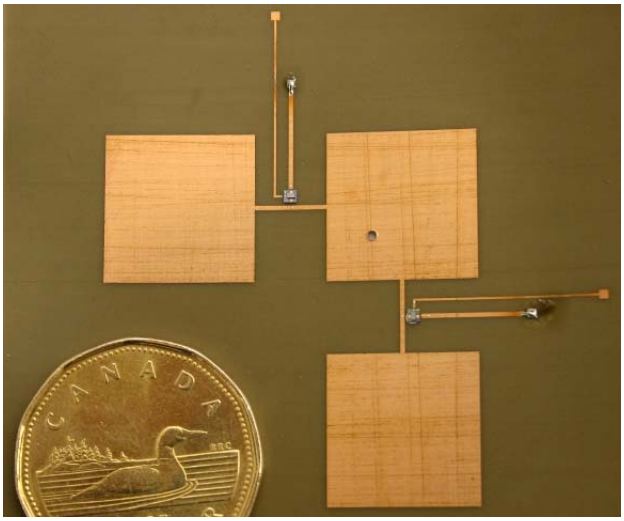

Figure 3.30. Fabricated MEMS switched parasitic patch array.

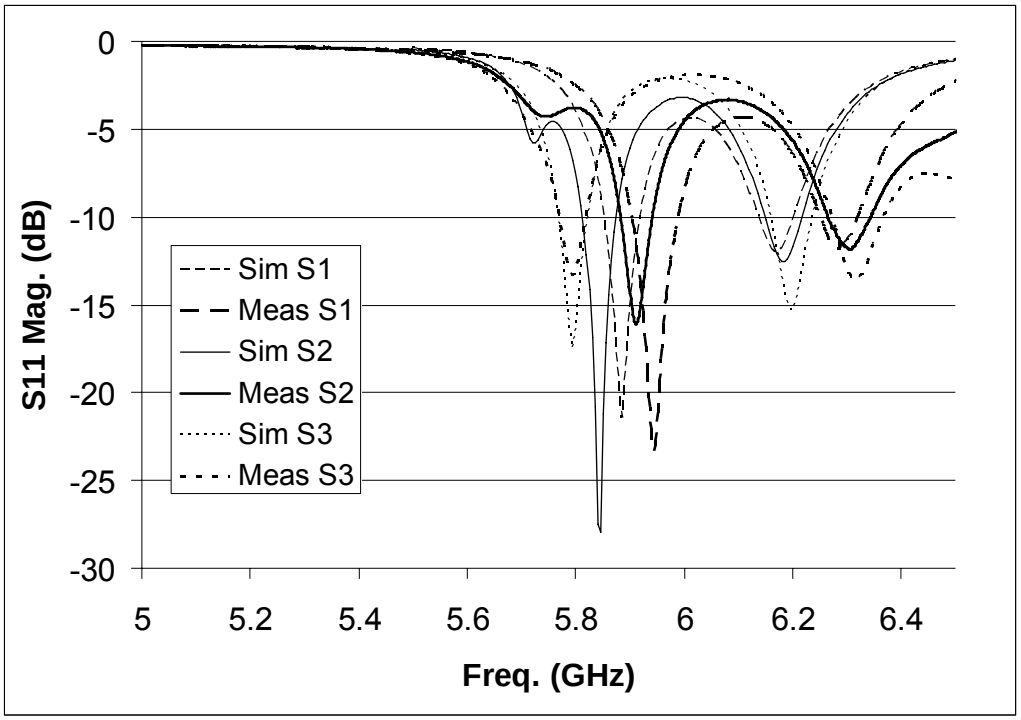

Figure 3.31. Comparison of simulated and measured S_{11} for the MEMS switched parasitic array for three states. State S1 has both switches open, state S2 has one switch closed and one switch open, and state S3 has both switches closed.

When both switches are off, the resonant frequencies of the parasitic elements coupled to both the TM_{10} and TM_{01} modes overlap. There is a single endfire frequency at which the structure radiates simultaneously in the ±x and ±y directions. Closing a single switch loads one of the coupling lines, thus lowering the resonant frequency in only one direction. The result is the added ability to steer the antenna pattern while operating at a single frequency.

Figure 3.31 shows good correlation between simulated and measured S_{11} for the condition where one switch is open, and the other is closed (S2). Due to symmetry, the response is identical for both directions. Figure 3.31 also shows the S_{11} values for both switches open (S1) and for both switches closed (S3). As can be seen from Figure 3.31, there was an increase in measured resonant frequencies by 1.2%-2.1% over the simulated values. As discussed previously, this frequency increase was a result of the fabrication tolerances.

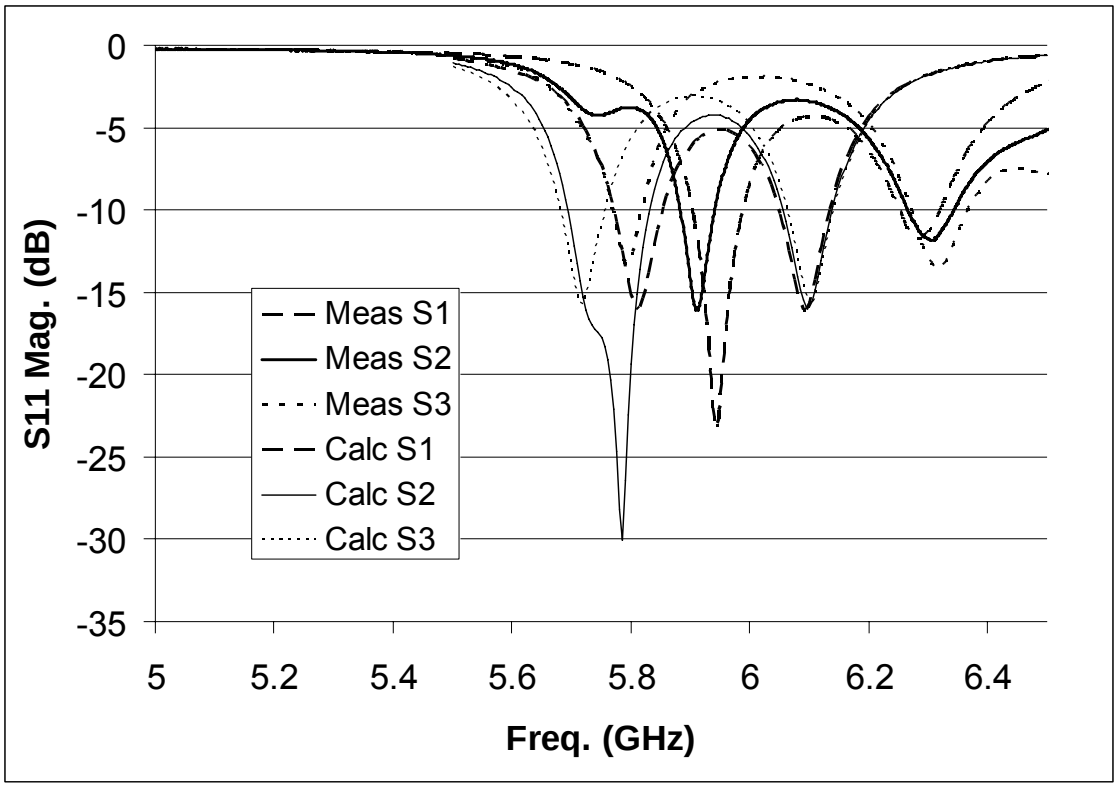

Figure 3.32. Comparison of calculated and measured S_{11} for the MEMS switched parasitic array for three states. State S1 has both switches open, state S2 has one switch closed and one switch open, and state S3 has both switches closed.

Figure 3.32 shows a comparison of measured S_{11} with results calculated using the aforementioned analysis method. The state S2 has one switch open, and the other closed. Due to symmetry, the response is identical for both directions. Figure 3.32 also shows the S_{11} values for both switches open (S1) and for both switches closed (S3). The relative changes in resonant frequencies correlated well for the switching states, with the measured frequencies between 1.2% and 3.4% higher than calculated results. This frequency increase was likely a result of the fabrication tolerances as well as loading effects of the actual MEMS switches which were not included in the coupled patch analysis.

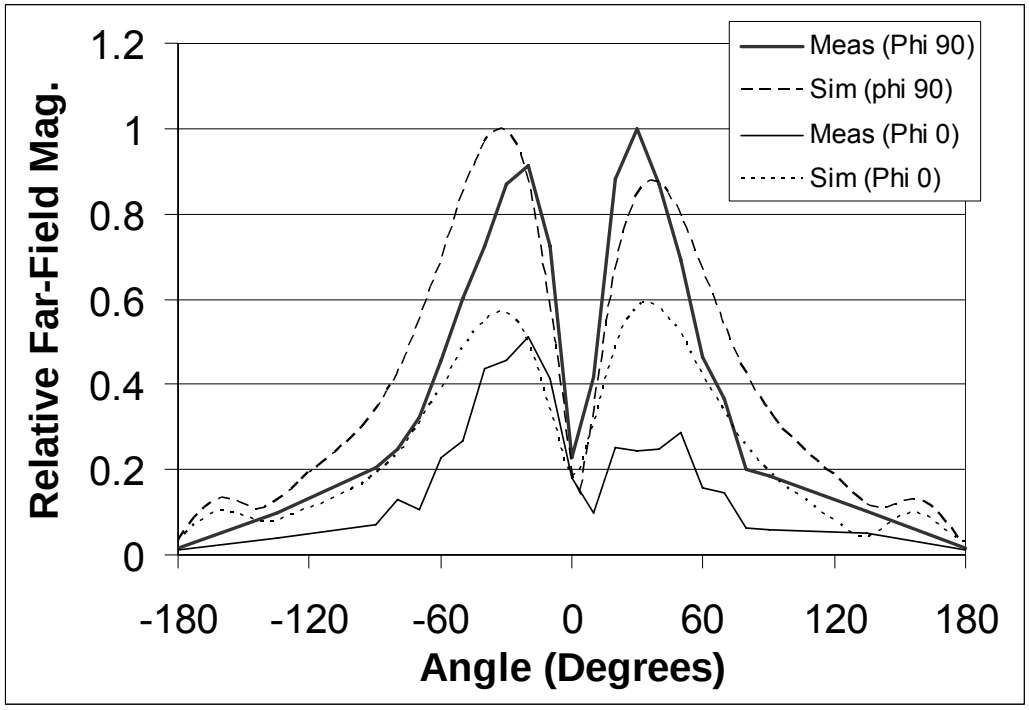

Figure 3.33. Comparison of the simulated and measured radiation pattern for the MEMS switched antenna at the endfire resonant frequency (5.92 GHz) with one switch open and one switch closed.

Figure 3.33 shows a comparison of the simulated and measured far-field radiation pattern for the endfire mode (5.85GHz simulated/5.92GHz measured) with one switch open and one switch closed. Figure 3.34 shows a comparison of the simulated and measured far-field

radiation pattern for the broadside mode (6.18GHz simulated/6.31GHz measured) with one switch open and one switch closed. Figure 3.33 and Figure 3.34 show good correlation between simulated and measured far-field characteristics.

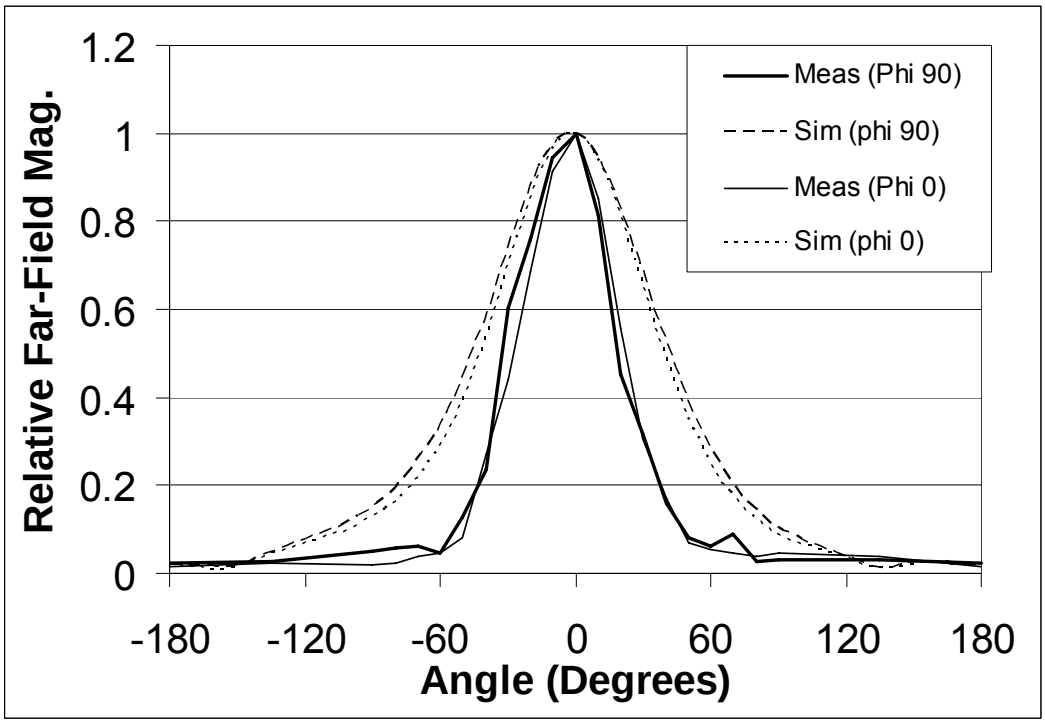

Figure 3.34. Comparison of the simulated and measured radiation pattern for the MEMS switched antenna at the broadside resonant frequency (6.31 GHz) with one switch open and one switch closed.

3.7 MULTI-MODE EBG ARRAY

Electromagnetic Bandgap (EBG) structures are periodic arrays of electrically small unit cells that suppress surface currents over a limited bandwidth [18]. This approximates a zero tangential magnetic field causing the structure to behave as a magnetic conductor [18]. At the EBG resonant frequency, a reflected electromagnetic wave is in phase with the incident wave.

Using conventional technology, a monopole or dipole antenna in close proximity to a ground plane will not radiate since the reflected radiated field from an electrical conductor is out of phase with the incident signal, canceling the radiated energy. For the band over which an EBG structure behaves as a magnetic conductor, the incident and reflected fields are in phase, resulting in constructive interference that permits low-profile printed monopole and dipole antennas to radiate [18]. This offers additional degrees of freedom to design frequency-steerable antenna arrays that have additional radiating modes unavailable to conventional microstrip technology.

This section presents the initial investigation into design enhancements of multi-mode radiating structures using EBG technology and the engineering trade-offs. First, the EBG structure design is presented. The structure is then combined with a single patch antenna to add additional radiating modes. Simulated and measured impedance measurements validate the initial simulated results. Finally, an EBG-based multi-mode radiating structure design is presented which offers frequency-switchable beam steering. The antenna area is significantly reduced compared to structure of Section 3.2, but at a considerable cost in terms of gain and efficiency.

3.7.1 EBG STRUCTURE

Figure 3.35 shows the EBG unit cell of a structure simulated using HFSS. The unit cell dimensions are 5.334mm^2 (210mil^2), with a 1.016mm (40mil) thick copper ring spaced 0.254mm (10mil) from adjacent copper rings. The copper rings are separated from the ground plane by a 0.635mm (25mil) Rogers RO3010 substrate having a relative dielectric constant of 10.2 and 0.0035 loss tangent. The EBG is topped by a 0.508mm (20mil) Rogers RT/Duroid superstrate having a relative dielectric constant of 2.2 and 0.0009 loss tangent.

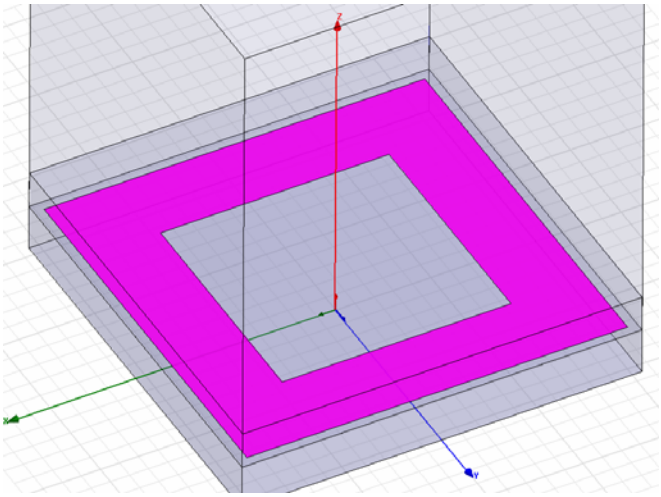

Figure 3.35: Single unit cell of electromagnetic bandgap structure

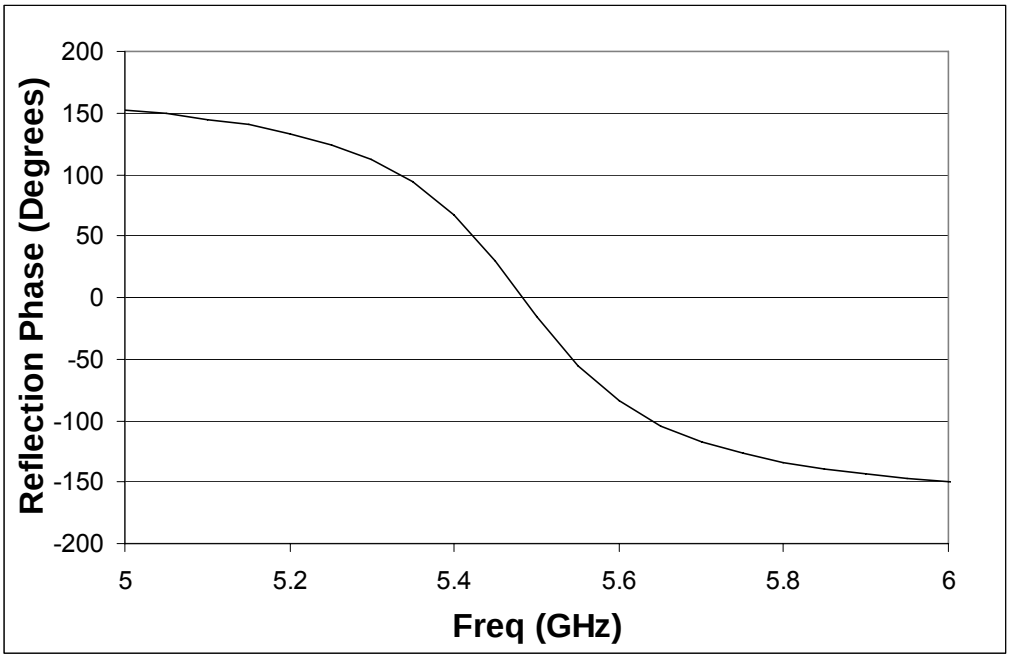

Figure 3.36: Simulated reflection phase of the EBG structure of Figure 3.35

HFSS simulations of the EBG structure of Figure 3.35 model a single unit cell with periodic boundary conditions and a normally incident plane wave. As shown in Figure 3.36, the resonant frequency of the EBG structure is 5.48 GHz, where the reflection phase is 0

degrees (in phase with the incident wave). According to [18], the EBG structure approximates a magnetic conductor across the bandwidth over which the reflection phase is within ±90º of the incident phase. The simulated ±90º reflection bandwidth is 0.26 GHz as shown in Figure 3.36.

3.7.2 PATCH ANTENNA OVER EBG

After characterizing the EBG structure in Section 3.7.1, the next step is to evaluate the performance of a patch antenna over the structure. A microstrip-fed patch antenna is positioned over a 5x7 array of EBG unit cells as shown in Figure 3.37. The portion of the microstrip line centered over the EBG is 14.2mm long (from the EBG edge to the patch edge). The inset feed is located 4mm from the patch edge, with 0.7mm gaps on either side. The patch itself is 12mm^2. The fabricated EBG is printed on a 0.635mm (25mil) Rogers RO3010 substrate which is backed by a ground plane. The fabricated antenna and microstrip line are printed on a 0.508mm (20mil) Rogers RT/Duroid substrate with the copper cladding removed from the back side. The patch antenna substrate is bonded to the EBG circuit such that the antenna is positioned over the EBG structure as shown in Figure 3.37.

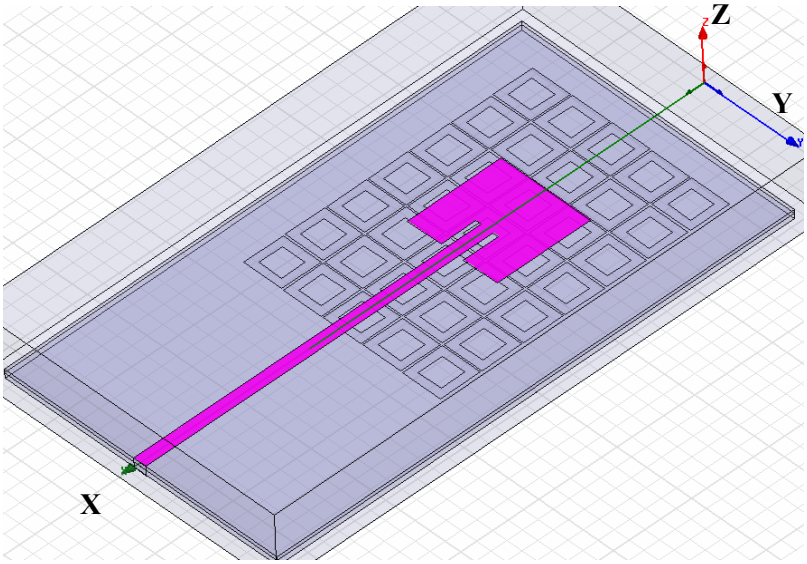

Figure 3.37: Microstrip-fed patch antenna over EBG structure of Figure 3.35

HFSS simulated and measured results of the antenna of Figure 3.37 are shown in the S_{11} plot of Figure 3.38. The simulated results show resonances at 5.28GHz, 5.84GHz and 6.00GHz. The measured curve has a similar shape, with resonances 2.3%-3.7% higher than simulated values. This disparity is likely due to manufacturing tolerances as well as the presence of a silicone adhesive layer used to bond the two different substrate materials together.

Upon examination of the simulated current distribution of Figure 3.39a, the first resonance at 5.28GHz shows a current distribution on the patch that is consistent with a radiating patch antenna. The far-field radiation characteristics of Figure 3.40a show a distorted broadside pattern with a 3.90 maximum gain and 84.8% radiation efficiency at 5.28GHz. The simulated 5.84GHz current distribution of Figure 3.39b shows little current on the patch itself, but a considerable amount of current at the microstrip patch junction indicating that the feed line is functioning as a short-circuited transmission line. The far-field radiation plot of Figure 3.40b shows that the resonance at 5.84GHz is a radiating mode with a maximum gain of 4.30, but a reduced radiation efficiency of 64.0%. HFSS simulations indicate that the radiation efficiency further drops to 53% for the 6GHz resonance. From basic antenna theory, a single microstrip-fed patch antenna over a regular ground plane only resonates at frequencies where the electrical length of the patch is close to a half-wavelength multiple. The simulated and measured performance indicate that the EBG structure adds additional resonances in which the microstrip line feeding the patch antenna acts as a radiating short-circuit terminated monopole antenna.

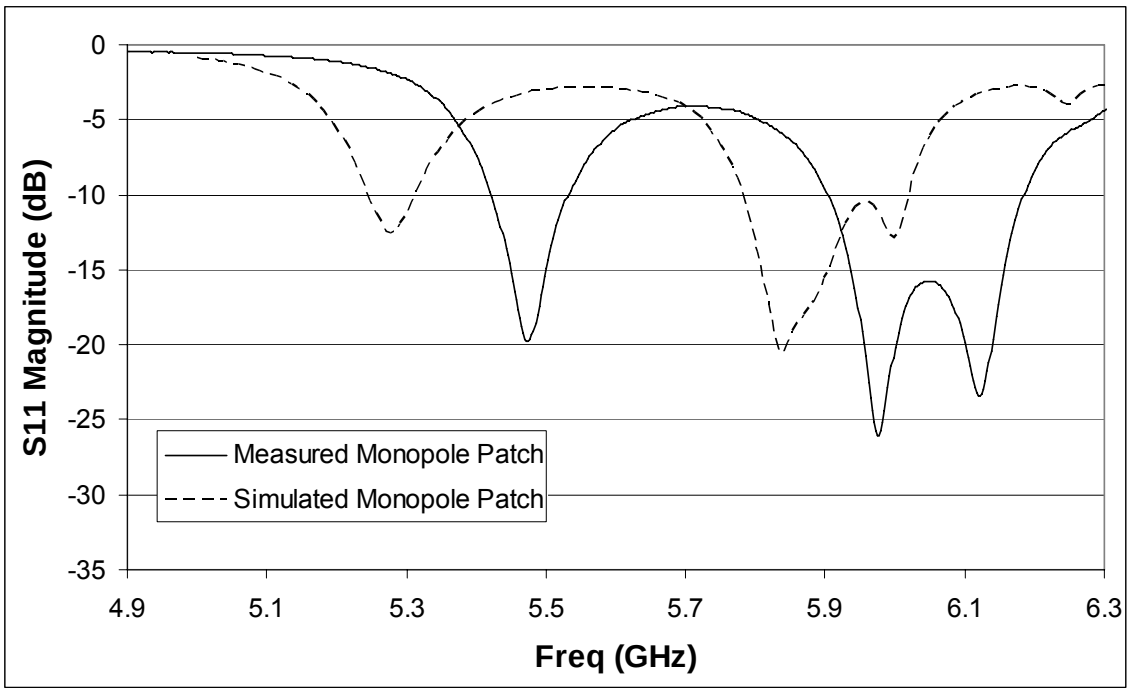

Figure 3.38: Comparison of HFSS simulated and measured S11 of microstrip-fed patch antenna over EBG structure of Figure 3.37, where the microstrip line behaves as a loaded monopole antenna.

Additional experiments were carried out to provide further confirmation that the first resonant mode arises due to radiation as a patch antenna. Figure 3.41 shows S_{11} measurements of the original structure of Figure 3.37, and the same structure with conductive copper tape extending the patch length. As expected, the low frequency resonance decreased by 210MHz with the extension of the patch. The second resonance shifted by only 20MHz and the third resonant frequency remained constant. The impedance match, however, degraded for the second and third resonance. These measured results further confirm that the first resonant mode arises due to radiation as a patch antenna, and the additional resonances arise from the feed line and EBG structure radiating as a monopole antenna, with frequencies determined by the EBG characteristics and coupling.

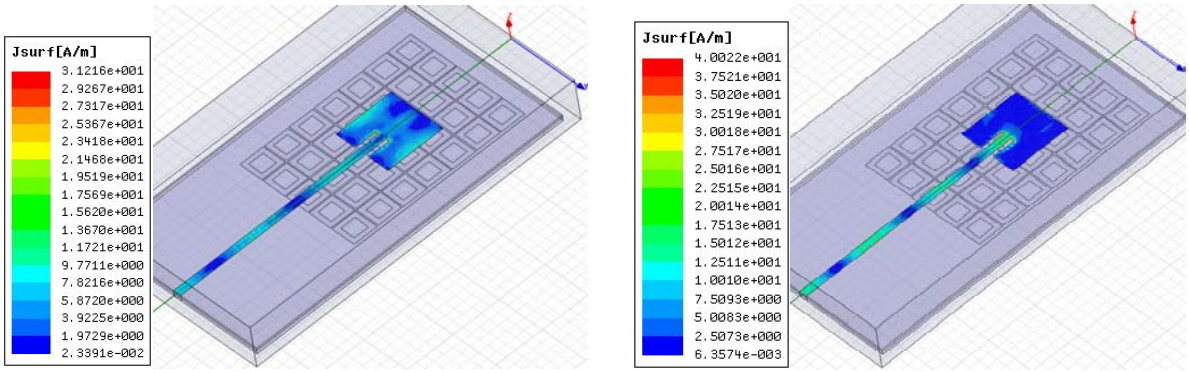

(a) (b)

Figure 3.39: HFSS simulated surface current distribution for (a) first resonance at 5.28GHz and (b) second resonance at 5.84GHz.

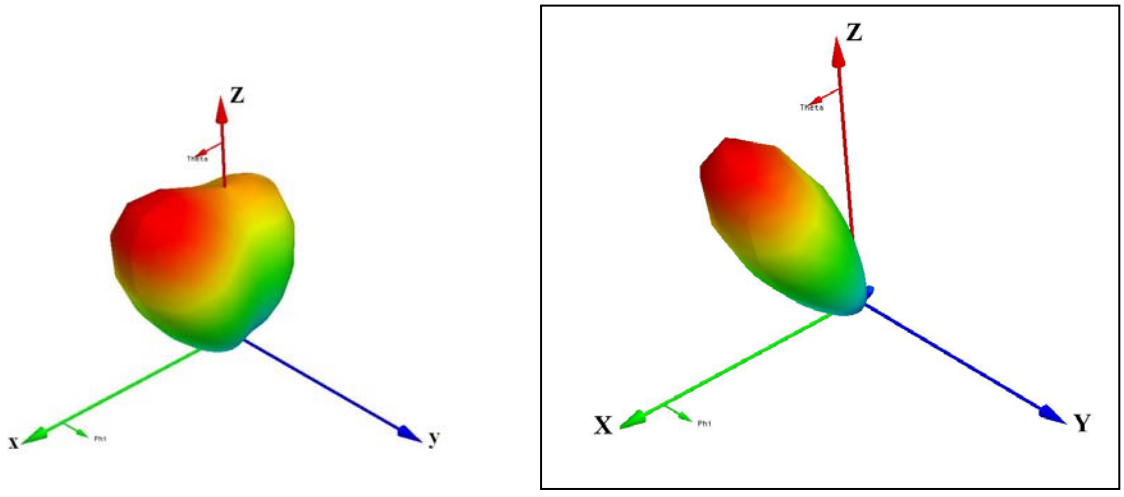

(a) (b)

Figure 3.40: HFSS simulated far-field radiation for (a) first resonance at 5.28GHz having 3.90 maximum gain and 84.8% radiation efficiency and (b) second resonance at 5.84GHz having 4.30 maximum gain and 64.0% radiation efficiency.

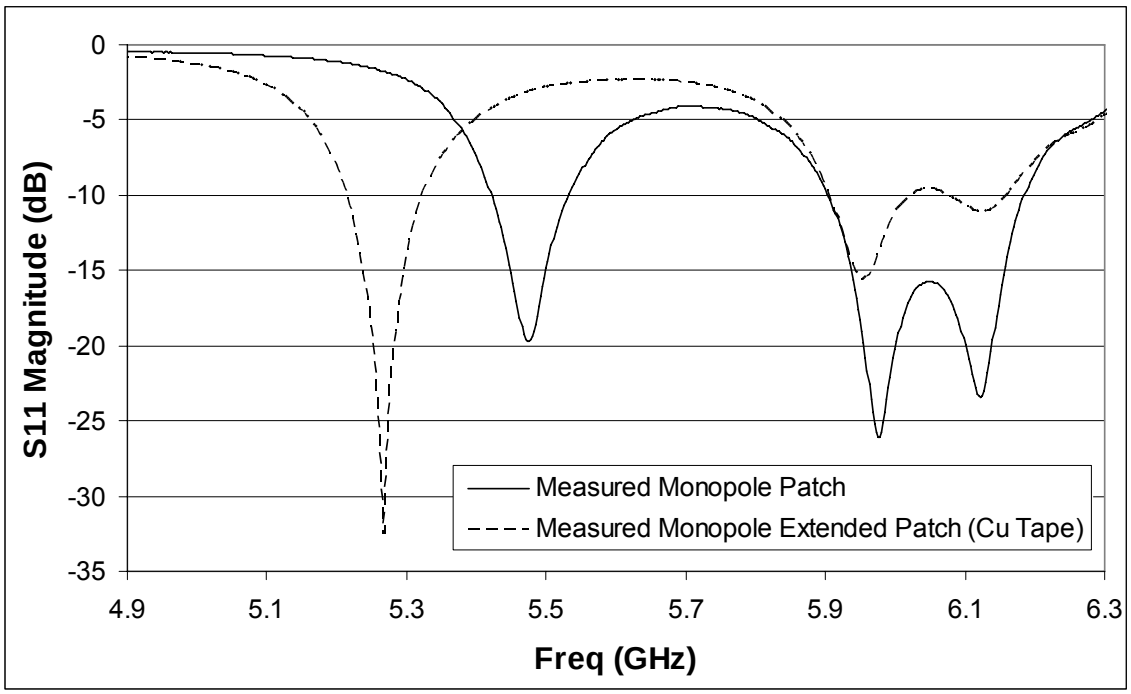

Figure 3.41: Measured results for (a) Original structure of Figure 3.37 and (b) structure of Figure 3.37 with conductive copper tape extending the length of the patch.

3.7.3 FREQUENCY-SWITCHABLE EBG ANTENNA

The results of Section 3.7.2 led to the idea of designing a compact structure to accomplish frequency-dependent beam steering similar to the multi-mode parasitic patch arrays of Section 3.2, but with resonant frequencies more closely spaced. A single large full-wavelength patch with different x and y dimensions has two resonant endfire modes in the ±x and ±y directions, which may be closely spaced in frequency. Although this antenna will radiate broadside when the frequency is reduced by approximately 50%, there is no broadside mode at frequencies close to the endfire modes.

A microstrip-fed full-wavelength patch was designed to be fabricated over the EBG structure of Figure 3.35. The purpose of adding the EBG structure is twofold. Firstly, the EBG and microstrip feed interact to create a broadside resonance where the microstrip feed line acts like a monopole antenna. Secondly, the EBG acts as a slow-wave structure, due to inductive and capacitive loading, which significantly reduces the antenna size.

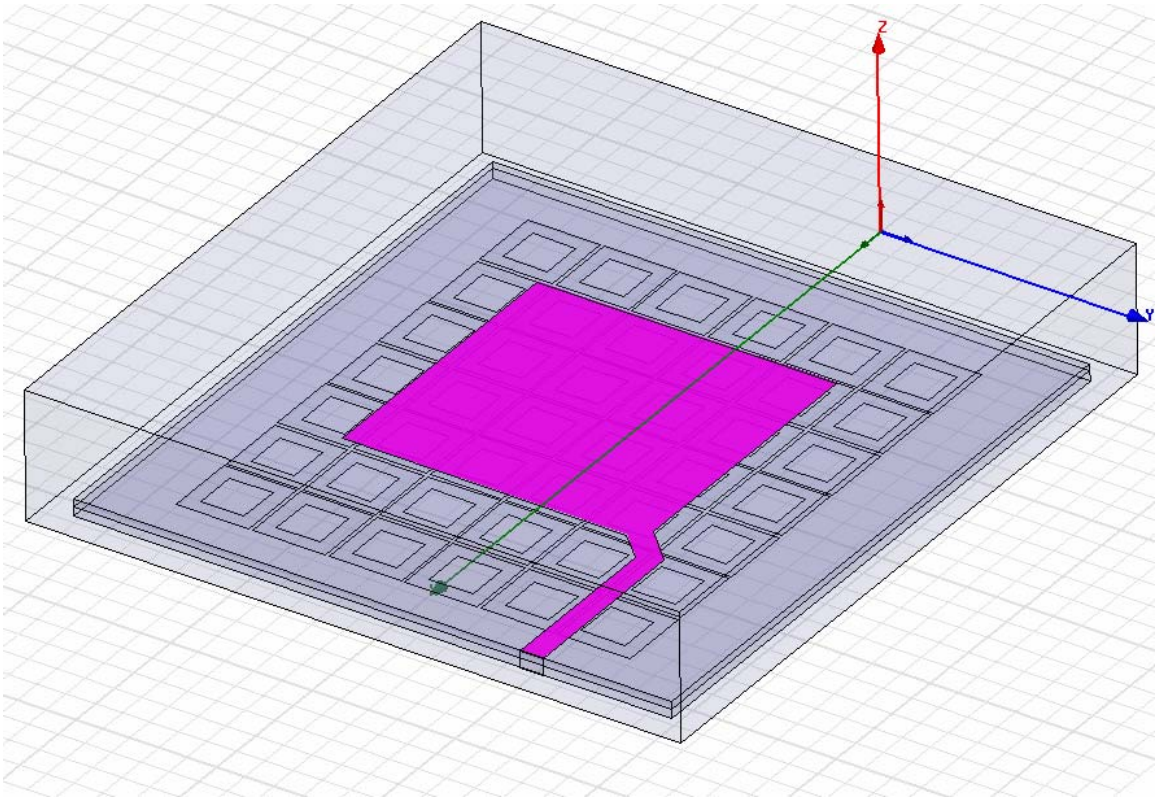

Figure 3.42: Frequency-switchable EBG antenna over the EBG structure of Figure 3.35.

The frequency-switchable EBG patch antenna design is shown in Figure 3.42. The patch antenna is situated over a 6x7 array of EBG unit cells as in Figure 3.35. The patch dimensions are 20.5mm x 21mm. The 1.6mm wide microstrip feed length is 9.4mm between the EBG edge and 45 degree bend. The line length is 4mm between the bend and patch. The centre of the feed line begins 4.6mm from the EBG corner. The EBG pattern is situated on a 0.635mm (25mil) Rogers RO3010 substrate which is backed by a ground plane. The antenna and microstrip line are on the top side of the 0.508mm (20mil) Rogers RT/Duroid EBG superstrate. Figure 3.43 shows a size comparison of the multi-mode parasitic patch arrays of Section 3.2 and the frequency-switchable EBG patch antenna design shown in Figure 3.42. The parasitic patch array of Section 3.2 has a 5920cm^2 area, and the EBG antenna area is reduced by 80% to 1184 cm^2.

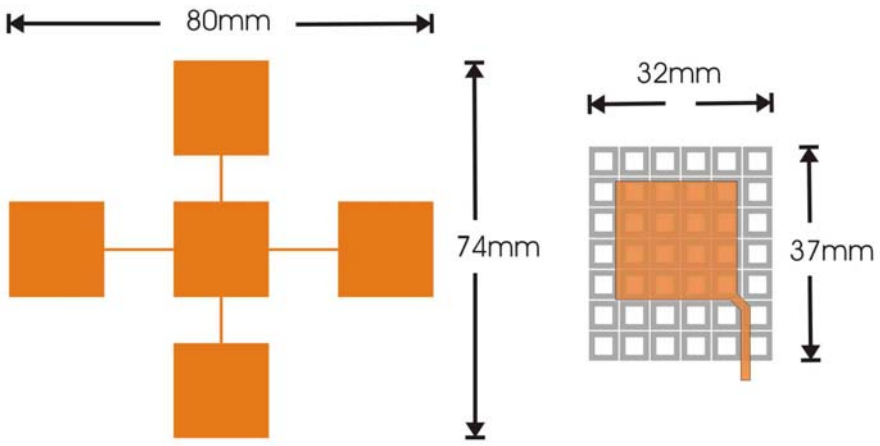

(a) (b)

Figure 3.43: Antenna dimensions for (a) the multi-mode parasitic patch arrays of Section 3.2 and (b) the frequency-switchable EBG patch antenna design shown in Figure 3.42

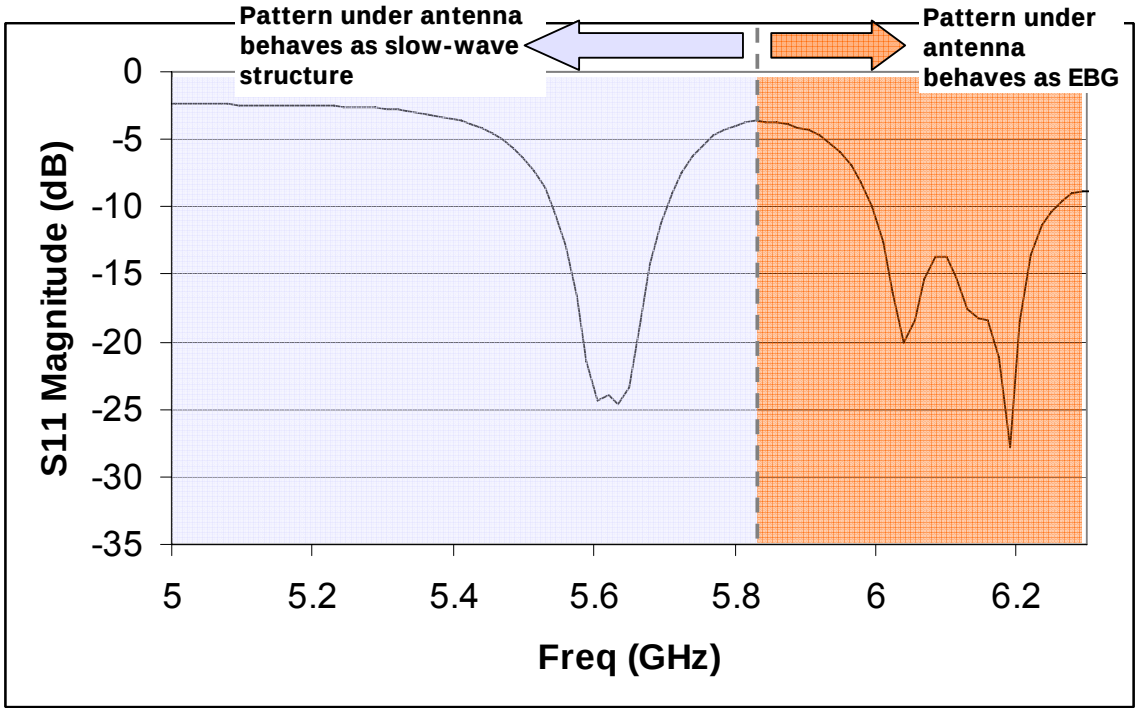

Figure 3.44: Simulated S_{11} response of the frequency-switchable EBG patch antenna design shown in Figure 3.42

The simulated S_{11} response of Figure 3.44 shows the closely spaced full-wavelength patch resonances between 5.58GHz and 5.70GHz where the pattern under the antenna behaves as a slow-wave structure. Additional resonances arise in the region above 5.85GHz where the pattern under the antenna and feed line act as an EBG structure. Radiation patterns for the endfire resonances are plotted in Figure 3.45a and b, which show 90 degree beam steering from 5.58GHz to 5.70GHz. A broadside resonant mode radiates at 6.04GHz as shown in Figure 3.45c. The antenna can therefore steer the pattern along three axes in a manner similar to the patch arrays of Section 3.2, but with substantially reduced gain and efficiency. This performance degradation arises from the reduced antenna size as well as the energy storage and losses in the EBG structure. In terms of frequency range required for steering, there is an in incremental 10% reduction compared to 5-element patch design. Further work is required to improve performance if this antenna is to be used in practical RFID applications.

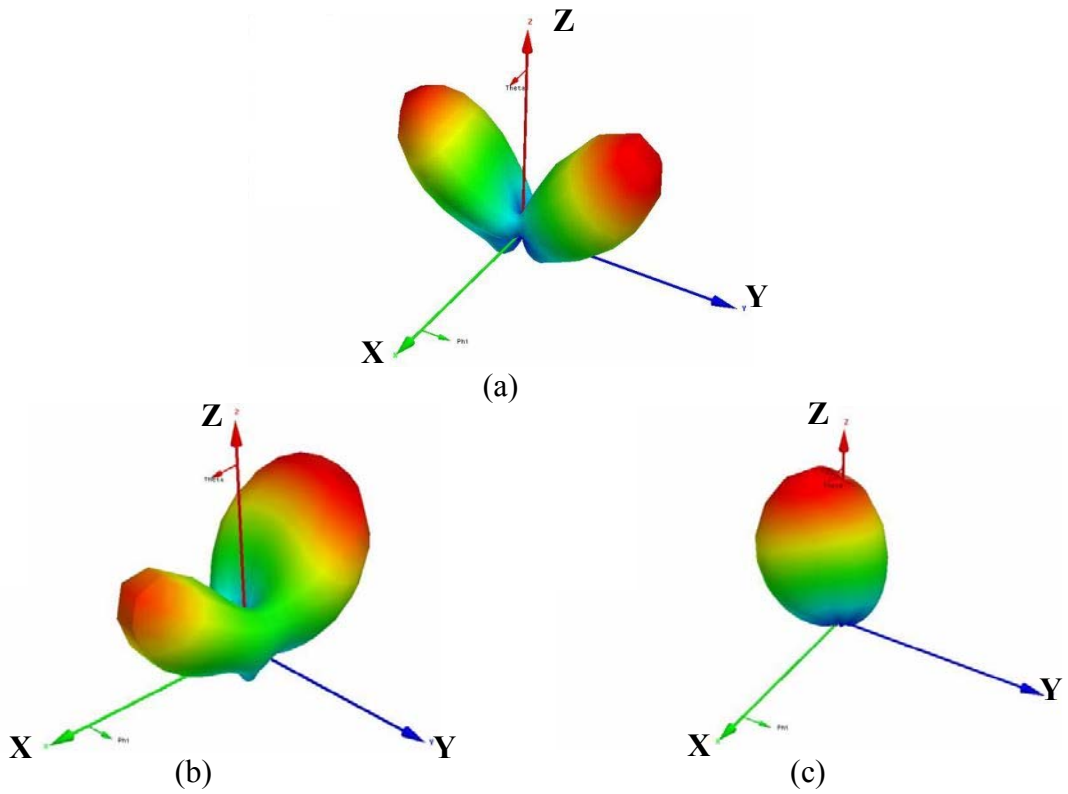

Figure 3.45: Far-field radiation patterns for the frequency-switchable EBG patch antenna. (a) First endfire mode at 5.58 GHz with 2.38 gain and 74.6% radiation efficiency. (b) Second endfire mode at 5.70 GHz with 1.82 gain and 70.6% radiation efficiency. (c) Broadside mode at 6.04 GHz with 3.25 gain and 56.8% radiation efficiency.

3.8 SUMMARY

This chapter has introduced an analysis and design methodology for a class of multi-mode parasitic patch arrays. The antenna arrays consist of a centre microstrip patch antenna and direct coupled parasitic elements having multiple resonant frequencies. Hardware has been fabricated and tested for two applications of these structures.

The first is a novel passive RFID tag which has an adaptive antenna array that can be steered without the need for any internal power supply. Each resonant frequency has an associated high-gain radiation pattern that allows the RFID reader to remotely change the direction of communication. The second is a novel MEMS-based switched parasitic antenna array which has additional beam-steering capabilities at each frequency. Hardware has been fabricated and tested, with good correlation between simulated and measured results.

For the purpose of designing the parasitic arrays, we have developed a novel analysis technique that combines well-established models. The purpose of the analysis is to provide an approximation of the input impedance and variation of the radiation pattern with frequency. The analysis allows the designer to avoid a time-consuming trial-and-error process by combining models based on electromagnetic theory and circuit theory to provide a reasonable approximation of the parasitic array characteristics. The new analysis method was validated alongside measured and simulated results, with good correlation for both impedance characteristics and far-field radiation patterns.

The final section of this chapter provided an initial investigation into design enhancements of multi-mode radiating structures using EBG technology and the engineering trade-offs. An EBG-based multi-mode radiating structure design was presented, which is capable of frequency-switchable beam steering. The antenna area is significantly reduced compared to the parasitic patch array structure, but at a considerable cost in terms of gain and efficiency.

CHAPTER 4

MEMS ON FLEXIBLE SUBSTRATES

4.1 INTRODUCTION

There were many significant challenges that arose in developing a process to fabricate MEMS devices on flexible substrates. The process of photolithography requires substrates to remain flat for spin-coating, hot plate baking, alignment and exposure. The 250°C Plasma-Enhanced Chemical Vapour Deposition (PECVD) process temperature precludes the use of organic adhesives for temporary adhesion of the flexible substrate to a rigid carrier. Furthermore, MEMS devices have moving mechanical structures that are prone to distortion when bending the substrate.

This chapter documents the development of a novel process to fabricate MEMS devices on flexible substrates. DuPont Kapton was selected as a flexible substrate material as it may

handle temperatures in excess of 350°C, and it is resistant to the required process chemicals [74]. Kapton has a smooth surface with better than 100nm flatness [75].

The first step in the MEMS process is to chemically etch the bulk Kapton substrate to leave thicker islands of material separated by a flexible membrane (See Figure 4.1). The advantages of this configuration are twofold. First, MEMS devices are fabricated over the thicker regions which provide mechanical support. The second benefit arises since a grid pattern of thick islands, surrounded by a thin membrane, allows the rigid-flex circuit to be held flat by vacuum during photolithography.

Figure 4.1: Rigid-flex substrate on vacuum chuck

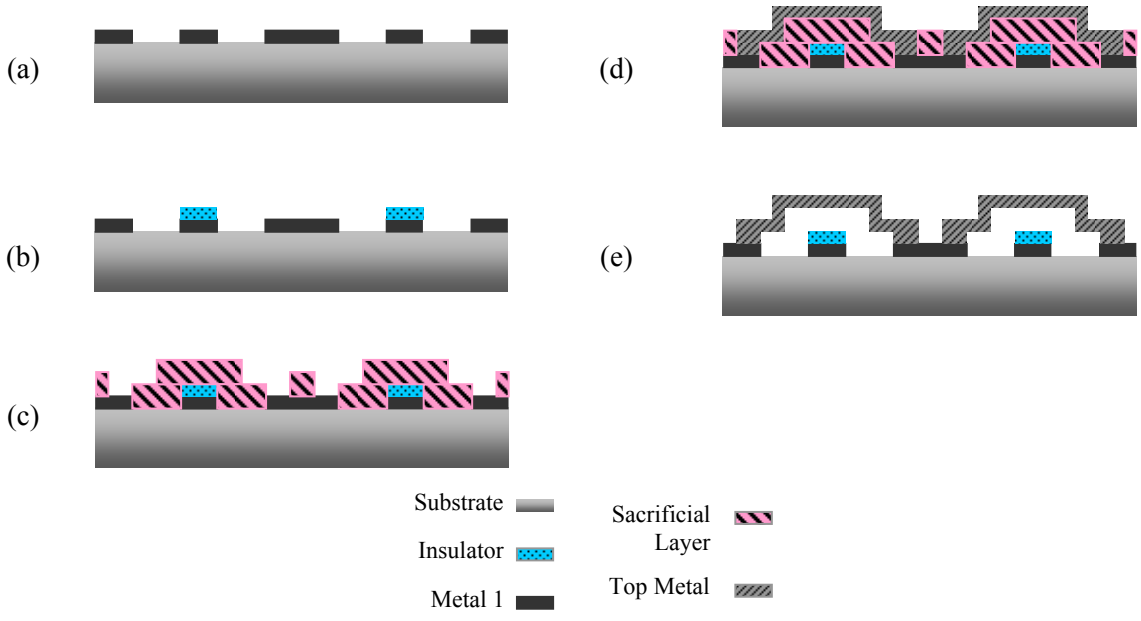

Figure 4.2: Overview of 4-mask MEMS process. (a) Mask 1: Pattern first metal (Metal 1) layer (b) Mask 2: Pattern insulator layer (c) Mask 3: Pattern sacrificial layer for anchors (d) Mask 4: Pattern top metal layer (e) Release MEMS devices.

A flat aluminum wafer with small vacuum holes (See Figure 4.1) provides sufficient flatness and mechanical support during spin coating and mask alignment. Consequently, the flexible substrate does not need to be bonded to a rigid carrier once the islands have been machined. Upon completion of the process, the released MEMS devices remain on a flexible substrate which is not bonded to any rigid carrier.

The flexible substrate MEMS process is based on a 4-mask fabrication technique as in [76] and [77]. The 4-mask process, shown in Figure 4.2, is best suited for fabricating electrostatically actuated cantilever structures. A DC bias applied between a pull-down electrode and cantilever results in electrostatic force that pulls the beam downwards such that the device acts as a capacitive switch or variable capacitor. The first mask patterns the bottom metal (metal 1) layer which forms the electrical circuit connections as well as the pull-down electrodes. The second mask patterns an insulating layer, which provides DC isolation between the cantilever and pull-down electrode to prevent a short circuit in the down-state. The third mask patterns a sacrificial layer to produce anchors which provide electrical continuity and mechanical support between the bottom and top metal layers. The sacrificial layer thickness defines the up-state air gap of the cantilever. The fourth mask patterns the top metal layer to shape the cantilever beams. Finally, the release process removes the sacrificial layer to leave the freely standing MEMS structures.

Since standard MEMS fabrication processes are designed to produce devices on rigid substrates such as silicon, glass or alumina, several process modifications were required to handle flexible materials. Section 4.2 documents the adaptation of each fabrication process step to handle flexible substrates.

Several combinations of process and materials are available to fabricate MEMS devices on flexible substrates. Only a limited number of specific combinations are viable due to compatibility between processes, materials and chemicals. In many cases, incompatibilities may be avoided by consulting with data from manufacturers, and from excellent references such as [78] and [79]. In developing a novel process, however, data is not always available, and many experiments were carried out using trial and error methods. Section 4.3 documents

the selection of compatible materials and also highlights incompatibilities that were encountered to aid future researchers in developing MEMS processes. Section 4.4 documents the newly developed process which has been used to successfully fabricate working MEMS devices on flexible substrates. Appendix B provides detailed recipes for each step of the MEMS process of Section 4.4.

4.2 PROCESS ADAPTATION TO FLEXIBLE SUBSTRATES

Standard MEMS processes are designed to fabricate devices on rigid substrates such as silicon, glass or alumina. One common method of processing flexible substrates is by means of temporary bonding to a rigid wafer that acts as a carrier. This method, however, is only viable under limited conditions. In practice, it was found that adhesive material peel strength increases significantly when cycled through temperatures greater than 120ºC, conditions encountered during sputtering and PECVD processes.

Experiments were carried out using 3M-100 adhesive, double-sided Kapton Tape, as well as cured AZ3330 photoresist to bond the entire back side of a flexible substrate to a rigid glass wafer. This bonding method ensured intimate thermal contact between the flexible substrate and glass wafer, a requirement for adequately baking the photoresist during photolithography processes. The photoresist blistered and oxidized at high temperatures, damaging the flexible substrate. The 3M-100 adhesive was too strong for temporary adhesion even with no temperature cycling. The double-sided Kapton tape, with its silicone-based adhesive, became so strong after temperature cycling that it was difficult to remove the flexible substrate without tearing it. Substrates that were not torn after removal were distorted from stretching in addition to having visible stress marks.

Since it was not possible to temporarily bond the flexible substrates to rigid carriers for all processes, creative workarounds were developed for each specific process. The process-specific adaptations are documented in this section.

4.2.1 Substrate Cleaning

Many integrated circuit processes begin with an RCA cleaning step, in which the substrate is immersed in a heated mixture of ammonium hydroxide and hydrogen peroxide. This process is incompatible with Kapton due to the presence of ammonium hydroxide [80]. To clean a Kapton substrate, it must first be soaked in acetone, then isopropyl alcohol, then rinsed with DI water and dried. The substrate is then cleaned in RIE oxygen plasma prior to depositing metal or dielectric.

4.2.2 Photolithography

Photolithography processes require the flexible substrate to be securely held flat for spin coating, alignment and exposure, as well as for hot plate baking. An additional requirement for hot plate baking is intimate thermal contact between the substrate and the vacuum hot plate itself. Proper contact ensures adequate heat flow through the substrate to the photoresist. This is not possible if only the corners or edges of the flexible substrate are secured, since there will be an air gap in the centre.

If the flexible substrate is secured to a rigid wafer using a double-sided adhesive covering the entire area, the photolithography process is almost identical to the rigid wafer version. The only required modification is doubling the soft bake time and increasing the post-exposure bake duration by 50%. This ensures adequate baking of photoresist on flexible organic substrates that have lower thermal conductivity than alumina, silicon and glass.

Figure 4.3: Flexible substrate held to rigid wafer by (a) placing a small drop of DI water between the substrate and carrier and (b) heating substrate such that the surface tension pulls the substrates together as the water evaporates.

Since the double-sided adhesive cannot be used for high-temperature processes as previously discussed, other alternatives were considered since repeatedly bonding and removing the flexible substrate would greatly increase the likelihood of damage. Figure 4.3 shows a temporary adhesion method that employs the same principle which causes stiction in wet released MEMS devices (Refer to Section 4.2.7 for more detail). A small drop of DI water is first placed on a rigid wafer, followed by the flexible substrate as shown in Figure 4.3a. The wafer is then heated, causing the water to evaporate. As the water volume decreases, the flexible substrate is pulled down by surface tension until it contacts the rigid substrate as shown in Figure 4.3b. Although this method was used successfully during the initial process development stage, there is a risk that the substrate will not hold during the spin-coating process. Additionally, the flexible substrate tends to release from the rigid carrier when immersed in liquid developer.

The most reliable flexible circuit photolithography adaptation uses a rigid-flex substrate. A grid pattern of rigid islands, separated by narrow channels with a thin surrounding membrane as shown in Figure 4.1, ensures the structure will be held flat on a vacuum chuck with minimal distortion. Figure 4.4 shows an overhead view of the rigid-flex substrate on a photoresist spinner. A lightweight aluminum vacuum jig was machined with holes in the centre. The jig sits on the spinner vacuum chuck, and the rigid-flex substrate is placed over the holes on the jig. No adhesive is required since the vacuum is strong enough to hold the entire assembly firmly in place. The smooth jig also ensures the substrate is held flat while spinning.

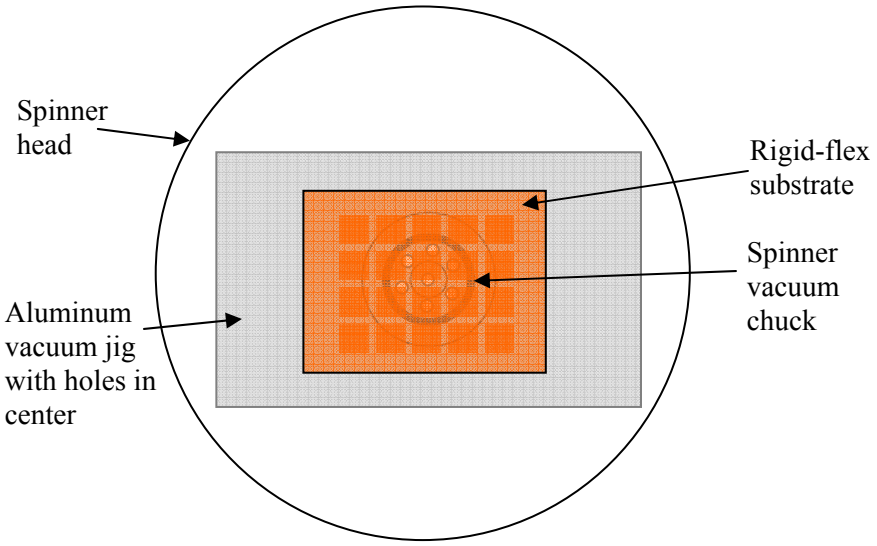

Figure 4.4: Overhead view of rigid-flex substrate over a vacuum jig held in place on the spinner head.

After spin-coating the photoresist, the substrate is easily removed once the vacuum has been turned off. Baking the substrate is straightforward provided it is positioned over vacuum holes in the hot plate in a similar configuration to Figure 4.1. As previously discussed, the photoresist soft bake time should be doubled and the post-exposure bake duration is increased by 50%. For alignment and exposure, the vacuum jig may be used between the rigid-flex substrate and the mask aligner vacuum chuck if large grooves are present that would otherwise distort the circuit. The rigid-flex substrate and vacuum jig combination were successfully used to fabricate working MEMS devices.

4.2.3 Vacuum Metal Deposition

The first attempts at depositing metal on flexible substrates were carried out by using double-sided adhesives to hold the material in place. In addition to substrate damage when removing the temperature-cycled adhesive, the quality of sputter deposited metal films was severely compromised. Air bubbles invariably trapped in the adhesive would expand and escape under vacuum. This was further exacerbated when the substrate was heated during metal deposition. As shown in Figure 4.5, the escaping air oxidized the deposited metal

around the periphery of the flexible substrate. The oxide contamination spread to the surface of the flexible substrates, which would directly impact device quality.

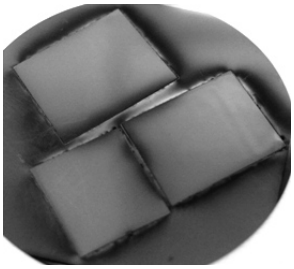

Figure 4.5: Oxidation of sputtered metal around Kapton substrates held in place by double-sided adhesive.

Alternatively, the four corners of a flexible substrate may be taped to a rigid support using single-sided Kapton tape as shown in Figure 4.6. Although the trapped air under the adhesive does cause some oxidation, it is limited to a 1-2mm perimeter around the small pieces of tape at the corners. Provided the substrate is large enough that the devices are at least 4mm away from the tape edge, there should be no adverse impact on device quality.

Figure 4.6: Kapton substrate held in place on a metal chuck for vacuum metal deposition.

Prior to depositing metal on polyimide flexible substrates, it is essential to perform a dehydration bake since the materials absorb ambient moisture which adversely affects adhesion [81]. Samples must be placed immediately in the vacuum chamber following the bake as moisture re-absorption may occur within minutes [81]. It is most practical to first

mount the flexible circuits onto a metal chuck used in the vacuum chamber, and then bake the entire assembly. This permits the fastest possible transfer to the vacuum chamber, minimizing any moisture intake to the flexible substrate.

4.2.4 PECVD OXIDE DEPOSITION

Depositing silicon dioxide at 250ºC is the highest temperature process used in this MEMS fabrication procedure. It was found that high-temperature silicone adhesives leave a residue when cycled through 250ºC, and are even more difficult to remove than after a vacuum metal deposition process. For this reason, any contact between adhesive and flexible substrate should be avoided. The flexible substrates must be attached to a rigid carrier during the PECVD process. Initially, flexible substrates were placed on a 6" silicon wafer, and glass microscope slides were placed over the substrate edges, with only gravity holding everything in place as shown in Figure 4.7a. Due to stress between the deposited silicon dioxide and flexible material, there is significant substrate warping which tends to lift the glass slides. To overcome this effect, Kapton tape is used to hold down the slides as shown in Figure 4.7b. This configuration provides sufficient pressure to hold down the flexible material while avoiding direct contact between the substrate and adhesive.

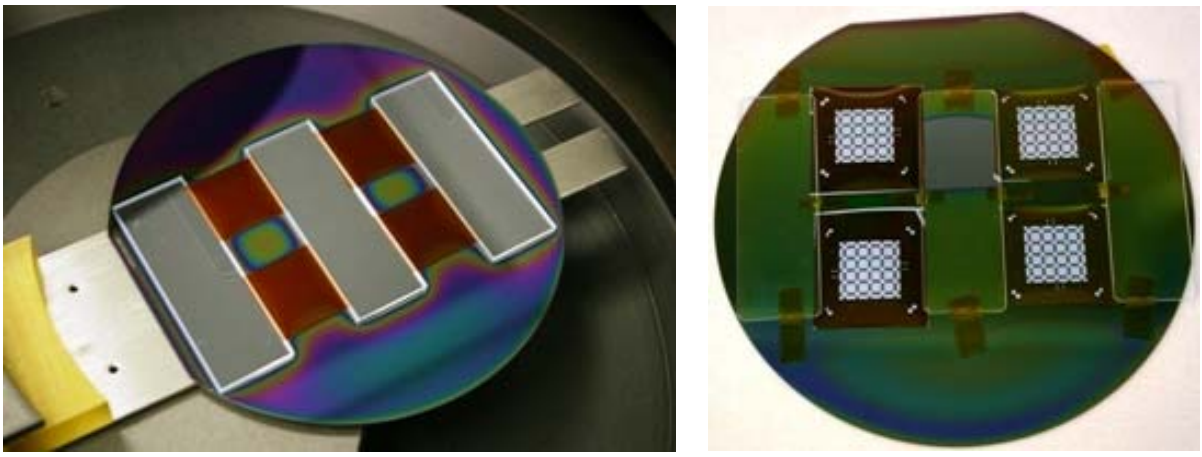

(a) (b)

Figure 4.7: (a) Flexible substrates loaded onto PECVD on supporting 6" Si wafer, held in place by the weight of glass microscope slides (b) Kapton tape added to hold down glass slides, with no adhesive contacting the flexible substrates.

4.2.5 REACTIVE ION ETCH

The RIE system is used for oxygen plasma cleaning as well as dry etching. Processing flexible substrates is straightforward using the RIE system since circuits are simply placed in the chamber by hand. Glass microscope slides must be placed over the substrate edges, in a manner similar to Figure 4.7a, to hold down the circuits. The weight of the slide is sufficient to hold the circuits in place. The only significant issue arises when unsecured substrates are flipped over by the rush of air during chamber pressurization and depressurization.

4.2.6 WET ETCH

For wet etch processes, the circuit is immersed in a corrosive liquid which dissolves exposed areas of the layer being patterned. Flexible circuits are easily etched by placing the substrate in a Teflon basket which is immersed in the liquid etchant.

4.2.7 SUPERCRITICAL DRYER

The supercritical dryer prevents stiction, which is a significant yield issue that arises in MEMS devices that are released by using a liquid solvent to remove the sacrificial layer. After a wet release, the MEMS structures are no longer supported by the sacrificial layer. As the devices dry, the liquid beneath the unsupported structures evaporates. As the liquid volume decreases, surface tension forces pull the MEMS structures down until all liquid has evaporated. In many instances, the MEMS devices become permanently stuck. This condition is known as stiction.

To mitigate the effects of stiction, the MEMS devices are kept submerged in high purity isopropyl alcohol following the release process. To dry the circuits, the submerged MEMS devices are first placed in the supercritical dryer chamber which is filled with isopropyl alcohol. After sealing the chamber, the machine flushes out the isopropyl alcohol, replacing it with liquid CO_2. The chamber is then pressurized and heated beyond the critical point of

CO_2, where there is no distinction between liquid and gas, and thus no surface tension. Pressure is then slowly released such that the CO_2 remains in the gas phase, and the MEMS devices are dry with no effects of stiction.

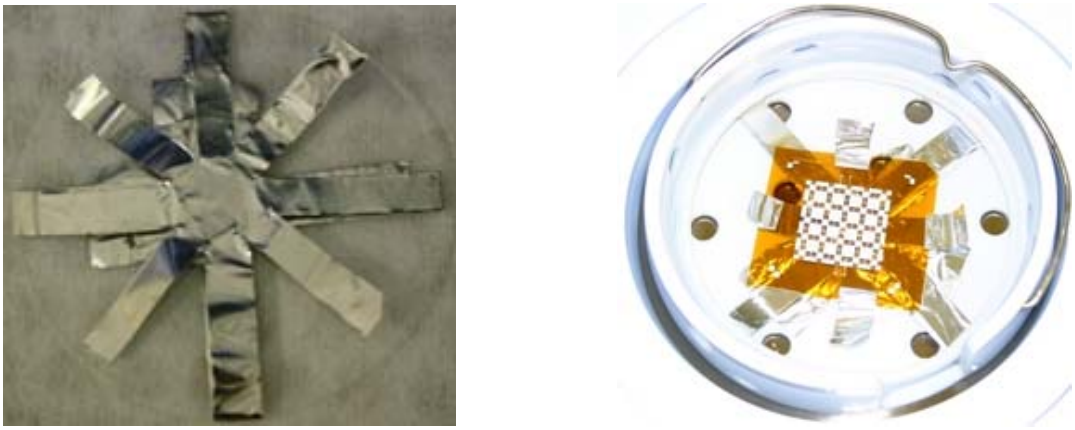

(a) (b)

Figure 4.8: (a) Aluminum foil jig to mount flexible substrate onto 3" glass wafer (b) Flexible MEMS circuits in critical point dryer.

Due to the nature of this process, great care must be taken to ensure absolutely no contaminants are introduced into the supercritical dryer chamber. Any contamination could potentially damage the MEMS devices in the flexible substrate process, and remain in the chamber causing harm to the devices of other lab users. The flexible substrate, however, must be attached to a supporting carrier and held firmly in place during the drying process. Silicone adhesives cannot be used since they are attacked by isopropyl alcohol and will contaminate the supercritical dryer. An adhesive-less aluminum foil jig was used to attach the flexible substrate to a 3" glass wafer as shown in Figure 4.8a. The flexible circuit, along with the entire jig and wafer assembly, is held in place by the 3" wafer holder in the supercritical dryer as shown in Figure 4.8b. This configuration was successfully used many times to release MEMS devices on flexible substrates.

4.3 SELECTION OF MATERIALS

4.3.1 SUBSTRATE

Several different options were considered when selecting a flexible substrate material. The substrate must be able to handle process temperatures of at least 250ºC with minimal distortion. Additionally, the material must be resistant to all of the process chemicals, and be sufficiently smooth for MEMS device fabrication. Two candidates which may handle the temperature and chemical resistance requirements are Dupont Pyralux AP [86] and Rogers ULTRALAM 3850 Liquid Crystal Polymer (LCP) [87]. SEM micrographs shown in Figure 4.9 indicate that the surfaces are too rough for MEMS device fabrication without some form of planarization. It should be noted that LCP materials are inexpensive and have excellent microwave properties [87]. Future work should be done to planarize LCP material for use as a substrate for MEMS devices.

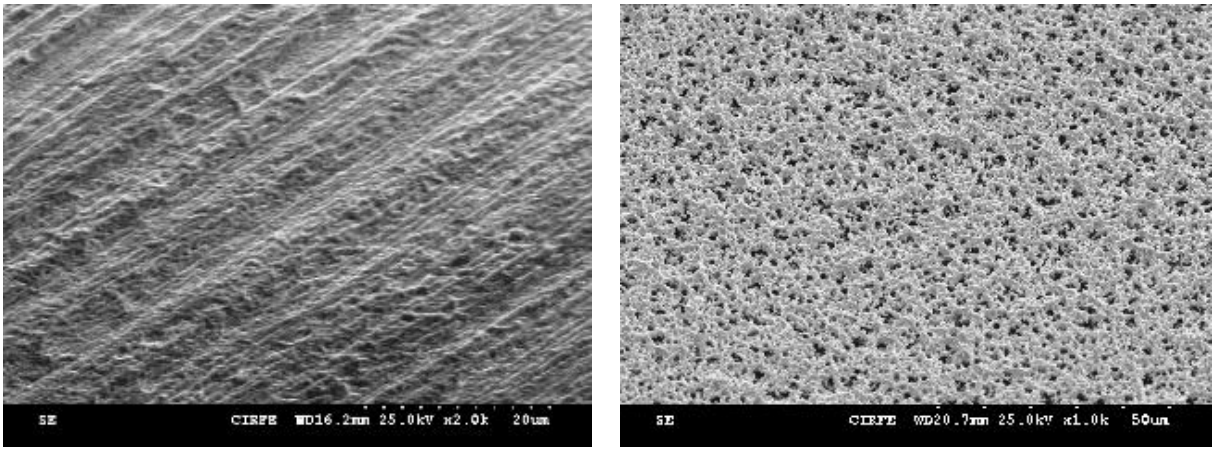

(a) (b)

Figure 4.9: (a) SEM Micrograph of Dupont Pyralux AP Surface (b) SEM Micrograph of Rogers ULTRALAM 3850 LCP Surface

The other flexible substrate materials that were evaluated are three different types of Dupont Kapton [9]. The first, shown in Figure 4.10a, is Kapton HPP-ST. A significant number of bumps, many of which were greater than 10μm in diameter, were observed on the surface of

the material. Initial fabrication runs using Kapton HPP-ST yielded MEMS devices that short-circuited upon actuation since bumps on the pull-down electrode protruded through the insulating silicon dioxide layer. It was possible to significantly improve planarization by spin-coating and curing a layer of HD Microsystems PI2562 polyimide [88]. As can be seen in Figure 4.10b, the polyimide planarization shows significant surface improvement. The bumps have not been completely smoothed out in this case, and an additional planarization layer may need to be added before fabricating MEMS devices.

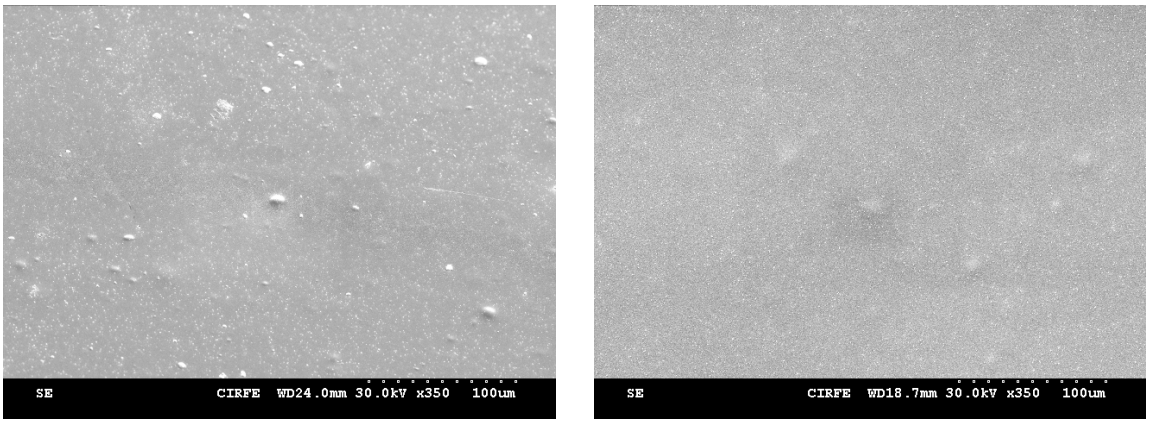

(a) (b)

Figure 4.10: SEM Micrograph of (a) Non-Planarized Kapton HPP-ST, (b) Planarized Kapton HPP-ST

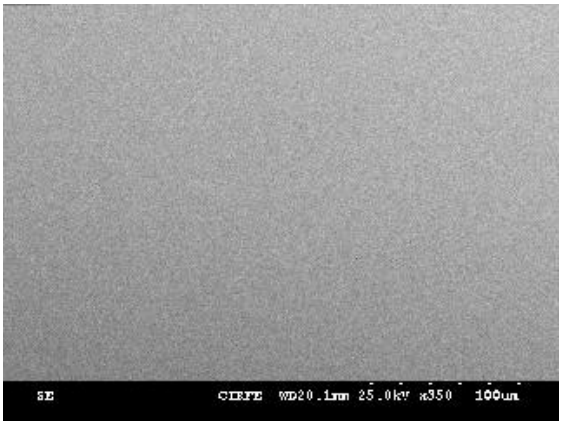

Figure 4.11: SEM Micrograph of Non-Planarized Kapton H

It was found that Kapton H and Kapton E have much smoother surfaces than Kapton HPP-ST, and are thus well-suited to be used as a MEMS substrate layer. Figure 4.11 shows the smooth surface texture of Kapton 500H, which does not require an additional planarization process step. Kapton H and Kapton E are therefore used for the fabrication of MEMS devices.

4.3.2 DIELECTRIC

During the initial stages of process development, experiments were carried out to deposit silicon dioxide and silicon nitride dielectric materials on Kapton. There was a considerable amount of interlayer stress following silicon nitride deposition, which resulted in visible cracks in the dielectric. Although silicon dioxide is not immune to stress as can be seen in the curved substrates of Figure 4.12, the dielectric showed no signs of developing cracks, even when flattened on a vacuum chuck during the photolithography process. Silicon dioxide, deposited at 250ºC, is therefore used as an insulating material for the flexible substrate MEMS process.

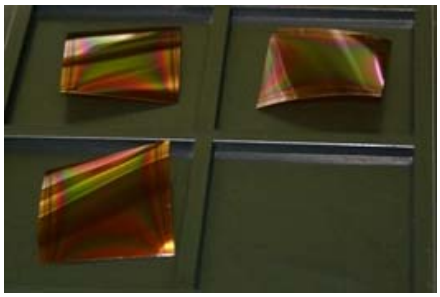

Figure 4.12: Kapton substrate after PECVD deposition of silicon dioxide

It is important to note a significant process limitation that may impact certain designs. The PECVD oxide exhibits pinhole defects as can be seen in Figure 4.13. During the development process, some circuits were fabricated having parallel-plate capacitors connected between DC bias lines. Since the top metal layer was sputtered directly onto the oxide, short circuits were formed between the top and bottom layers by metal deposited in the pinholes. This resulted in failure of the circuit.

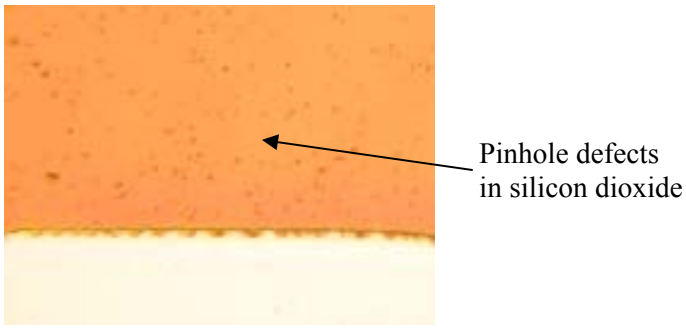

Figure 4.13: Pinhole defects in PECVD oxide deposited on a Kapton flexible circuit.

For standard electrostatically actuated MEMS devices, however, the top metal is not deposited directly on the insulator. As discussed in Section 4.4.2, the sacrificial layer is first spun onto the circuit, which provides a vertical spacing of 2-3 microns and planarizes the area over the pinholes. For electrical continuity, Figure 4.2 shows that the top metal is anchored to the bottom metal and not the insulator. The slightly porous dielectric will still provide the physical separation necessary to prevent a MEMS cantilever from contacting the pull-down electrode upon actuation. The silicon dioxide with pinhole defects therefore functions effectively as an insulator over the pull-down electrode of a MEMS device.

4.3.3 METAL

Several metals were available for vacuum deposition, including aluminum, copper, gold and silver. In practice, it was found that aluminum and silver had excellent adhesion properties and did not require an intermediary adhesion layer to first be deposited on the substrate. Gold and copper, however, require adhesion layers of chromium or titanium to prevent the metal from peeling away from the substrate. Chromium is typically used between the substrate and first metal layer provided that the circuit remains under vacuum throughout the process due to rapid oxidation of chromium.

4.3.3.1 COPPER

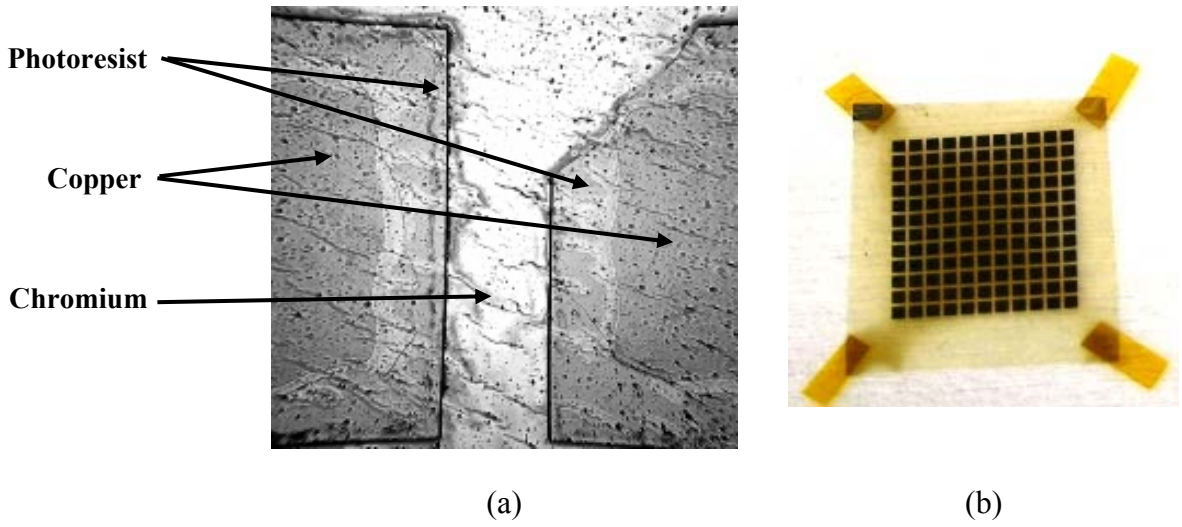

Figure 4.14: (a) Copper was sputtered over a Cr adhesion layer and patterned. The Cr etchant attacked the Cu resulting in a severe undercut, and did not remove the Cr. (b) Copper on a Teflon film cleaned in oxygen plasma.

Copper was sputtered over an evaporated 400Å Chromium adhesion layer and patterned using standard photolithography. As shown in Figure 4.14, the chromium etchant (Transene 1020 Chromium Etch [82]) attacked the copper resulting in a severe undercut, and did not remove even the thin chromium adhesion layer. Although different etching chemistries are available, copper is incompatible with oxygen plasma processes. In one experiment, a copper-clad Teflon substrate was patterned to produce a grid of copper islands, and then cleaned in oxygen plasma. The Cu was severely oxidized and even contaminated the surrounding substrate as can be seen in Figure 4.14. For this reason, copper was not used for MEMS device fabrication.

4.3.3.2 SILVER

Initially, silver appeared to be a good choice for MEMS device fabrication, provided the application did not require DC contact switching which would be affected by oxidation. In addition to excellent conductivity, processing is straightforward since silver was found to

adhere readily to Kapton with no adhesion layer. Unfortunately, silver oxidation presented issues that were more serious than increased contact resistance.

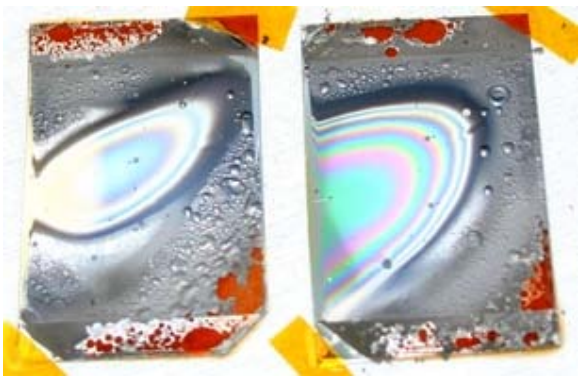

Figure 4.15: Sputtered silver over Kapton after oxygen plasma cleaning.

In a compatibility experiment, silver was sputtered onto Kapton, and subjected to oxygen plasma cleaning as shown in Figure 4.15. The silver was so severely oxidized that it blistered and flaked off of the substrate. Silver is therefore not a viable choice of metal for MEMS devices since exposure to oxygen plasma is required during multiple cleaning and processing steps.

However, silver is the best choice for a temporary layer that is removed before starting MEMS device fabrication. Silver is used as a KOH etch mask to produce the rigid-flex Kapton substrate as discussed in Section 4.4.1. The three available metals that are compatible with KOH are silver, gold and copper [79]. Gold is far too costly to use, since the etch mask is a temporary layer. Copper requires an adhesion layer which adds unnecessary complexity to the process, and also requires the etchant to be heated. Silver is the best mask option since it is relatively inexpensive and has the most straightforward process since there is no adhesion layer and etching can be done at room temperature using KI-I_2.

4.3.3.3 Gold and Adhesion Layers

Gold is an excellent material for producing MEMS DC contact switches, since its electrical properties are not affected by rapid oxidation experienced by many other conductors. In addition to its high cost, however, gold presents significant processing challenges. As discussed previously, an adhesion layer is required between the substrate and gold. Chromium and titanium were both used as adhesion layers to enable gold to successfully adhere to Kapton. The dielectric layer used to insulate the pull-down electrode from the cantilever also requires an adhesion layer to stick to the gold. Titanium was chosen for two reasons. Firstly, titanium does not oxidize rapidly like chromium. This is essential since the circuit must be removed from vacuum to pattern the bottom metal layer and then be transferred to the PECVD for silicon dioxide deposition. Secondly, titanium may be etched using HF [79], which is also used to etch the silicon dioxide layer. Once the silicon dioxide has been etched, the newly exposed thin (500 Å) grey titanium adhesion layer will rapidly dissolve. This provides an excellent visual reference since all of the exposed grey areas turn gold, indicating when to stop etching, which helps to avoid undercutting the insulators. The grey titanium remains under the oxide insulator as shown in Figure 4.16.

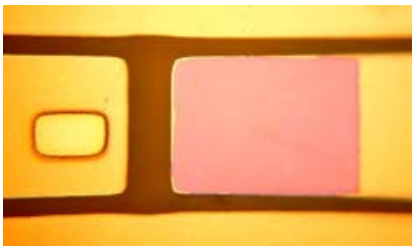

Figure 4.16: Partially fabricated MEMS device showing titanium adhesion layer under silicon dioxide dielectric region.

4.3.3.4 Aluminum

Sputtered aluminum was found to have excellent adhesion to Kapton without the need for an adhesion layer. Additionally, PECVD silicon dioxide adheres well to aluminum, and also does not require an adhesion layer. The result is a straightforward process that produces reliable MEMS devices. The significant drawbacks of using aluminum are its low

conductivity as well as the resistance of aluminum oxide. For capacitive switches, however, the DC contact resistance is not an issue. For the reconfigurable electromagnetic structures fabricated for this thesis research, the aluminum conductivity does not significantly impact RF performance as will be shown in Section 5.2.2.2. As the results of Section 5.2.2.2 show, the differences in RF performance between gold and aluminum for this application do not justify the increased cost in materials and process complexity required to fabricate a gold structure. The final process used to fabricate reconfigurable MEMS electromagnetic structures thus uses aluminum for the top and bottom metal layers.

4.3.4 SACRIFICIAL LAYER

Two previously established MEMS processes at the University of Waterloo used photoresist as a sacrificial layer [76], [77]. AZ3330 photoresist [83] was used as a sacrificial layer in [76], in which the top metal layer is gold, deposited using E-Beam evaporation. For the flexible substrate process, the top metal layer is deposited by sputtering, for which the deposition temperature is considerably hotter than for E-beam evaporation. The sputtering deposition temperature exceeds the 125ºC temperature of maximum thermal stability of AZ3330 [83], which results in a failure of the release process as shown in Figure 4.17. Filaments of hardened photoresist material remained after release, preventing the MEMS devices from properly actuating.

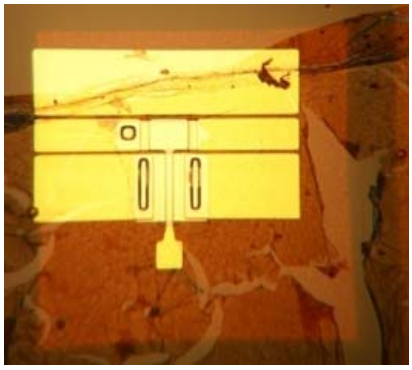

Figure 4.17: Hardened AZ3330 remaining on MEMS device after unsuccessful release.

Since the AZ3330 photoresist sacrificial layer is not compatible with the high sputtering temperatures, the flexible substrate MEMS process was leveraged from [77], which uses Microchem LOR series photoresists [84] as a sacrificial layer. LOR photoresists may handle 200ºC [84], which is compatible with sputtering. The only drawback is that extra processing steps are required since LOR is not photo-definable.

4.4 FINAL PROCESS

This section provides an overview of the newly developed rigid-flex MEMS process. Please refer to Appendix B for a detailed recipe that includes all of the process parameters.

4.4.1 RIGID-FLEX SUBSTRATE PREPARATION

The first stage of the process is to fabricate the rigid-flex Kapton substrate. Kapton has a smooth side, onto which the devices are fabricated, as well as a rougher side. The back-side etching to produce the pattern of rigid islands targets the rough side. Once the substrates are properly oriented, the Kapton samples must be first cleaned as outlined in Section 4.2.1. Since the metal layer is only temporary, it was found that oxygen plasma cleaning was not necessary prior to silver deposition. The first step is to sputter 1µm of silver onto the back (rough) side of the Kapton film, as shown in Figure 4.18a, after a 120°C dehydration bake. It is important to note that if the substrate baking temperature is excessively high, the Kapton becomes partially resilient to KOH, causing the etch process to fail.

The smooth side of the Kapton substrate must be protected during the initial processing steps. Figure 4.18b shows that a 3µm layer of AZ3330 photoresist is spun onto the smooth side of the Kapton, followed by a soft bake. The Kapton substrate is then temporarily bonded to a glass wafer using double-sided Kapton tape with the silver coated side up and the photoresist-coated smooth side protected as in Figure 4.18c. This provides mechanical support to the Kapton which is temporarily softened during the KOH etch. Additionally, it protects the smooth Kapton side from KOH etching. The photoresist layer can later be dissolved to release the substrate from the Kapton tape, thus preventing damage caused by

excessive peeling force as discussed in Section 4.2. The photoresist will not be damaged during this stage of the process since all temperatures are well below the 125ºC maximum thermal stability value for AZ3330.

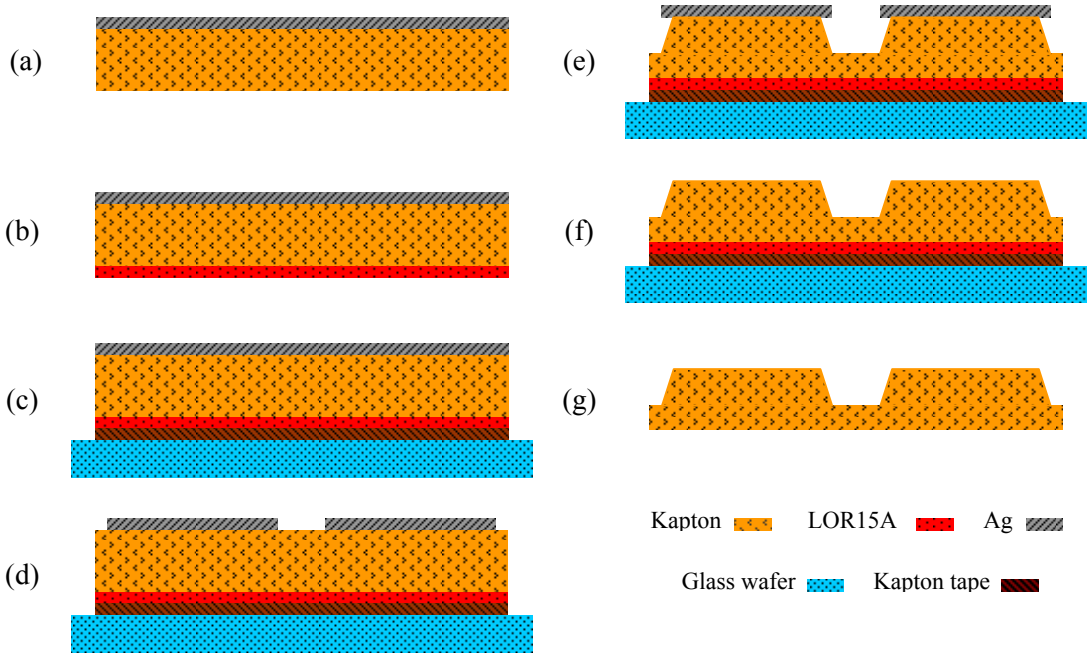

Figure 4.18: Rigid-flex Kapton substrate fabrication process.

After mounting the Kapton substrate, the silver is then patterned using standard photolithography to form an etch mask as shown in Figure 4.18d. Following a slight modification of [85], bulk material is etched from the Kapton substrate using 9 wt. % KOH in a solution of 80 wt. % ethanol and 20 wt. % water. The static etch time is 15 minutes to remove 3.5mil of Kapton as shown in Figure 4.18e. Upon completion of etching, the substrate must be rinsed under flowing DI water for at least 5 minutes to remove insoluble reacted material [85]. The substrates must then be baked for 30 minutes at 100ºC to remove moisture absorbed during the etch process. Figure 4.19a shows the rigid-flex substrate after the etching and bake processes.

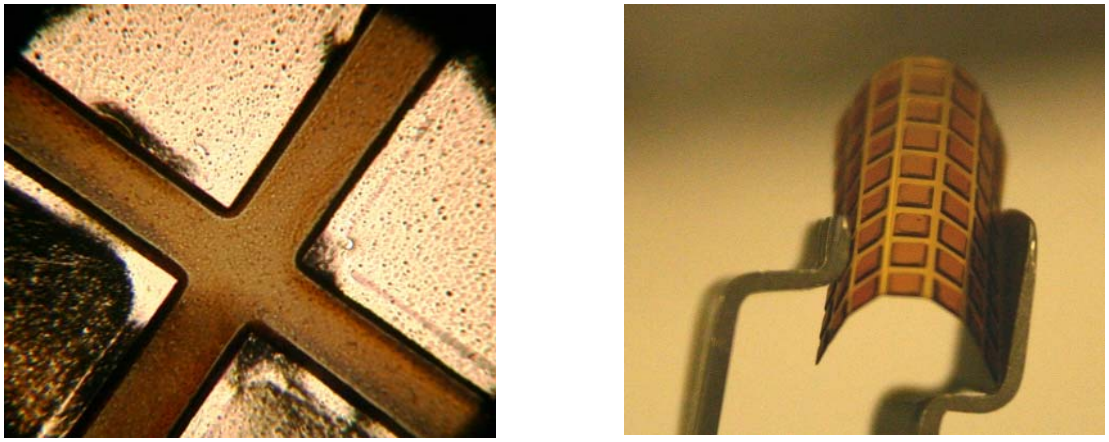

(a) (b)

Figure 4.19: (a) Rigid-flex substrate with silver mask after KOH etch (b) Completed rigid-flex substrate.

The remaining silver is then removed, as shown in Figure 4.18f. The Kapton is now ready to be released by immersion in warm acetone. The rigid-flex substrates are easily peeled from the glass wafers and double-sided Kapton tape using wafer tweezers to slowly lift the substrate as the acetone dissolves the protective photoresist layer. The released substrate, shown in Figure 4.18g and Figure 4.19b, is then cleaned in fresh acetone, then isopropyl alcohol and finally DI water.

4.4.2 MEMS DEVICE FABRICATION ON RIGID-FLEX SUBSTRATE

The rigid-flex substrate has thicker regions of Kapton which provide mechanical support to the MEMS devices. Proper alignment is required to ensure that the top-side MEMS devices are positioned over the rigid islands. Since the Kapton is translucent, alignment marks may be added to the top side of the substrate at the outermost corners of the island pattern. As shown in Figure 4.20, the alignment marks are small squares of ablated material removed using an ultraviolet laser. Once the opaque first metal layer has been deposited, the alignment marks will show through to enable accurate positioning of MEMS devices over the rigid islands.

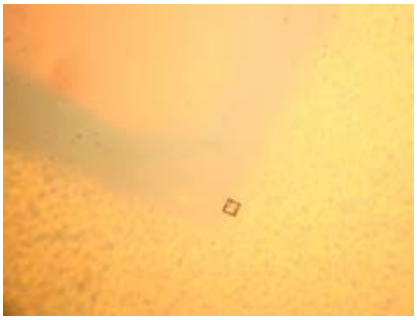

Figure 4.20: Laser Mark for Front/Back Alignment on Rigid-Flex Kapton Substrate

After the rigid-flex substrate has been prepared, it is important to bake it for at least 1h at 250°C, the maximum MEMS process temperature, to minimize any substrate shrinkage during MEMS fabrication. Oxygen plasma cleaning is required to ensure maximum adhesion of the first metal layer to the rigid-flex substrate.

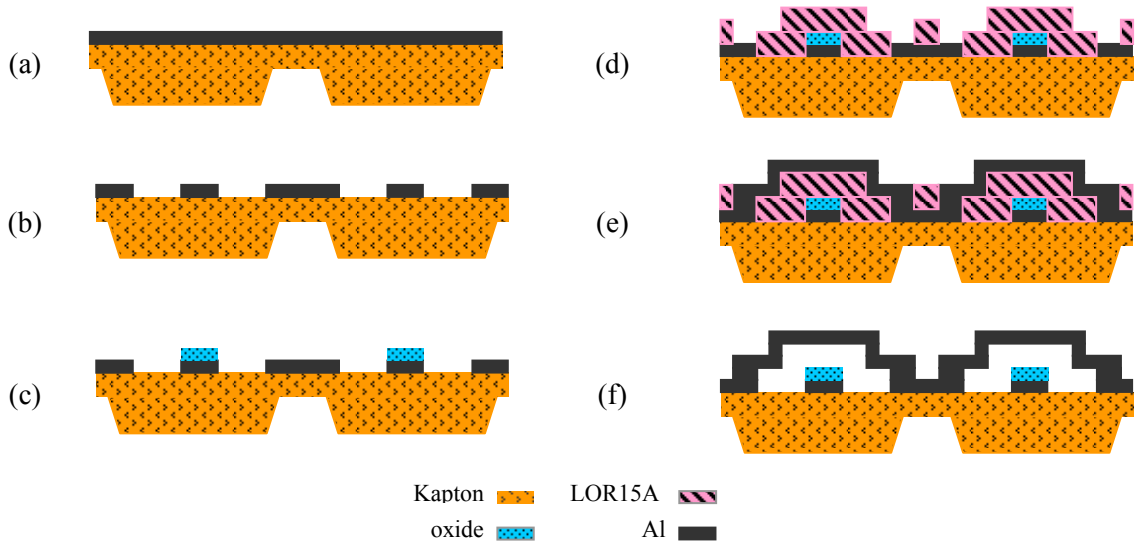

Figure 4.21: Rigid-flex MEMS process flow

The bottom metal layer is 1μm thick sputtered aluminum, as shown in Figure 4.21a, deposited immediately after the 250°C bake. The first of four masks is used to pattern the bottom metal layer as shown in Figure 4.21b.

Prior to depositing the insulating layer, the circuits are cleaned using RIE oxygen plasma for 15s. The samples are then mounted on a 6" silicon wafer as described in Section 4.2.4, then baked for 45min at 250°C. The circuits are then immediately transferred to the PECVD chamber for deposition of a silicon dioxide layer.

The second mask is used to pattern the oxide insulating layer. Due to the stresses in the oxide as discussed in Section 4.3.2, alignment is most difficult for this layer since there is some distortion of the flexible substrate. MEMS devices developed for this thesis research are have been designed to tolerate a small amount of misalignment without impacting capacitance and pull-down voltage as shown in Figure 4.22. An important future research project will be to quantify the amount of distortion and correspondingly adjust the mask size. This will dramatically increase alignment accuracy and allow much smaller devices to be fabricated.

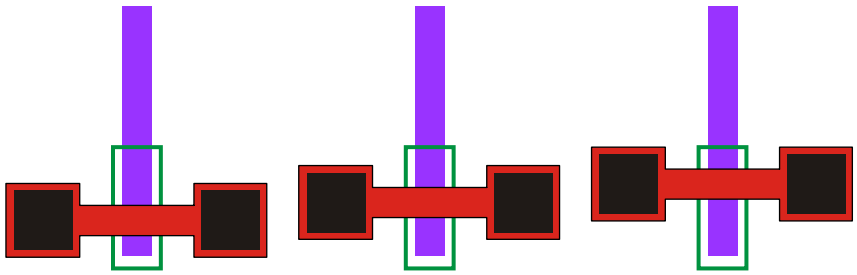

Figure 4.22: Cantilever design which can tolerate misalignment without significantly affecting pull-down voltage and capacitance since overlap area and fringing are constant.

The oxide is then patterned using 8:1 buffered HF, which also attacks Aluminum, but at an etch rate 45 times slower than for oxide [79]. The aluminum surface is noticeably roughened since it is attacked towards the end of the etch process, and appears white. Figure 4.21c shows the circuit with patterned insulators over the pull-down electrodes.

The next process step is to deposit and pattern the sacrificial layer as shown in Figure 4.21d. Microchem LOR15A forms a 2μm layer when spun at 2000rpm. Following the process from [77], the LOR15A is first soft baked on a hotplate at 160°C for 4min, and then hard baked in a furnace oven for 30min at 190°C. Failing to hard-bake the LOR15A may result in its reaction with the Phosphoric/Acetic/Nitric (PAN) etch used to pattern aluminum. Following the hard bake, a layer of AZ3312 photoresist is spun over the LOR15A, and the anchors are patterned using the third mask. An extended developing time of approximately 4 minutes is required to ensure the hard-baked LOR15A is properly patterned.

During process development, some circuits exhibited high resistance between the top and bottom metal layers due to the formation of aluminum oxide. A process step was added to remove a very thin layer of exposed aluminum by dipping the circuits for 20s in 8:1 buffered HF after patterning the anchors. The HF dip should be done on the same day as the top metal layer deposition process to ensure a new aluminum oxide layer does not form.

The AZ3312 patterning resist must be removed from the LOR15A since it cannot handle the temperatures encountered during sputter deposition of the top metal layer. The patterning resist is removed by RIE using CF_4 and O_2. The 1μm aluminum top metal layer is sputtered as shown in Figure 4.21e, and patterned using the fourth mask.

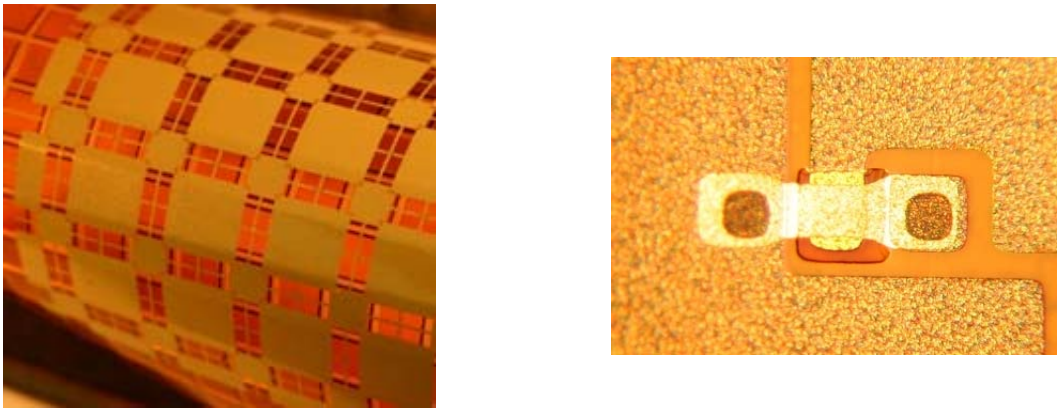

(a) (b)

Figure 4.23: (a) Curved rigid-flex MEMS circuit (b) Individual MEMS switch on rigid-flex circuit.

After patterning the top metal, the MEMS devices are ready to be released. The circuits are affixed to glass wafers using adhesiveless jigs as shown in Section 4.2.7. The entire assembly is then immersed in warm Microchem PG remover [89] to dissolve the LOR15A sacrificial layer, and then placed in high-purity isopropyl alcohol. The PG remover/isopropyl alcohol step is repeated three times in total. Next, the devices are transferred into clean high purity isopropyl alcohol during two more soaking steps. The MEMS devices are finally dried using the supercritical dryer as discussed in Section 4.2.7, resulting in the completed circuit of Figure 4.21f. Figure 4.23 shows a MEMS frequency-selective surface, to be discussed in Chapter 5, fabricated using the newly developed MEMS process on rigid-flex substrates.

4.5 SUMMARY

This chapter has documented the development of a novel process to fabricate MEMS devices on flexible substrates. This innovative process has been used to successfully fabricate working MEMS devices on flexible substrates.

The first step in the new process is to chemically etch a Kapton substrate to leave thicker islands of material separated by a flexible membrane. The advantages of this configuration are twofold. First, MEMS devices are fabricated over the thicker regions which provide mechanical support. The second benefit arises since a grid pattern of thick islands, surrounded by a thin membrane, allows the rigid-flex circuit to be held flat by vacuum during photolithography.

Since standard MEMS fabrication processes are designed to produce devices on rigid substrates such as silicon, glass or alumina, several process modifications were required to handle flexible materials. The adaptation of each fabrication process step to handle flexible substrates has been documented. Furthermore, detailed information regarding the selection of compatible materials, as well as incompatibilities that were encountered, has been presented to aid future researchers in developing flexible MEMS processes. The end result is a viable MEMS fabrication process that yields devices on an all-dielectric rigid-flex substrate, which

is amenable to fabricating reconfigurable electromagnetic structures as documented in Chapter 5.

CHAPTER 5

MEMS-BASED RECONFIGURABLE EBG STRUCTURES AND FSS

5.1 INTRODUCTION

This chapter documents the design and measurement of MEMS-based reconfigurable electromagnetic structures fabricated using the newly developed process outlined in Chapter 4. Section 5.2 documents a frequency selective surface that acts as a 2-dimensional filter to propagating electromagnetic waves. The FSS has a bandpass response that switches between the Ku and Ka bands, targeting satellite applications. The FSS design and simulated results are first presented in Section 5.2.1, followed by a detailed discussion of the choice of parameters in Section 5.2.2. Section 5.2.3 outlines the results of a parametric sensitivity analysis used to establish the robustness of the design. Prior to obtaining accurate

measurements, several issues arose in the development of a test methodology. In spite of these issues, a successful test strategy was developed, which is documented in Section 5.2.4. Finally, measured results of individual MEMS devices as well as the entire FSS structure are compared with theoretical predictions in Section 5.2.5.

Section 5.3 documents the design and measurement of a MEMS-based reconfigurable electromagnetic bandgap structure on a flexible substrate. Section 5.3.1 provides an overview of the EBG design. Section 5.3.2 discusses the theoretical modeling of the EBG structure. Section 5.3.3 documents the hardware verification in detail, beginning with test set design and measurement considerations, and finally a comparison of simulated and measured results. Section 5.4 adds a planar monopole antenna over the EBG structure of Section 5.3, separated by an air gap. Measured results are presented which show the performance of this reconfigurable low-profile antenna structure.

5.2 MEMS RECONFIGURABLE FSS

The MEMS-Tunable FSS is designed to have a bandpass response that switches between the Ku and Ka bands. The frequency selective surface consists of 2 overlapping grids of interconnected patches that are DC isolated, represented by the purple (dark) and red (light) regions of Figure 5.1. The interconnecting traces between each patch are connected together using cross-over bridges (Figure 5.1d) that provide the DC isolation between the two separate grids. The FSS resonant frequency is controlled by MEMS switched capacitors integrated between the purple (dark) and red (light) patch corners, as shown in Figure 5.1b-c. The bottom electrodes of all MEMS switched capacitors are connected to the purple (dark) grid, while the moveable cantilevers are all connected to the red (light) grid, as shown in Figure 5.1c. This simplifies biasing since an applied voltage between the purple (dark) and red (light) grids actuates all MEMS devices simultaneously.

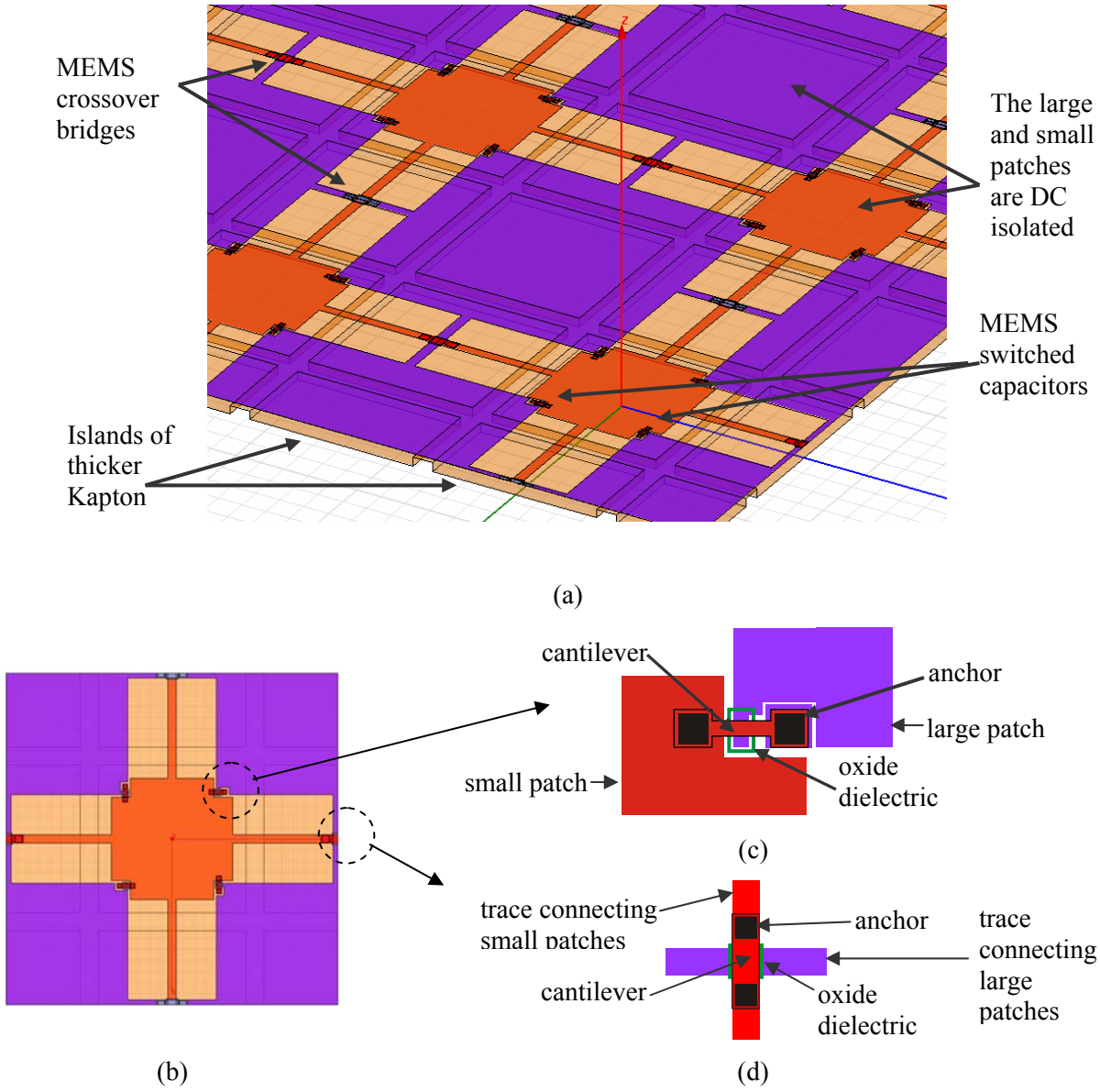

Figure 5.1: (a) Integrated MEMS FSS structure on rigid-flex Kapton substrate. The overlapping red (light) and purple (dark) grids are DC isolated. (b) Single FSS unit cell with MEMS structures over thick Kapton islands. (c) 2-State MEMS switched capacitor. (d) Cross- over bridge which provides DC isolation between the overlapping grids.

The FSS unit cell, shown in Figure 5.1b is 3.81mm^2. Figure 5.1a and Figure 5.1b show the FSS on the rigid-flex substrate, where 1.7mm^2 islands of 5mil thick Kapton material, spaced apart by 0.205mm of flexible 1.5mil Kapton, support the MEMS structures. The larger purple (dark) patches of Figure 5.1a are 2.794mm^2, and the small red (light) patches are 1.397mm^2.

Figure 5.1c shows the square patch corners cut away to accommodate the MEMS device. The gaps between the patches are all 25.4µm. The double anchored cantilever is 154µm long by 40µm wide. The pull-down electrode is also 40µm wide. The SiO_2 dielectric, shown in Figure 5.1c, is 65µm x 130µm by 1.2µm thick. The black squares represent the 80 μm^2 anchors that support the cantilever structure. The traces connecting the patch elements together are 100µm wide, and are connected using MEMS bridges as shown in Figure 5.1d.

5.2.1 SIMULATED RESPONSE

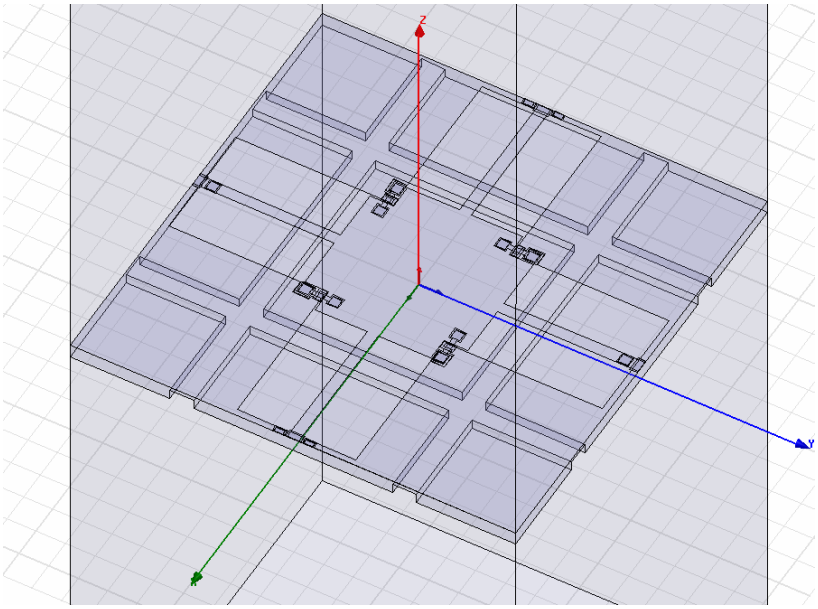

Figure 5.2: HFSS simulation used to model transmission and reflection of a single FSS unit cell with plane wave incidence and periodic boundary conditions.

Figure 5.2 shows the HFSS simulation model of a single FSS unit cell with periodic boundary conditions, used to model the FSS transmission and reflection response to an incident plane wave. The structure is simulated using this model with the MEMS switches in the up-state and down-state. As shown in the simulated plots of Figure 5.3, the up-state resonant frequency is 22.9GHz, with a 0.49dB minimum insertion loss and 21.5dB minimum return loss. The up-state 3dB bandwidth is 5.2GHz. The simulated down-state centre

frequency is 15.7GHz as shown in Figure 5.3, with a 0.90dB minimum insertion loss and 18.6dB return loss. The down-state 3dB bandwidth is 2.5GHz.

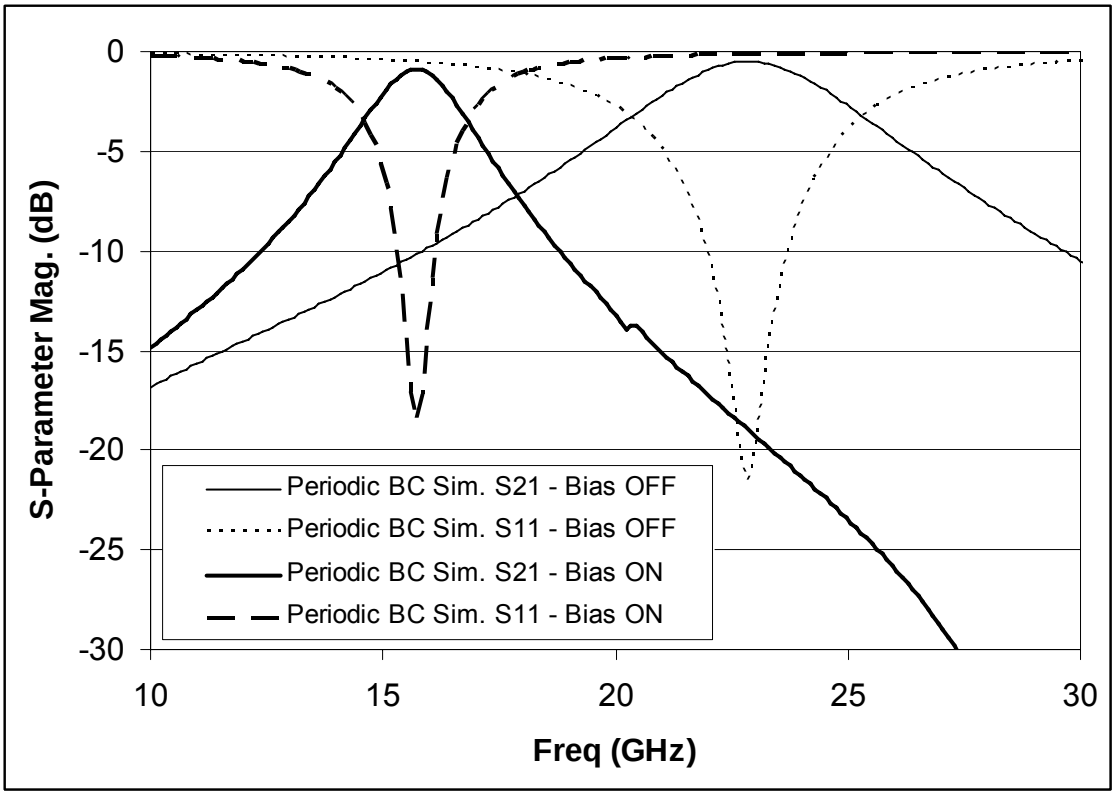

Figure 5.3: HFSS Simulated S-parameters for MEMS tunable FSS using periodic boundary conditions.

5.2.2 CHOICE OF DESIGN PARAMETERS

This section provides an overview of the key design parameters and associated performance trade-offs for the MEMS tunable FSS design.

5.2.2.1 CAPACITANCE: OXIDE THICKNESS AND MEMS CANTILEVER AND ELECTRODE WIDTH

As can be seen in Figure 5.4, the FSS down-state S-parameter performance degrades as the oxide thickness decreases and the capacitive loading on the structure increases. As shown previously and in Figure 5.4, the FSS with a 1.2μm MEMS capacitor oxide thickness has a 15.7GHz resonant frequency, with 0.90dB insertion loss and 18.6dB return loss at resonance.

Figure 5.4 shows that the resonant frequency is 9.6GHz for a 0.5µm oxide thickness, with a degraded 3.0dB insertion loss and 6.4dB return loss at resonance. The resonant frequency is further reduced to 7.4GHz for a 0.2µm oxide thickness, with a 3.2dB insertion loss and 8.5dB return loss at resonance.

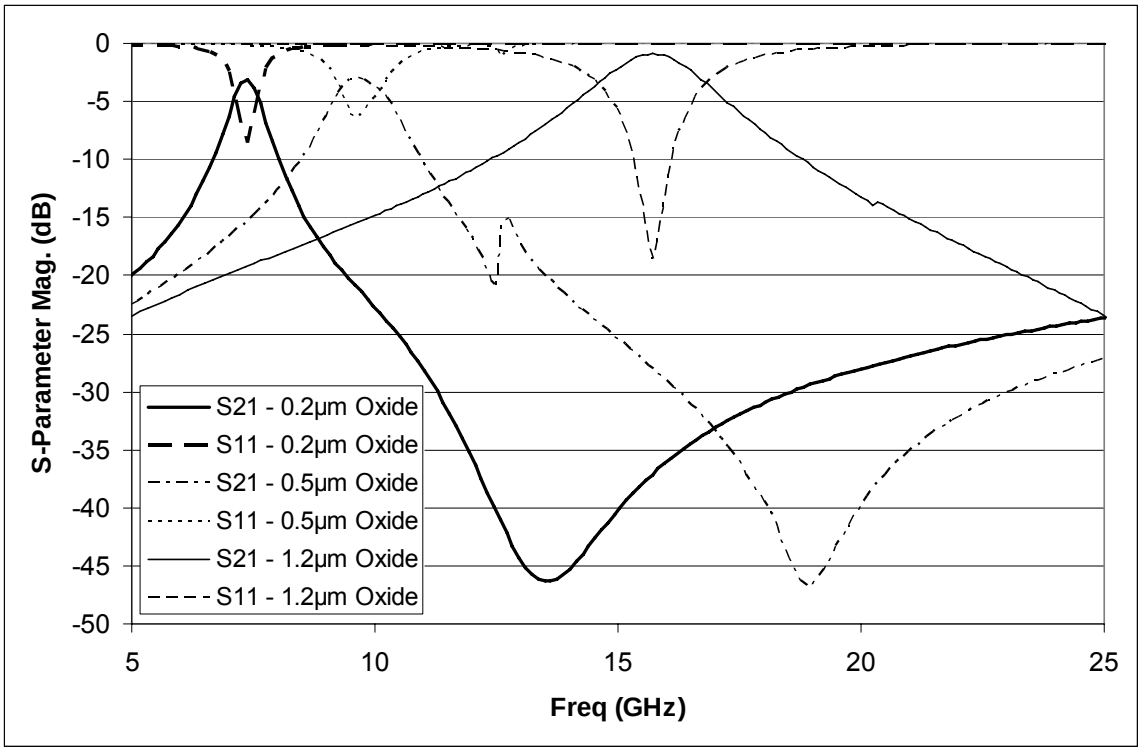

Figure 5.4: Simulated FSS down-state S-parameters for MEMS pull-down electrode insulating oxide thickness of 0.2µm, 0.5µm and 1.2µm.

Typical MEMS capacitive switches have pull-down electrode oxide thickness values of 0.2µm or less [90]. Minimizing oxide thickness and maximizing cantilever height increases the capacitance ratio between up and down states for improved switch insertion loss/isolation performance. For the FSS application, it is not necessary to achieve a high up/down state MEMS capacitance ratio since we are tuning a resonant frequency by loading the FSS and not switching microwave signals through the device. As shown in Figure 5.4, the FSS performance degrades if the capacitance loading the structure is too high. We therefore use a thick 1.2µm oxide layer for the MEMS capacitor pull-down electrode insulator. To minimize

down-state capacitance while maintaining a reasonable MEMS pull-down voltage, the cantilever and electrode width values are 40μm.

5.2.2.2 CHOICE OF METAL FOR THE FSS

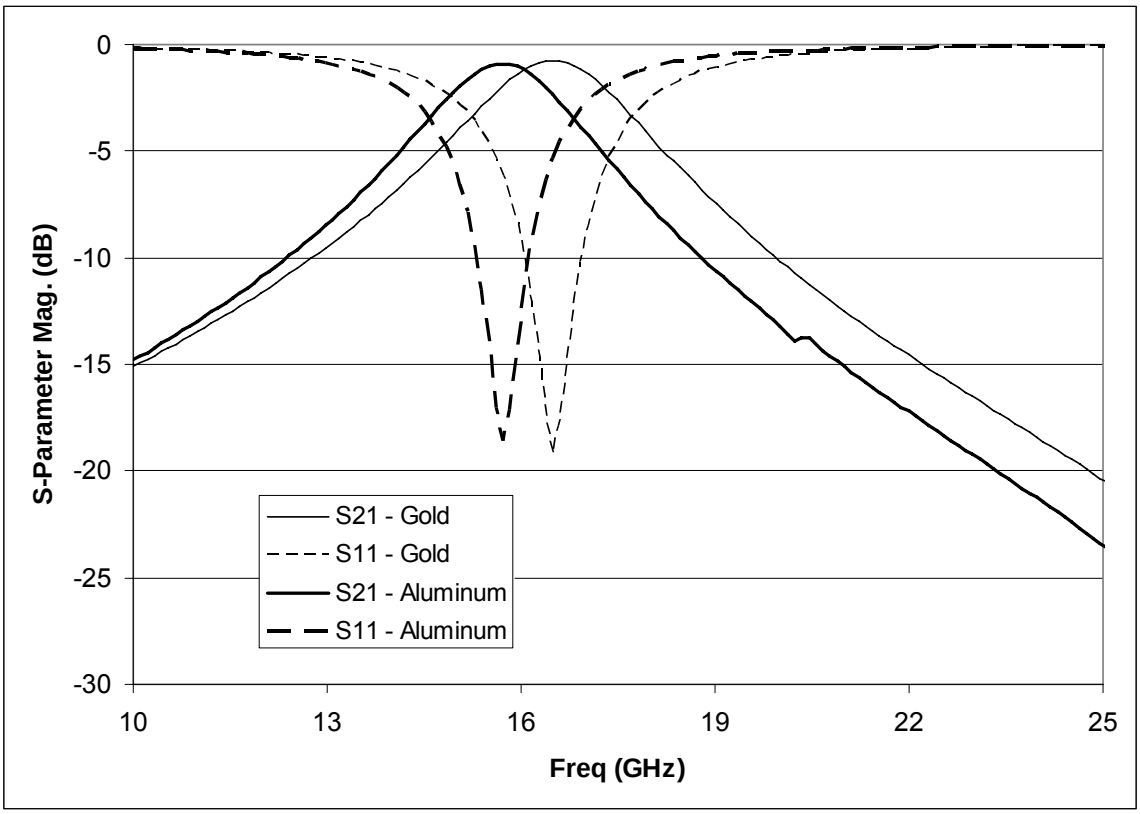

Figure 5.5: Comparison of simulated down-state S-parameters for the FSS structure fabricated using aluminum and gold.

Figure 5.5 shows a comparison of simulated down-state S-parameters for the FSS structure fabricated using aluminum and gold. The aluminum FSS has a 15.7GHz resonant frequency, with 0.90dB insertion loss and 18.6dB return loss at resonance. As shown in Figure 5.5, the resonant frequency of the gold FSS is 0.8GHz higher. The gold FSS insertion loss is 0.14dB better than for the aluminum FSS. The minimum return loss 0.58dB better for the gold FSS. These performance improvements are so small that it does not justify the significant increase

in material cost and added process steps required to fabricate a gold FSS. We therefore fabricated the FSS structures using aluminum.

5.2.2.3 Inductance: MEMS Cantilever and Electrode Width

The MEMS cantilever and electrode should be designed with sufficient overlap to allow for a reasonable pull-down voltage. As discussed in Section 5.2.2.1, this presents a design trade-off as FSS performance degrades with excessive capacitance loading the structure. As would be expected, excessive inductance also degrades FSS performance. This section illustrates the sensitivity to small MEMS structure design variations that affect inductance as shown in Figure 5.6. The fabricated FSS has a step in the electrode trace width as shown in Figure 5.6a, which reduces the series inductance between the metal FSS patches. The simulated S-parameter response of the down-state fabricated FSS, shown in Figure 5.7, has the previously discussed 15.7GHz resonant frequency, with 0.90dB insertion loss and 18.6dB return loss at resonance. The higher inductance layout, with no step in electrode width, is shown in Figure 5.6b. The simulated FSS response for the higher inductance layout is shown in Figure 5.7. As expected, the resonant frequency decreases by 1.6GHz to 14.1GHz. The insertion loss degrades to 1.5dB and the return loss degrades to 10.3dB at resonance. The high current density and resistive loss in the narrow trace has a significant impact on the overall performance of the FSS structure.

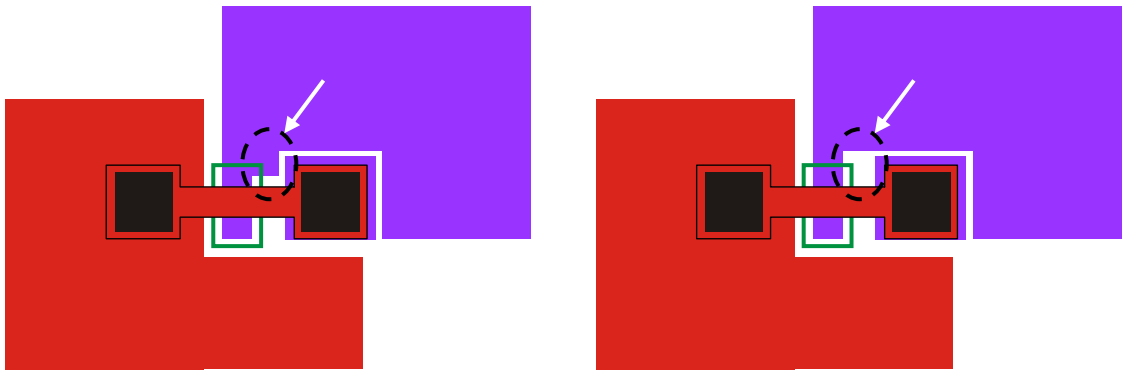

Figure 5.6: Variations in MEMS capacitor layout used to illustrate the effects of the pull-down electrode inductance. (a) Fabricated FSS MEMS capacitor layout with step in electrode trace width to reduce inductance (highlighted area). (b) Modified MEMS layout without the step in electrode trace width (highlighted area).

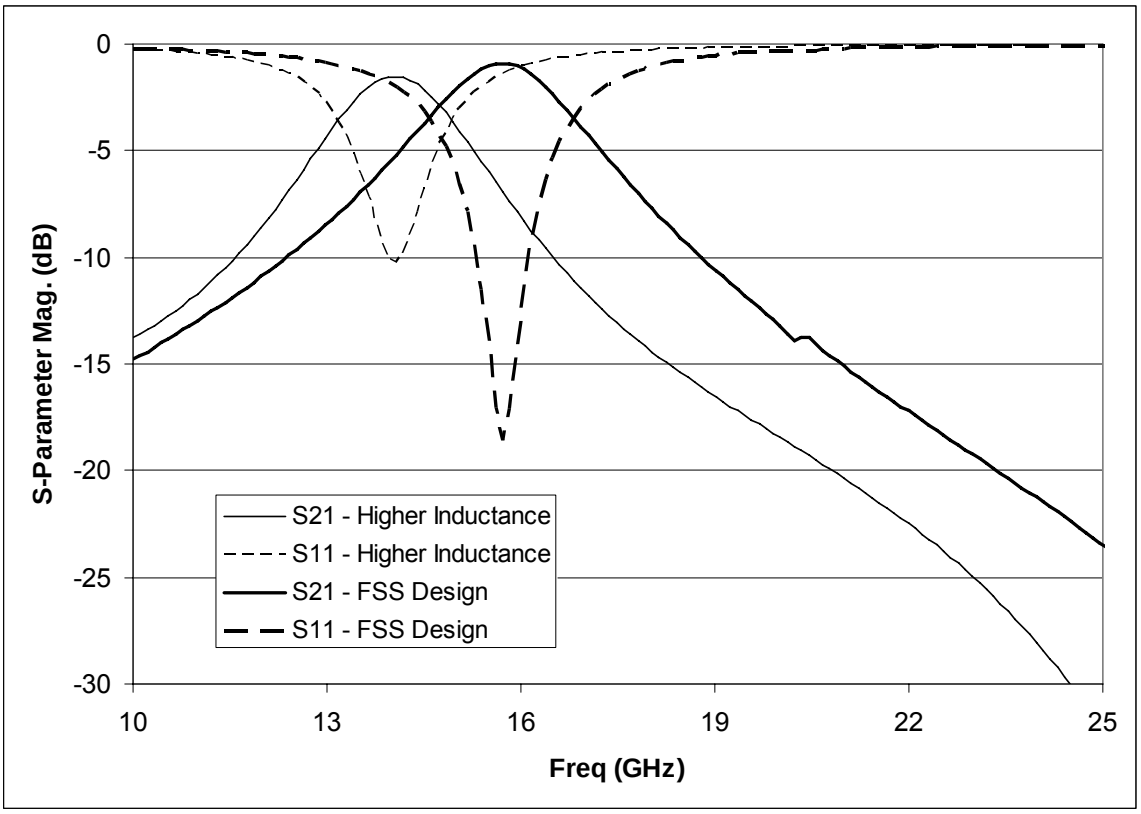

Figure 5.7: Comparison of simulated down-state S-parameters for the FSS structure actual design (Figure 5.6a) and with a higher inductance electrode (Figure 5.6b).

5.2.3 PARAMETRIC SENSITIVITY ANALYSIS

A parametric sensitivity analysis was carried out using Ansoft HFSS to establish the robustness of the FSS design. The parameters which are most likely to experience variation in production are summarized in Table 5.1. The FSS performance sensitivities are summarized in Table 5.2 for MEMS capacitors in the up-state, and Table 5.3 for the down-state MEMS capacitors.

5.2.3.1 UP-STATE AIR GAP (SACRIFICIAL LAYER) THICKNESS

The sacrificial layer thickness, which determines the up-state air gap height between the MEMS cantilever and electrode, is the property likely to experience the most variation in the

entire fabrication process. As discussed in Chapter 4, the sacrificial layer is a spin-on photoresist, which will experience variations in thickness across the entire circuit. As shown in Table 5.2, an extremely large 66.7% decrease in air gap thickness results in only a 5.4% decrease in resonant frequency. If the air gap increases by 40%, the corresponding frequency shift is only 2.2%. This insensitivity to potentially large variations increases our confidence in the feasibility of using this MEMS process to fabricate tunable FSS structures.

5.2.3.2 Down-State Air Gap

The most significant performance variation occurs when the MEMS cantilever does not fully contact the insulator over the pull-down electrode. This may occur as a due to mechanical distortion of the cantilever as it is pulled down, non-uniformity of the oxide dielectric, as well as a non-planar cantilever resulting from a lack of planarization of the sacrificial layer. This effect is further exacerbated by the thick 1.2μm oxide layer over the pull-down electrode, discussed in section 5.2.2.1. The result is a small down-state air-gap which acts as an air dielectric capacitor in series with the oxide dielectric capacitor. The combined effect of this contact impedance is a reduced overall capacitance, increasing the resonant frequency. Table 5.3 shows that a 0.25μm air gap increases the resonant frequency by 19.6%. Care must be taken in designing MEMS structures that minimize down-state air gaps.

5.2.3.3 Kapton Dielectric Constant

The dielectric constant of Kapton may vary as a result of moisture absorption and manufacturing tolerances [9]. The material undergoes many temperature cycles and exposure to a diverse range of process chemicals throughout the fabrication process. It is beyond the scope of this thesis to characterize changes in the microwave electrical properties of Kapton through the different processing steps. It is, however, prudent to analyze the FSS performance sensitivity to significant variations in Kapton electrical properties. Table 5.2 shows that a change in Kapton dielectric constant of +9.8% or -13.7% results in an up-state resonant frequency shift of -3.4% and +4.2% respectively. Table 5.3 shows that a -13.7% change in Kapton dielectric constant results in a down-state resonant frequency shift of

+5.5%. As shown in Table 5.3, increasing the Kapton dielectric constant by 9.8% did not change the resonant frequency.

Table 5.1: FSS parameter reference values

FSS Parameter	Reference Value
Kapton ε_r	3.9
Oxide ε_r	4.0
Up-State air gap (sacrificial layer) thickness	2μm
Down-State air gap	0μm

Table 5.2: Summary of parametric sensitivity analysis for the FSS with MEMS switches in the up-state

Description of HFSS Simulated MEMS FSS	Centre Freq. (GHz)	Insertion Loss (dB)	Return Loss (dB)	% Change in Parameter	%Change in Centre Frequency
UP State (Bias OFF) Reference	22.87	0.49	21.51		
3μm air gap	23.38	0.48	25.63	40.0	2.2
1μm air gap	21.66	0.54	24.06	-66.7	-5.4
Kapton $\varepsilon_r = 4.3$	22.10	0.54	24.02	9.76	-3.4
Kapton $\varepsilon_r = 3.4$	23.86	0.46	23.68	-13.7	4.2
oxide $\varepsilon_r = 3.5$	22.98	0.48	25.32	-13.3	0.48
oxide $\varepsilon_r = 4.5$	22.87	0.48	21.34	11.8	0.00

Table 5.3: Summary of parametric sensitivity analysis for the FSS with MEMS switches in the down-state

Description of HFSS Simulated MEMS FSS	Centre Freq. (GHz)	Insertion Loss (dB)	Return Loss (dB)	% Change in Parameter	%Change in Centre Frequency
DOWN State (Bias ON) Reference	15.72	0.90	18.59		0.00
Kapton $\varepsilon_r = 4.3$	15.72	0.89	19.43	9.76	0.00
Kapton $\varepsilon_r = 3.4$	16.60	0.82	19.85	-13.70	5.5
oxide $\varepsilon_r = 3.5$	16.82	0.80	20.19	-13.33	6.8
oxide $\varepsilon_r = 4.5$	15.61	0.87	18.24	11.76	-0.70
Down State 0.25μm Air Gap	19.13	0.64	22.27		19.6

5.2.3.4 OXIDE DIELECTRIC CONSTANT

The silicon dioxide insulator is deposited using a low-temperature PECVD process. The dielectric constant may vary depending on process conditions. As shown in Table 5.2, a 13.3% decrease in oxide dielectric constant results in a very small 0.48% increase in up-state resonant frequency. A dielectric constant increase of 11.8% did not change the resonant frequency as shown in Table 5.2. As expected, the down-state FSS performance had a higher sensitivity to the oxide dielectric constant. As shown in Table 5.3, a change in oxide dielectric constant of +11.8% or -13.3% results in a down-state resonant frequency shift of -0.70% and +6.8% respectively.

5.2.4 MEMS-BASED FSS MEASUREMENT CONSIDERATIONS

Several challenges arose when developing a test strategy to evaluate the performance of MEMS-tunable frequency selective surfaces. A typical test setup to measure FSS transmission uses a transmitting horn antenna on one side of the FSS, and a receiving horn antenna on the other side [11]. This setup requires the FSS to have a relatively large area. The MEMS fabrication process is currently limited to producing a maximum FSS size of approximately 1 square inch in area as discussed in Chapter 4. This size is too small for a far-field test setup since there would be significant edge diffraction that would degrade the measurements.

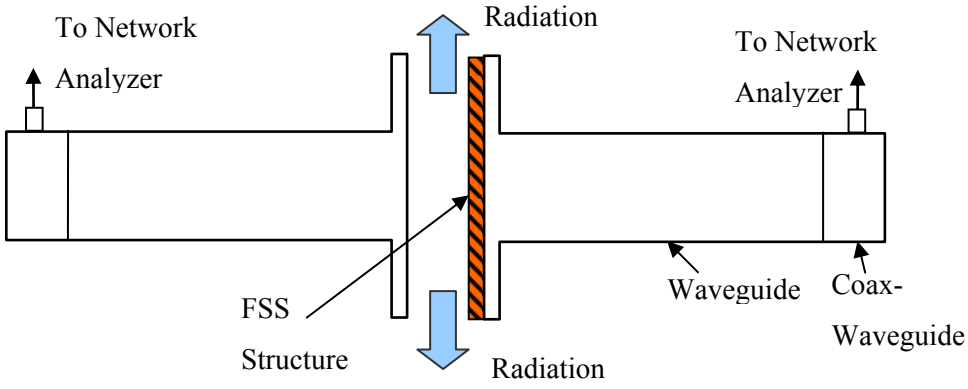

Figure 5.8: Waveguide test set used to measure FSS transmission and reflection

The alternative option was to use waveguides to measure a small MEMS FSS. This presented a different set of challenges. Figure 5.8 shows the waveguide test set used to measure FSS transmission and reflection. The FSS is placed with one side against the flange of a waveguide. The MEMS devices are on the side of the FSS opposite to the flange. An air gap is required to prevent the MEMS devices from being damaged by the other waveguide flange. Higher order modes are excited at the waveguide junction, some of which propagate between the parallel flanges and radiate as shown in Figure 5.8. The S-parameters of an unreleased MEMS FSS, measured using the waveguide setup, are shown in Figure 5.9. There are a number of parasitic resonances that arise due to the excitation of higher order modes at the junction. Most significantly, however, is the lack of correlation between S_{21} and S_{11} which can be seen in Figure 5.9 around 18GHz and 30GHz. For a 2-port network, S_{21} and S_{11} are inversely related. If the reflection decreases, the transmission must correspondingly increase since the only alternative signal path is through to the second port. Figure 5.9 shows that the reflection and transmission simultaneously decrease at certain frequencies. The signal must therefore be radiating from the gap between waveguides, which acts as a third port.

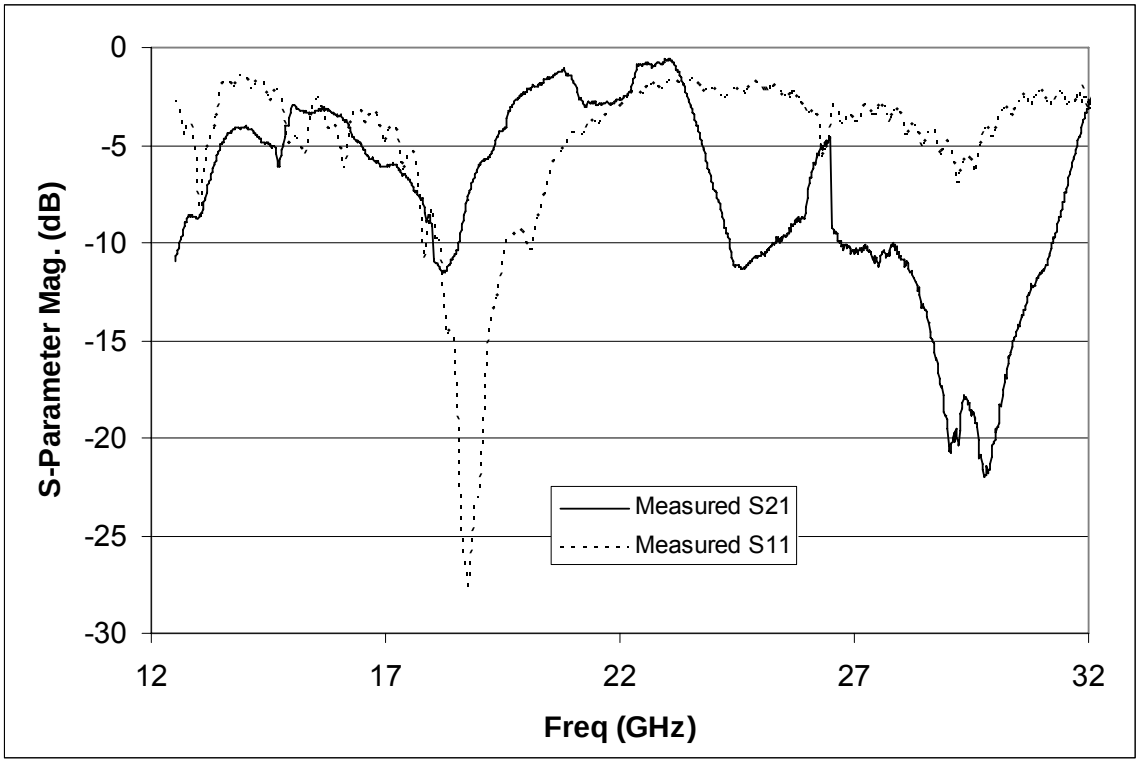

Figure 5.9: 2-port S-parameter measurements of an unreleased MEMS FSS with an air gap between the waveguide sections.

To further verify that the poor measurement quality seen in Figure 5.9 is due to the radiation and excitation of modes at the junction, the same unreleased MEMS FSS was clamped between two waveguides with no air gap, with measured results shown in Figure 5.10. The S-parameter curves of Figure 5.10 show the expected bandpass response, and do not exhibit the effects of multi-moding and radiation seen in Figure 5.9. The resonant frequency seems to be affected by the size of the waveguide aperture and FSS loading by the flange, as seen in the transition from WR62 to WR42 frequencies. Since the MEMS FSS used in this evaluation was unreleased, the sacrificial layer provided mechanical support to prevent the cantilever structures from collapsing. This measurement cannot be performed on released devices without causing significant damage.

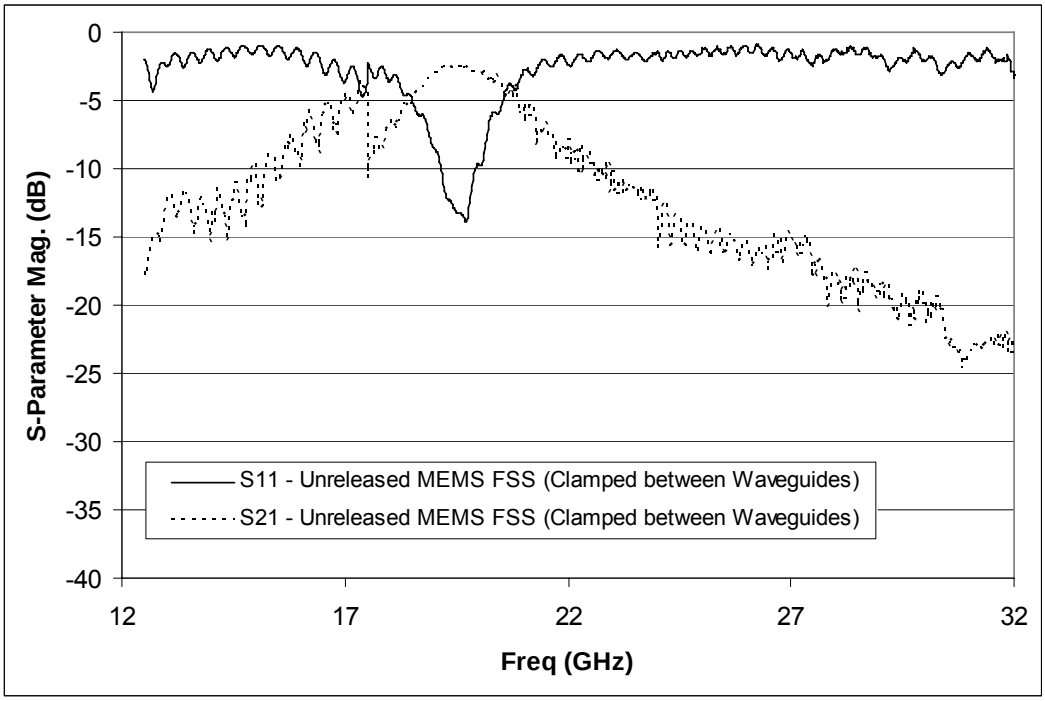

Figure 5.10: S-Parameter measurements of an unreleased FSS clamped between waveguides.

A 20 mil Teflon spacer was added to prevent the waveguide flange from contacting the device side of the unreleased MEMS FSS. The S_{21} and S_{11} of the unreleased FSS, clamped between 2 waveguides with the 20mil Teflon spacer, were measured and plotted in Figure 5.11 and Figure 5.12 respectively. The measured results with the unreleased MEMS FSS, clamped between waveguides with no spacer, are also plotted in Figure 5.11 and Figure 5.12 for comparison. Some form of spacer would be necessary to measure released MEMS devices in this manner, but the effects of multi-moding can be seen in the results of Figure 5.11 and Figure 5.12 even though the spacing is small. We therefore cannot obtain reliable S_{21} measurements since there must be a gap between the FSS and waveguide to avoid damaging the MEMS devices. A single waveguide can be used to reliably measure the S_{11} of a MEMS FSS placed against the flange since there is no air gap to allow radiation through unwanted modes at the junction. S_{11} measurement results will be discussed in Section 5.2.5 and plotted in Figure 5.20.

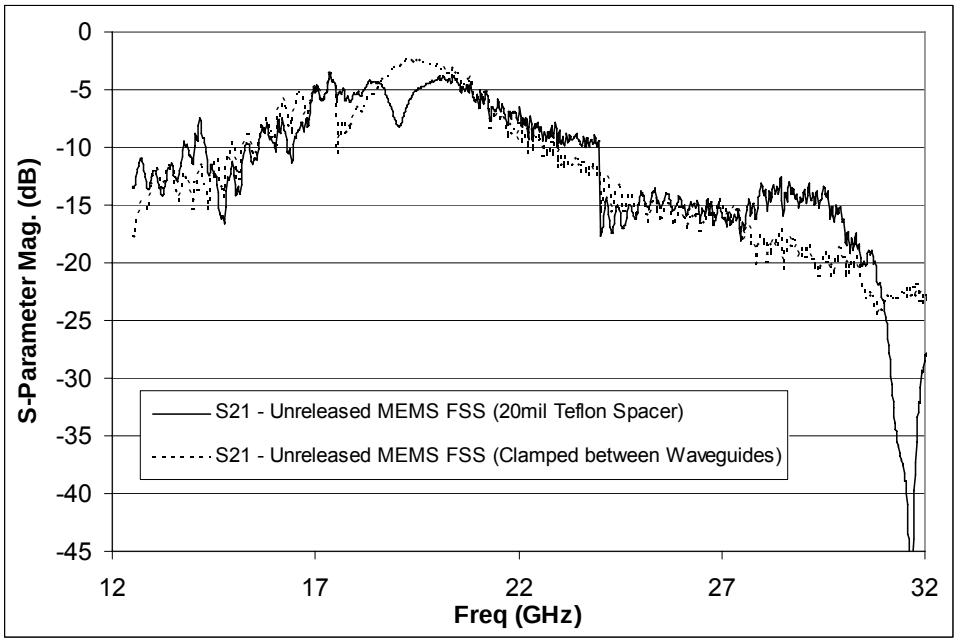

Figure 5.11: Comparison of measured S_{21} for an unreleased FSS with and without a 20mil Teflon spacer between the FSS device side and waveguide flange

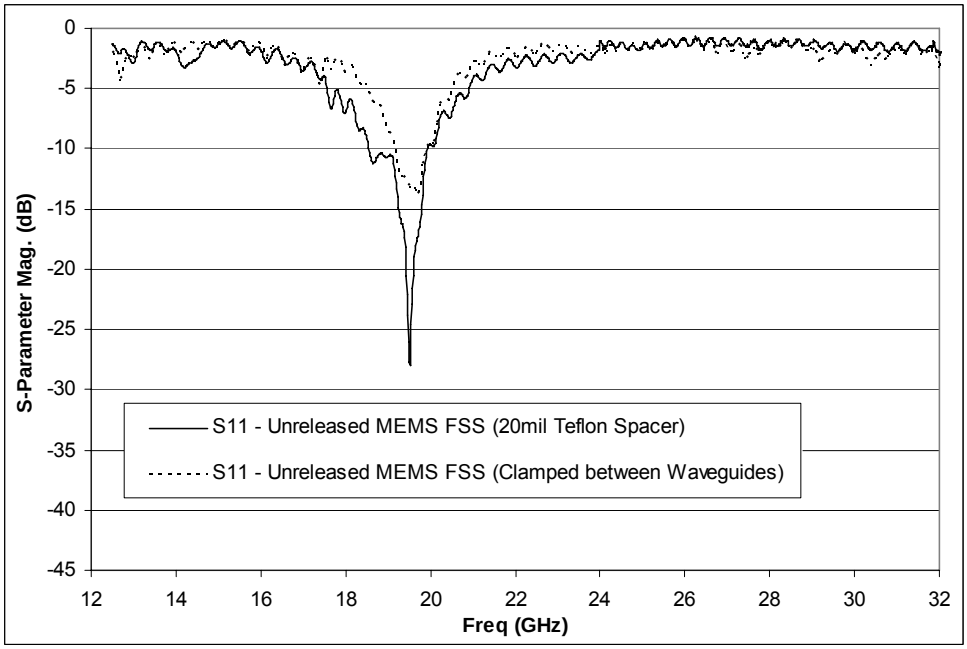

Figure 5.12: Comparison of measured S_{11} for an unreleased FSS with and without a 20mil Teflon spacer between the FSS device side and waveguide flange

5.2.5 MEMS-BASED FSS HARDWARE VERIFICATION

5.2.5.1 INDIVIDUAL MEMS SWITCHED CAPACITOR MEASUREMENTS

MEMS-tunable FSS hardware was fabricated on rigid-flex Kapton substrates following the process outlined in Chapter 4. The DC and RF performance of individual MEMS devices are first characterized before evaluating the entire FSS structure. Coplanar test circuits with individual MEMS switched capacitors, as shown in Figure 5.13, were fabricated and tested to characterize the individual devices. The switched capacitor is connected in series between 50 ohm coplanar waveguides. The MEMS switched capacitor geometry is identical to the FSS devices described above.

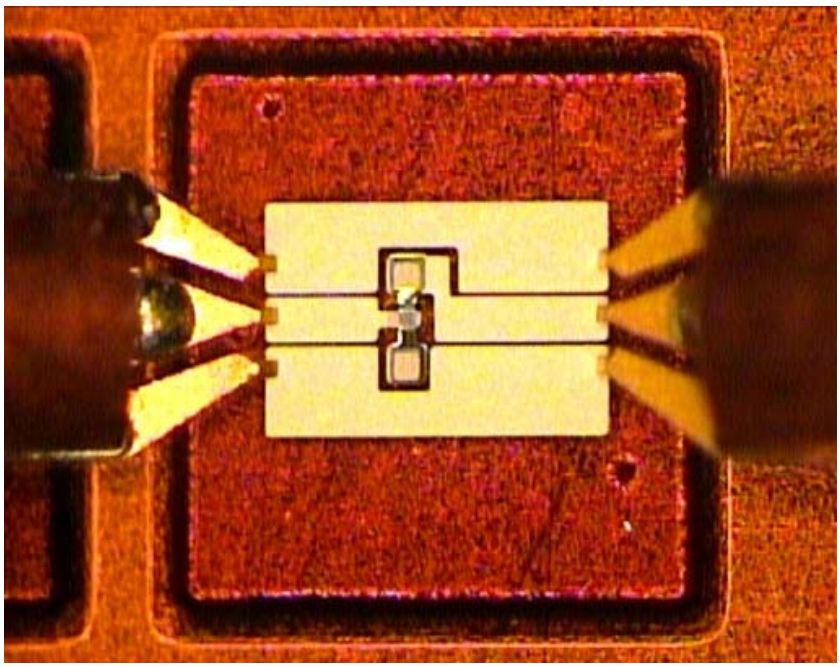

Figure 5.13: Fabricated coplanar test circuit with a series-connected individual MEMS switched capacitor on the Kapton rigid-flex substrate

The MEMS capacitors consist of a fixed-fixed beam, having a spring constant k given by Rebeiz in [90]

$$k = 32Ew\left(\frac{t}{l}\right)^3 \frac{1}{8(x/l)^3 - 20(x/l)^2 + 14(x/l) - 1}, \tag{5.1}$$

where E is the Young's modulus (69GPa for Aluminum), t is the 1μm beam thickness, w is the 40μm beam width, l is the 154μm beam length and l-2x is the 40μm pull-down electrode width. This expression assumes a flat, uniform beam with no residual stresses, and thus provides only an approximation of the actual spring constant. The pull-down voltage V_p may be estimated using [90]

$$V_p = \sqrt{\frac{8k}{27\varepsilon_0 W w} g_0^3}, \tag{5.2}$$

where W is the pull-down electrode width and g_0 is the up-state beam height, which was found to be 4.2μm including the 1.2μm electrode thickness. The calculated actuation voltage for the MEMS structure using Equations (5.1) and (5.2) is 142V.

The MEMS switched capacitor design was measured as shown in Figure 5.13. The measured actuation voltage was 189V. As expected, the measured actuation voltage was higher than the calculated value since the actual device is not uniform, will have residual stress and will be prone to distortion. These effects are not modeled in the above equations. Further evidence of distortion arises from the RF measurements of Figure 5.14, which indicate the presence of a down-state air gap between the beam and pull-down electrode insulator.

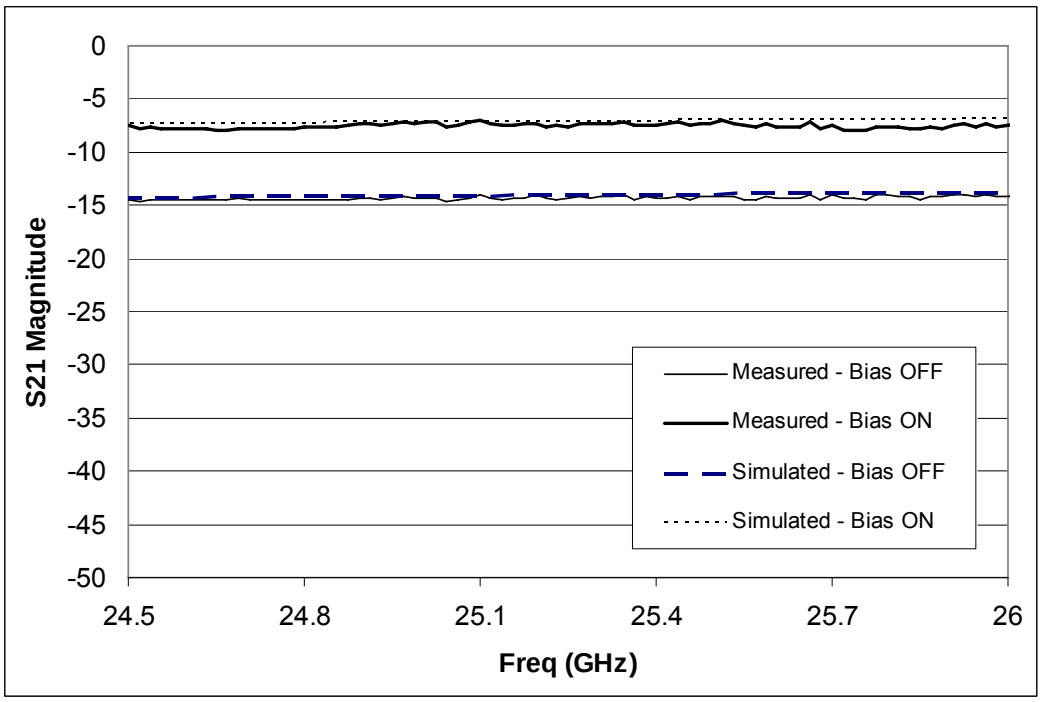

Figure 5.14: Simulated and measured S_{21} magnitude of a fabricated coplanar test circuit with an individual series-connected MEMS switched capacitor on the Kapton rigid-flex substrate

A comparison of simulated and measured S-parameter data for an individual series-connected MEMS switched capacitor is shown in Figure 5.14. The up-state air gap of the fabricated structure was found to be 3μm by comparing measured results with HFSS simulations. Similarly, a 0.25μm air gap exists in the down-state, which significantly reduces the down-state capacitance, resulting in an upward frequency shift in measured down-state FSS centre frequency compared with the original design simulations. The equivalent capacitance for the up-state, determined using Agilent ADS, is 13.6nF. The equivalent down-state capacitance is 34.1nF. Consequently, there is a capacitance ratio of 2.5 for the fabricated MEMS device.

5.2.5.2 MEMS-TUNABLE FSS MEASUREMENTS

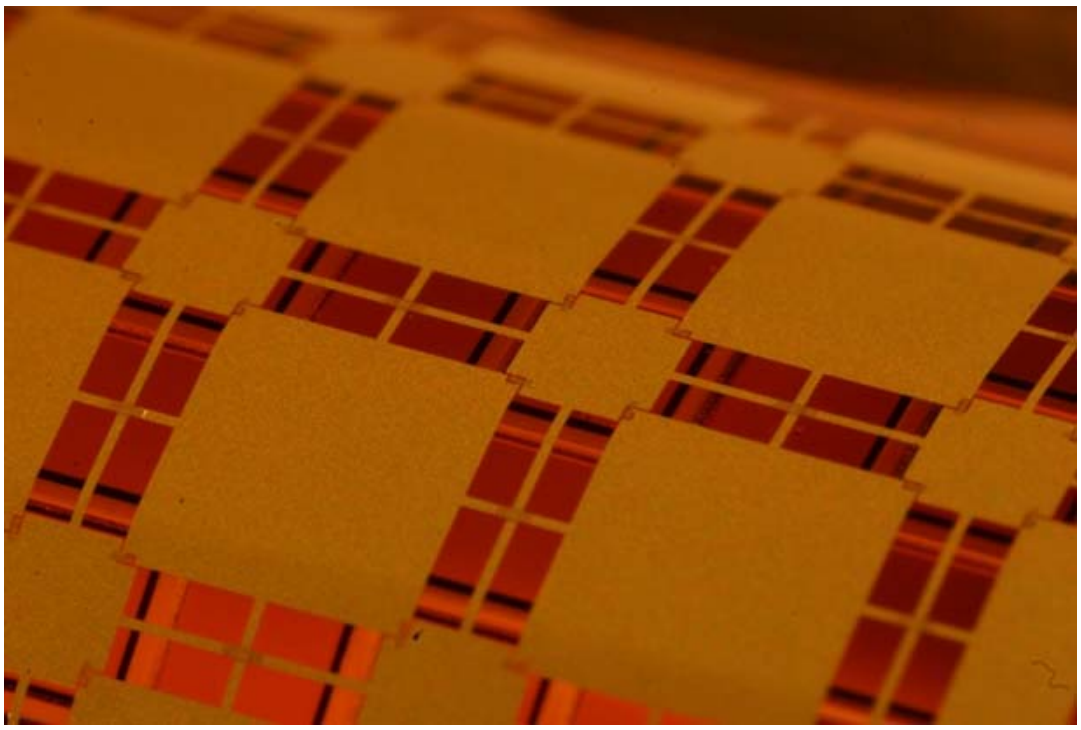

Figure 5.15: Fabricated MEMS FSS on rigid-flex substrate showing the MEMS devices supported over rigid islands while the substrate is curved.

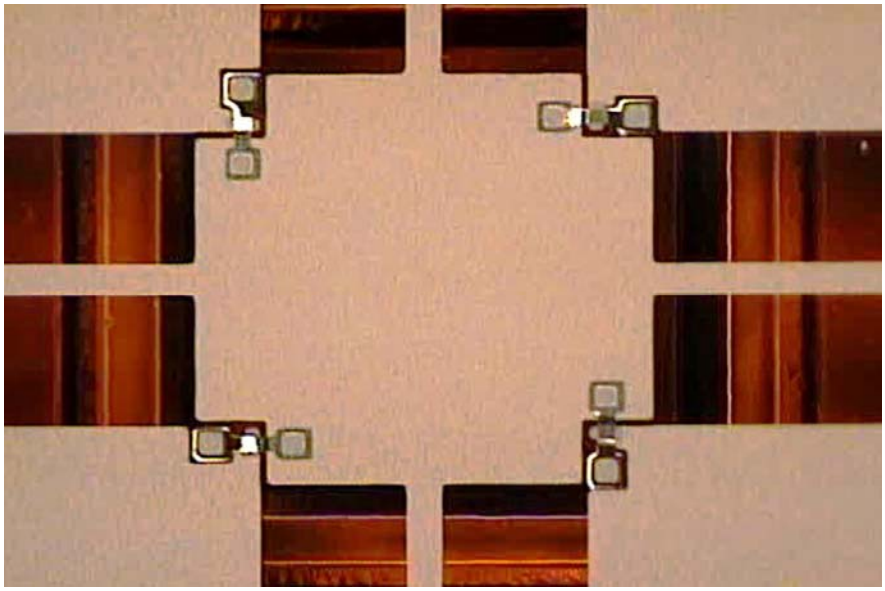

Figure 5.16: Fabricated MEMS switched capacitors over a thicker Kapton island in one unit cell of the FSS.

The MEMS-Tunable FSS was fabricated using the process of Chapter 4. The fabricated prototype consists of a 5x5 unit cell array. Figure 5.15 and Figure 5.16 respectively, show the fabricated structure and 2-state MEMS switched capacitors.

S-parameter measurements of the 5x5 unit-cell FSS structure are carried out by first mounting the device on a rigid support as shown in Figure 5.17. The support has an aperture that is slightly larger than the FSS, and maximizes flatness. Using the rigid support and clamp, the FSS is placed over the open end of a WR-42 waveguide as shown in Figure 5.17. The MEMS devices are on the side facing away from the waveguide to prevent damage to the fragile structures. The S_{11} measurements are performed using an Agilent network analyzer calibrated to the end of the coaxial cable which connects to the coax-waveguide adapter. A short-circuit reference measurement is first taken for the waveguide with a shorting plate over the open end. The FSS is then measured at each DC bias voltage. The measured MEMS FSS results, shown in the plots of Figure 5.20, are taken relative to the measured short-circuit reference.

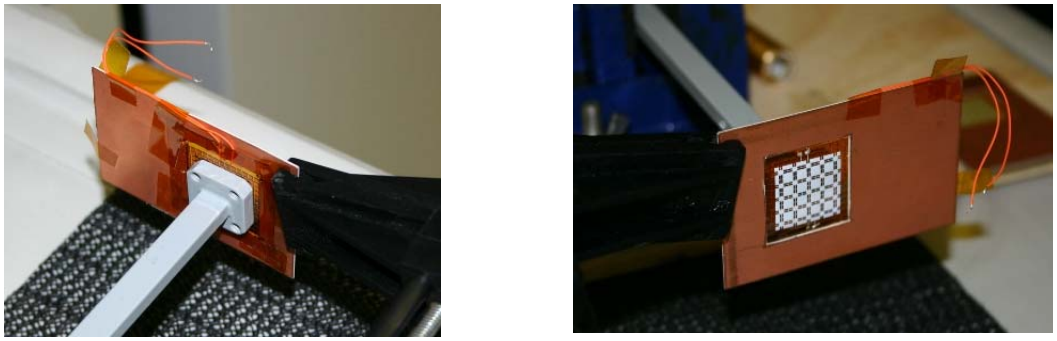

(a) (b)

Figure 5.17: Test set used to measure FSS. (a) View from back. (b) View from Front.

Simulations of the FSS in a waveguide test set were carried out using Ansoft HFSS to model the actual test conditions, which differ from the original design simulations that model plane wave excitation of the FSS. The test set model consists of a waveguide excited in its

fundamental mode by a wave port as shown in Figure 5.18a. The FSS is a reduced size 3x3 array of unit cells centered over the waveguide and flange.

Due to the symmetry of the structure, it is possible to add electric and magnetic wall symmetry boundaries to reduce the model size by 75%. A validation was carried out by comparing simulated results with the full-sized and reduced models. Some errors are expected when using symmetry boundaries since electric fields must be normal to the electric wall and tangential to the magnetic wall, and magnetic fields must be normal to the magnetic wall and tangential to the electric wall. Higher order modes excited at the waveguide-air junction that do not meet these criteria will be neglected in the reduced size symmetric model, resulting in some error.

HFSS simulations were carried out for the full-size model of Figure 5.18a and the reduced size model of Figure 5.18b. As shown in Figure 5.19, the resonant frequency of the structure simulated using the reduced-size model is only 0.4% lower than the full-size model simulation. The 10dB bandwidth is 6.4% for the full-size model and 6.1% for the reduced model. The reduced-size FSS model provides a sufficiently accurate approximation to the full size model, and is thus used to simulate the MEMS tunable FSS structure.

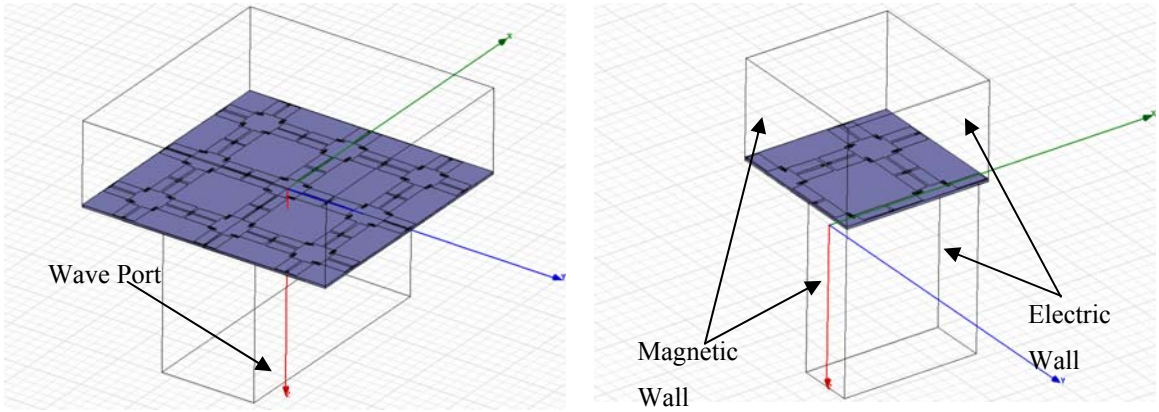

Figure 5.18: HFSS Simulation geometry for a 3x3 unit-cell FSS segment (a) with a full-size waveguide feed, (b) with electric and magnetic wall symmetry boundaries.

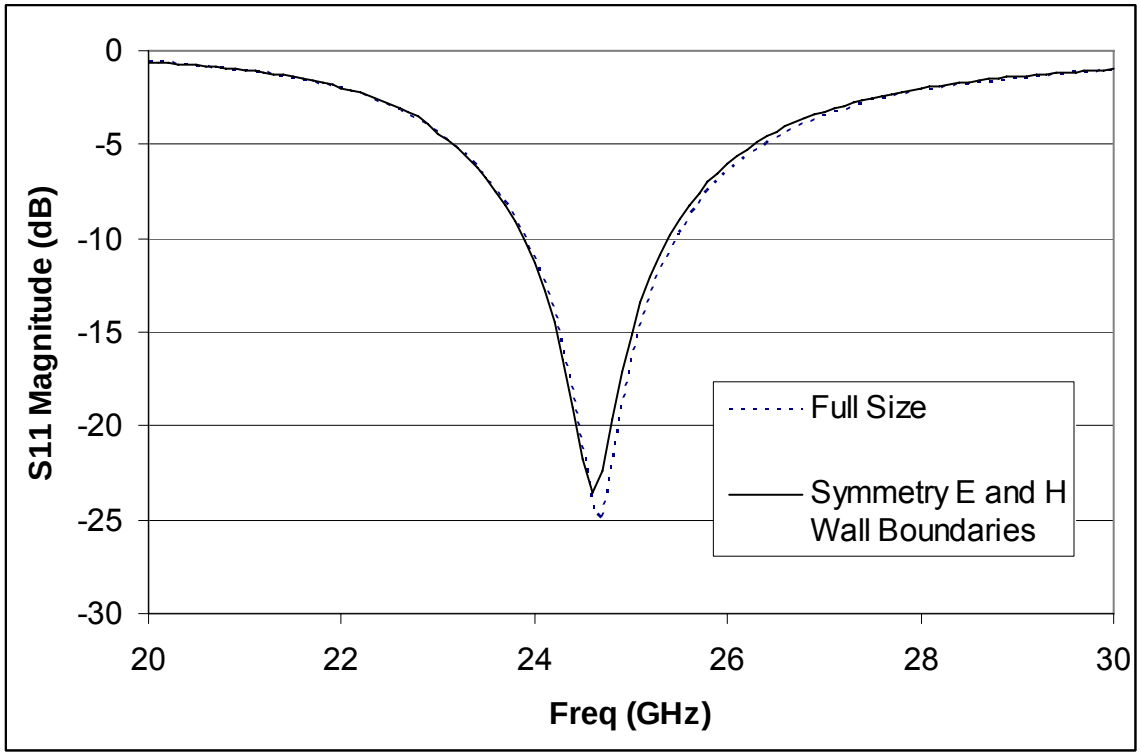

Figure 5.19: Simulated S_{11} magnitude of a simplified FSS structure with electric and magnetic wall symmetry boundaries compared with a full-size simulation

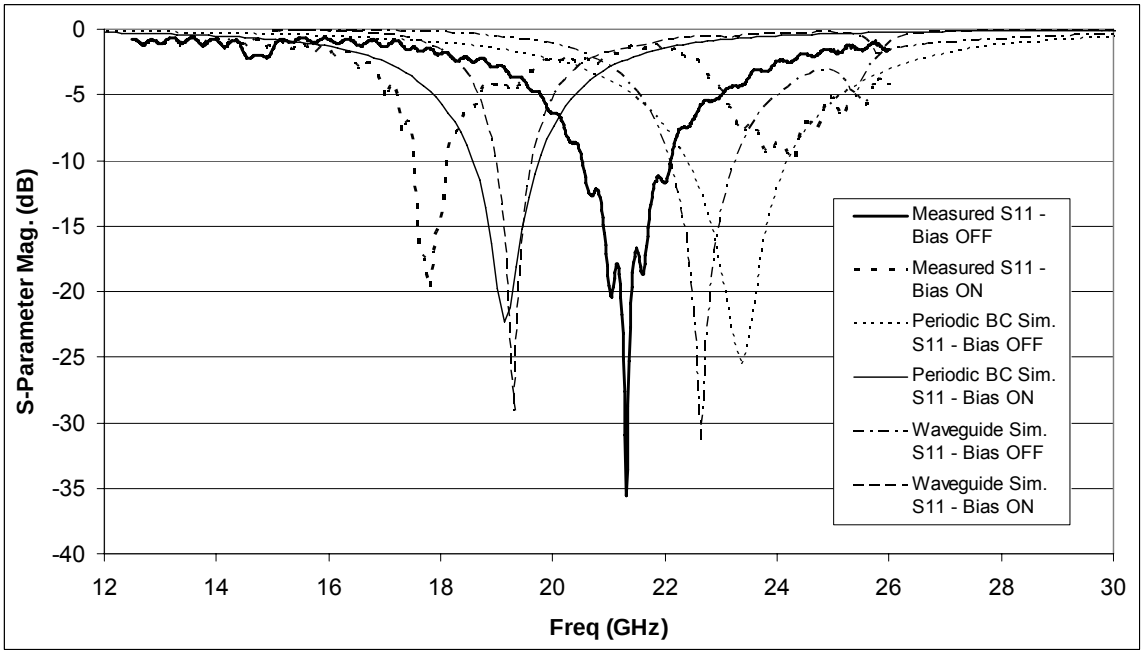

Figure 5.20: Comparison of simulated and measured S_{11} for the MEMS-tunable FSS

The simulated and measured results for the MEMS-tunable FSS are shown in Figure 5.20. HFSS simulations were carried out with a plane wave incident on the FSS having periodic boundary conditions as in Figure 5.2, as well as with the waveguide test setup of Figure 5.18b. The measured tuning range is significantly reduced compared with simulations of the original design shown in Figure 5.3, due to the lower than expected down-state fabricated MEMS capacitance. This is a consequence of a 0.25μm down-state air gap as discussed in Section 5.2.5.1. The simulated plots of Figure 5.20 reflect the actual 0.25μm down-state air gap and 3μm up-state air gap of the fabricated devices. The measured frequencies are lower than simulated values, likely due to parameter variation in fabrication as discussed in Section 5.2.3. The measured relative change in frequency when tuning the FSS correlates well with simulations as will be discussed below.

The measured down-state response of Figure 5.20 shows an additional 24GHz resonance in the S_{11} plot. As shown in Figure 5.21, a similar S_{11} performance is observed when the FSS structure is simulated with a MEMS switch stuck in the up-state while the bias is turned on. The additional parasitic resonance in the measured down-state response is most likely due to one or more MEMS switches that did not properly actuate. Since the measured parasitic resonant frequency is higher than the up-state resonant frequency as shown in Figure 5.20, it does not significantly impact the FSS switching performance.

Table 5.4: Summary of Simulated and Measured Performance

	f_0 (GHz) (Bias On)	10dB BW (GHz) Bias On	f_0 (GHz) (Bias Off)	10dB BW (GHz) Bias Off	% Decrease in f_0
Measured	17.8	0.60	21.3	1.37	16.4
Sim. (Waveguide)	19.3	0.66	22.6	1.22	14.8
Sim. (Periodic B.C.)	19.1	1.21	23.4	1.82	18.4

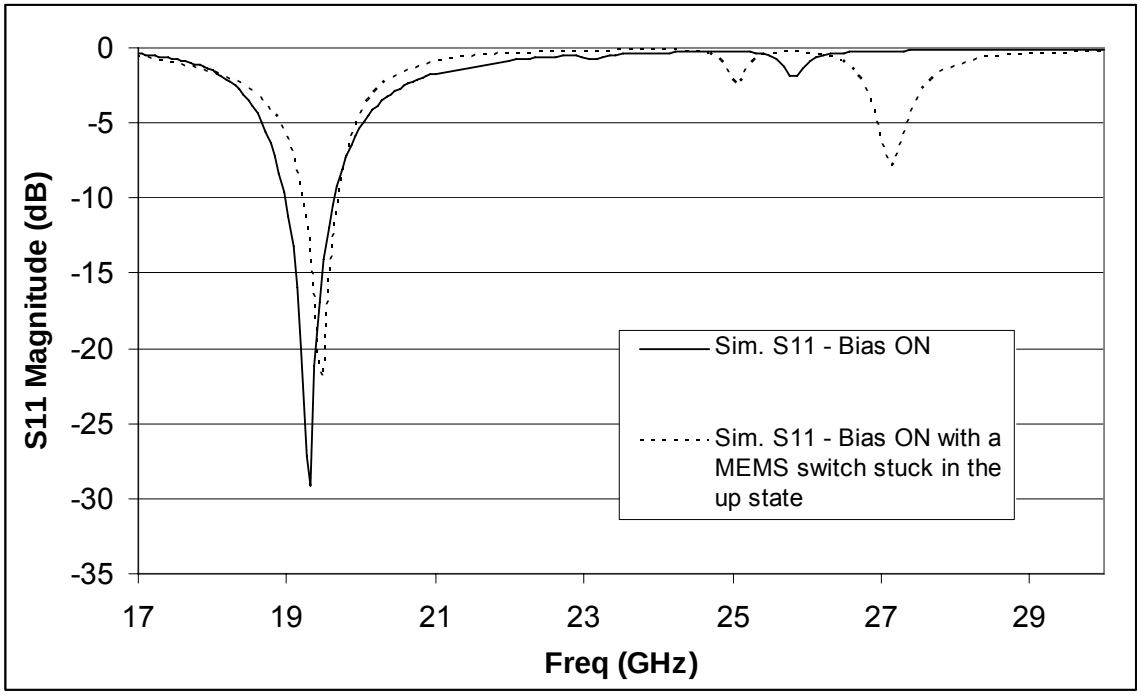

Figure 5.21: Effect on FSS performance of a MEMS switch stuck in the up-state when the bias is turned on

Table 5.4 summarizes the simulated and measured results shown in the plots of Figure 5.20. As expected, the disparity with the periodic boundary simulation and measured results is greater than the difference in waveguide simulated and measured results. The periodic boundary simulation models the FSS performance in filtering a propagating plane wave, where the electric and magnetic fields are perpendicular to each other. The actual measurements are taken by exciting the FSS with a guided TE_{10} wave. Although the electric and magnetic fields of the guided wave are perpendicular to each other, there is also a component of magnetic field along the direction of propagation. Unlike for a plane wave, the TE_{10} electric field varies in intensity across the longer cross-sectional waveguide dimension. Additionally, there is capacitive loading from the waveguide flange. As can be seen in Table 5.4, the aforementioned differences between propagating and guided wave characteristics result in reduced FSS bandwidth as measured using the waveguide test set of Figure 5.17, as well as a decreased tuning range. The waveguide simulated and measured bandwidth and

tuning range correlate well as summarized in Table 5.4. Disparity between simulated and measured results arise from parameter variations as previously discussed, as well as variation in the capacitance of the MEMS devices across a single fabricated FSS, as will be discussed below.

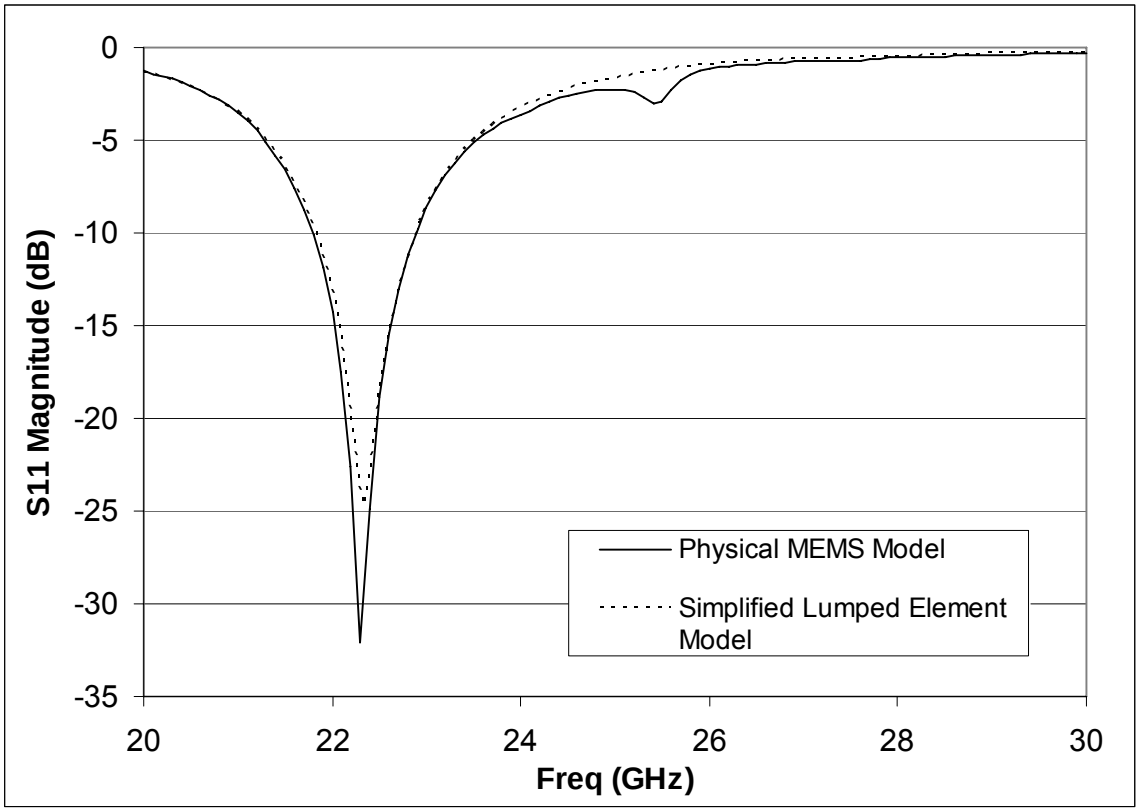

Figure 5.22: Comparison of simulated physical MEMS FSS model with a simplified FSS model where lumped-element capacitors replace the MEMS switches.

A simplified HFSS model is used to simulate the effects of random capacitance variations of the MEMS devices across the FSS. The MEMS devices are replaced by lumped-element capacitors. The lumped element model is first validated by comparing results with the physical MEMS simulation model as shown in Figure 5.22. The FSS model with physical MEMS capacitors has a resonant 22.36GHz resonant frequency. The simplified model using lumped capacitors has a resonant frequency 0.27% lower as shown in Figure 5.22. The

minimum S_{11} changes increases by 7.2dB to -24.9dB for the simplified model. The simplified model, however, provides a reasonable approximation to the FSS characteristics which is sufficient to model trends in performance when varying the values of the MEMS capacitors.

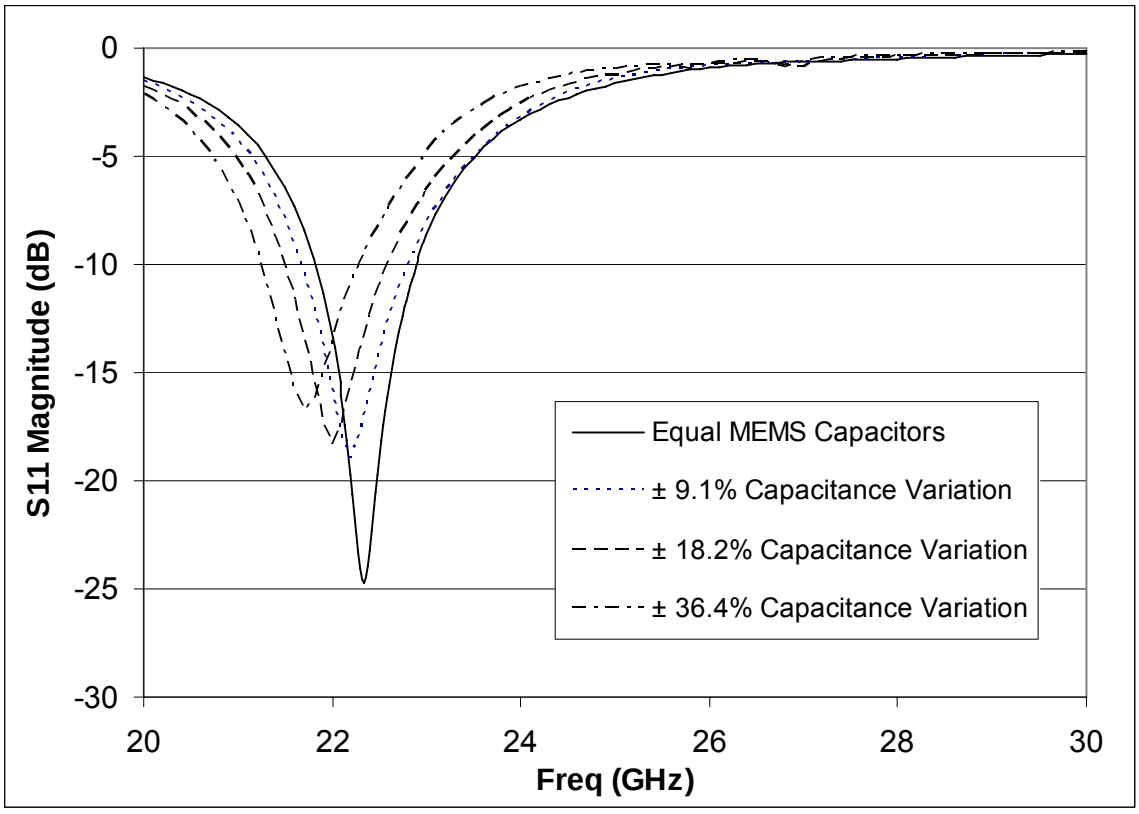

Figure 5.23: Simulated results showing the effects of random MEMS device capacitance variation across the MEMS FSS.

Figure 5.23 shows the results of HFSS simulations for varying distributions of MEMS device capacitance across the FSS, with key figures of merit summarized in Table 5.5. The capacitance values were randomly distributed with maximum deviations of ±9.1%, ±18.2%, and ±36.4%. As the maximum deviation increased, the resonant frequency decreased. For a ±36.4% maximum variation, the resonant frequency decreased by only to 2.7%, and the minimum S_{11} increased by 8dB. The FSS resonant frequency is therefore very tolerant to significant variations that arise due to manufacturing tolerances.

Table 5.5: Summary of resonant frequency shift and minimum S11 for different random MEMS capacitance distributions.

MEMS Capacitor Variation	Resonant Freq.(GHz)	Minimum S_{11} (dB)
0%	22.3	-24.7
9.10%	22.2	-18.9
18.20%	22.0	-18.3
36.40%	21.7	-16.7

5.3 MEMS RECONFIGURABLE EBG STRUCTURE

5.3.1 RECONFIGURABLE EBG DESIGN

The fabricated MEMS EBG structure, shown in Figure 5.24, has a top-side geometry identical to that of the FSS structure of Section 5.2, but there are no islands in the dielectric substrate. The substrate is Kapton 500H, with a uniform thickness of 5mil. From an EBG point of view, the MEMS structure is similar to the three-layer Sievenpiper structure [18], with a few modifications. The Sievenpiper structure, shown in Figure 5.25a, consists of square patches, each having a via to ground, with overlapping corners. The fabricated EBG structure, however, does not have grounding vias, and the square patches are connected together using thin inductive traces that simplify biasing the MEMS devices (See Figure 5.24). The overlapping corners of the Sievenpiper structure are replaced by MEMS switched capacitors, shown in the simplified cross-sectional view of Figure 5.25b. The actual MEMS devices are fixed-fixed beams as in Figure 5.1c, and crossover bridges maintain DC isolation between the large and small patches as in Figure 5.1d. Actuating the MEMS devices increases the capacitance between the overlapping patches, reducing the EBG structure resonant frequency.

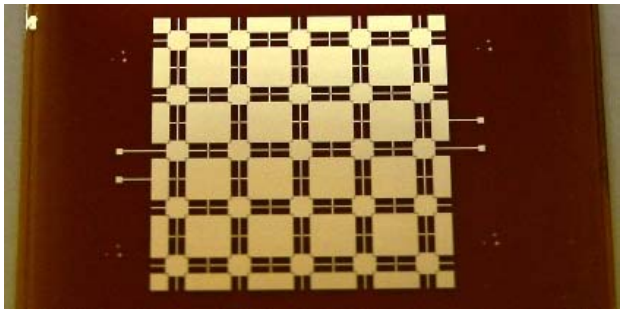

Figure 5.24: Fabricated MEMS-switchable EBG structure

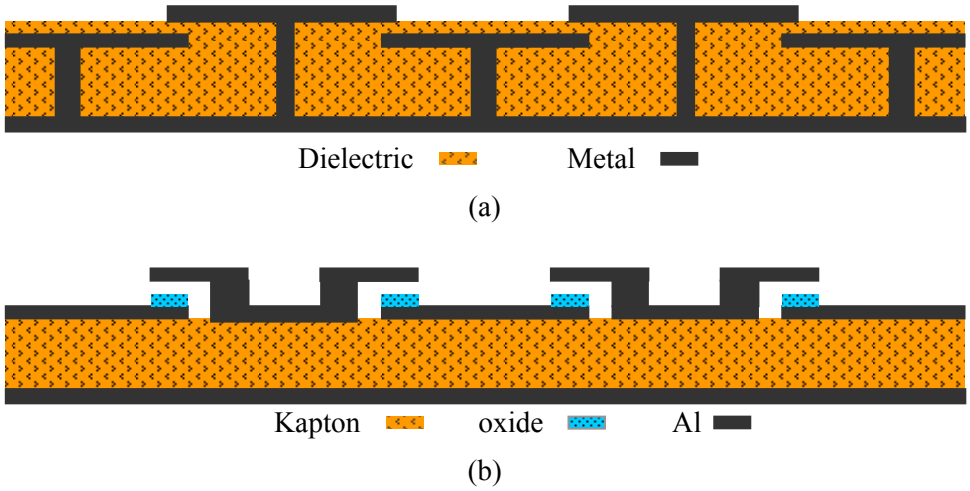

Figure 5.25: (a) 3-Layer Sievenpiper EBG structure [18] (b) Simplified cross-section of MEMS-switchable EBG structure.

5.3.2 EBG Structure Modeling

EBG simulations were carried out using Ansoft HFSS. The model consists of a WR-28 waveguide excited in its fundamental mode by a wave port as shown in Figure 5.26a. The EBG is a reduced size 2x3 array of unit cells placed over the ground plane. The waveguide and flange are centered over the EBG structure. Radiation boundaries surround the periphery of the gap between the flange and ground plane. For practical measurements, it was not possible to maintain perfect flatness of the EBG structure. A 35um air gap under the dielectric models this effect.

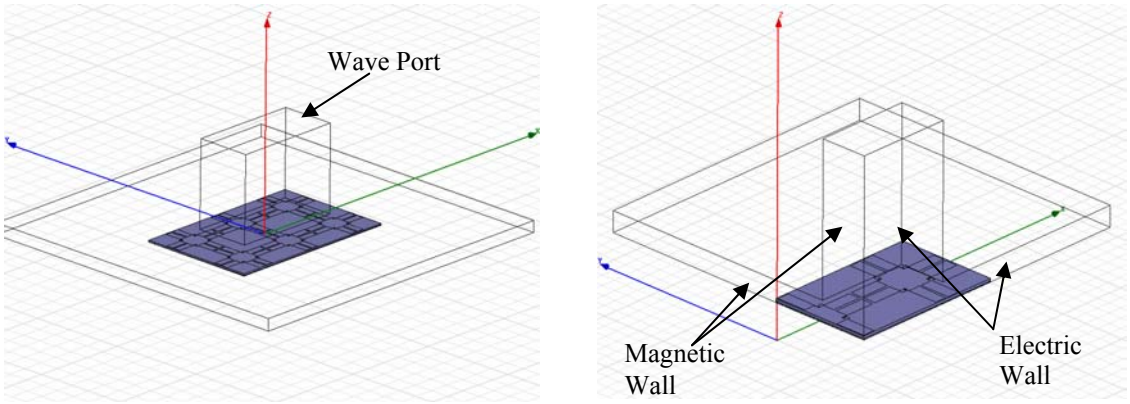

(a) (b)

Figure 5.26: HFSS Simulation geometry for a 3x2 unit-cell EBG segment (a) with a full-size WR-28 waveguide feed, (b) with electric and magnetic wall symmetry boundaries.

After adding the MEMS devices, the full-size model, shown in Figure 5.26a, became prohibitively large. Due to the symmetry of the structure, it is possible to add electric and magnetic wall symmetry boundaries to reduce the model size by 75%. A simplified EBG structure, with the MEMS devices removed, was first used to validate the reduced model. Some errors are expected when using symmetry boundaries since electric fields must be normal to the electric wall and tangential to the magnetic wall, and magnetic fields must be normal to the magnetic wall and tangential to the electric wall. Higher order modes excited at the waveguide-air junction that do not meet these criteria will be neglected in the reduced size symmetric model, resulting in some error.

HFSS simulations were carried out for the full-size model of Figure 5.26a and the reduced size model of Figure 5.26b. The resonant frequency of the structure simulated using the full-size model is 33.5GHz, as shown in Figure 5.27. The resonant frequency of the structure simulated using the reduced-size model is 0.8% higher, which is expected since there is less reactance compared to the full size model as a result of the neglected higher-order modes at the waveguide junction. The ±90º bandwidth is 2.7% for the full-size model and 2.4% for the reduced model. The reduced-size EBG model therefore provides a sufficiently accurate approximation to the full size model, and is thus used to simulate the MEMS tunable EBG structure.

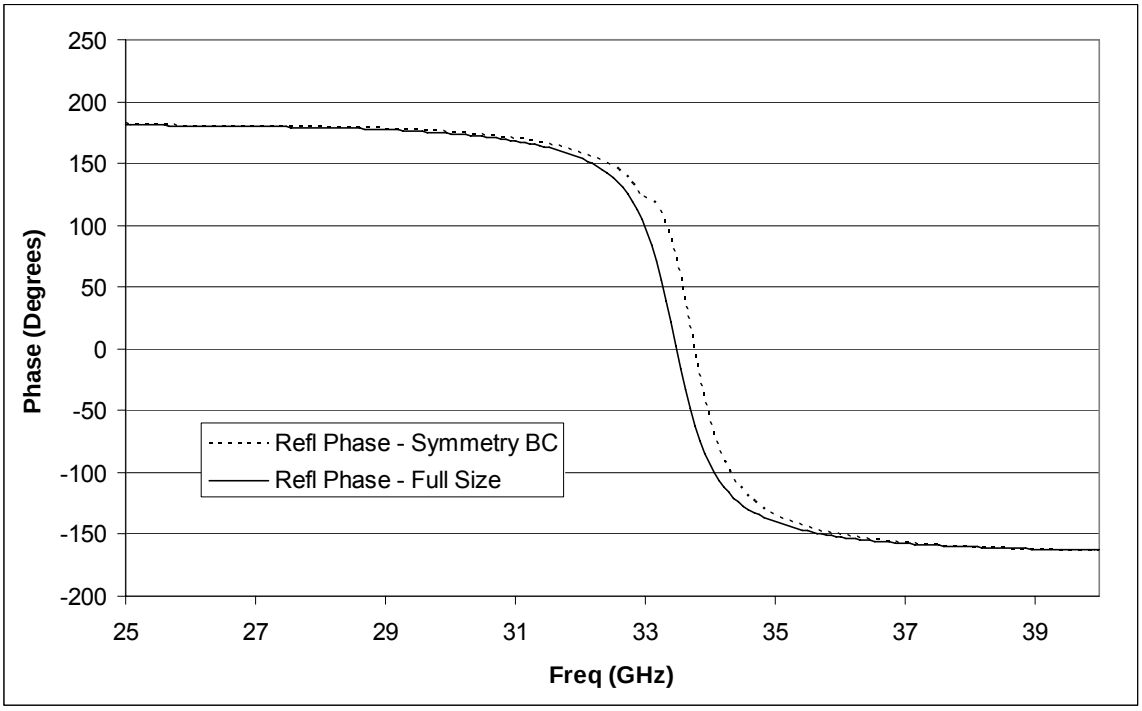

Figure 5.27: Simulated reflection phase of a simplified EBG structure with electric and magnetic wall symmetry boundaries compared with a full-size simulation

5.3.3 HARDWARE VERIFICATION

5.3.3.1 EBG TEST SETUP

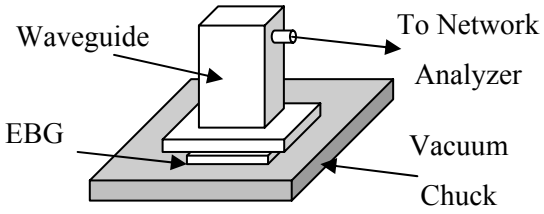

(a)

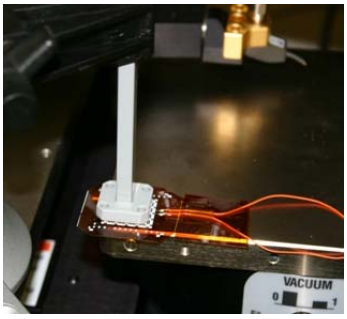

(b)

Figure 5.28: Test set used to measure EBG reflection phase. (a) Test set diagram (b) Photo of actual test set.

Reflection measurements of the fabricated 5x5 unit-cell EBG structure are carried out by placing the device on a vacuum chuck to maximize flatness. As shown in Figure 5.28, a WR-28 waveguide is clamped in place over the EBG, and separated by an air gap to prevent damage to the MEMS structures. The S_{11} measurements are performed using an Agilent network analyzer calibrated to the end of the coaxial cable which connects to the coax-waveguide transition. A short-circuit reference measurement is first taken for the empty test set consisting of the waveguide over the vacuum chuck surface. The EBG is then placed under the waveguide, and measured at each DC bias voltage. The measured MEMS EBG results, shown in the plots of Figure 5.32 - Figure 5.35, are taken relative to the measured short-circuit reference.

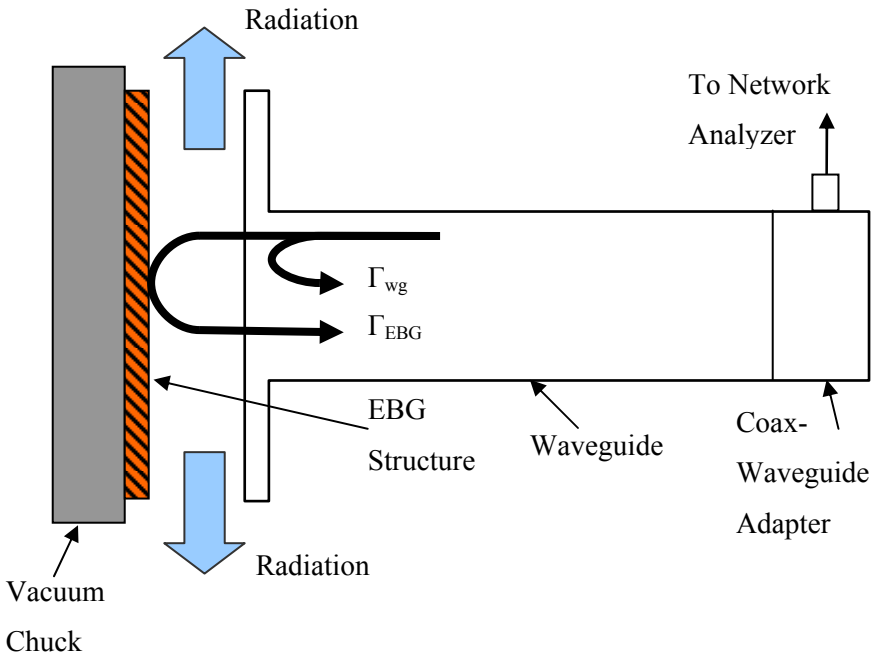

Figure 5.29: Multiple reflected signals and radiation from the waveguide test set used to measure EBG structures.

It is important to note the limitations in measurement uncertainty inherent to this test setup, and the effects on measured data quality. The accuracy of any reflection measurement is

compromised by the presence of interfering signals which are superimposed onto the reflected signal. This form of interference cannot be calibrated out of a test setup. For this reason, the use of adapters should be minimized, and the directional couplers used to separate the incident and reflected signals for S-parameter measurements must have a high directivity to prevent the incident signal from leaking over to the reflected signal path.

Two principal sources of reflection are present in the test setup: the mismatch due to the open-circuit end of the waveguide, and the discontinuity of the coax-waveguide adapter. Figure 5.30 shows the measured S_{11} of two coax-waveguide adapters connected back-to-back, with one port terminated in a 50 ohm load. The maximum reflection magnitude is -21.3dB at 28.9 GHz, and the peak-peak frequency spacing of the ripple is 2.3GHz.

The reflection from the open-circuited waveguide is the dominant effect. The open-circuited waveguide is not a perfect radiator as can be seen in Figure 5.30, where the S_{11} magnitude varies between -12.5dB and -18dB from 28-34GHz. Consequently, a substantial interfering signal is superimposed onto the signal reflected back from the EBG structure due to reflection at the waveguide-air junction as shown in Figure 5.29. Measurement errors are exacerbated by radiation from the sides of the test fixture, which further decreases the reflected signal magnitude from the EBG device under test.

The reflection and radiation effects can be seen in the measured empty test set amplitude response of Figure 5.30, which exhibits periodic one-port S_{11} maxima and minima. The 0.4GHz spaced ripple arises from the transmission line effects of the waveguide which has the open-circuit discontinuity at one end, and the coax-waveguide adapter discontinuity at the other end. The frequency spacing of the ripple is inversely proportional to the waveguide electrical length. A slowly varying envelope is superimposed over the open-circuit waveguide and empty test set measurements of Figure 5.30. This envelope, which has a 2.3GHz peak-trough frequency spacing, arises due to the single coax-waveguide transition. As expected, the envelope frequency spacing is twice the value of the measured S_{11} frequency ripple for the two back-to-back coax waveguide adapters.

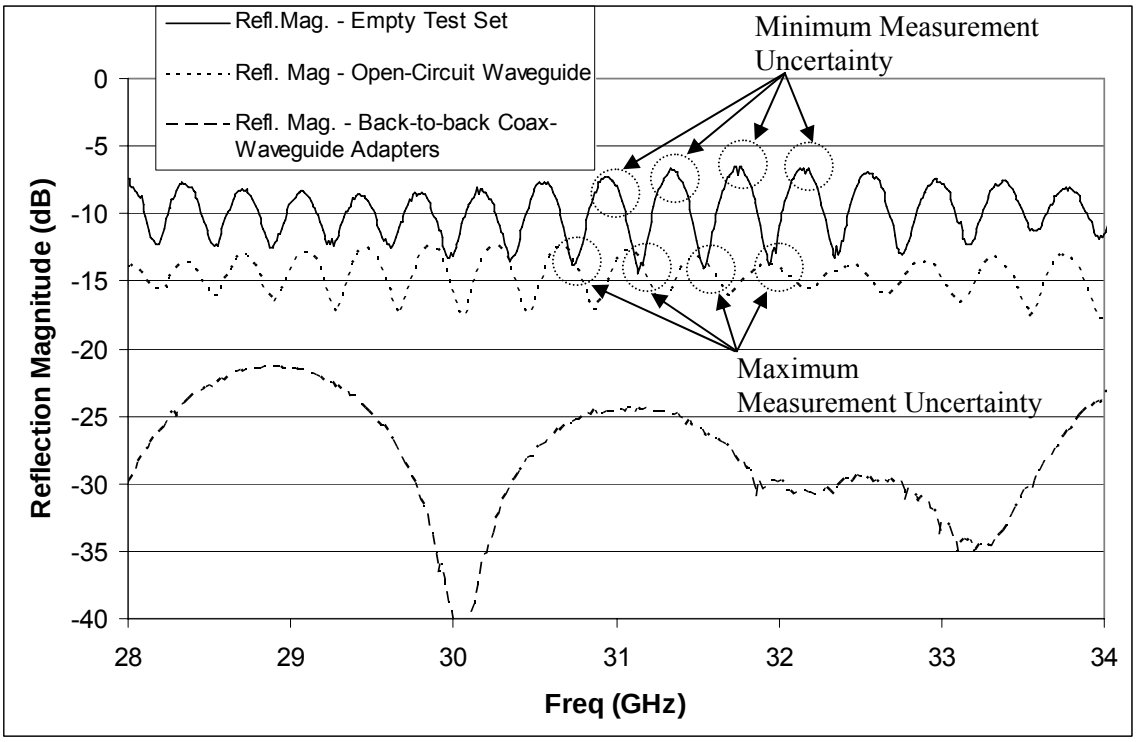

Figure 5.30: Measured reflection magnitude of empty test set and open-circuited waveguide, showing regions of minimum and maximum measurement uncertainty.

Upon closer examination, the reflected signal measured by the network analyzer is the sum of signals reflected from the EBG (or empty test set) and from the waveguide-air junction. The reflection from the coax-waveguide adapter will be neglected since the magnitude is significantly lower than the waveguide-air junction reflection as shown in Figure 5.30. The measured reflection amplitude ripple arises due to the addition of two reflected signal phasors (one from the EBG and one from the waveguide-air junction) which have a frequency-dependent relative phase. When both reflected signals are in-phase, the amplitude response is at a local maximum, and the measured phase is equal to the EBG reflected phase as shown in Figure 5.31a. We assume that the amplitude of each rotating phasor does not vary within narrow bands. When the reflected signals are not in-phase, the measured amplitude is lower than the peak value, and the measured phase is no longer equal to the

EBG reflection phase as shown in Figure 5.31b. As the relative EBG reflection magnitude decreases, the disparity between EBG reflection phase and measured phase will increase for reflection measurements where the amplitude is not at a ripple maximum. The measured phase values, however, will remain accurate provided the reflection amplitude is at a ripple maximum since the EBG phase is equal to the measured phase regardless of the relative phasor amplitude, as can be seen in Figure 5.31a.

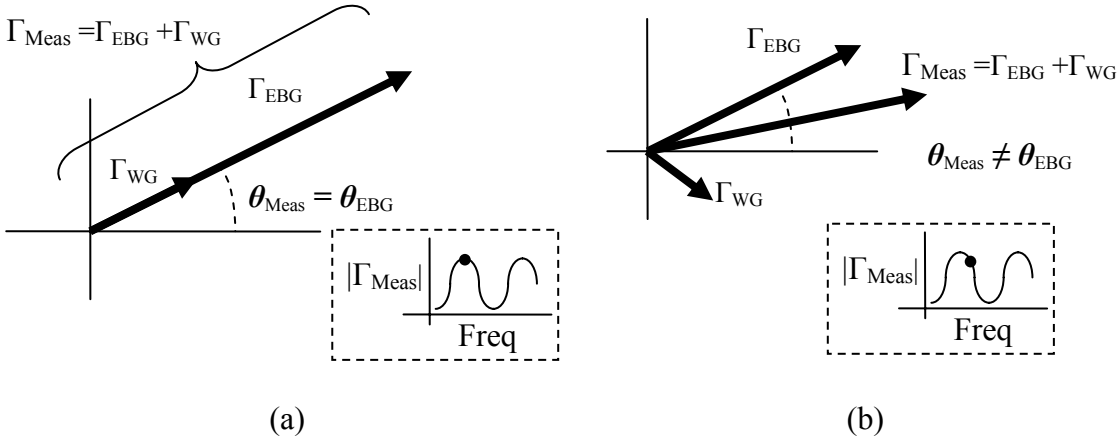

Figure 5.31: (a) Position on the reflection magnitude plot and corresponding phasor diagram where the measured reflection phase equals the EBG reflection phase. (b) Position on the reflection magnitude plot and corresponding phasor diagram where the measured reflection phase is not equivalent to the EBG reflection phase.

5.3.3.2 Comparison of simulated and measured Results

The measured reflection magnitude and phase response of the MEMS EBG, with the bias turned off, is shown in Figure 5.32. There is a significant ripple in the phase response which arises due to the measurement errors discussed above. As can be seen in Figure 5.32, there is an inverse correlation between the depth of the phase ripple and the reflection magnitude. The largest phase errors occur in the frequency range of 30.5GHz-31.5GHz, where the EBG resonates and the S_{11} magnitude is lowest. The line of best fit for the phase response is determined by measuring the phase at the frequencies of maximum reflection amplitude, as shown in Figure 5.32, where the measurement uncertainty is lowest. Similarly, the measured data and minimum error curve for the MEMS EBG response, with the bias turned on, is

shown in Figure 5.33. As expected, the resonant frequency decreases due to additional loading of the EBG structure by the down-state MEMS capacitors.

Figure 5.34 and Figure 5.35 show a comparison of HFSS simulated and measured reflection phase for the MEMS-tunable EBG. In Figure 5.34, the raw measured data is plotted along with the minimum error curves. In Figure 5.35, the raw data has been removed for clarity.

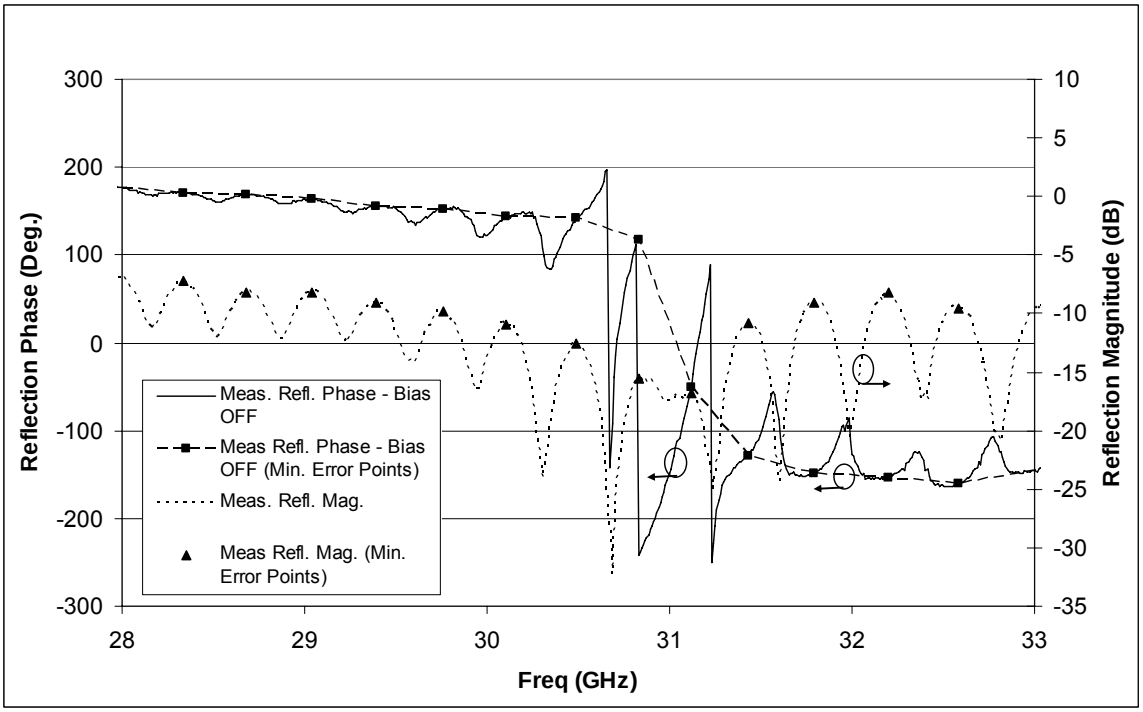

Figure 5.32: Measured MEMS EBG magnitude and phase response with the bias off. The points of minimum measurement uncertainty are shown for the magnitude and phase response.

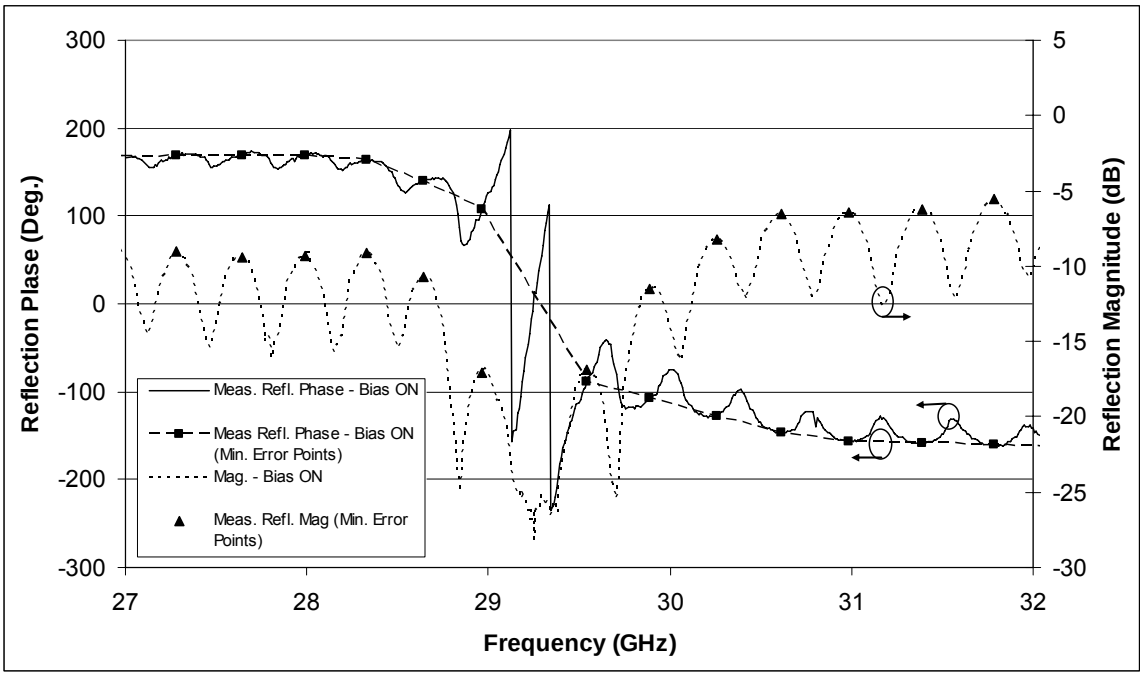

Figure 5.33: Measured MEMS EBG magnitude and phase response with the bias on. The points of minimum measurement uncertainty are shown for the magnitude and phase response.

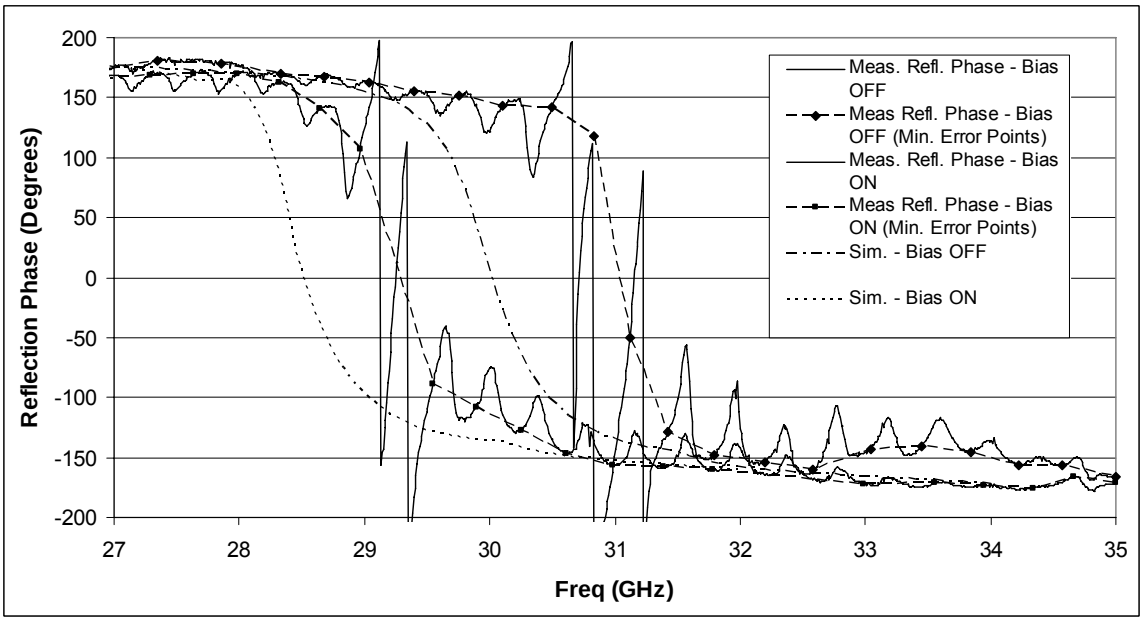

Figure 5.34: Comparison of HFSS simulated and measured MEMS EBG phase response with the bias off and on. The points of minimum measurement uncertainty are shown over the raw measured phase response.

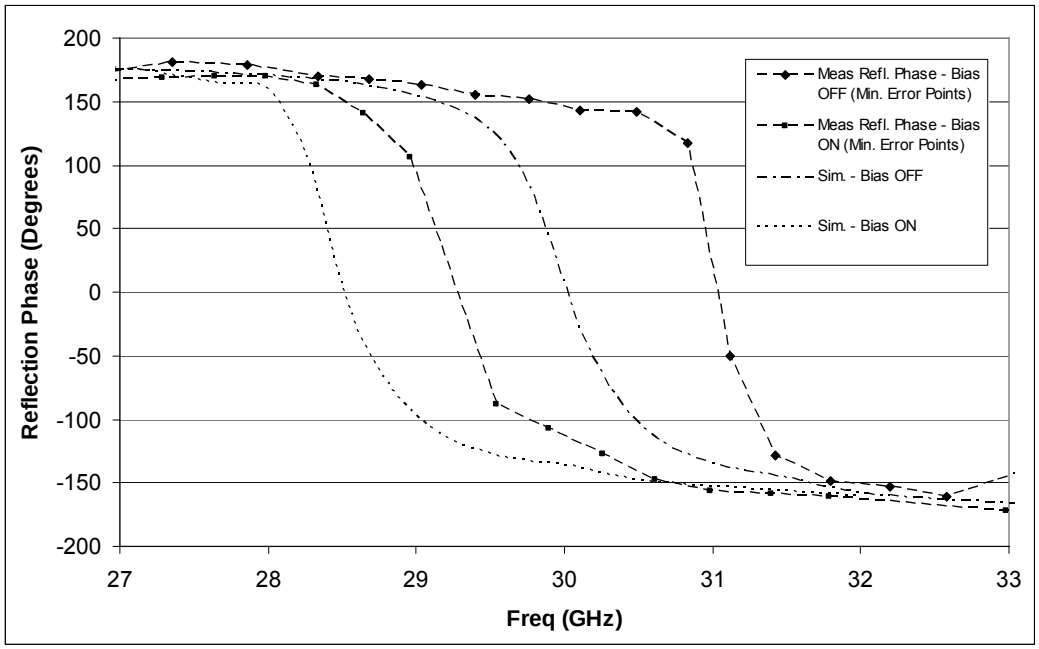

Figure 5.35: Comparison of HFSS simulated and measured MEMS EBG phase response with the bias off and on. The points of minimum measurement uncertainty are shown for the measured results.

As can be seen from Figure 5.34 and Figure 5.35, there is good correlation between simulated and measured trends in the EBG tuning performance. The measured resonant frequencies are higher than simulated values as can be seen in Table 5.6, but the EBG tuning performance when actuating the MEMS devices is similar. The simulated decrease in resonant frequency is 1.51GHz upon actuation of the MEMS capacitors, compared to the measured decrease of 1.75GHz. The simulated ±90º bandwidth is 2.19% and 2.20%, respectively, for the EBG with bias on and off. The measured ±90º bandwidth is narrower than simulated results. Measured bandwidth values for the EBG with bias on and off are 1.91% and 1.29% respectively.

Table 5.6: Comparison of simulated and measured EBG resonant frequency and bandwidth

	Centre Freq. (GHz)	% Bandwidth
Meas. Bias On	29.28	1.91
Meas. Bias Off	31.03	1.29
Sim. Bias On	28.51	2.19
Sim. Bias Off	30.02	2.20

As discussed previously, several sources of error arise due to limitations of the test set used to measure the EBG. The results presented here are sufficient for proof of concept, but improvements in test strategy are essential to characterize structures with the level of accuracy necessary for practical designs.

5.4 ANTENNA OVER MEMS RECONFIGURABLE EBG STRUCTURE

This section presents the experimental results for a low-profile coplanar-fed monopole antenna over the MEMS-reconfigurable EBG structure of Section 5.3. Figure 5.36 shows the layout of the antenna, which is 2.15mm long and 260μm wide. The aluminum antenna and ground plane are patterned on one side of a 5mil Kapton substrate. The antenna is fed by a coplanar waveguide with a 260μm wide centre conductor and 25μm gaps. The centre conductor is tapered to a 120μm width to fit the coplanar probes of the RF probe station used to measure the structure. If the antenna were isolated in free-space, the resonant frequency would be 34.9GHz. The measured resonant frequency will be significantly lower due to loading effects of the substrate and EBG structure as will be discussed below.

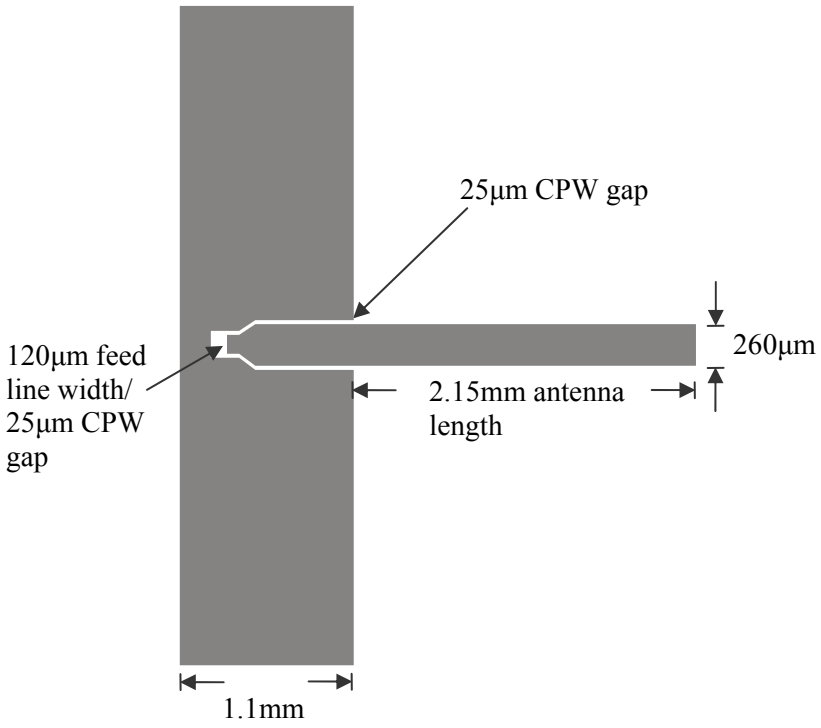

Figure 5.36: Coplanar-fed monopole antenna which is placed over the MEMS EBG structure

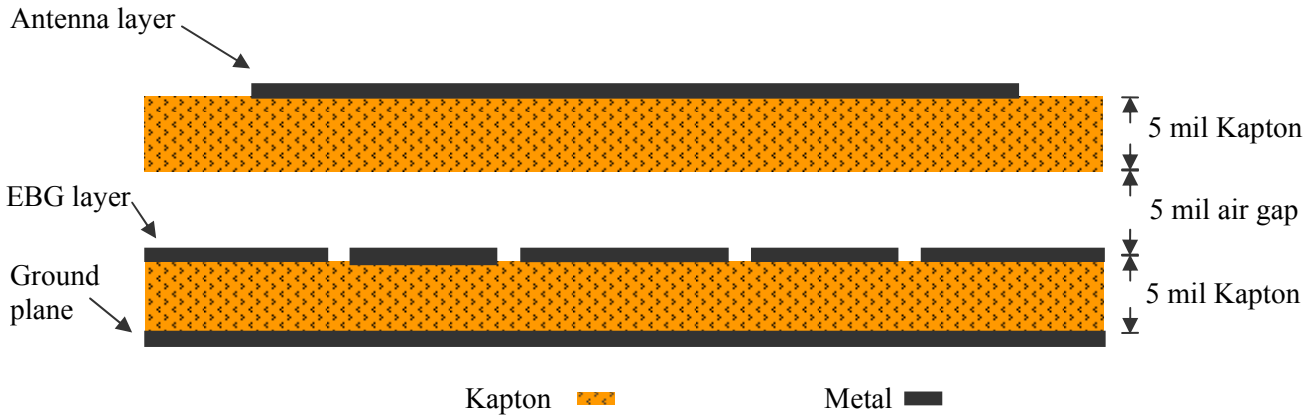

Figure 5.37: Cross-sectional view of the coplanar-fed monopole antenna on 5mil Kapton, separated from the MEMS-reconfigurable EBG structure by a 5mil air gap.

Figure 5.37 shows a cross-sectional view of the fabricated structure. The EBG is fabricated on 5mil Kapton as discussed in Section 5.3. The antenna structure is separated from the EBG by a 5mil air gap, which ensures the MEMS devices will not be damaged.

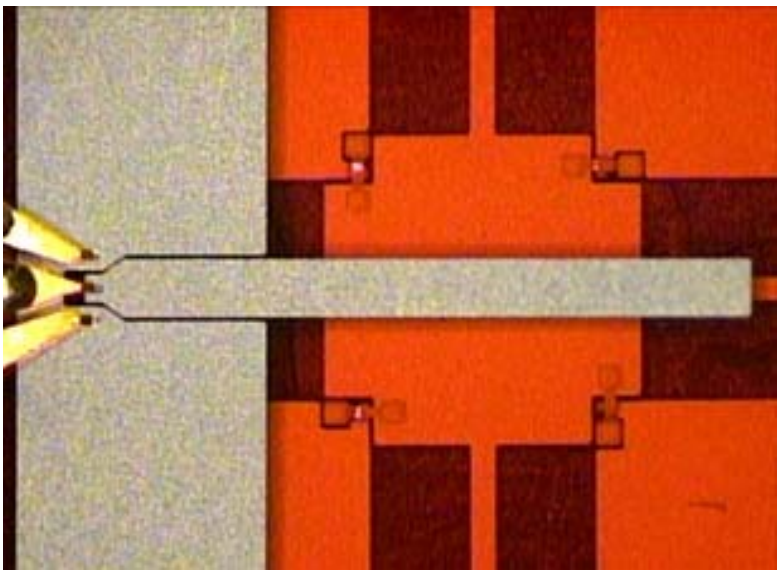

Figure 5.38: Test setup of the coplanar-fed monopole antenna on 5mil Kapton, separated from the MEMS-reconfigurable EBG structure by a 5mil air gap.

The antenna and EBG structure are measured using an RF probe station as shown in Figure 5.38. The coplanar waveguide probe connects to the monopole antenna input to measure the S_{11}. The EBG structure is biased, as in Section 5.3, to actuate the MEMS switched capacitors, which dynamically reconfigures the resonant characteristics of the antenna and EBG. The measured results are shown in Figure 5.39. With the bias off (MEMS capacitors in the up-state), there is a single resonance at 29.6GHz, with -7.9dB magnitude. Upon actuating the devices by turning the bias on, a second resonance appears at 22.5GHz with -7.4dB magnitude as a result of the additional capacitive loading. The original resonance experiences a slight shift to 29.8GHz with a -10.3dB magnitude when the bias is turned on.

As seen from the measured results of Figure 5.39, the EBG structure under a planar antenna adds an additional resonance to the low-profile structure when the MEMS devices

are actuated. Simulation of the entire structure using HFSS is quite onerous, and future work using more efficient modeling techniques is required for proper analysis. Further work is required to optimize the structure to improve performance. The experimental results presented here, however, provide insight into the capabilities of MEMS-based EBG structures as part of a conformal reconfigurable low-profile antenna system.

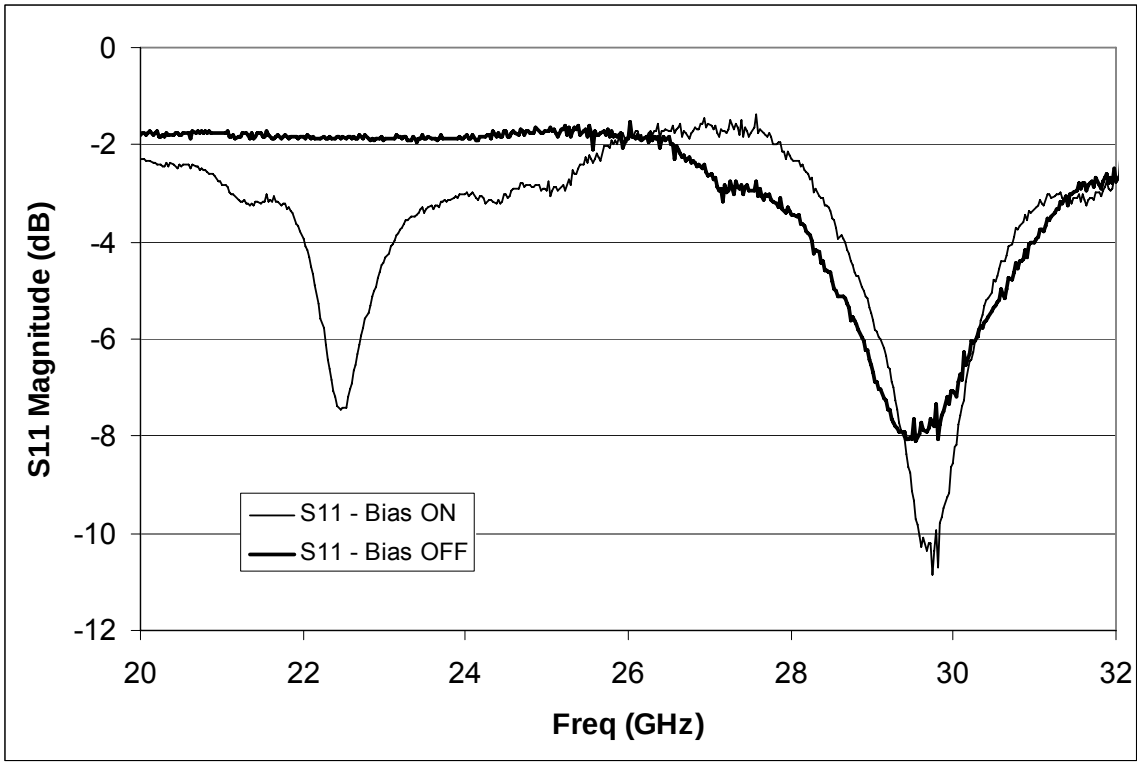

Figure 5.39: S_{11} measured at the input to the coplanar-fed monopole antenna positioned over the MEMS EBG structure as shown in Figure 5.38. Results are shown for the MEMS switched capacitors in the up-state (bias off) and the down-state (Bias on).

5.5 SUMMARY

This chapter has documented the design and measurement of MEMS-based reconfigurable electromagnetic structures fabricated using the newly developed process outlined in Chapter 4.

The first category of fabricated device is the reconfigurable frequency-selective surface which filters propagating electromagnetic waves. The FSS has a bandpass response that switches between the Ku and Ka bands, targeting satellite applications. The choice of design parameters were discussed in detail and a parametric sensitivity analysis established that the design is robust. The largest source of discrepancy between theoretical and measured results arose due to a small unwanted down-state air gap that resulted from the mechanical MEMS switched capacitor performance. Future work will eliminate this issue through improved mechanical design. When accounting for this non-ideal MEMS performance, good correlation was achieved between simulated and measured results for individual devices as well as the entire FSS structure.

The second category of fabricated device is a reconfigurable EBG structure designed to operate in the Ka band. The EBG design and theoretical performance were presented, and measured trends in EBG tuning performance correlated well with simulated results.

Several sources of error arose due to limitations of the test set used to measure both the FSS and the EBG. The results presented in this thesis are sufficient for proof of concept, but improvements in test strategy are essential to characterize structures with the level of accuracy necessary for practical designs.

The EBG structure under a planar antenna adds an additional resonance to the low-profile structure when the MEMS devices are actuated. Simulation of the entire structure using HFSS is quite onerous, and future work using more efficient modeling techniques is required for proper analysis. The experimental results, however, demonstrate the potential of this reconfigurable low-profile antenna.

CHAPTER 6

CONCLUSIONS

6.1 CONTRIBUTIONS

The most significant contributions of this thesis research are summarized as follows:

- A MEMS fabrication process has been developed to monolithically integrate high-performance MEMS devices onto a rigid-flex organic substrate using low-temperature processes [94]. Low-loss electromagnetic structures may be fabricated using this process since the rigid-flex substrate is all dielectric. The substrate maintains overall flexibility while providing mechanical support to the MEMS devices. The adaptation of each fabrication process step to handle flexible substrates has been documented. Furthermore, detailed information regarding material compatibility has been thoroughly studied.

- The newly-developed MEMS process has been used to fabricate a MEMS reconfigurable frequency-selective surface. A conformal FSS structure capable of switching between the Ku and Ka bands was fabricated and tested, with good correlation between simulated and measured results for individual devices as well as the entire FSS structure [94]. All devices were actuated simultaneously since a practical bias network was incorporated into the structure design. A parametric sensitivity analysis characterized the changes in electrical properties due to variations in the dielectric constant of the oxide and Kapton, as well as the sacrificial layer thickness. The newly-developed MEMS process has also been used to fabricate a Ka band MEMS reconfigurable electromagnetic bandgap structure. EBG hardware that was fabricated and tested showed good correlation between simulated and measured results. When the EBG structure is positioned under a planar antenna, an additional resonance arises in the low-profile structure when the MEMS devices are actuated.

- Frequency-switchable parasitic antenna arrays have been developed, fabricated and measured. The new structures offer improved range compared to conventional RFID systems since they radiate efficiently when placed over metal and absorbing material, as well as minimizing blind spots to provide continuous hemispherical coverage [91], [92].

- A novel analysis method has been developed to characterize frequency-switchable parasitic patch arrays. The purpose of the analysis is to provide an approximation of the input impedance and variation of the radiation pattern with frequency. The analysis is computationally efficient. It combines models based on electromagnetic theory and circuit theory to provide a reasonable approximation of the parasitic array characteristics. The new analysis method was validated alongside measured and simulated results, with good correlation for both impedance characteristics and far-field radiation patterns [93]. A novel MEMS-based switched parasitic antenna array has been designed, fabricated and measured with good correlation between simulated and measured results. The structure is a direct-coupled parasitic patch

array which is capable of frequency steering and has additional MEMS-enabled beam-steering capabilities at each frequency [93]. An EBG-based multi-mode radiating structure design was also presented, which is capable of frequency-switchable beam steering. The antenna area is significantly reduced compared to the parasitic patch array structure, but at a considerable cost in terms of gain and efficiency.

6.2 FUTURE WORK

Several areas of future work would expand on the research presented in this thesis. The following areas of future work expand on the ideas presented in Chapter 3:

- The frequency switchable antenna idea may be expanded to add additional parasitic elements as well as modifying the existing geometry to increase the number of resonant frequencies, allowing for greater control of the antenna pattern.
- A frequency switchable antenna with orthogonal mode resonant frequencies that all fit within an unlicensed band would have great potential as a commercially viable RFID product. Future work should endeavour to reduce the tuning bandwidth for frequency-switchable arrays.
- Investigations into impedance matching networks could be carried out to match the real parasitic antenna array impedance to the highly capacitive input impedance of passive RFID chips.
- An interesting project would be to develop a more generalized version of the parasitic array analysis technique. The result would be an augmented model that would include gap-coupled antennas, more diverse antenna structures, coupling between non-adjacent elements, multiple modes in parasitic elements as well as higher order modes.
- Future research could improve the performance, in terms of gain and efficiency, of frequency switchable antennas using EBG structures.

- The topology of the frequency-switchable patch arrays results in a different linear polarization for each of the two endfire modes. This property may benefit Multiple Input Multiple Output (MIMO) systems which utilize polarization diversity. Parasitic patch antenna arrays may be designed with multiple feed configurations which enable pattern reconfigurability and simultaneous communication via multiple polarizations at single or multiple frequency bands.

The following areas of future work expand on the ideas presented in Chapter 4:

- The Kapton substrate thermal expansion and interlayer stresses should be characterized in detail. This will enable the designer to compensate for geometry changes during fabrication by varying the size of masks to improve alignment and reduce minimum feature size. Additionaly, this information may be used to determine the operating temperature range of MEMS devices on Kapton substrates.
- The electrical properties of the Kapton substrate should be characterized after being subjected to the different fabrication process steps and temperature cycling.
- The MEMS fabrication process currently uses semiconductor fabrication equipment which limits the substrate dimensions to an 8 inch wafer size. Over the longer-term, converting the fabrication procedure to a large-area roll-to-roll process would greatly reduce cost and produce large-area structures that would lead to new applications.

The following areas of future work expand on the ideas presented in Chapter 5:

- The thick oxide dielectric resulted in mechanical performance limitations of the MEMS switches, specifically an undesirable small down-state air gap. The mechanical properties of the fabricated MEMS switches should be studied in detail, including the capacitance variation that was studied in the simulations of Figure 5.23. A future research project should focus on improving the mechanical MEMS design to use a thinner dielectric with smaller area to prevent excessive capacitive loading, as well as separate pull-down electrodes to maintain a reasonable actuation voltage.

- MEMS-based EBG designs having low losses should be investigated for conformal reflective beam-steering applications. Additionally, higher loss structures may also be investigated for conformal tunable absorber applications.
- The all-dielectric rigid-flex substrate would be amenable to reconfigurable electromagnetic structures based on ferroelectric materials. This approach may prove to have a better long-term reliability, and may become commercially viable for satellite and space exploration applications.

Appendix A

PARASITIC ANTENNA ARRAY ANALYSIS

This appendix provides a more detailed description of the coupled parasitic patch array analysis method outlined in Chapter 3. We begin by using a modified version of the coupling matrix model [69]-[70], which is traditionally used for filter analysis, combined with the patch antenna cavity model of [71]-[72] as described in Chapter 3. The combined circuit model and corresponding physical layout are shown in Figure A.1. As discussed in Chapter 3, each resonant mode of a patch antenna is represented by an RLC circuit, and all patch resonators are identical. The resistor R (shown in Figure A.1a) represents the radiated power, dielectric loss and finite conductivity, and is assumed constant at frequencies close to resonance. We obtain the RLC values using an electromagnetic simulator such as HFSS. The patches are numbered as shown in the physical layout of Figure A.1b.

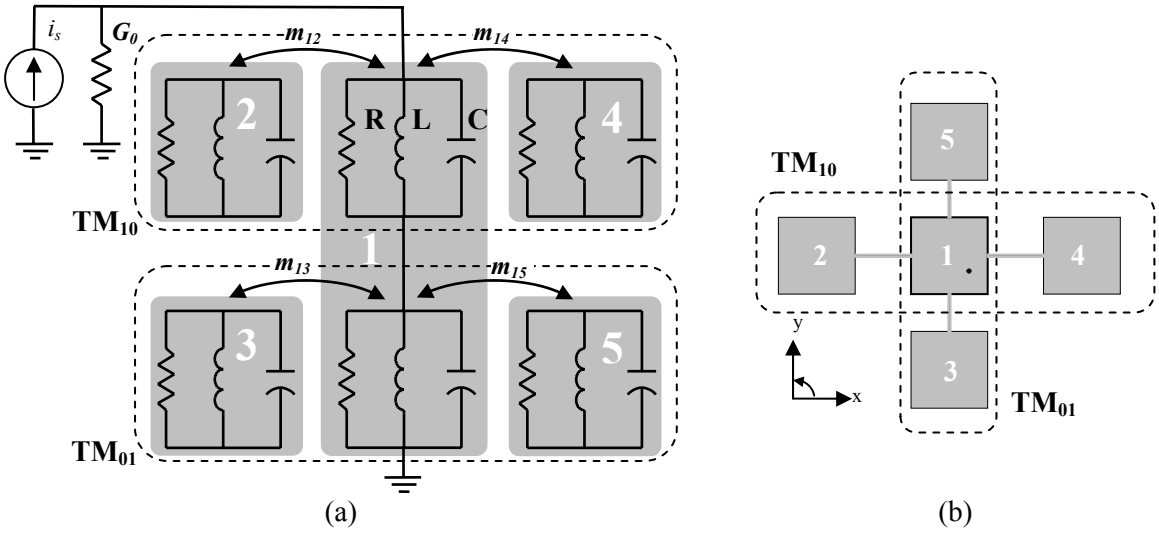

Figure A.1: (a) Equivalent circuit of the multi-mode parasitic patch array and (b) Physical layout of multi-mode parasitic patch array.

As a first-order approximation, it is assumed that there is no coupling between non-adjacent patch antennas and only a single mode is excited in the parasitic patches. Each mode

of the centre patch has a separate normalized admittance matrix. For the array of Figure A.1, patch numbers 2 and 4 couple to the centre patch TM_{10} mode, and patch numbers 5 and 3 couple to the centre patch TM_{01} mode. The normalized admittance matrix for a given TM_{mn} mode, which is a 3x3 matrix for the array of Figure A.1, is given by

$$Y_{TMmn} = \frac{1}{q} I + p_{mn} I - \mathrm{j} M_{TMmn} \,. \tag{A.1}$$

The matrix I is the identity matrix and q is the normalized unloaded resonator quality factor given by

$$q = \frac{R}{\omega_0 L} FBW \tag{A.2}$$

For the purpose of this analysis, the fractional bandwidth term FBW, typically used for filter design, has little meaning. We therefore set FBW to 1 since it cancels out at the end of the analysis.

The matrix M_{TMmn} of Equation (A.1) is the coupling matrix which consists of the coupling coefficients representing the mutual impedance between the coupled patch resonators. Following the analysis outlined in [70], the diagonal elements of the coupling matrix are zero for synchronously tuned resonators. The non-diagonal terms are the normalized coupling coefficients between the patches.

Coupling coefficients between two patches may be calculated from the electric (even-mode) and magnetic (odd-mode) coupling frequencies. As discussed in Chapter 3, an

effective way to determine the frequencies of electric and magnetic coupling is to simulate a patch antenna in HFSS with half of the coupling structure terminated, respectively, in an electric or magnetic wall as shown in Figure A.2.

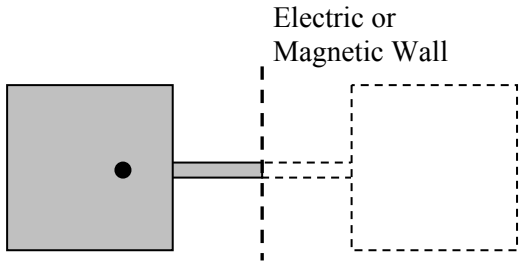

Figure A.2: Equivalent coupled patch antenna model for electric and magnetic wall analysis.

By simulating the electric and magnetic coupling frequencies, while varying the coupling line length, we may generate a set of design curves for any type of patch antenna. The coupling coefficient *k* may be calculated from [70] as

$$k = \frac{f_e^2 - f_m^2}{f_e^2 + f_m^2},$$

(A.3)

where f_e is the electric coupling frequency determined using the electric wall simulation. The value f_m is the magnetic coupling frequency determined using the magnetic wall simulation. The normalized elements for the coupling matrix in Equation (A.1) are given by [70]

$$m_{ij} = \frac{k_{i,j}}{FBW}.$$

(A.4)

Due to symmetry, coupling coefficients m_{10} and m_{01} are used to represent coupling to parasitic patches for the TM_{10} and TM_{01} modes respectively. It is important to note that the centre frequency of the coupled resonators changes with trace length due to loading caused by the transmission line effects of the coupling trace. The calculated coupled resonator centre frequency, for each centre patch mode, is the f_{nm} frequency in the expression for the normalized frequency variable p_{nm} given by

$$p_{10} = \mathrm{j}\frac{1}{FBW}\left(\frac{f}{f_{10}} - \frac{f_{10}}{f}\right) \tag{A.5}$$

for the TM_{10} mode, and

$$p_{01} = \mathrm{j}\frac{1}{FBW}\left(\frac{f}{f_{01}} - \frac{f_{01}}{f}\right) \tag{A.6}$$

for the TM_{01} mode. Combining Equations (A.1)-(A.6), a separate 3x3 admittance matrix may be written for the centre patch TM_{10} and TM_{01} modes coupling to the parasitic patches, respectively, as

$$Y_{TM10} = \left[\begin{pmatrix} \frac{1}{q} & 0 & 0 \\ 0 & \frac{1}{q} & 0 \\ 0 & 0 & \frac{1}{q} \end{pmatrix} + p_{10}\begin{pmatrix} 1 & 0 & 0 \\ 0 & 1 & 0 \\ 0 & 0 & 1 \end{pmatrix} - \mathrm{j}\begin{pmatrix} 0 & m_{10} & m_{10} \\ m_{10} & 0 & 0 \\ m_{10} & 0 & 0 \end{pmatrix}\right] \tag{A.7}$$

and

$$Y_{TM01} = \left[\begin{pmatrix} \frac{1}{q} & 0 & 0 \\ 0 & \frac{1}{q} & 0 \\ 0 & 0 & \frac{1}{q} \end{pmatrix} + p_{01} \begin{pmatrix} 1 & 0 & 0 \\ 0 & 1 & 0 \\ 0 & 0 & 1 \end{pmatrix} - \mathrm{j} \begin{pmatrix} 0 & m_{01} & m_{01} \\ m_{01} & 0 & 0 \\ m_{01} & 0 & 0 \end{pmatrix} \right].$$

(A.8)

The coupling coefficients m_{10} and m_{01} represent coupling between the parasitic patches and centre patch TM_{10} and TM_{01} modes respectively. The overall admittance matrix of the coupled patch array combines the admittance matrices for each centre patch mode as

$$Y = \begin{pmatrix} \frac{1}{q_e} & 0 & 0 \\ 0 & 0 & 0 \\ 0 & 0 & 0 \end{pmatrix} + \left({Y_{TM10}}^{-1} + {Y_{TM01}}^{-1} \right)^{-1}.$$

(A.9)

Following the analysis of [70], we add the reciprocal of the normalized external quality factor, given by

$$\frac{1}{q_e} = \frac{\omega_0 L G_0}{FBW},$$

(A.10)

to the matrix element $Y_{1,1}$ to account for the loading effects of the source impedance. The S_{11} is calculated as

$$S_{11} = \left[1 - \frac{2}{q_e} \left(Y^{-1} \right)_{1,1} \right]$$

(A.11)

The next step in the analysis is to calculate the radiation pattern, starting with the standard patch model as described in [73]. The two radiating slots of each patch antenna mode are modeled by two magnetic line sources with magnitude and phase directly proportional to the current input to the patch antenna [73]. The radiation from the individual patch antennas is combined, using an array factor, to model the overall far-field pattern of the array.

The electric field distribution under the patch antennas must first be calculated using the cavity model of [71]-[72], which is assumed to be the same for each identical patch antenna. Following the analysis of [71]-[72],

$$E(x,y) = \mathrm{j}\, k_0 \eta_0 \sum_{m=0}^{M} \sum_{n=0}^{N} \left(\frac{\phi_{mn}(x,y)\, \phi_{mn}(x_0, y_0)}{k^2 - k_{mn}{}^2} sinc\left(\frac{m \pi d}{2a} \right) sinc\left(\frac{n \pi d}{2b} \right) \right),$$

(A.12)

where a and b are the patch dimensions in the x and y directions, respectively. Since the substrate thickness is small compared to the wavelength, the field is assumed to be uniform in the z direction. The field expression includes the effects of higher order TM modes, where the values M and N correspond to the maximum order of modes to be included in the field calculation. The value d is the effective width of the feed, k_0 is the free-space propagation constant and η_0 is the free-space impedance. The values (x_0,y_0) are the feed position co-ordinates. The expression

$$\phi_{mn}(x,y) = \sqrt{\frac{\varepsilon_{0m}\, \varepsilon_{0n}}{a\, b}} cos\left(\frac{m \pi x}{a} \right) cos\left(\frac{n \pi y}{b} \right)$$

(A.13)

has values

$$\varepsilon_{0n} = \begin{cases} 1 & n = 0 \\ 2 & n > 0 \end{cases},$$

(A.14)

and

$$\varepsilon_{0m} = \begin{cases} 1 & m = 0 \\ 2 & m > 0 \end{cases}.$$

(A.15)

The expression

$$k = \sqrt{\varepsilon_r \left(1 - \mathrm{j}\, tan\delta\right) k_0{}^2}$$

(A.16)

models the relative substrate dielectric constant ε_r and loss tangent $tan\delta$. Finally, the expression for k_{mn} is given by

$$k_{mn} = \sqrt{\left(\frac{m\,\pi}{a}\right)^2 + \left(\frac{n\,\pi}{b}\right)^2}.$$

(A.17)

The current on the centre patch, which is used as the reference, is set to unity. The current on each parasitic patch arises due to the mutual coupling as discussed above. The relative parasitic patch current is therefore calculated from the admittance matrices for each centre patch $TM_{m,n}$ mode. The relative magnitude of the parasitic patch current for the TM_{10} coupled patches is

$$I_{p10} = \left| \frac{\left(Y_{TM10}{}^{-1} \right)_{i,1}}{\left(Y_{TM10}{}^{-1} \right)_{1,1}} \right|,$$

(A.18)

and the relative phase is given by

$$\theta_{p10} = arg\left[\frac{\left(Y_{TM10}{}^{-1} \right)_{i,1}}{\left(Y_{TM10}{}^{-1} \right)_{1,1}} \right].$$

(A.19)

The index *i* corresponds to a parasitic patch. Since the structure is symmetric, the current on each parasitic patch antenna coupled to the TM_{10} centre patch mode is the same, and therefore the index *i* may be set to either 2 or 3. Similarly, for the TM_{10} coupled patch antennas, the relative magnitude is

$$I_{p01} = \left| \frac{\left(Y_{TM01}{}^{-1} \right)_{i,1}}{\left(Y_{TM01}{}^{-1} \right)_{1,1}} \right|,$$

(A.20)

and the relative phase is given by

$$\theta_{p01} = arg\left[\frac{\left(Y_{TM01}{}^{-1}\right)_{i,1}}{\left(Y_{TM01}{}^{-1}\right)_{1,1}}\right], \tag{A.21}$$

where the index i may be set to either 2 or 3 as for the TM_{10} case. The relative current magnitude and phase values will be used as weighting functions in the array factors used to model the overall parasitic patch array. A separate array of magnetic line sources models each resonant mode. The equivalent antenna array for the centre patch TM_{10} mode, and x-directed parasitic patches, is shown in Figure A.3.

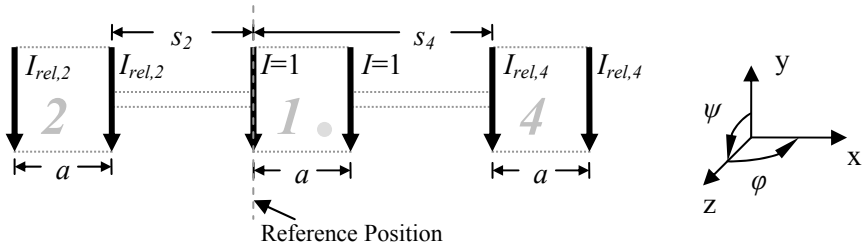

Figure A.3: Equivalent antenna array for the centre patch TM_{10} mode, and x-directed parasitic patches.

The following expression is the TM_{10} array factor for the equivalent arrangement of magnetic line sources shown in Figure A.3:

$$AF_{10}(\psi,\phi) = \left[\begin{array}{l} 1 + e^{\mathrm{j}k_0 a \sin(\psi)\sin(\phi)} \\ \quad \ldots \\ + I_{p10} e^{\mathrm{j}\theta_{p10}} e^{\mathrm{j}k_0(a+s_{10})\sin(\psi)\sin(\phi)} \\ \quad \ldots \\ + I_{p10} e^{\mathrm{j}\theta_{p10}} e^{\mathrm{j}k_0(s_{10}+2a)\sin(\psi)\sin(\phi)} \\ \quad \ldots \\ + I_{p10} e^{\mathrm{j}\theta_{p10}} e^{\mathrm{j}k_0(-s_{10})\sin(\psi)\sin(\phi)} \\ \quad \ldots \\ + I_{p10} e^{\mathrm{j}\theta_{p10}} e^{\mathrm{j}k_0-(s_{10}+a)\sin(\psi)\sin(\phi)} \end{array}\right]. \tag{A.22}$$

The value s_{10} is the spacing between x-directed patch antennas, a is the patch x-dimension, φ is the azimuthal angle in the xz plane and ψ is the polar angle. The radiated fields may be calculated using the aperture integration method to determine the equivalent magnetic line source [73]. From [73], the array factor and magnetic line sources are combined to calculate the vector potential of the centre path TM_{10} mode and x-directed parasitic patches using the expression

$$A_{my}(\psi,\phi) = -2h\left(\frac{\varepsilon_0}{4\pi r}e^{-\mathrm{j}k_0 r}AF_{10}(\psi,\phi)\right)\int_0^b E(x_m,y)\,e^{\mathrm{j}k_0 y\cos(\psi)}\,dy \quad \text{(A.23)}$$

The factor of 2 accounts for the simplification using image theory to double the strength of the magnetic source. The value h is the substrate thickness and x_m is the reference position along the x-axis as shown in Figure A.3. Since the far-field radiation patterns are normalized, the r radius term may be set to an arbitrary value. The electric and magnetic field values are calculated from the vector potential as

$$E_{\phi 10}(\psi,\phi) = -\mathrm{j}\,\omega\sqrt{\frac{\mu_0}{\varepsilon_0}}A_{my}(\psi,\phi)\sin(\psi), \quad \text{(A.24)}$$

and

$$H_{\psi 10}(\psi,\phi) = \mathrm{j}\,\omega A_{my}(\psi,\phi)\sin(\psi). \quad \text{(A.25)}$$

The TM_{01} mode radiation patterns are determined using a similar method. The equivalent antenna array for the centre patch TM_{01} mode, and y-directed parasitic patches, is shown in Figure A.4.

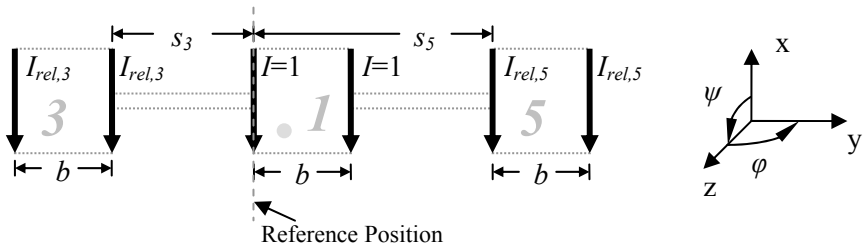

Figure A.4: Equivalent antenna array for the centre patch TM_{01} mode, and y-directed parasitic patches.

The following expression is the TM_{01} array factor for the equivalent arrangement of magnetic line sources shown in Figure A.4:

$$AF_{01}(\psi,\phi) = \left[\begin{array}{l} 1 + e^{\mathrm{j}\,k_0\,b\,\sin(\psi)\,\sin(\phi)} \\ \quad \ldots \\ + I_{p01}\,e^{\mathrm{j}\,\theta_{p01}}\,e^{\mathrm{j}\,k_0\,(b+s_{01})\,\sin(\psi)\,\sin(\phi)} \\ \quad \ldots \\ + I_{p01}\,e^{\mathrm{j}\,\theta_{p01}}\,e^{\mathrm{j}\,k_0\,(s_{01}+2\,b)\,\sin(\psi)\,\sin(\phi)} \\ \quad \ldots \\ + I_{p01}\,e^{\mathrm{j}\,\theta_{p01}}\,e^{\mathrm{j}\,k_0\,(-s_{01})\,\sin(\psi)\,\sin(\phi)} \\ \quad \ldots \\ + I_{p01}\,e^{\mathrm{j}\,\theta_{p01}}\,e^{\mathrm{j}\,k_0\,-\,(s_{01}+b)\,\sin(\psi)\,\sin(\phi)} \end{array}\right]. \tag{A.26}$$

The value s_{01} is the spacing between y-directed patch antennas, b is the patch y-dimension, and the polar angle ψ is offset by 90 degrees to account for the x-oriented magnetic line sources. The TM_{10} mode the vector potential of the y-directed array is calculated as

$$A_{mx}(\psi,\phi) = -2h\left(\frac{\varepsilon_0}{4\pi r}e^{-jk_0 r}AF_{01}(\psi,\phi)\right)\int_0^a E(x,y_{ref})\,e^{jk_0 x\cos(\psi)}\,dx \quad , \tag{A.27}$$

where y_m is the reference position along the y-axis as shown in Figure A.4. The electric and magnetic field values are calculated from the vector potential as

$$E_{\phi 01}(\psi,\phi) = -j\omega\sqrt{\frac{\mu_0}{\varepsilon_0}}A_{mx}(\psi,\phi)\sin(\psi) \quad , \tag{A.28}$$

and

$$H_{\psi 01}(\psi,\phi) = j\omega A_{mx}(\psi,\phi)\sin(\psi) \quad . \tag{A.29}$$

The overall radiation pattern of the parasitic patch array is calculated by adding the field expressions for the TM_{10} and TM_{01} modes. Note that the array factors of (A.22) and (A.26) assume the equivalent magnetic line sources for each half-wave patch antenna are in-phase, which is valid for the TM_{10} and TM_{01} modes. It may be necessary to add a phase shift of π radians for higher order modes where the two radiating slot magnetic currents, representing a single patch antenna, are out of phase.

Appendix B

MEMS ON RIGID-FLEX SUBSTRATE PROCESS INSTRUCTIONS

Process Instructions Part 1: Fabricate Rigid-Flex Organic Substrate

1-1: Sputter Silver onto Kapton to act as an Etch Mask for Substrate Etching

- Clean Kapton – acetone, then isopropyl alcohol (IPA) and then rinse with de-ionized (DI) water
- Immediately before metal deposition, bake Kapton film at 120C for 45min to remove absorbed moisture
- Place samples in Vacuum chamber and pump down immediately (Kapton may re-absorb moisture from the atmosphere within 10 minutes!)
- Sputter Silver onto the rough side of the Kapton for 55min 30s (1μm at 180Å/min)

1-2: Substrate Preparation for Silver and Kapton Etching:

- Protect smooth side of Kapton by spin-coating and soft-baking AZ3330 photoresist.
- Affix 2-sided Kapton tape to the protected smooth side of the Kapton circuit substrate.
- Affix substrate to GLASS rigid support wafer
- The metal to be patterned for the etch mask should be facing up, and the smooth side of the substrate is protected by the photoresist, wafer and double-sided tape
- Clean the silver-coated substrate with acetone and IPA. Scrubbing with a swab and IPA will remove any adhesive that may have contaminated the metal surface
- Rinse with DI water and dry
- The wafer is now ready to be processed using standard photolithography processes

1-3: Pattern Silver using Rigid-flex island pattern MASK.

- The silver acts as an etch mask for etching the bulk substrate to produce islands of thicker material which provide mechanical support to the MEMS devices.

Lithography Process:

- AZ3330 Photoresist
- Spin at 3000rpm for 30s
- Soft Bake (SB) 90˚C for 2min
- UV Exposure for 20s
- Post-Exposure Bake (PEB) 110˚C for 1.5min
- Develop for approx. 1min (depends on previous usage of developer)
- Inspect quality of patterned resist under microscope

Metal Etch Process (Silver)

- For fast etch, use undiluted gold etch at Room temperature (The gold etch works well for silver etching)
- Etching time approximately 2min for 1.5μm Silver
- Inspect quality of etching under microscope
- Remove positive photoresist using acetone
- Rinse with IPA, DI water and dry
- Substrate is now ready for KOH etching

1-4: Bulk substrate etch using potassium hydroxide (KOH).

Etchant:

- 9wt. % KOH in a solvent mixture of 80 wt. % ethanol and 20 wt. % water

Preparation:

- Use reagent-grade ethanol and DI water
- Mix 400 grams ethanol with 100 grams DI water
- Dissolve 48 grams reagent-grade KOH in the ethanol/water mixture
- Heat etchant to 70˚C (A setting of approximately 3.3 on the hotplate)
- Cover beaker to prevent vapour from escaping

KOH Etch Process

- Use wafer holder to place sample in beaker, ensuring the flexible circuit is completely covered by the etchant
- *NOTE: Etching is static, no agitation is required
- **Etch Step**: Leave in covered beaker for 15-18 minutes
- **Rinse step**: Remove sample, and rinse with flowing DI water for 5 min. This is extremely important since the etching products are insoluble in the etchant. The flowing water removes the etching products.
- Dry flexible substrate and bake at 100˚C for 30min
- Immerse Kapton substrate/supporting wafer in warm acetone to dissolve protective photoresist and carefully peel the rigid-flex Kapton away from the double-sided Kapton tape and glass wafer.
- After bake: Immerse in silver etchant to remove metal mask from the flexible substrate

Process Instructions Part 2: Fabricate MEMS Devices on Rigid-Flex Substrate

2-1: Substrate Preparation:

- Use laser or other tool to mark corners of island pattern to facilitate alignment of MEMS devices over the thicker substrate regions after metal has been deposited
- Acetone/IPA Wash, DI Water Rinse
- Inspect under microscope - Ensure smooth side faces up
- Pre-bake at maximum process temperature (250 C) for at least 1h to minimize changes in dimensions during processing
- Mount samples on vacuum chamber plate for high-temperature bake, and wrap in Al foil to avoid contamination from furnace oven
- *NOTE: Do not bake at high-temperatures prior to bulk KOH etch of substrate. The high-temperature bake increases Kapton resilience to etching, causing failure of rigid-flex substrate etching.

2-2: Bottom Metal Deposition

- Place samples in Intelvac sputter deposition system immediately after removing from dehydration/pre-shrink bake
- Use N2 gun to remove any particles prior to placing samples in Intelvac
- Sputter 1um Al

2-3: Pattern bottom metal layer using MASK 1

- Use Aluminum vacuum jig to support flexible substrate on spinner chuck
- Clean vacuum jig using acetone/IPA after spinning resist on each sample

Photolithography Process:

- Resist: AZ3330
- Spin 3K RPM, 30s
- SB 90C, 2min
- 40s exposure
- PEB 110C, 1.5min
- Develop 1-1.5min (depending on age of developer)
- No hard bake

Etch:

- PAN Etch, 38C (Approx. 3 on hotplate)
- Etch time: Approx. 4.5min for 1um Al
- Acetone/IPA Wash, DI Water Rinse

2-4: OXIDE Deposition

- Mount Samples on 6" Si wafer
- RIE 15s O2 plasma Descum
- Wrap mounted samples in Al foil to avoid contamination
- Furnace Oven Bake 250C for 45min
- Immediately place samples in PECVD

- PECVD Recipe: LT_Oxide (250C Oxide), 1230s

2-5: Pattern OXIDE using MASK 2

- Resist: AZ3330
- Spin 3K RPM, 30s
- SB 90C, 2min
- Expose 20s
- PEB 110C, 1.5min
- Develop 1min (New Developer)

2-6: OXIDE Etch

- Use 8:1 Buffered Hydrofluoric acid (BHF) Solution
- Static Etch - did not agitate
- Approx. 3min00s to 3min50s etch time for 1230s PECVD Oxide
- Significant undercut
- BHF Attacks Aluminum, but at a much slower etch rate than for oxide. Surface is noticeable roughened and appears white.
- After completing etch, Acetone/IPA wash, DI water rinse to remove photoresist

2-7: Deposit Sacrificial Layer (LOR15A)

- Set furnace oven to 190C, place glass Petri dish in oven for thermal stability
- Spin LOR15A at 2000rpm, accel. 10, 30s
- SB 160C, 4min
- Hard bake covered in glass Petri dish at 190C 30min (Furnace Oven)

2-8: Pattern Sacrificial Layer using AZ3312 – MASK 3

- Spin 3krpm
- SB 90C 2min
- Expose 24s for anchor (Dark-Field) mask
- PEB 1.5min
- Develop Approx. 4min (must develop LOR under patterning resist)
- No hard bake

2-9: Hydrofluoric Acid Dip

- Dip circuits in 8:1BHF for 20s to remove Al oxide and ensure DC contact between bottom and top metals

2-10: Remove Patterning Resist using Reactive Ion Etching (RIE)

Recipe:

- Pressure: 50mT
- Inductively-coupled Power (ICP): 250W
- RIE Power: 100W
- CF_4 gas flow: 2sccm
- O_2 gas flow: 48sccm
- Time: 20-39s

2-11: Top Metal Deposition

- Mount samples on plate for vacuum chamber plate
- Sputter 1um Al

2-12: Pattern Top Metal – MASK 4

- Mount samples on plate for vacuum chamber plate
- Resist: AZ3330
- Spin 3K RPM, 30s
- SB 90C, 2min
- Expose 20s
- PEB 110C, 1.5min
- Develop 1min (New Developer)

Etch:

- PAN Etch, 38C (Approx. 3 on hotplate)
- Etch time: Approx. 4.5min for 1um Al

2-13: Release MEMS Devices

- Mount samples on adhesiveless drying jigs
- Immerse in warm PG Remover for 15min
- Immerse in IPA for 5min
- Immerse in warm PG Remover for 15min
- Immerse in IPA for 5min
- Immerse in warm PG Remover for 10min
- IPA Rinse 1: 5min
- IPA Rinse 2: 5min
- IPA Rinse 3: 5min
- Use Supercritical Dryer to dry devices while preventing stiction

LIST OF ACRONYMS

ADS	Advanced Design System
C Band	4-8GHz microwave frequency band
CIRFE	Centre for Integrated Radio Frequency Engineering
CW	continuous wave
DI Water	deionized water
DRIE	deep reactive ion etch
EBG	electromagnetic bandgap
EM	electromagnetic
FHSS	frequency hopping spread spectrum
FR-4	fire-retardant 4
FSS	frequency-selective surface
HF	hydrofluoric acid
HFSS	High-Frequency Structure Simulator
IP	internet protocol
Ka Band	26.5-40GHz microwave frequency band
KOH	potassium hydroxide
Ku Band	12-18GHz microwave frequency band
LCP	liquid crystal polymer
MEMS	microelectromechanical systems
PAN Etch	phosphoric acid, acetic acid and nitric acid etchant mixture
PDMS	polydimethylsiloxane
PECVD	plasma enhanced chemical vapour deposition
RF	radio frequency
RFID	radio frequency identification
RIE	reactive ion etch
RLC	resistance, inductance and capacitance
SPST	single-pole single-throw
TMAH	tetra methyl ammonium hydroxide

WR 28 waveguide having single-mode operation over the frequency range of 26.5-40GHz

WR 42 waveguide having single-mode operation over the frequency range of 18-26.5GHz

WR 62 waveguide having single-mode operation over the frequency range of 12.4-18GHz

REFERENCES

[1] K. Finkenzeller, RFID Handbook, John Wiley & Sons Ltd., Chichester, 2003.

[2] G. Kumar and K. C. Gupta, "Directly coupled multiple resonator wide-band microstrip antennas," IEEE Trans. On Antennas and Propagation, v. 33, n. 6, pp. 588-593, June 1985.

[3] G. Kumar and K. C. Gupta, "Nonradiating edges and four edges gap-coupled multiple resonator broad-band microstrip antennas," IEEE Trans. On Antennas and Propagation, vol. 33, no. 2, pp. 173-178, Feb. 1985.

[4] G. Kumar and K. C. Gupta, "Broad-band microstrip antennas using additional resonators gap-coupled to the radiating edges," IEEE Trans. On Antennas and Propagation, vol. 32, no. 12, pp. 1375-1379, Dec. 1984.

[5] Kota, S.L., "Broadband satellite networks: trends and challenges," *2005 IEEE Wireless Communications and Networking Conference*, vol. 3, pp. 1472-1478, March 2005.

[6] Whitefield, D.; Gopal, R.; Arnold, S., "Spaceway now and in the Future: On-Board IP Packet Switching Satellite Communication Network,", MILCOM 2006, Oct. 2006.

[7] Le Boulc'h, D, "Which trends for future telecommunication satellites?", *2005 European Microwave Conference*, Vol. 1, Oct. 2005.

[8] Lutz, E.; Bischl, H.; Ernst, H.; Giggenbach, D.; Holzbock, M.; Jahn, A.; Werner, M., "Development and future applications of satellite communications,", *15th IEEE International Symposium on Personal, Indoor and Mobile Radio Communications*, vol. 4, pp. 2342 – 2346, Sept. 2004.

[9] DuPont High Performance Materials, U.S. Rt. 23 & DuPont Road, Circleville, OH, USA, www.dupont.com/kapton.

[10] T. K. Wu (ed.), "Frequency Selective Surface and Grid Array," Wiley, New York, 1995.

[11] B. Schoenlinner, A. Abbaspour-Tamijani, L.C. Kempel, G.M. Rebeiz, "Switchable low-loss RF MEMS Ka-band frequency-selective surface," *IEEE Trans. on Microwave Theory and Techniques*, vol. 52, no. 11, pp. 2474-2481, Nov. 2004.

[12] Chambers, B., "Progress towards reconfigurable electromagnetic structures," *IEE Colloquium on Advances in Electromagnetic Screens, Radomes and Materials*, pp. 4/1-4/6 Oct. 1996.

[13] Mias, C, "Varactor-tunable frequency selective surface with resistive-lumped-element biasing grids," IEEE Microwave and Wireless Components Letters, vol. 15, iss. 9, pp. 570-572, Sept. 2005.

[14] Chang, T.K.; Langley, R.J.; Parker, E., "An active square loop frequency selective surface," IEEE Microwave and Guided Wave Letters, pp. 387-388, vol. 3, iss. 10, Oct. 1993.

[15] Chang, T.K.; Langley, R.J.; Parker, E.A., "Frequency selective surfaces on biased ferrite substrates," Electronics Letters, vol. 30, iss. 15, pp. 1193-1194, July 1994.

[16] F. Jiang et al., "A Flexible MEMS Technology and its First Application to Shear Stress Sensor Skin," *Proc. IEEE MEMS-97 Workshop*, pp. 465-470, 1997.

[17] T. Lisby, O. Hansen and J. Branebjerg "Fabrication and Characterization of Flexible Silicon Substrates with Electroplated Gold Leads," *Proc. IEEE Sensors 2002*, vol. 1, pp. 568-571, 2002.

[18] Sievenpiper, D., Lijun Zhang, Broas, R.F.J., Alexopolous, N.G., Yablonovitch, E., "High-Impedance Electromagnetic Surfaces with a Forbidden Frequency Band," IEEE Trans. On Microwave Theory and Techniques, vol. 47, no. 11, pp. 2059-2074, Nov. 1999.

[19] Sievenpiper, D.F., Schaffner, J.H., Song, H.J., Loo, R.Y., Tangonan, G., "Two-dimensional beam steering using an electrically tunable impedance surface," *IEEE Transactions on Antennas and Propagation*, vol. 51, iss.10, pp. 2713-2722, Oct. 2003.

[20] Mias, C.; Yap, J.H., "Lumped-element loaded metamaterial structure," *36th European Microwave Conference*, pp. 1566-1569, Sept. 2006.

[21] Liang, T., Li, L., Bossard, J.A., Werner, D.H., Mayer, T.S., "Reconfigurable ultra-thin EBG absorbers using conducting polymers," *2005 IEEE Antennas and Propagation Society International Symposium*, vol. 2B, pp. 204-207, July 2005.

[22] Kern, D.J., Bossard, J.A., Werner, D.H., "Design of reconfigurable electromagnetic bandgap surfaces as artificial magnetic conducting ground planes and absorbers," *2006 IEEE Antennas and Propagation Society International Symposium*, pp. 197-200, Jul. 2006.

[23] J. H. Yap, C. Mias, "Tunable absorber based on electromagnetic band gap surface and a lossy resistance sheet," IEE Wideband and Multi-band Antennas and Arrays, pp. 171-175, Sept. 2005.

[24] de Maagt, P., Gonzalo, R., Vardaxoglou, Y.C., Baracco, J.-M., "Electromagnetic bandgap antennas and components for microwave and (Sub)millimeter wave applications," *IEEE Transactions on Antennas and Propagation*, vol. 51, iss. 10, pp. 2667-2677, Oct. 2003.

[25] Association for Automatic Identification and Mobility, "Radio Frequency Identification – RFID: A Basic Primer," AIM WP-98/002R White Paper, http://www.aimglobal.org, 1999.

[26] N. Akamatsu *et al.*, "Fabrication and Evaluation of a Silicon Probe Array on a Flexible Substrate for Neural Recording," *Proc. Of the 25th Annual International Conference of the IEEE EMBS*, pp. 3802-3805, 2003.

[27] A. Mahmood et al., "Micromachined Infrared Sensor Arrays on Flexible Polyimide Substrates," *Proc. IEEE Sensors 2003*, vol. 2, pp. 777-782, 2003.

[28] A. Yaradanakul et al., "Fabrication of Micromachined Devices on Flexible Substrates," *2001 IEEE Symposium on Emerging Technologies*, pp. 79-83, 2001.

[29] C. Li et al., "Polymer Flip-Chip Bonding of Pressure Sensors on Flexible Kapton Film for Neonatal Catheters," *17th IEEE International Conference on MEMS*, pp. 749-752, 2004.

[30] G. Wang, D. Thompson, E. M. Tentzeris and J. Papapolymerou, "Low cost RF MEMS switches using LCP substrate," *34th European Microwave Conference*, vol. 3, pp. 1441–1444, Oct. 2004.

[31] N. Kingsley, G. Wang and J. Papapolymerou, "14 GHz microstrip MEMS phase shifters on flexible, organic substrate," *2005 European Microwave Conference*, vol. 1, 3 pp., Oct. 2005.

[32] X Wang, J Engel and C Liu, "Liquid crystal polymer (LCP) for MEMS: processes and applications," *J. Micromech. Microeng.*, vol. 13, no. 5, pp. 628-633, Sept. 2003.

[33] Q.X. Zhang, A.B. Yu, L.H. Guo, R. Kumar, K.W. Teoh, A.Q. Liu, G.Q. Lo, and D.-L Kwong, "RF MEMS switch integrated on printed circuit board with metallic membrane first sequence and transferring," *IEEE Electron Device Letters*, vol. 27, no. 7, pp. 552–554, July 2006.

[34] Q.X. Zhang, A.B. Yu, L.H. Guo, R. Kumar, K.W. Teoh, A.Q. Liu, G.Q. Lo, and D.-L Kwong, "Development of RF MEMS Switch on Flexible Organic Substrate with Wafer Transfer Technology (WTT)," *Proceedings of the 56th Electronic Components and Technology Conference*, pp. 523-527, 30 May-2 June 2006.

[35] A. C. de C Lima, E. A. Parker and R. J. Langley, "Tunable frequency selective surface using liquid substrates," Electronics Letters, vol. 30, no. 4, pp. 281-282, Feb. 1994.

[36] D. Lockyer, C. Moore, R. Seager, R Simpkin and J. C. Vardaxoglou, "Coupled dipole arrays as reconfigurable frequency selective surfaces," Electronics Letters, vol. 30, no. 16, pp. 1258-1259, Aug. 1994.

[37] D. S. Lockyer, C. Vardaxoglou, "Reconfigurable FSS response from two layers of slotted dipole arrays," Electronics Letters, vol. 32, no. 6, pp. 512-513, March 1996.

[38] P. Edenhofer and A. Alpaslan, "Active frequency selective surfaces for antenna applications electronically to control phase distribution and reflective/transmissive amplification," 2005 IEEE/ACES International Conference on Wireless Communications and Applied Computational Electromagnetics, pp. 237-240, April 2005.

[39] C. Mias, "Waveguide and free-space demonstration of tunable frequency selective surface," Electronics Letters, vol. 39, no. 11, pp. 850-852, May 2003.

[40] C. Mias, "Tunable C-band frequency selective surface," IEE Wideband and Multi-band Antennas and Arrays, pp. 165-169, Sept. 2005.

[41] A. E. Martynyuk, J. I. M. Lopez, N. A. Martynyuk, "Active frequency-selective surfaces based on loaded ring slot resonators," Electronics Letters, vol. 41, no. 1, pp. 2-4, Jan 2005.

[42] J.P. Gianvittorio, J. Zendejas, Y. Rahmat-Samii and J. Judy, "Reconfigurable MEMS-enabled frequency selective surfaces," Electronics Letters, vol. 38, no. 25, pp. 1627-1628, Dec. 2002.

[43] J.P. Gianvittorio, J. Zendejas, Y. Rahmat-Samii and J. Judy, "MEMS enabled reconfigurable frequency selective surfaces: design, simulation, fabrication, and measurement," 2002 IEEE Antennas and Propagation Society International Symposium, vol. 2, pp. 404-407, June 2002.

[44] J. M. Zendejas, J. P. Gianvittorio, Y. Rahmat-Samii and J. Judy, "Magnetic MEMS reconfigurable frequency-selective surfaces," Journal of Microelectromechanical Systems, vol. 15, no. 3, pp. 613-623, June 2006.

[45] J. S. Blakemore, "Solid State Physics, Second Edition," W. B. Saunders Company, Philadelphia, 1974.

[46] R. E. Collin, "Foundations for Microwave Engineering, Second Edition," McGraw-Hill, Inc., New York, 1966.

[47] J.-C. Chiao, "MEMS RF devices for antenna applications," *2000 Asia-Pacific Microwave Conference*, pp. 895–898, Dec. 2000.

[48] M.F. Karim *et al*, "CPW band-stop filter using unloaded and loaded EBG structures," *IEE Proceedings - Microwaves, Antennas and Propagation*, pp. 434-440, Dec. 2005.

[49] X. J. Zhang *et al*, "MEMS-based photonic bandgap (PBG) band-stop filter," *2004 IEEE MTT-S International Microwave Symposium Digest*, vol. 3, pp. 1463-1466, June 2004.

[50] M.F. Karim *et al*, "MEMS-based tunable bandstop filter using electromagnetic bandgap (EBG) structures," *2005 Asia-Pacific Conference Microwave Conference Proceedings*, vol. 3, 4pp., Dec. 2005.

[51] J.C. Vardaxoglou, A. Chauraya and P. de Maagt, "Reconfigurable electromagnetic band gap based structures with defects for MM wave and antenna applications," *Twelfth International Conference on Antennas and Propagation*, vol. 2, pp. 763-766, April 2003.

[52] F. Martin *et al.*, "Frequency tuning in electromagnetic bandgap nonlinear transmission lines," *Electronics Letters*, vol. 39, no. 5, pp. 440-442, March 2003.

[53] E. Pistono et al., "Hybrid Narrow-Band Tunable Bandpass Filter Based on Varactor Loaded Electromagnetic-Bandgap Coplanar Waveguides," *IEEE Transactions on Microwave Theory and Techniques*, vol. 53, no. 8, pp. 2506-2514, Aug. 2005.

[54] V. Sanchez and E. Paller, "A tunable artificial magnetic conductor using switched capacitance in a concentric overlapping geometry," *2003 IEEE Antennas and Propagation Society International Symposium*, vol. 2, pp. 439-442, June 2003.

[55] M.G. Bray and D.H. Werner, "A novel design approach for an independently tunable dual-band EBG AMC surface," *2004 IEEE Antennas and Propagation Society International Symposium*, vol. 1, pp. 289-292, June 2004.

[56] M.G. Bray, Z. Bayraktar and D.H. Werner, "GA optimized ultra-thin tunable EBG AMC surfaces," *2006 IEEE Antennas and Propagation Society International Symposium*, pp. 410-413, July 2006.

[57] M.G. Bray and D.H. Werner, "A broadband open-sleeve dipole antenna mounted above a tunable EBG AMC ground plane," *2004 IEEE Antennas and Propagation Society International Symposium*, vol. 2, pp. 1147-1150, June 2004.

[58] J.A Higgins, H. Xin and A. Sailer, "Characteristics of Ka band waveguide using electromagnetic crystal sidewalls," *2002 IEEE MTT-S International Microwave Symposium Digest*, vol. 2, pp. 1071-1074, June 2002.

[59] J.A Higgins, H. Xin , A. Sailer and M. Rosker, "Ka-band waveguide phase shifter using tunable electromagnetic crystal sidewalls," *IEEE Transactions on Microwave Theory and Techniques*, vol. 51, no. 4, Part 1, pp. 1281–1288, April 2003.

[60] D. Chicherin *et al*, "Millimetre Wave Phase Shifters Based on a Metal Waveguide with a MEMS-Based High-Impedance Surface," *36th European Microwave Conference*, pp. 372-375, Sept. 2006.

[61] G. Kumar and K. C. Gupta, "Directly coupled multiple resonator wide-band microstrip antennas," *IEEE Trans. On Antennas and Propagation*, v. 33, n. 6, pp. 588-593, June 1985.

[62] G. Kumar and K. C. Gupta, "Nonradiating edges and four edges gap-coupled multiple resonator broad-band microstrip antennas," *IEEE Trans. On Antennas and Propagation*, vol. 33, no. 2, pp. 173-178, Feb. 1985.

[63] G. Kumar and K. C. Gupta, "Broad-band microstrip antennas using additional resonators gap-coupled to the radiating edges," *IEEE Trans. On Antennas and Propagation*, vol. 32, no. 12, pp. 1375-1379, Dec. 1984.

[64] RADANT MEMS Inc., 255 Hudson Road, Stow, MA, USA, www.radantmems.com.

[65] M. L. Ng, K. S. Leong and P. H. Cole, "Analysis of Constraints in Small UHF RFID Tag Design," *2005 IEEE International Symposium on Microwave, Antenna, Propagation and*

EMC Technologies for Wireless Communications Proceedings, vol. 1, pp. 507 – 510, Aug. 2005.

[66] P. V. Nikitin, et al, "Power Reflection Coefficient Analysis for Complex Impedances in RFID Tag Design," *IEEE Trans. on Microwave Theory and Techniques*, vol. 53, no. 9, pp. 2721-2725, Sept. 2005.

[67] I. J. Bahl, "Broadband and Compact Impedance Transformers for Microwave Circuits," *IEEE Microwave Magazine*, pp. 56-62, Aug. 2006.

[68] www.semiconductors.philips.com.

[69] R. J. Cameron, "The Analysis, Synthesis and Multiplexion of Bandpass Dual-Mode Filters," *ESA J.*, vol. 1, pp. 177-188, 1977.

[70] J.-S. Hong and M. J. Lancaster, Microstrip Filters for RF/ Microwave Applications, Wiley, New York, 2001.

[71] Y. T. Lo, D. Soloman and W. F. Richards, "Theory and Experiment on Microstrip Antennas," *IEEE Trans. on Antennas and Propagation*, vol. AP-27, no. 2, pp. 137-145, March 1979.

[72] W. F. Richards, Y. T. Lo, D. D. Harrison, "An Improved Theory for Microstrip Antennas and Applications," *IEEE Trans. on Antennas and Propagation*, vol. AP-29, no. 1, pp. 38-46, January 1981.

[73] R. E. Collin, Antennas and Radiowave Propagation, McGraw-Hill, Inc., New York, 1985.

[74] "Summary of Properties for Kapton Polyimide Films," DuPont High Performance Materials, U.S. Rt. 23 & DuPont Road, Circleville, OH, USA, www.kapton.com.

[75] A. Sazonov and A. Nathan, "120˚C fabrication technology for a-Si:H thin film transistors on flexible polyimide substrates," *J. Vac. Sci. Technology A* 18(2), pp. 780-782, March/April 2000.

[76] M. Daneshmand, "Multi-Port RF MEMS Switches and Switch Matrices," E&CE Dept., University of Waterloo, Waterloo, Ontario, Canada, 2006.

[77] S. Chang, "Design, Optimization and Fabrication of Amorphous Silicon Tunable RF MEMS Inductors and Transformers," E&CE Dept., University of Waterloo, Waterloo, Ontario, Canada, 2006.

[78] K.R Williams, and R. S. Muller, "Etch rates for micromachining processing," *Journal of Microelectromechanical Systems*, vol. 5, iss. 4, pp. 256–269, Dec. 1996.

[79] K.R.Williams, K. Gupta and M. Wasilik, "Etch rates for micromachining processing-Part II," *Journal of Microelectromechanical Systems*, vol.12, iss. 6, pp. 761-778, Dec. 2003.

[80] "Chemical Exposure Data for Kapton 100HN and 200HN Polyimide Film," DuPont High Performance Materials, U.S. Rt. 23 & DuPont Road, Circleville, OH, USA.

[81] "Adhesion to Kapton Technical Bulletin," DuPont High Performance Materials, U.S. Rt. 23 & DuPont Road, Circleville, OH, USA.

[82] Transene Company, Inc. Danvers Industrial Park, 10 Electronics Avenue, Danvers, MA, USA, www.transene.com.

[83] "AZ 3300 Series Crossover Photoresists Datasheet," AZ Electronic Materials, Somerville, NJ, USA, www.az-em.com.

[84] "LOR and PMGI Resists Datasheet," MicroChem Corp., 1254 Chestnut Street, Newton, MA, USA, www.microchem.com.

[85] "Faster Caustic Etching of Kapton H, E, and KN Types," DuPont High Performance Materials, U.S. Rt. 23 & DuPont Road, Circleville, OH, USA, www.dupont.com/kapton.

[86] DuPont Electronic Materials, 14 T.W. Alexander Drive, Research Triangle Park, NC, USA, www.pyralux.com.

[87] Rogers Corporation, One Technology Drive, PO Box 188, Rogers, CT, USA, www.rogerscorporation.com.

[88] HD Microsystems, 250 Cheesequake Road, Parlin, NJ, USA, www.hdmicrosystems.com.

[89] MicroChem Corp., 1254 Chestnut Street, Newton, MA, USA, www.microchem.com.

[90] G. M. Rebeiz, "RF MEMS Theory, Design, and Technology," John Wiley & Sons, Inc., Hoboken, New Jersey, 2003.

[91] G.M. Coutts, R. R. Mansour, S. K. Chaudhuri and W.-C. Tang, "Multi-Mode Parasitic Antenna Array," U.S. Patent Application serial no. 11/422,238, Date of Filing June 5, 2006.

[92] G. M. Coutts, R. R. Mansour and S. K. Chaudhuri, "A Frequency-Steerable Multi-Mode Parasitic Patch Array for Passive RFID Applications," *2006 IEEE MTT-S International Microwave Symposium*, June 2006. **Fourth Place Student Paper Award**

[93] G. M. Coutts, R. R. Mansour and S. K. Chaudhuri, "Analysis Technique for Frequency-Switchable and MEMS-Based Multi-Mode Parasitic Patch Arrays," *submitted to IET Microwaves, Antennas & Propagation.*

[94] G. M. Coutts, R. R. Mansour and S. K. Chaudhuri, "A MEMS-Tunable Frequency-Selective Surface Monolithically Integrated on a Flexible Substrate," *2007 IEEE MTT-S International Microwave Symposium*, June 2007.

[95] G. M. Coutts, R. R. Mansour and S. K. Chaudhuri, "A MEMS-based electronically steerable switched parasitic antenna array," *2005 IEEE APS International Microwave Symposium*, July 2005.